Title
Electronic, optical, and phononic properties of graphene, boron nitride, and related materials

Author
PARK, CHEOL HWAN

Publication Date
2009

Peer reviewed|Thesis/dissertation

Electronic, optical, and phononic properties of graphene, boron nitride, and related materials

by

Cheol Hwan Park

A dissertation submitted in partial satisfaction of the
requirements for the degree of
Doctor of Philosophy

in

Physics

in the

GRADUATE DIVISION
of the
UNIVERSITY OF CALIFORNIA, BERKELEY

Committee in charge:
Professor Steven G. Louie, Chair
Professor Eugene E. Haller
Professor Michael F. Crommie

Fall 2009

The dissertation of Cheol Hwan Park, titled Electronic, optical, and phononic properties of graphene, boron nitride, and related materials, is approved:

Chair Date

Date

Date

University of California, Berkeley

Electronic, optical, and phononic properties of graphene, boron nitride, and related materials

Abstract

Electronic, optical, and phononic properties of graphene, boron nitride, and related materials

by

Cheol Hwan Park
Doctor of Philosophy in Physics

University of California, Berkeley

Professor Steven G. Louie, Chair

Since the isolation of graphene, a single layer of carbon atoms in honeycomb structure, in 2004, this new material has gotten huge attention from communities in physics, chemistry, materials science, and engineering not only because the charge carriers of graphene show neutrino-like linear energy dispersion as well as chiral behavior near the Dirac point but also because graphene is considered to be a promising candidate for nano- and micro-scale electronic and spintronic device applications.

On the other hand, a hexagonal sheet of boron nitride has a similar honeycomb-like structure, except that the two different sublattices are occupied by boron and nitrogen atoms, respectively. Notwithstanding its structural similarity to graphene, a hexagonal boron nitride sheet is an insulator with a large bandgap and is considered to be useful for optical applications such as ultra-violet lasers.

In this work, we investigate the electronic, optical, and vibrational properties of graphene, hexagonal boron nitride, and related materials such as nanotubes or nanoribbons from first-principles calculations as well as from simple model considerations.

In the first chapter, we briefly review the methodologies used in our work such as density functional theory, the GW approximation, the Bethe-Salpeter equation method, and density functional perturbation theory.

In the following four chapters (2–5), we discuss the calculated spectral features of graphene and compare the results mainly with recent angle-resolved photoemission experiments. In our work, we have explicitly taken into account the effects of electron-electron and electron-phonon interactions from first-principles. Our calculations reproduce some of the key experimental observations related to many-body effects, including a mismatch between the upper and lower halves of the Dirac cone and the non-trivial energy dependence of carrier linewidths on the binding energy.

The following three chapters (6–8) are on bilayer graphene. In chapters 6 and 7, we discuss the effects of many-body interactions on the dynamics of electrons and phonons in bilayer graphene, in similar ways as in chapters 2 to 5. We show that the interlayer interaction between the two graphene layers change electron-phonon and electron-electron

interactions. In chapter 8, we discuss the excitons in biased bilayer graphene. We show that bound excitons qualitatively change the optical response of this novel material.

In the following four chapters (9–12), we discuss the interesting behaviors of charge carriers in graphene subjected to an external periodic potential. For example, we show that the carrier group velocity is anisotropically reduced and that, under certain conditions, electrons can be supercollimated. We also discuss newly generated massless Dirac fermions in graphene superlattices as well as their signatures in quantum Hall conductance measurements.

In chapter 13, we discuss the possibility of generating massless Dirac fermions in a conventional two-dimensional electron gas with an external periodic potential, i. e. , a way of making artificial graphene.

In the last four chapters, we discuss several different aspects of boron nitride compounds. In chapter 14, we present the calculated electronic energy bandgaps and effective masses of boron nitride nanoribbons and their changes in response to a transverse electric field. In chapters 15 and 16, we discuss excitons and optical response of boron nitride nanotubes and bulk hexagonal boron nitride, respectively. Finally, in the last chapter, we discuss a novel behavior of electric dipole moment reversal upon hydrogen passivation in boron nitride as well as other III-V or II-VI compound nanostructures.

To my parents who have raised me and Young Hwan with love and sacrifice.

Contents

List of Figures

List of Tables

Acknowledgments

First and foremost, I would like to thank my advisor, Prof. Steven G. Louie, for his care, guidance, advice, and support during all the years of my doctoral studies. Under his excellent guidance, I could work on several important topics of condensed matter research. If there was any improvement in me as a physicist during the past several years, it is entirely due to him. I also thank him and Mrs. Louie for their kind invitations to the annual thanksgiving dinners, which will remain as the best part of my memory of Berkeley.

I would like to thank Prof. Marvin L. Cohen for his various kinds of care, advice, and warm guidance, which helped me greatly in the course of my studies. It was bliss for me to see his wisdom revealed on several different occasions and his care for people whom he even does not know, let alone for his own people.

I would like to thank Prof. Jisoon Ihm for his guidance and support since I was a high-school student. I also thank him for introducing the movie 'The Graduate' to me when I was more interested in going to Harvard for graduate studies partly because of the movie 'Love Story'.

It was a pleasure to collaborate with Prof. Alex Zettl, Prof. Mike Crommie, Prof. Feng Wang, Caglar, Yuanbo, Victor, and Sebastian, from whom I could learn what important things in experiments are. Fruitful discussions with Prof. Alessandra Lanzara and Dr. Eli Rotenberg are also gratefully acknowledged.

I thank Prof. Eugene Haller, Prof. Mike Crommie, and Prof. Alessandra Lanzara for their service as the committee members of my qualifying examination, and for their helpful advice.

I am indebted to Katherine de Raadt for her kindness and caring help. Because of her, I could concentrate on my research without worrying about many other important things. I must also acknowledge the excellent help of Anne Takizawa and Donna Sakima.

Catalin and Feliciano have been great and patient teachers to me. I am grateful to Li for our fruitful collaborations. I thank Young-Woo, Liang, and Sangkook for the collaborations on graphene superlattices. I thank all the past and present Cohen-Louie group members for their help in physics, computer codes, and life. I especially thank Georgy for his kind help regarding to graphene and nanotubes.

I started gaining weight and learning to think by myself when Jay, the best person to play tennis with and the best person to discuss physics with, left for Maryland. I thank Manos for his help and advice ever since I joined the Louie group. For example, when I was depressed for the data loss, he tried to encourage me by saying that data loss is one of the three unavoidable things in life. I am grateful to my office mates Amy and Jesse for always being kind and nice. I thank Hoonkyung and Sheng for the pleasant conversations on the bus and over dinners.

I thank my non-academic friends Sang Ryul, Eunhwa, Yoon Pyo, Byung-Ick, Chan-Ho, Kyung-Sik, and Seungwan who have gathered at my place every Saturday evening for chatting and playing cards. My life in Berkeley was never boring because of these guys.

Last but not the least, I thank my parents, my brother Young Hwan, and my lovely wife Hee Won for their love and support. I especially thank Hee Won for enjoying her life here.

Chapter 1

Theoretical methods

1.1 Density functional theory

1.1.1 Introduction

It is in general impossible to calculate the electronic properties of realistic systems by solving the interacting many-electron Hamiltonian [11]:

$$\hat{H}_{\rm el} = -\frac{\hbar}{2m_e}\sum_i \nabla_i^2 + \sum_i V_{\rm ext}(\mathbf{r}_i) + \frac{1}{2}\sum_{i\neq j}\frac{e^2}{|\mathbf{r}_i - \mathbf{r}_j|}\,. \tag{1.1}$$

According to the density-functional theory, however, any ground-state property of a system of many interacting electrons can be viewed as a functional of the ground state density $n_0(\mathbf{r})$, a simple scalar function of the position $\mathbf{r}$. The density-functional theory makes the problem at hand tractable because one does not have to deal with the many-particle wavefunction directly.

1.1.2 The Hohenberg-Kohn theorems

The first theorem of Hohenberg and Kohn is that for any system of interacting particles in an external potential $V_{\rm ext}(\mathbf{r})$, the potential $V_{\rm ext}(\mathbf{r})$ can be determined uniquely, except for a constant, by the ground state particle density $n_0(\mathbf{r})$ [12]. A direct consequence of this theorem is that, since the Hamiltonian is uniquely determined within an arbitrary constant, all properties of the system in principle are completely determined by the ground state density $n_o(\mathbf{r})$ only.

The second theorem of Hohenberg and Kohn is that for any particular $V_{\rm ext}(\mathbf{r})$, the exact ground state density $n_0(\mathbf{r})$ minimizes the universal energy functional $E[n]$ [12]. According to this second theorem, the functional $E[n]$ alone is sufficient to determine the exact ground state energy and charge density.

However, density-functional theory does not provide a practical way to calculate the properties of a material from the density, although it should be sufficient in principle. The Kohn-Sham Ansatz enables this task.

1.1.3 The Kohn-Sham equation

Density functional theory is widely used today for electronic structure calculations because of the work by Kohn and Sham [13]: replacing the original many-electron problem by an auxiliary independent-electron problem. This *Ansatz* assumes that the ground state density of the original interacting system is equal to that of some non-interacting system, which leads to independent-particle equations for the non-interacting system that are exactly soluble.

The Kohn-Sham Ansatz has its root on two assumptions. The first assumption is that the exact ground state density can be represented by the ground state density of an auxiliary system of non-interacting particles, although there are no rigorous proofs. The second assumption is that the auxiliary Hamiltonian is chosen to have the usual kinetic energy operator $-\hbar^2\hat{\nabla}^2/2m_e$ and an effective *local* potential potential $V^\sigma_{\rm eff}(\mathbf{r})$ acting on an electron at $\mathbf{r}$ with spin σ.

The Kohn-Sham approach to obtain the equation for auxiliary non-interacting particles starts with writing down the ground state energy functional as

$$E_{\rm KS} = T_0[n] + \int d\mathbf{r} V_{\rm ext}(\mathbf{r})\, n(\mathbf{r}) + E_{\rm Hartree} + E_{\rm II} + E_{\rm xc}[n]\,. \tag{1.2}$$

Here, $n(\mathbf{r})$ is the ground state charge density given by sums of squares of $N = N^\uparrow + N^\downarrow$ lowest-energy orbitals

$$n(\mathbf{r}) = \sum_\sigma \sum_i^{N^\sigma} \left|\psi_i^\sigma(\mathbf{r})\right|^2\,, \tag{1.3}$$

$T_0[n]$ is the non-interacting kinetic energy given by

$$T_0 = -\frac{\hbar^2}{2m_e} \sum_\sigma \sum_i \left\langle \psi_i^\sigma \right| \nabla^2 \left| \psi_i^\sigma \right\rangle \tag{1.4}$$

$E_{\rm Hartree}[n]$ is the Hartree energy, $E_{\rm II}$ is the interaction energy between the nuclei, and $E_{\rm xc}[n]$ is the exchange-correlation energy.

In order to solve the Kohn-Sham auxiliary system for the ground state, a variational equation is derived by taking the variation of Eq. (1.2) with respect to the wavefunctions, i. e. ,

$$\frac{\delta E_{\rm KS}}{\delta \psi_i^{\sigma *}(\mathbf{r})} = \frac{\delta T_0}{\delta \psi_i^{\sigma *}(\mathbf{r})} + \left[\frac{\delta E_{\rm ext}}{\delta n(\mathbf{r},\sigma)} + \frac{\delta E_{\rm Hartree}}{\delta n(\mathbf{r},\sigma)} + \frac{\delta E_{\rm xc}}{\delta n(\mathbf{r},\sigma)}\right] \frac{\delta n(\mathbf{r},\sigma)}{\delta \psi_i^{\sigma *}(\mathbf{r})} = 0\,. \tag{1.5}$$

Now, using the Lagrange multiplier method for handling the constraint that the total number of electrons is fixed, we arrive at the Kohn-Sham Schrödinger-like equations:

$$\left(H^\sigma_{\rm KS} - \varepsilon_i^\sigma\right) \psi_i^\sigma(\mathbf{r}) = 0\,, \tag{1.6}$$

where ε_i^σ's are the eigenvalues and

$$H_{\rm KS}^\sigma(\mathbf{r}) = -\frac{\hbar^2}{2m_e}\nabla^2 + V_{\rm KS}^\sigma(\mathbf{r})\,, \tag{1.7}$$

with

$$\begin{aligned} V_{\rm KS}^\sigma(\mathbf{r}) &= V_{\rm ext}(\mathbf{r}) + \frac{\delta E_{\rm Hartree}}{\delta n(\mathbf{r},\sigma)} + \frac{\delta E_{\rm xc}}{\delta n(\mathbf{r},\sigma)} \\ &= V_{\rm ext}(\mathbf{r}) + V_{\rm Hartree}(\mathbf{r}) + V_{\rm xc}^\sigma(\mathbf{r})\,. \end{aligned} \tag{1.8}$$

Equations (1.3) and (1.6) are solved self-consistently to find the ground state energy $n(\mathbf{r},\sigma)$ and the total energy $E_{\rm KS}$. Although the exact form of the exchange-correlation functional, $E_{\rm xc}[n]$, is not known, it can reasonably be approximated in many cases by a local or nearly local functional of the density.

1.1.4 The local density approximation

Within the local density approximation (LDA), the total exchange-correlation energy $E_{\rm xc}[n]$ is a simple integration over all space of the exchange-correlation energy density which is approximated by that of a homogeneous electron gas with that density,

$$E_{\rm xc}^{\rm LDA}[n] = \int d^3\mathbf{r}\, n(\mathbf{r})\, \epsilon_{\rm xc}^{\rm hom}(n(\mathbf{r}))\,. \tag{1.9}$$

Here, $\epsilon_{\rm xc}^{\rm hom}(n)$ is the exchange-correlation energy of a homogeneous electron gas and has been calculated with quantum Monte Carlo simulations [14].

1.1.5 Pseudopotentials

Due to the strong Coulomb potential of the nucleus and the effects of the tightly bound core electrons, the Kohn-Sham equations are very hard to solve. However, the core electron states of an atom hardly changes in forming molecules or solids. Therefore, an effective potential felt by valence electrons, which preserves several important properties of the true atomic potentials including the scattering amplitudes over a wide range of energies, can be defined.

The basic idea is as follows. Suppose that the valence wavefunction $\psi_i^v(\mathbf{r})$ satisfies the Kohn-Sham equation

$$\left(-\frac{\hbar^2}{2m_e}\nabla^2 + V_{\rm KS}(\mathbf{r})\right)\psi_i^v(\mathbf{r}) = \varepsilon_i^v\,\psi_i^v(\mathbf{r})\,. \tag{1.10}$$

If we define the pseudowavefunction $\tilde{\psi}_i^v(\mathbf{r})$ as

$$\psi_i^v(\mathbf{r}) \equiv \tilde{\psi}_i^v(\mathbf{r}) - \sum_j \psi_j^c(\mathbf{r})\,\left\langle \psi_j^c | \tilde{\psi}_i^v \right\rangle\,, \tag{1.11}$$

then the pseudowavefunction satisfies

$$\left(-\frac{\hbar^2}{2m_e}\nabla^2 + \hat{V}_{\rm KS}^{\rm PS}\right)\tilde{\psi}_i^v(\mathbf{r}) = \varepsilon_i^v\,\tilde{\psi}_i^v(\mathbf{r})\,. \tag{1.12}$$

where

$$\hat{V}_{\rm KS}^{\rm PS}\,\tilde{\psi}_i^v(\mathbf{r}) \equiv V_{\rm KS}(\mathbf{r})\tilde{\psi}_i^v(\mathbf{r}) + \sum_j (\varepsilon_i^v - \varepsilon_j^c)\,\left\langle \psi_j^c|\tilde{\psi}_i^v\right\rangle\,\psi_i^c(\mathbf{r})\,. \tag{1.13}$$

Now the pseudopotential operator $\hat{V}_{\rm KS}^{\rm PS}$ is much smoother than the original potential $V_{\rm KS}(\mathbf{r})$ although it is nonlocal. Because of this smoothness, it is computationally much easier to solve the pseudo Kohn-Sham equation.

A way to define *ab initio* pseudopotential is to impose norm-conservation condition [15]. Once the critical radius $R_{\rm c}$ is defined, norm-conserving pseudopotentials require that the following quantities agree for all-electron and pseudo valence calculations: (i) eigenvalues, (ii) wavefunctions beyond $R_{\rm c}$, (iii) the logarithmic derivative of wavefunctions at $R_{\rm c}$, (iv) the integrated charge inside $R_{\rm c}$, and (v) the first energy derivative of the logarithmic derivatives of wavefunctions at $R_{\rm c}$. Indeed, it has been shown that the condition (iv) is equivalent to (v) [16].

Non-local pseudopotential corresponding to different angular momentum eigenvalues are different and can be written as

$$V_l(r) = V_{\rm local}(r) + \delta V_l(r)\,, \tag{1.14}$$

where $V_{\rm local}(r)$ is the local part of the pseudopotential and $\delta V_l(r)$ is the l-dependent non-local part. Kleinman and Bylander proposed a method of constructing a separable pseudopotential operator to a good approximation [17].

$$\hat{V}^{\rm KB} = V_{\rm local}(\mathbf{r}) + \sum_{lm}\frac{\left|\psi_{lm}^{\rm PS}\delta V_l\right\rangle\left\langle\delta V_l\psi_{lm}^{\rm PS}\right|}{\langle\psi_{lm}^{\rm PS}|\delta V_l|\psi_{lm}^{\rm PS}\rangle}\,, \tag{1.15}$$

where the second term is a non-local operator written in separable form.

1.2 The GW approximation

Ground state properties such as the total energies, equilibrium geometries, structural phase transitions, bulk moduli, lattice vibration frequencies, and so on are very well predicted by solving the Kohn-Sham equation in good agreement with the experiment. However, the excited state properties like the quasiparticle band gaps of semiconductors or insulators are poorly reproduced by the density functional theory calculations. Most of the important modern experimental techniques like scanning tunneling microscopy or angle-resolved or time-resolved photoemission spectroscopy measure the quasiparticle properties and hence cannot be described by standard density-functional theory calculations.

The GW approximation is a way of calculating the excited state quasiparticle self energies and wavefunctions from many-body Green's function perturbation theory. The electron self energy Σ can be expanded by the electron Green's function G and the screened Coulomb interaction W. The first term of the series expansion is GW and hence the approximation of truncating higher-order terms in the self-energy operator is called the GW approximation. The formalism was first established by Hedin [18, 19] and *ab initio* implementation of the methodology was first done by Hybertsen and Louie [20].

Within the GW approximation [18, 19], the electron self-energy operator, using a contracted notation for the space and time arguments ($1 \equiv (\mathbf{r}_1, t_1)$, $1^+ \equiv (\mathbf{r}_1, t_1 + \delta)$, etc.), is

$$\Sigma(1,2) = iG(1,2)W(1^+,2)\,, \tag{1.16}$$

where the screened Coulomb interaction is given by

$$W(1,2) = v(1,2) + \int v(1,3)P(3,4)W(4,2)d(34) \tag{1.17}$$

and the polarizability is given by

$$P(1,2) = -iG(1,2^+)G(2,1)\,. \tag{1.18}$$

Equation (1.17) can equivalently be written, in terms of the inverse dielectric matrix, as

$$W(\mathbf{r},\mathbf{r}';\omega) = \int \varepsilon^{-1}(\mathbf{r},\mathbf{r}'';\omega)\, v(\mathbf{r}'',\mathbf{r}')\, d\mathbf{r}''\,, \tag{1.19}$$

where the dielectric matrix is expressed in terms of the polarizability as

$$\varepsilon(\mathbf{r},\mathbf{r}';\omega) = \delta(\mathbf{r}-\mathbf{r}') - \int v(\mathbf{r},\mathbf{r}'')\, P(\mathbf{r}'',\mathbf{r}';\omega)\, d\mathbf{r}''\,. \tag{1.20}$$

Equation (1.18), also known as the random phase approximation (RPA), can be evaluated using the mean-field wavefunctions $[\psi_i(\mathbf{r})]$ and energy eigenvalues (ϵ_i) as [21, 22]

$$P(\mathbf{r},\mathbf{r}';\omega) = \sum_{i,i'} \psi_i^*(\mathbf{r})\psi_{i'}(\mathbf{r})\psi_{i'}^*(\mathbf{r}')\psi_i(\mathbf{r}') \left(\frac{f_i(1-f_{i'})}{\epsilon_i - \epsilon_{i'} + \omega + i\delta} + \frac{f_{i'}(1-f_i)}{\epsilon_{i'} - \epsilon_i - \omega + i\delta} \right)\,, \tag{1.21}$$

where f_i's are the Fermi-Dirac occupation factors. If one uses a planewave basis, the polarizability and the RPA dielectric matrix are given by

$$\begin{aligned} P_{\mathbf{G},\mathbf{G}'}(\mathbf{q};\omega) =& \frac{1}{V} \sum_{i,i'} \langle i|e^{i(\mathbf{r}+\mathbf{G})\cdot\mathbf{r}}|i'\rangle\langle i'|e^{-i(\mathbf{r}+\mathbf{G}')\cdot\mathbf{r}'}|i\rangle \\ & \times \left(\frac{f_i(1-f_{i'})}{\epsilon_i - \epsilon_{i'} + \omega + i\delta} + \frac{f_{i'}(1-f_i)}{\epsilon_{i'} - \epsilon_i - \omega + i\delta} \right) \end{aligned} \tag{1.22}$$

and

$$\varepsilon_{\mathbf{G},\mathbf{G}'}(\mathbf{q};\omega) = \delta_{\mathbf{G},\mathbf{G}'} - \frac{4\pi e^2}{|\mathbf{q}+\mathbf{G}|^2} P_{\mathbf{G},\mathbf{G}'}(\mathbf{q};\omega)\,, \tag{1.23}$$

respectively.

Frequency space representation of the self-energy operator within the GW approximation is given by the Fourier transform of Eq. (1.16),

$$\Sigma(\mathbf{r},\mathbf{r}';\omega) = \frac{i}{2\pi}\int e^{-i\omega'\delta} G(\mathbf{r},\mathbf{r}';\omega-\omega') W(\mathbf{r},\mathbf{r}';\omega') d\omega'\,. \tag{1.24}$$

Using the spectral representation, the screened Coulomb interaction can be written as [20]

$$W(\mathbf{r},\mathbf{r}';\omega) = v(\mathbf{r},\mathbf{r}') + \int_0^\infty \frac{2\omega' B(\mathbf{r},\mathbf{r}';\omega')}{\omega^2-(\omega'-i\delta)^2} d\omega'\,, \tag{1.25}$$

where $B(\mathbf{r},\mathbf{r}';\omega)$ is the spectral function for the screened interaction. By using this spectral representation, we can divide the quasiparticle self energy into the screened-exchange part and the Coulomb-hole part, $\Sigma = \Sigma_{\rm SX} + \Sigma_{\rm CH}$. The screened-exchange term arises from the poles of the Green's function and is given by [20]

$$\Sigma_{\rm SX}(\mathbf{r},\mathbf{r}';\omega) = -\sum_i^{\rm occ} \phi_i(\mathbf{r})\phi_i^*(\mathbf{r}')\, W(\mathbf{r},\mathbf{r}';\omega-\epsilon_i)\,, \tag{1.26}$$

whereas the Coulomb-hole term has its origin in the poles of the screened Coulomb interaction and is given by [20]

$$\Sigma_{\rm CH}(\mathbf{r},\mathbf{r}';\omega) = \sum_i \phi_i(\mathbf{r})\phi_i^*(\mathbf{r}') P\int_0^\infty \frac{B(\mathbf{r},\mathbf{r}';\omega')}{\omega-\epsilon_i-\omega'} d\omega'\,. \tag{1.27}$$

Obtaining the frequency dependence of the dielectric matrix within the RPA requires very heavy calculations. The generalized plasmon pole model approximation [20] significantly reduces the computational load. In the model, the imaginary part of the dielectric function is represented by a pair of delta functions as

$$\mathrm{Im}\,\varepsilon^{-1}_{\mathbf{G},\mathbf{G}'}(\mathbf{q},\omega) = A_{\mathbf{G},\mathbf{G}'}(\mathbf{q})\left\{\delta\left[\omega-\widetilde{\omega}_{\mathbf{G},\mathbf{G}'}(\mathbf{q})\right] - \delta\left[\omega+\widetilde{\omega}_{\mathbf{G},\mathbf{G}'}(\mathbf{q})\right]\right\}\,, \tag{1.28}$$

and the real is given by

$$\mathrm{Re}\,\varepsilon^{-1}_{\mathbf{G},\mathbf{G}'}(\mathbf{q},\omega) = 1 + \frac{\Omega^2_{\mathbf{G},\mathbf{G}'}(\mathbf{q})}{\omega^2-\widetilde{\omega}^2_{\mathbf{G},\mathbf{G}'}(\mathbf{q})}\,. \tag{1.29}$$

Since there are three parameters ($\widetilde{\omega}$, A and Ω) in the model, one needs three equations to determine them. Those three are (i) the Kramers-Kronig relation between the real and imaginary part of the inverse dielectric function, (ii) the condition that the model dielectric

function with zero frequency should reproduce the calculated static dielectric function, and (iii) a generalized *f*-sum rule relating the dielectric matrix to the plasma frequency and the electronic charge density [20].

In calculating the quasiparticle wavefunctions and energy eigenvalues, it is known that calculating the diagonal matrix elements of the self-energy operator is good enough [20]. Or, in other words, the LDA wavefunctions are a good approximation for the quasiparticle wavefunctions and the self-energy corrections are simply calculated by taking the expectation value of the self-energy operator for the LDA wavefunctions. The quasiparticle energy bandgaps of semiconductors and insulators obtained in this way are in excellent agreement with the experimental findings [20].

1.3 The Bethe-Salpeter equation approach

Although the *GW* approximation formalism successfully describes the results of various kinds of experiments based on the single-particle excitation phenomena, it is not formulated to explain the results of optical measurements which necessarily involve a two-particle excitation, i. e. , an electron-hole pair generation process. Excitons, coherent superpositions of electron-hole pair configurations, change the optical response drastically.

The Bethe-Salpeter equation (BSE) describes the two-particle amplitude propagation under Coulomb interaction. The BSE formalism for the optical response was first applied to semiconductors within a tight-binding bond orbital model [23, 24] and then in the last decade the formalism was implemented in a first-principles scheme [25, 26, 27]. In this section, we mainly follow the discussion of Rohlfing and Louie [25, 28].

According to Rohlfing and Louie [28], the exciton wavefunction $|S\rangle$ (i. e. , the electron-hole amplitude) with the excitation energy Ω_S is given as a linear combination of electron-hole pair states $|vc\mathbf{k}\rangle$ by

$$|S\rangle = \sum_{v}^{\text{occ}} \sum_{c}^{\text{empty}} \sum_{\mathbf{k}} A^S_{vc\mathbf{k}} |vc\mathbf{k}\rangle \,, \tag{1.30}$$

where the coefficients $A^S_{vc\mathbf{k}}$'s are obtained by solving the BSE within the Tamn-Dancoff approximation,

$$(E_{c\mathbf{k}} - E_{v\mathbf{k}}) A^S_{vc\mathbf{k}} + \sum_{v'c'\mathbf{k}'} K_{vc\mathbf{k},v'c'\mathbf{k}'}(\Omega_S) A^S_{v'c'\mathbf{k}'} = \Omega_S A^S_{vc\mathbf{k}} \,. \tag{1.31}$$

Here, the interaction kernel $K_{vc\mathbf{k},v'c'\mathbf{k}'}$ is divided into two terms. The direct term K^d describes the attractive screened Coulomb interaction and is responsible for the exciton formation. The exchange term K^x describes the repulsive bare Coulomb interaction and is the source of singlet-triplet splitting. Using the notation that $\mathbf{x}$ includes the real-space coordinate $\mathbf{r}$ and

the spin σ, These two terms are evaluated as

$$\langle vc|K^d|v'c'\rangle = -\int \psi_c^*(\mathbf{x})\psi_{c'}(\mathbf{x})W(\mathbf{r},\mathbf{r}';\omega=0)\psi_v(\mathbf{x}')\psi_{v'}(\mathbf{x}')d\mathbf{x}d\mathbf{x}' \tag{1.32}$$

$$\langle vc|K^x|v'c'\rangle = \int \psi_c^*(\mathbf{x})\psi_v(\mathbf{x})v(\mathbf{r},\mathbf{r}')\psi_{c'}(\mathbf{x}')\psi_{v'}^*(\mathbf{x}')d\mathbf{x}d\mathbf{x}'\,. \tag{1.33}$$

In the direct term, the energy argument ω should actually be $\Omega^S-(E_c-E_v)$; however, when $\omega \ll \Omega_S$, we can, to a good approximation, neglect the dynamical effect and set $\omega=0$.

Considering the spin degree of freedom of valence band electron (not hole) and conduction band electron, the BSE can be written in terms of the four basis states (($v\uparrow c\uparrow$), ($v\uparrow c\downarrow$), ($v\downarrow c\uparrow$) and ($v\downarrow c\downarrow$)) as

$$\begin{pmatrix} D+K^d+K^x & 0 & 0 & K^x \\ 0 & D+K^d & 0 & 0 \\ 0 & 0 & D+K^d & 0 \\ K^x & 0 & 0 & D+K^d+K^x \end{pmatrix} \begin{pmatrix} v\uparrow c\uparrow \\ v\uparrow c\downarrow \\ v\downarrow c\uparrow \\ v\downarrow c\downarrow \end{pmatrix}, \tag{1.34}$$

where $D=(E_c-E_v)$. These equations decouples into a spin-triplet set of three equations with the Hamiltonian $D+K^d$ and a spin-singlet equation with the Hamiltonian $D+K^d+2K^x$. Therefore, the excitation energy difference between the singlet and triplet states comes from the exchange term. After this decoupling, the BSE can be solved for spin-singlet states and spin-triplet states independently. However, when the spin-orbit coupling cannot be neglected, the spin-singlet and spin-triplet terms mix with each other and hence Eq. (1.34) should be solved as is.

Using the exciton wavefunctions and excitation energies, we can straightforwardly calculate the imaginary part of the transverse dielectric function $\mathrm{Im}\,\epsilon_2(\omega)$, which can directly be compared with the optical measurements. Suppose that the light is linearly polarized in parallel to a unit vector λ and that $\mathbf{v}=i/\hbar[H,\mathbf{r}]$ is the velocity operator. Within the single-particle picture, i. e. , neglecting the excitonic effects, the imaginary part of the dielectric function is given by

$$\epsilon_2^{(0)}(\omega) = \frac{16\pi e^2}{\omega^2}\sum_v^{\mathrm{occ}}\sum_c^{\mathrm{empty}} |\lambda\cdot\langle v|\mathbf{v}|c\rangle|^2\,\delta(\omega-(E_c-E_v))\,, \tag{1.35}$$

showing that the optical absorption arises from the interband momentum-conserving transitions. However, the effects of mixing between different interband transitions on the optical response are not considered in this single-particle picture. When the excitonic effects are considered, the imaginary part of the dielectric function can be written in terms of the exciton eigenstates obtained by solving the BSE as

$$\epsilon_2(\omega) = \frac{16\pi e^2}{\omega^2}\sum_S |\lambda\cdot\langle 0|\mathbf{v}|S\rangle|^2\,\delta(\omega-\Omega_S)\,, \tag{1.36}$$

where the optical transition matrix element is given by

$$\langle 0|\mathbf{v}|S\rangle = \sum_{v}^{\text{occ}} \sum_{c}^{\text{empty}} A_{vc}^{S} \langle v|\mathbf{v}|c\rangle \,, \tag{1.37}$$

allowing for the coherent superposition of electron-hole pair states with different momentum and band indices. It is well known that the coherent effects significantly change the optical response [28].

1.4 Density functional perturbation theory

Lattice vibrational, or phononic, properties of solids are of of interest because they play a crucial role in charge or heat transport as well as in superconductivity and other phenomena. In order to obtain the phonon eigenmodes and eigenfrequencies one needs the dynamical matrix, i. e. , to calculate the derivatives of the total electronic energy E_{KS} with respect to the ionic displacements $\mathbf{R}_i$'s [29]. According to the Hellmann-Feynman theorem [30],

$$\frac{\partial E_{\text{KS}}}{\partial \mathbf{R}_i} = \int \frac{\partial V_{\text{KS}}}{\partial \mathbf{R}_i}\, n(\mathbf{r})\, d\mathbf{r} \,, \tag{1.38}$$

and

$$\frac{\partial^2 E_{\text{KS}}}{\partial \mathbf{R}_i \partial \mathbf{R}_j} = \int \frac{\partial V_{\text{KS}}}{\partial \mathbf{R}_i \partial \mathbf{R}_j}\, n(\mathbf{r})\, d\mathbf{r} + \int \frac{\partial V_{\text{KS}}}{\partial \mathbf{R}_i}\, \frac{\partial n(\mathbf{r})}{\partial \mathbf{R}_j}\, d\mathbf{r} \,. \tag{1.39}$$

The electron-density response $\partial n(\mathbf{r})/\partial \mathbf{R}_j$ can be evaluated by linearizing Eq. (1.3),

$$\Delta n(\mathbf{r}) = 2 \sum_{n}^{\text{occ}} \psi_n^*(\mathbf{r}) \Delta\psi_n(\mathbf{r}) \,, \tag{1.40}$$

where the finite-differential operator Δ is defined as

$$\Delta F = \sum_i \frac{\partial F}{\partial \mathbf{R}_i} \Delta \mathbf{R}_i \,. \tag{1.41}$$

The variation to the Kohn-Sham wavefunction $\Delta\psi_n(\mathbf{r})$ is obtained by first-order perturbation theory as

$$(H_{\text{KS}} - \epsilon_n)|\Delta\psi_n\rangle = -(\Delta V_{\text{KS}} - \Delta\epsilon_n)|\psi_n\rangle \,, \tag{1.42}$$

where, according to Eq. (1.8),

$$\Delta V_{\text{KS}}(\mathbf{r}) = \Delta V_{\text{ext}}(\mathbf{r}) + e^2 \int \frac{\Delta n(\mathbf{r}')}{|\mathbf{r} - \mathbf{r}'|} d\mathbf{r}' + \frac{d\, v_{\text{xc}}(n(\mathbf{r}))}{d\, n(\mathbf{r})} \Delta n(\mathbf{r}) \tag{1.43}$$

is the first-order correction to the self-consistent potential and $\Delta\epsilon_n = \langle\psi_n|\Delta V_{\text{KS}}|\psi_n\rangle$ is the first-order correction to the Kohn-Sham eigenvalue. Equations (1.40), (1.42), and (1.43) form a self-consistent set of equations for the perturbed system.

On the other hand, the first-order correction to the wavefunction $\Delta\psi_n(\mathbf{r})$ is given as a sum over the unperturbed states,

$$\Delta\psi_n(\mathbf{r}) = \sum_{m\neq n} \psi_m(\mathbf{r}) \frac{\langle\psi_m|\Delta V_{\rm KS}|\psi_n\rangle}{\epsilon_n - \epsilon_m} \,. \tag{1.44}$$

Plugging this expression into Eq. (1.40), we obtain

$$\Delta n(\mathbf{r}) = 2\sum_{n}^{\rm occ}\sum_{m\neq n} \psi_n^*(\mathbf{r})\psi_m(\mathbf{r}) \frac{\langle\psi_m|\Delta V_{\rm KS}|\psi_n\rangle}{\epsilon_n - \epsilon_m} \,. \tag{1.45}$$

An important conclusion that can be drawn from Eq. (1.45) is that the first-order correction to the charge density is not affected when the state m is an occupied state due to the cancellation with the summand where n and m are replaced by m and n, respectively. Therefore, we can confine our interest in the first-order correction to the wavefunction in Eq. (1.42) to empty state components only. Using the projection operator into the conduction band states $P_c = 1 - P_v$, we can rewrite Eq. (1.42) as

$$(H_{\rm KS} - \epsilon_n)|\Delta\psi_n\rangle = -P_c\Delta V_{\rm KS}|\psi_n\rangle \,. \tag{1.46}$$

By solving Eqs. (1.40), (1.46), and (1.43) self-consistently, one can obtain the first-order corrections to the perturbing Hamiltonian. An advantage of this linear response formalism is that one does not need to know empty state wavefunctions or energy eigenvalues at all. The force constants (related to the second derivatives of the total energy), phonon eigenmodes, and phonon frequencies can be obtained by evaluating Eqs. (1.38) and (1.39) using the described density functional perturbation theory [29].

1.5 The electron-phonon coupling matrix elements

Electrons and phonons are by far the two most important elementary excitations in solids. The interaction between these two types of excitations, i. e. , electron-phonon interactions, renormalize the properties of both of them. For example, the electron lifetime and velocity are determined by this interaction and hence the carrier transport properties are significantly affected by phonons. On the other hand, the phonon linewidths and bandstructures measured from various kinds of experiments are also influenced by the interaction with the electrons. Therefore, in understanding the properties of solids, it is very important to accurately calculate the electron-phonon interaction matrix elements

$$\langle m\,\mathbf{k}+\mathbf{q}|\Delta V_{\mathbf{q}}^{\nu}(\mathbf{r})|n\,\mathbf{k}\rangle \,, \tag{1.47}$$

where $|m\,\mathbf{k}+\mathbf{q}\rangle$ and $|n\,\mathbf{k}\rangle$ are the Kohn-Sham electronic wavefunctions and $\Delta V_{\mathbf{q}}^{\nu}(\mathbf{r})$ is the first-order perturbation in the Kohn-Sham self-consistent potential due to a phonon with branch index ν and wavevector $\mathbf{q}$.

In our study, we have used a recently developed methodology [31], based on the use of maximally localized Wannier functions [32, 33], in calculating the electron-phonon matrix elements. The main idea is to use the property that the electron-phonon interaction matrix element in Wannier basis

$$\langle m\,\mathbf{R}_e|\Delta V^{\nu}_{\mathbf{R}_{\rm ph}}(\mathbf{r})|n\,\mathbf{R}'_e\rangle\,, \tag{1.48}$$

is an integral of the product of three functions localized in real space. Therefore, the matrix element is negligible unless all three centers $\mathbf{R}_e$, $\mathbf{R}'_e$, and $\mathbf{R}_{\rm ph}$ are close to one another. Using this property, one can obtain the electron-phonon matrix elements in Bloch basis shown in Eq. (1.47) through an interpolation at a relatively low price [31].

Chapter 2

Velocity renormalization and carrier lifetime in graphene from electron-phonon interaction

2.1 Introduction

The recent fabrication of single-layer graphene [34] has attracted considerable interest because low-energy charge carriers in this material have dispersion curves similar to Dirac fermions with zero rest mass and constant group velocity [35, 36]. Because of the peculiar electronic structure of graphene, electrons and holes exhibit exceptionally large mobilities, and the density of states can be tuned over a wide range by applying a gate voltage [35, 36]. These properties make graphene a promising candidate for new-generation electronic and spintronic devices.

Angle-resolved photoemission spectroscopy (ARPES) is used as a powerful tool for investigating quasiparticle behavior with extremely fine energy and momentum resolution [37]. The photoelectron intensity provides information about the energy vs. momentum dispersions of the charge carriers and the associated lifetimes. Recent photoemission experiments performed on graphene showed a peculiar dependence of the hole lifetime on the binding energy, as well as a significant velocity renormalization [2]. The measured carrier lifetime has been discussed within a model including three different decay channels: electron-phonon (e-ph) scattering, electron-plasmon scattering, and electron-hole pair generation [2]. The linear dependence of the linewidth on the binding energy was attributed to the generation of electron-hole pairs. The phonon-induced lifetime was assumed to be energy-independent as found in conventional metallic systems [2]. A subsequent theoretical work analyzed the carrier lifetimes in graphene by adopting a two-dimensional electron-gas model, and concluded that the experimental results could be explained without invoking the e-ph interaction [38].

In this chapter we investigate the e-ph interaction in graphene within a *first-principles* approach. We calculated the electron self-energy arising from the e-ph interaction using a

dense sampling of the scattering processes in momentum space, and we extracted the velocity renormalization and the carrier lifetimes from the corresponding real and imaginary parts of the self-energy, respectively. Our analysis shows that the self-energy associated with the *e*-ph interaction in graphene is qualitatively different from that found in conventional metals. The imaginary part of the self-energy shows a linear energy dependence above the phonon emission threshold, which directly reflects the bandstructure of graphene. The real part of the self-energy leads to a Fermi velocity renormalization of 4-8 % depending on doping. We further propose a simple analytical model of the electron self-energy capturing the main features of our first-principles calculations. Our calculation allows us to assign the low-energy kink in the measured photoemission spectrum and part of the linear energy-dependence of the electronic linewidths to the *e*-ph interaction.

2.2 Theory and computation

The *e*-ph interaction in graphene is treated within the Migdal approximation [39]. The contribution to the electron self-energy $\Sigma_{n\mathbf{k}}(E;T)$ arising from the *e*-ph interaction at the temperature T is [39, 31]:

$$\Sigma_{n\mathbf{k}}(E;T) = \sum_{m,\nu} \int \frac{d\mathbf{q}}{A_{\mathrm{BZ}}} |g_{mn,\nu}(\mathbf{k},\mathbf{q})|^2 \times \left[\frac{n_{\mathbf{q}\nu} + 1 - f_{m\mathbf{k}+\mathbf{q}}}{E - \varepsilon_{m\mathbf{k}+\mathbf{q}} - \hbar\omega_{\mathbf{q}\nu} - i\delta} + \frac{n_{\mathbf{q}\nu} + f_{m\mathbf{k}+\mathbf{q}}}{E - \varepsilon_{m\mathbf{k}+\mathbf{q}} + \hbar\omega_{\mathbf{q}\nu} - i\delta} \right], \tag{2.1}$$

where $\varepsilon_{n\mathbf{k}}$ is the energy of an electronic state with band index n and wavevector $\mathbf{k}$, and $\hbar\omega_{\mathbf{q}\nu}$ the energy of a phonon with wavevector $\mathbf{q}$ and branch index ν. $f_{n\mathbf{k}}$ and $n_{\mathbf{q}\nu}$, are the Fermi-Dirac and Bose-Einstein distribution functions, respectively. The integration extends over the Brillouin zone (BZ) of graphene of area A_{BZ} and the sum runs over both occupied and empty electronic states and all phonon branches. The *e*-ph matrix element is defined by $g_{mn,\nu}(\mathbf{k},\mathbf{q}) = \langle m\mathbf{k}+\mathbf{q}|\Delta V_{\mathbf{q}\nu}|n\mathbf{k}\rangle$, $\Delta V_{\mathbf{q}\nu}$ being the change in the self-consistent potential due to a phonon with wavevector $\mathbf{q}$ and branch index ν, while $|n\mathbf{k}\rangle$, $|m\mathbf{k}+\mathbf{q}\rangle$ indicate Bloch eigenstates. Equation (2.1) takes into account the anisotropy of the *e*-ph interaction in $\mathbf{k}$-space, as well as retardation effects through the phonon frequency in the denominators.

The electronic structure was described within the local density approximation to density-functional theory [14, 40]. Valence electronic wavefunctions were expanded in a plane-waves basis [41] with a kinetic energy cutoff of 60 Ry. The core-valence interaction was treated by means of norm-conserving pseudopotentials [15, 42]. Lattice-dynamical properties were computed through density-functional perturbation theory [43]. We modeled an isolated graphene by a honeycomb lattice of carbon atoms within a periodic supercell. The graphene layers were separated by 8.0 Å of vacuum [44], and the relaxed C-C bond-length was 1.405 Å. Doped graphene was modeled by varying the electronic density and introducing a neutralizing

background charge. We first calculated electronic and vibrational states and the associated e-ph matrix elements on 72×72 $\mathbf{k}$-points and 12×12 $\mathbf{q}$-points in the BZ of graphene. Then, we determined the quantities needed to evaluate the self-energy given by Eq. (2.1) on a significantly finer grid of 1000×1000 $\mathbf{k}$ and $\mathbf{k}+\mathbf{q}$ points in the irreducible wedge of the BZ by using a first-principles interpolation based on electron and phonon Wannier functions [45, 46, 47]. The fine sampling of the BZ was found to be crucial for convergence of the self-energy. In the calculation of the self-energy we used a broadening parameter δ of 10 meV, comparable with the resolution of state-of-the-art photoemission experiments [37]. The calculations were performed with the electron and phonon occupations [Eq. (2.1)] corresponding to $T=20$ K to make connection with the ARPES experiment [2]. In what follows, we discuss the computed electron self-energy by focusing on a straight segment perpendicular to the ΓK direction and centered at the K point in the BZ [Fig. 2.1].

We note here that within 2.5 eV from the Dirac point, the angular dependence of the self-energy is insignificant (at fixed energy E) [5]. As a consequence, the e-ph coupling parameter $\lambda_n(\hat{\mathbf{k}}) = -\,\partial\ \mathrm{Re}\Sigma_{n\mathbf{k}}(E)/\partial E|_{E=E_\mathrm{F}}$ is isotropic in $\mathbf{k}$-space.

2.3 Results and discussion

2.3.1 Electron linewidth

Figure 2.1 shows the calculated imaginary part of the self-energy (which is closely related to the linewidth) as a function of carrier energy, corresponding to three representative situations: intrinsic, electron-doped, and hole-doped graphene. We here considered doping levels corresponding to $4{\cdot}10^{13}$ cm^{-2} electrons or holes. The corresponding Fermi levels were found to lie at $+0.64$ eV and -0.66 eV from the Dirac point, respectively. In the intrinsic system, we found that the electron linewidth due to e-ph interaction is negligible (<1 meV) within an energy threshold $\hbar\omega_\mathrm{ph}$ for the emission of optical phonons ($\hbar\omega_\mathrm{ph}\approx0.2$ eV being a characteristic optical phonon frequency), while it increases linearly beyond this threshold [Fig. 2.1(a)]. The scattering rate for electrons with energy below the optical phonon emission threshold is negligible because (i) only optical phonons are effective in e-ph scattering and (ii) Pauli's exclusion principle blocks transitions into occupied states. On the other hand, the linear increase of the linewidth above the optical phonon energy relates to the phase-space availability for electronic transitions, and reflects the linear variation of the density of states around the Dirac point in graphene. The energy dependence of the electron linewidths in the electron-doped and the hole-doped systems [Fig. 2.1(b) and Fig. 2.1(c), respectively] can be rationalized by a similar phase-space argument. We denote by E_D the energy of the Dirac point with respect to the Fermi level. For definiteness, we here consider the electron-doped situation ($E_\mathrm{D}<0$). When the energy of the hole is exactly equal to $|E_\mathrm{D}|+\hbar\omega_\mathrm{ph}$ (i.e., at $-|E_\mathrm{D}|-\hbar\omega$ in Fig. 2.1), there are no allowed final states for electronic transitions through optical phonon emission, resulting in a vanishing scattering rate at zero temperature. As the hole energy departs from $|E_\mathrm{D}|+\hbar\omega_\mathrm{ph}$, the linewidth increases linearly, and exhibits a

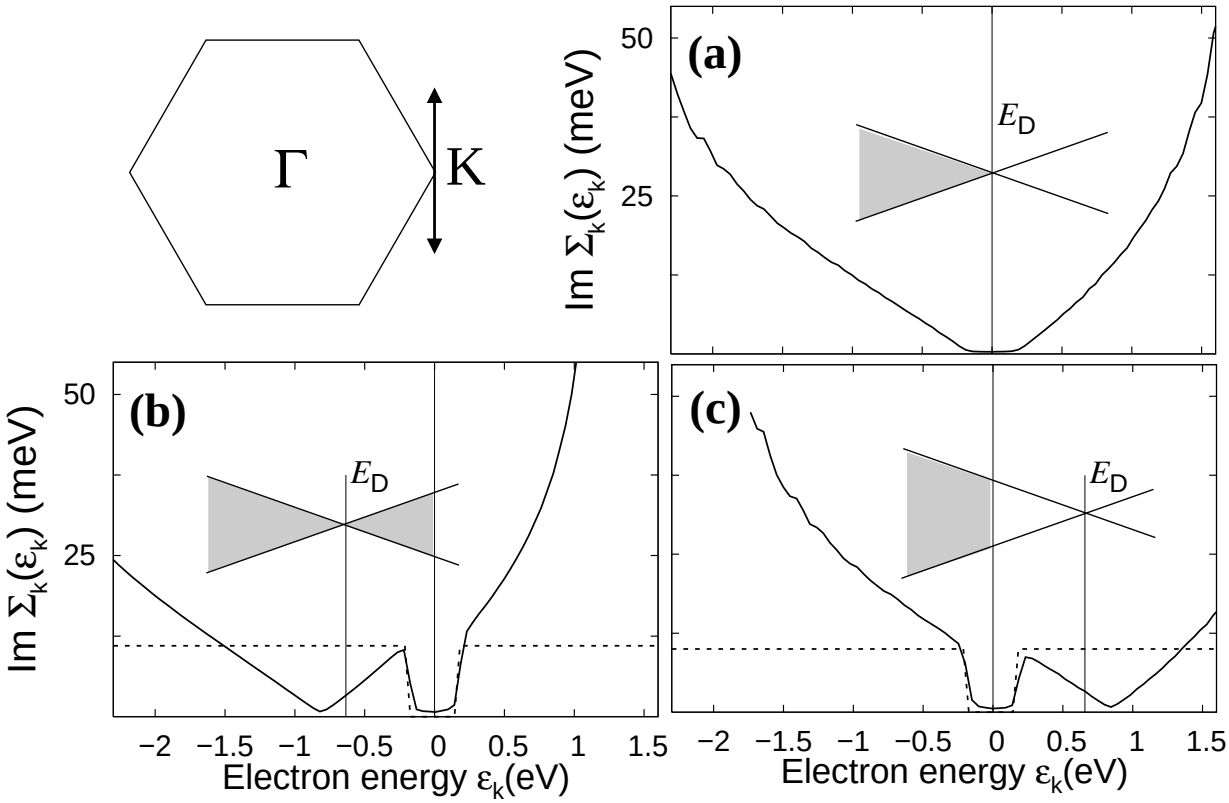

Figure 2.1: Calculated imaginary part of the electron self-energy arising from the e-ph interaction at $T = 20$ K (solid lines), for (a) intrinsic, (b) electron-doped, and (c) hole-doped graphene. The self-energy $\Sigma_{\mathbf{k}}(\varepsilon_{\mathbf{k}})$ was evaluated along the reciprocal space line segment shown in the upper-left corner. The Fermi level and the Dirac point are shown schematically in each case. We also show for comparison the imaginary part of the self-energy for a conventional metal (dashed lines) (Ref. [1]).

characteristic dip at the Fermi level. The latter feature corresponds to forbidden phonon emission processes, as discussed above for intrinsic graphene. The calculated energy dependence of the electron linewidth deviates substantially from the standard result which applies to conventional metals (Fig. 2.1, dashed line) [1]. The latter consists of a constant scattering rate above the phonon emission threshold, and fails in reproducing the features revealed by our *ab initio* calculations.

2.3.2 Velocity renormalization

Figure 2.2 shows the real part of the electron self-energy arising from the *e*-ph interaction, for intrinsic and for electron-doped graphene. The behavior of the hole-doped system is qualitatively similar to the electron-doped case. While in conventional metals the real part of the self-energy decays at large hole energies ($E < -\hbar\omega_{\rm ph}$) [Fig. 2.2(b), dashed line], the self-energy in graphene shows a monotonic increase in the same energy range [Fig. 2.2(b), solid line]. Since the wavevector dependence of the self-energy in graphene within a few eV from the Fermi level is negligible [i.e., $\Sigma_{n\mathbf{k}}(E) \simeq \Sigma_n(E)$] [5], we obtained the quasiparticle strength $Z_{n\mathbf{k}} = (1 - \partial\ \mathrm{Re}\Sigma_{n\mathbf{k}}/\partial E)^{-1}$ by evaluating $(1 - d\ \mathrm{Re}\Sigma_{n\mathbf{k}}(\varepsilon_{\mathbf{k}})/d\varepsilon_{\mathbf{k}})^{-1}$. In all cases considered, the *e*-ph interaction was found to reduce the non-interacting quasiparticle strength down to at most $Z_{n\mathbf{k}} = 0.93$ at the Fermi level. This suggests that a quasiparticle picture is still appropriate at low energy, the *e*-ph interaction largely preserving the weakly perturbed Fermi-liquid behavior. The quasiparticle strength is related to the velocity renormalization through $1 - Z_{n\mathbf{k}}^{-1} = (v_{n\mathbf{k}} - v_{n\mathbf{k}}^0)/v_{n\mathbf{k}}$, $v_{n\mathbf{k}}^0$ and $v_{n\mathbf{k}}$ being the non-interacting and the interacting velocity, respectively. The velocity renormalization is plotted in Fig. 2.2(c) and Fig. 2.2(d) for the intrinsic and the electron-doped system, respectively. The velocity renormalization at the Fermi level was found to increase with the doping level, and amounts to -4 %, -8 %, and -6 % in the intrinsic, the electron-doped, and in the hole-doped system considered here. Our results indicate that the velocity of Dirac fermions in graphene is affected by the *e*-ph interaction. This bears important implications for the transport properties of graphene-based electronic devices.

2.3.3 Toy model

In order to provide a simplified picture of the *e*-ph interaction in graphene, we analyzed the various *e*-ph scattering processes contributing to the electron lifetimes. We repeated our calculations by restricting either the energy $\hbar\omega_{\mathbf{q}\nu}$ or the momentum transfer $\mathbf{q}$ in Eq. (2.1) to limited ranges. When only the in-plane optical phonon modes between 174 and 204 meV are taken into account in Eq. (2.1), the electron linewidth is found to deviate from the full *ab initio* result by 15% at most. In contrast, when the momentum integration in Eq. (2.1) is restricted to small regions around the high-symmetry points Γ and K, the linewidth is found to deviate significantly from the full calculation, indicating that a proper account of the entire BZ is essential. Based on this analysis, we devised a simplified single-parameter model of the *e*-ph interaction in graphene. We assumed: (i) linear electronic dispersions up

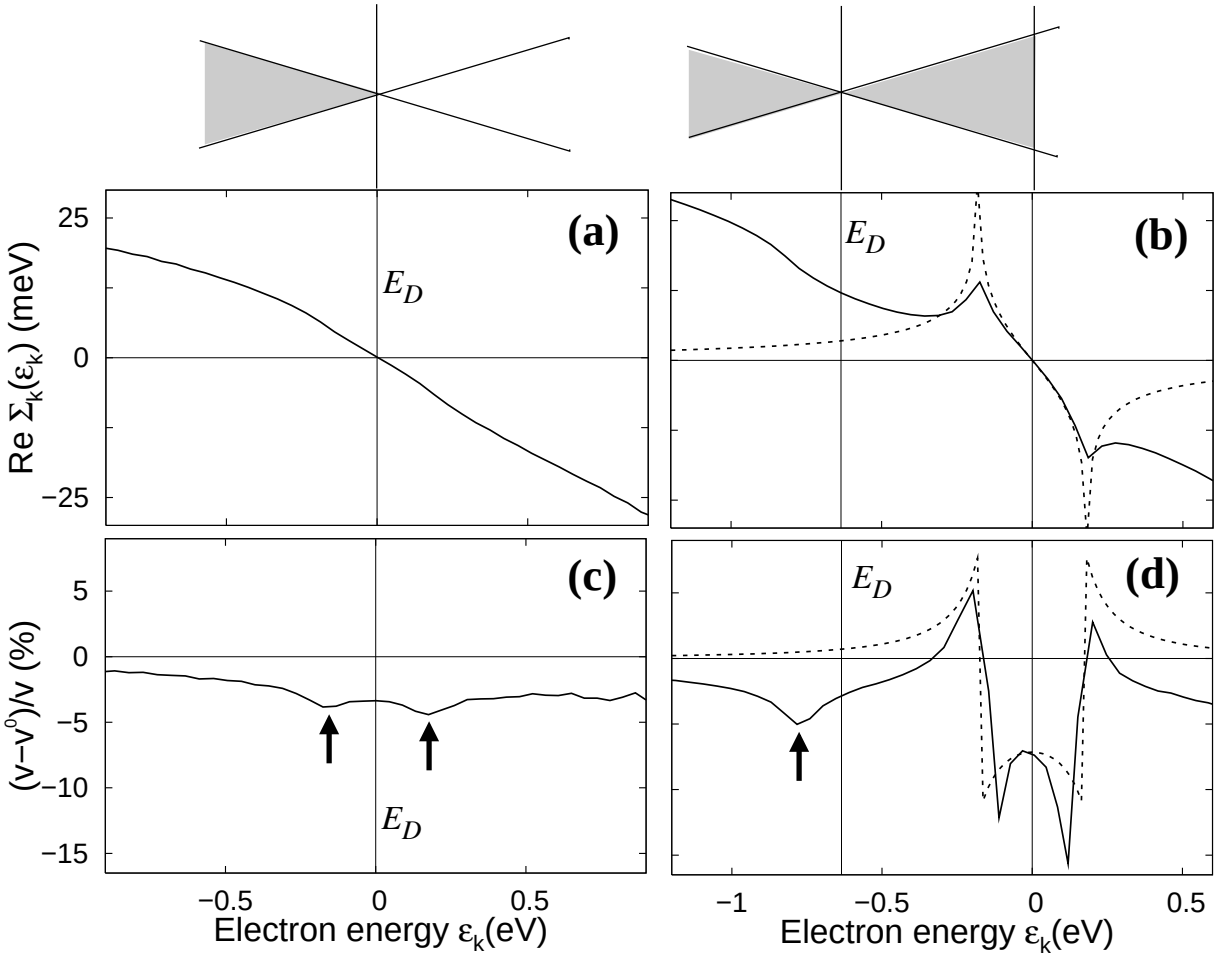

Figure 2.2: Calculated real part of the electron self-energy arising from the e-ph interaction at $T = 20$ K (solid lines), for (a) intrinsic and (b) electron-doped graphene. The self-energy was evaluated along the reciprocal space line segment shown in Fig. 2.1. The corresponding velocity renormalization $(v_{n\mathbf{k}} - v^0_{n\mathbf{k}})/v_{n\mathbf{k}}$ is shown in panels (c) and (d), respectively. We also report, for comparison, the real part of the self-energy and the velocity renormalization for a conventional metal (dashed lines) (Ref. [1]). At variance with conventional metals, the group velocity in graphene shows additional dips when the carrier energy is $|E_{\rm D}| + \omega_{\rm ph}$ (arrows), reflecting the vanishing density of states at the Dirac point.

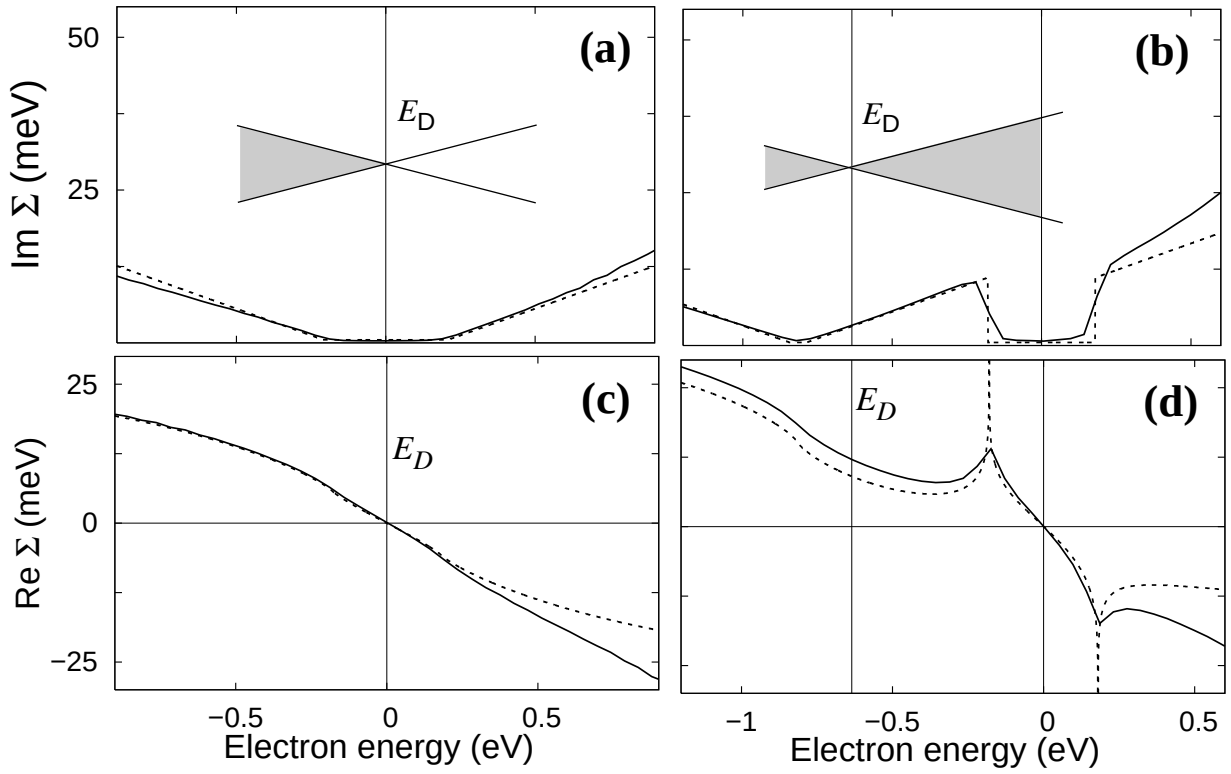

Figure 2.3: Comparison between the electron self-energy obtained from a first-principles calculation (solid lines) and a single-parameter model (dashed lines): imaginary (upper panels) and real (lower panels) part for the intrinsic system (left) as well as for the electron-doped system (right). Note that the horizontal energy ranges differ from those shown in Fig. 2.1.

to a few eV away from the Dirac point [48], (ii) an Einstein model with the effective phonon energy $\hbar\omega_{\rm ph}$ set to that of the highest degenerate zone-center mode, (iii) an effective e-ph vertex g, independent of the electron and phonon momenta [5]. The e-ph matrix element g represents a free parameter in our simplified model, and has been determined by matching the model self-energy with the full *ab initio* result. Within these assumptions, and with the Fermi level set to zero, the imaginary part of the self-energy reads

$$\text{Im } \Sigma(E) = \frac{\sqrt{3}\,a^2}{16}\alpha_{\rm G}^2\, g^2\, |E - \text{sgn}(E)\,\hbar\omega_{\rm ph} - E_{\rm D}|\,, \tag{2.2}$$

whenever $|E|$ exceeds the characteristic phonon energy $\hbar\omega_{\rm ph}$, and vanishes otherwise. In Eq. (2.2), a is the lattice parameter in Bohr units, $\alpha_{\rm G} = e^2/\hbar v^0 = 2.53$ is the effective fine structure constant of graphene, and g is the average e-ph matrix element in Rydberg units. The fitting to our calculated *ab initio* self-energy gave $g = 3.5 \cdot 10^{-2}$ Ry. The real part of the model self-energy can be straightforwardly obtained from Eq. (2.2) through Kramers-Kronig relations. Figure 2.3 shows that this simplified model is in fairly good agreement with the full first-principles calculation. Therefore, despite its simplicity, our single-parameter model captures the qualitative features of the e-ph interaction in graphene.

2.3.4 Comparison with experiment

In Fig. 2.4 we compare our first-principles calculations with the width of the momentum distribution curve (MDC) measured by ARPES experiments at 20 K on graphene with a similar doping [2]. The width $\Delta k_{n\mathbf{k}}$ of the MDC was calculated taking into account renormalization effects through $\Delta k_{n\mathbf{k}} = Z_{n\mathbf{k}}\, 2\text{Im } \Sigma_{n\mathbf{k}}/\hbar v_{n\mathbf{k}}$ [39]. Figure 2.4 shows that, contrary to previous findings [38], the e-ph interaction plays a significant role in reducing the carrier lifetime in graphene, as it accounts for about a third of the measured linewidth at large binding energies. The e-ph contribution to the width of the MDC is found to increase linearly at large binding energy, in agreement with experiment.

2.4 Conclusion

In conclusion, we have computed from first-principles the velocity renormalization and the carrier lifetimes in graphene arising from the e-ph interaction and we have reproduced these results with a simplified model. The calculated energy-dependence of the phonon-induced electronic linewidths is shown to originate from the linear electronic dispersions. The renormalization of the Fermi velocity was found to be -4 % for intrinsic graphene and -8 % for an electron doping of $4 \cdot 10^{13}$ cm^{-2}, and is expected to affect the mobility of graphene-based electronic and spintronic devices. Our results are in agreement with a recent publication [49].

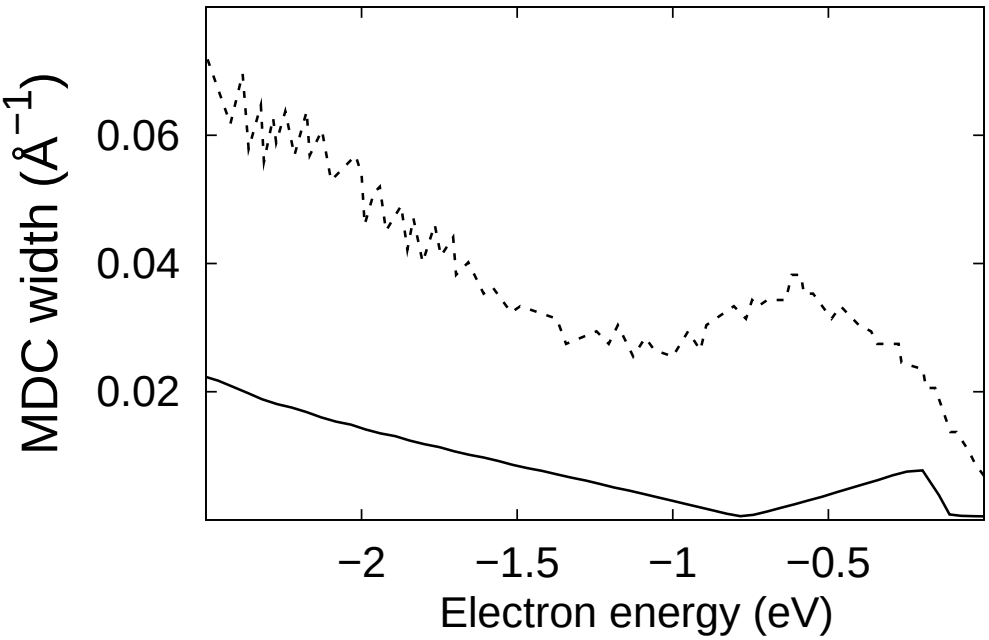

Figure 2.4: Calculated width of the ARPES momentum distribution curve for electron doped graphene (solid line) compared to the experimental result of Ref. [2] (dashed line). In our calculation, the Fermi level was set in order to simulate the sample with $2.1 \cdot 10^{13}$ electrons/cm^2 in Fig. 3 of Ref. [2].

Chapter 3

Van Hove singularity and apparent anisotropy in the electron-phonon interaction in graphene

3.1 Introduction

The energies and lifetimes of charge carriers in solids are significantly affected by many-body interactions including those with electron-hole pairs, plasmons, and phonons. Angle-resolved photoemission spectroscopy has emerged as an ideal tool for directly probing the effects of these interactions on the electron quasiparticle dynamics with good energy and momentum resolution [37].

In particular, the low-energy electron dynamics at metal surfaces [50], in layered materials, such as magnesium diboride [51], graphite [52], and cuprate superconductors [37], and in single layer graphene [2, 53, 54, 55, 56, 57, 58, 59, 60, 61, 62, 63], is significantly affected by the electron-phonon interaction. Since the electron-phonon interaction generally manifests itself as a kink in the quasiparticle dispersion relations measured by angle-resolved photoemission spectroscopy [64, 39], it is common practice to determine the strength of the electron-phonon coupling by taking the ratio between the group velocity at the Fermi level and below the phonon-induced kink [65, 66, 67, 55]. In the cases where this simple procedure is not applicable, more complicated self-consistent algorithms [68, 69] become necessary to extract the electron-phonon coupling strength. However, the application of these methods requires the knowledge of several adjustable parameters and is subject to some arbitrariness. Therefore, assessing in the first instance the validity of extraction procedures based on the linear slopes of the photoemission data is an important issue.

Graphene [70, 34, 35, 36, 71] is an ideal system to investigate these effects. Indeed, the Fermi level of graphene can be tuned over a wide energy range by chemical doping [2, 55] or by gating [35, 36, 72], and can almost be aligned with the van Hove singularity at the M point of the two-dimensional Brillouin zone [55].

In this chapter, we show that the apparent electron-phonon coupling strength in doped graphene obtained from the linear slopes of the renormalized quasiparticle dispersions, as calculated from first principles, is highly *anisotropic*, in good agreement with experimental results [55]. On the other hand, the phonon-induced electron self-energy is found to be only weakly dependent on the wavevector in the Brillouin zone. As a consequence, the actual electron-phonon coupling strength is *isotropic*. The apparent anisotropy of the electron-phonon interaction is shown to arise from the curvature of the bare electronic bands of graphene, which is strongly enhanced in proximity of the van Hove singularity at the M point. Our findings are relevant to the interpretation of photoemission spectra in materials where the Fermi level is aligned with a van Hove singularity, such as the hole-doped cuprates at optimal doping.

3.2 Theory and computation

The mass-enhancement parameter or electron-phonon coupling strength $\lambda_{\mathbf{k}}$ of an electronic state with wavevector $\mathbf{k}$ on the Fermi surface can be expressed through the energy derivative of the real part of the self-energy arising from the electron-phonon interaction [73]:

$$\lambda_{\mathbf{k}} = -\left.\frac{\partial\ \mathrm{Re}\Sigma_{\mathbf{k}}(E)}{\partial E}\right|_{E=E_\mathrm{F}} , \tag{3.1}$$

E_F being the Fermi level. Within the Migdal approximation, which corresponds to considering the non-crossing electron-phonon self-energy diagrams, this quantity can be calculated by [39, 31]:

$$\begin{aligned}\lambda_{\mathbf{k}} = &\sum_{m,\nu}\int \frac{d\mathbf{q}}{A_\mathrm{BZ}}\,|g_{mn,\nu}(\mathbf{k},\mathbf{q})|^2 \\ &\times\ \left[\frac{n_{\mathbf{q}\nu}+1-f_{m\mathbf{k}+\mathbf{q}}}{(E_\mathrm{F}-\epsilon_{m\mathbf{k}+\mathbf{q}}-\omega_{\mathbf{q}\nu})^2}+\frac{n_{\mathbf{q}\nu}+f_{m\mathbf{k}+\mathbf{q}}}{(E_\mathrm{F}-\epsilon_{m\mathbf{k}+\mathbf{q}}+\omega_{\mathbf{q}\nu})^2}\right] ,\end{aligned} \tag{3.2}$$

where $\epsilon_{n\mathbf{k}}$ is the energy of an electron in the band n with wavevector $\mathbf{k}$, $\omega_{\mathbf{q}\nu}$ the energy of a phonon in the branch ν with wavevector $\mathbf{q}$, and $f_{n\mathbf{k}}$ and $n_{\mathbf{q}\nu}$ are the Fermi-Dirac and Bose-Einstein occupations, respectively. The integration is performed within the two-dimensional Brillouin zone of area A_BZ. The electron-phonon matrix element $g_{mn,\nu}(\mathbf{k},\mathbf{q}) = \langle m\mathbf{k}+\mathbf{q}|\Delta V_{\mathbf{q}\nu}|n\mathbf{k}\rangle$ is the amplitude for the transition from an electronic state $|n\mathbf{k}\rangle$ to another state $|m\mathbf{k}+\mathbf{q}\rangle$ induced by the change in the self-consistent potential $\Delta V_{\mathbf{q}\nu}$ generated by the phonon $|\mathbf{q}\nu\rangle$. The technical details of the calculations are reported in Ref. [60].

It can be shown [39] that the actual electron-phonon coupling strength in Eq. (3.1) can also be written as

$$\lambda_{\mathbf{k}} = \frac{v^0_{\mathbf{k}}(E_\mathrm{F})}{v_{\mathbf{k}}(E_\mathrm{F})} - 1 , \tag{3.3}$$

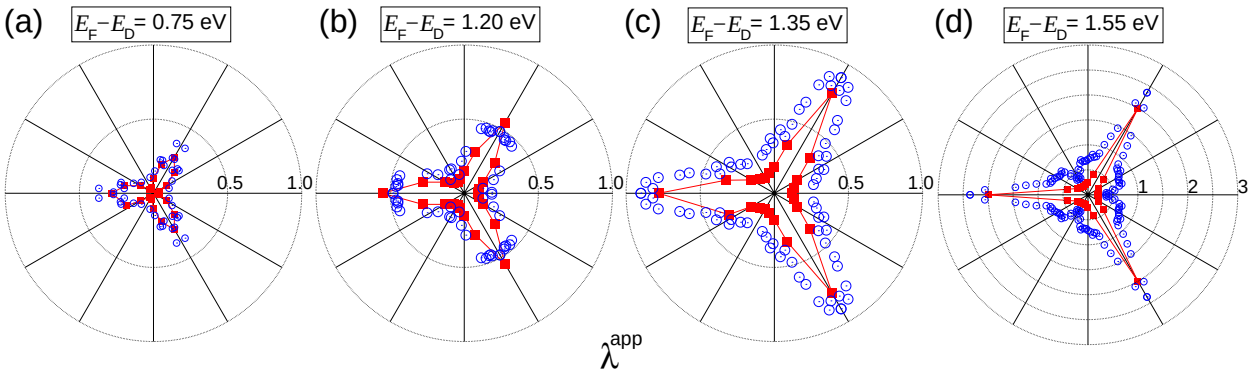

Figure 3.1: Polar plots of the apparent electron-phonon coupling strength $\lambda_{\mathbf{k}}^{\rm app}$ on the Fermi surface around the K point in the Brillouin zone. Filled squares and empty circles represent results from the *ab initio* calculation and from the experimental photoemission spectra, respectively. The lines are included as a guide to the eye. Different panels correspond to different doping levels. Note that the scale in (d) is different from that in (a)-(c).

where $v_{\mathbf{k}}(E_{\rm F})$ and $v_{\mathbf{k}}^0(E_{\rm F})$ are the renormalized and the bare velocities at the Fermi level, respectively. While Eq. (3.3) is useful for theoretical analyses, it cannot be used directly in determining the electron-phonon coupling strength from the experimental data since the bare group velocity is merely a conceptual tool and cannot be measured. To circumvent this difficulty, from the experimentally measured low-energy photoemission spectrum, the electron-phonon coupling strength is usually extracted [37, 55] by taking the ratio of the renormalized velocity below and above the phonon kink. This procedure rests on the assumptions that (i) well beyond the phonon energy scale the bare velocity is fully recovered and (ii) the bare band is linear over the energy range considered. We denote the value obtained from this procedure as the apparent electron-phonon coupling strength:

$$\lambda_{\mathbf{k}}^{\rm app} = \frac{v_{\mathbf{k}}(E_{\rm F} - \Delta E)}{v_{\mathbf{k}}(E_{\rm F})} - 1 \ , \tag{3.4}$$

where ΔE is taken slightly larger than the phonon energy $\omega_{\rm ph}$ so that the energy $E = E_{\rm F} - \Delta E$ falls below the phonon kink.

3.3 Results and comparison with experiment

3.3.1 The apparent electron-phonon coupling strength

In Fig. 3.1 we compare the apparent coupling strength $\lambda_{\mathbf{k}}^{\rm app}$ obtained from our first-principles calculations and that extracted from the experimental photoemission spectra of graphene at four different levels of doping [55]. To determine $v_{\mathbf{k}}(E_{\rm F} - \Delta E)$ in Eq. (3.4) from our first-principles calculations, we considered the slope of the quasiparticle band at the

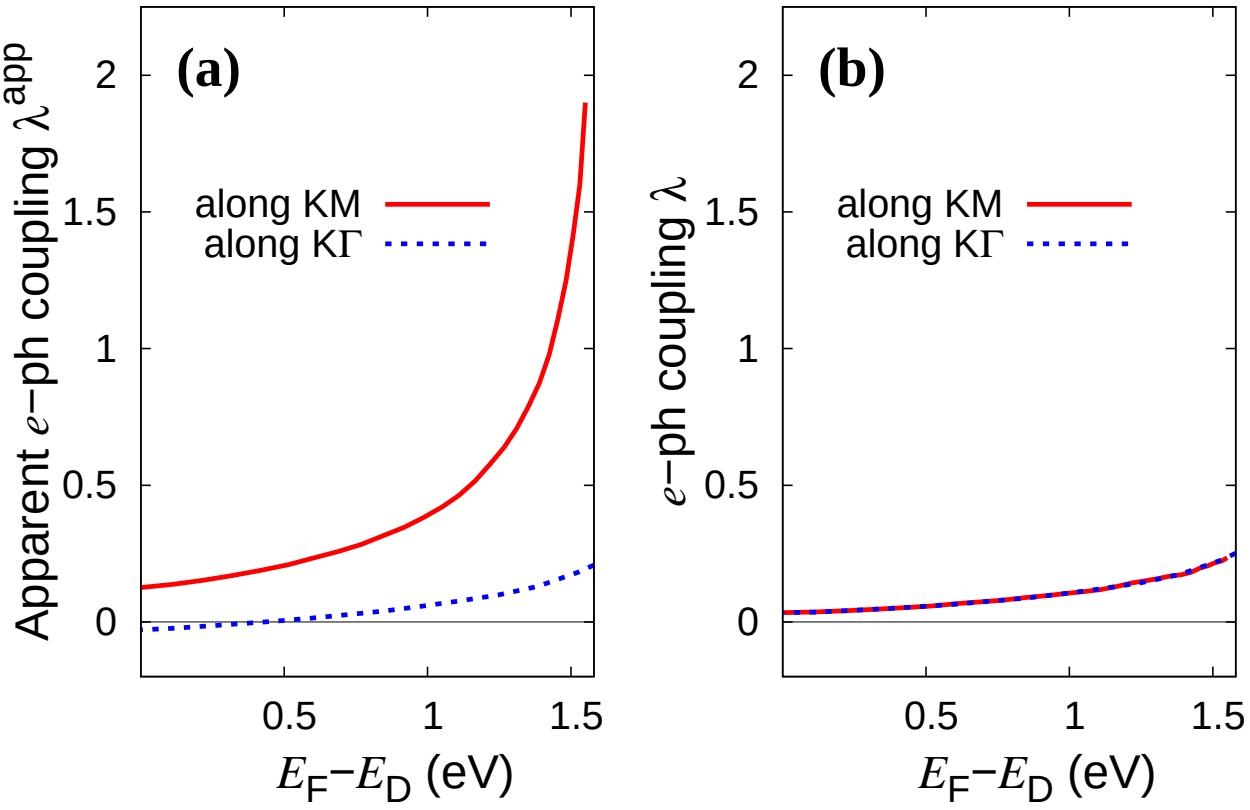

Figure 3.2: The apparent strength $\lambda^{\rm app}$ (a) and the actual electron-phonon coupling strength λ (b) calculated along two different directions in the two-dimensional Brillouin zone of graphene: along KM (solid lines) and along KΓ (dashed lines). Along the KΓ direction, $\lambda^{\rm app}$ can even become negative [cf. discussion around Eq. (3.5)].

energy ΔE =0.3 eV below the Fermi level [74]. We have checked that as the energy range ΔE varies within the interval 0.2∼0.4 eV, the apparent strength $\lambda^{\rm app}$ changes by less than 10 % along both the KM and KΓ directions. Theory and experiment are in good agreement with each other for all doping levels considered. For graphene at the highest doping level ($E_{\rm F} - E_{\rm D} = 1.55$ eV, where $E_{\rm D}$ being the energy at the Dirac point) the agreement between theory and experiment is slightly worse along the KΓ direction.

Figure 3.2(a) shows the calculated apparent strength $\lambda^{\rm app}$ [Eq. (3.4)] as a function of doping for two different directions in the Brillouin zone of graphene. The apparent electron-phonon coupling strength is highly anisotropic and can become as large as $\lambda^{\rm app} = 2$ along the KM direction for the doping levels considered here.

Now we consider the actual electron-phonon coupling strength λ as obtained from Eq. (3.2) [Fig. 3.2(b)]. The actual strength increases monotonically with doping, reaching $\lambda = 0.22$ when $E_{\rm F} - E_{\rm D} = 1.5$ eV. At variance with the apparent strength, the actual strength λ does not depend on the direction of the wavevector $\mathbf{k}$. We have checked that this holds for

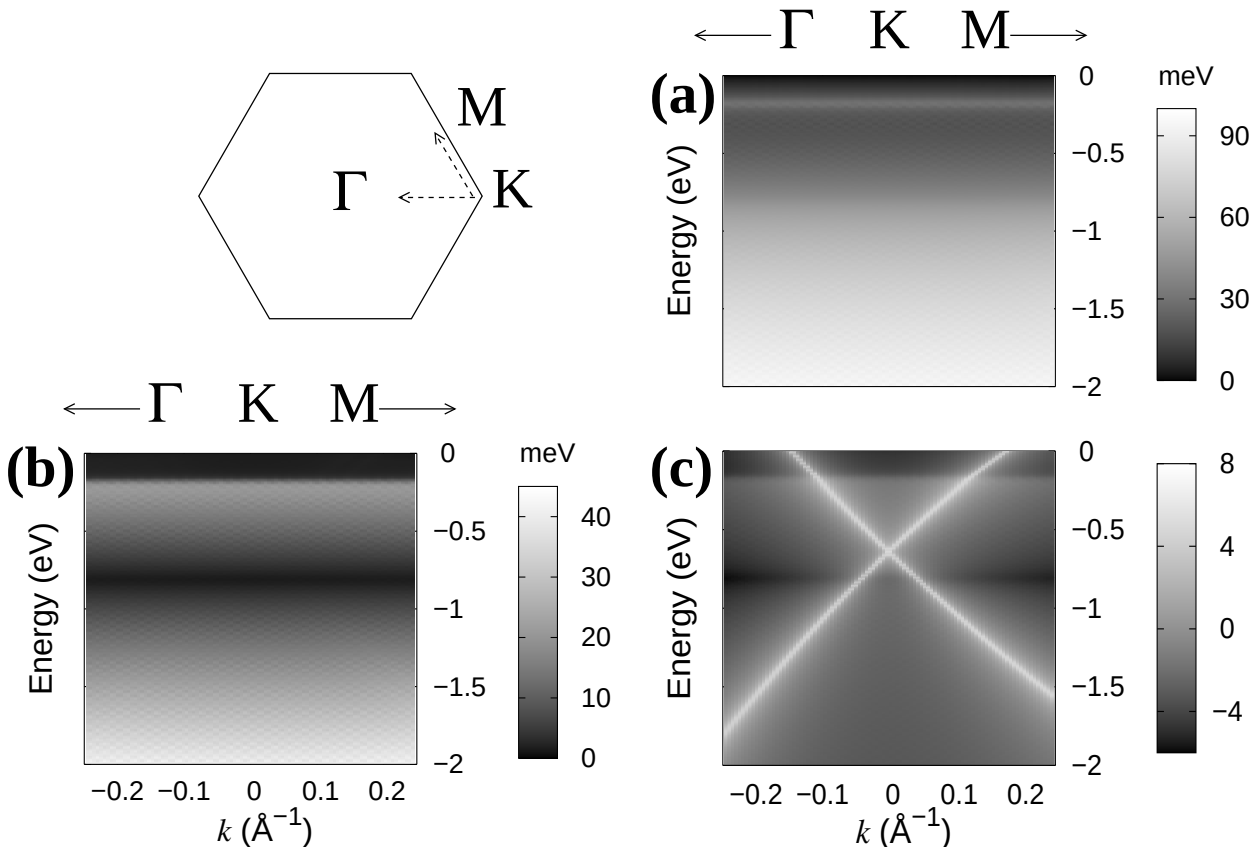

Figure 3.3: Calculated (a) real and (b) imaginary part of the electron self-energy $\Sigma(E, \mathbf{k})$ and (c) logarithm of the corresponding spectral function $A(E, \mathbf{k})$ arising from the electron-phonon interaction in n-doped graphene ($E_{\mathrm{F}} - E_{\mathrm{D}} = 0.64$ eV), along two different directions KM and KΓ in the Brillouin zone.

any path through the K point. The present results indicate that the actual electron-phonon coupling strength in doped graphene is extremely isotropic. Thus, the actual strength can differ substantially from the apparent strength, the more so as the Fermi surface approaches the van Hove singularity at the M point.

3.3.2 The electron self energy and spectral function

In order to analyze in detail the angular dependence of the electron-phonon coupling in graphene, we calculated the phonon-induced electron self-energy using Eq. (1) of Ref. [60]. While in Ref. [60] the electron self-energy was evaluated under the constraint $E = \epsilon_{\mathbf{k}}$, we here consider the complete energy-dependent self-energy $\Sigma_{\mathbf{k}}(E)$. Figure 3.3 (a) and (b) show the real and the imaginary part of the electron self-energy in n-doped graphene ($E_{\mathrm{F}} - E_{\mathrm{D}} = 0.64$ eV). The wavevector is varied along two different paths indicated in the upper left corner of Fig. 3.3. The dependence of the self-energy on the wavevector $\mathbf{k}$ is found

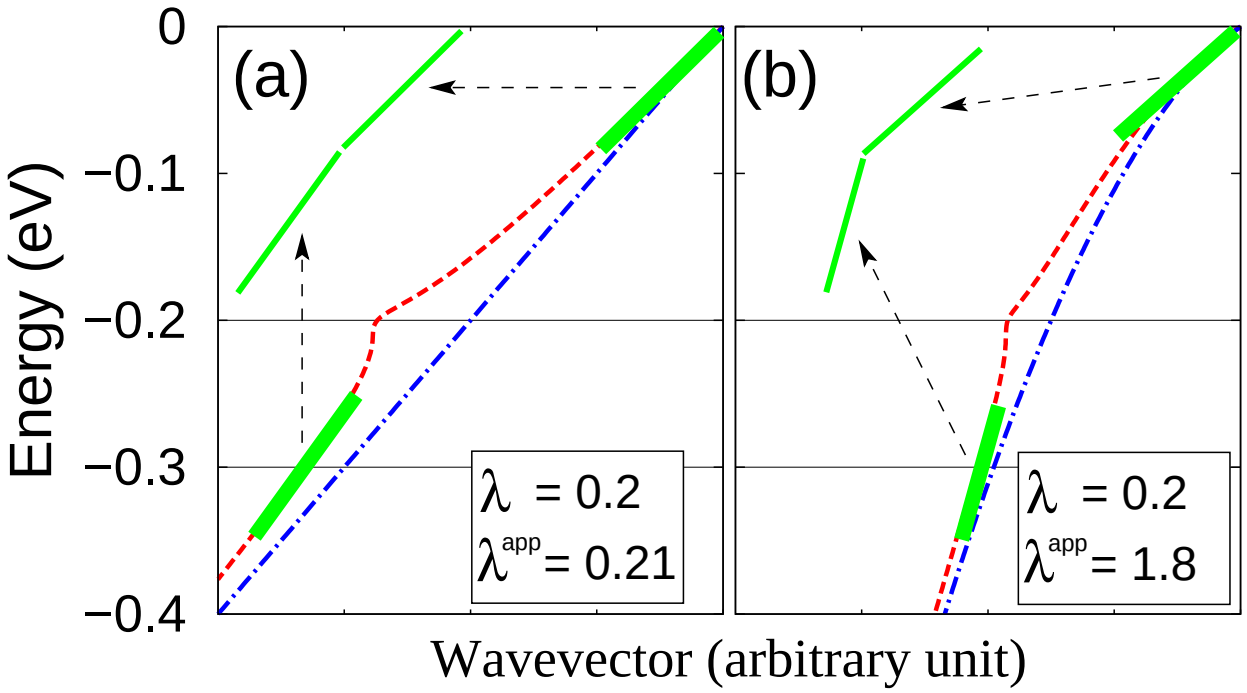

Figure 3.4: Quasiparticle bandstructures of model systems including the electron-phonon interaction (dashed lines). In (a) and (b) the bare electronic bands (dash-dotted lines) are assumed to be linear and quadratic, respectively. In each case, the actual electron-phonon coupling strength is set to $\lambda = 0.2$. The horizontal solid lines represent the phonon energy $\omega_{\rm ph} = 0.2$ eV, and the energy $\Delta E = 0.3$ eV below the Fermi level ($E_{\rm F} = 0$) at which the slope is taken to calculate the apparent strength $\lambda^{\rm app}$. The solid line segments are tangential to the quasiparticle bandstructure at $E = 0$ or $E = -\Delta E$.

to be extremely weak, the variation along the path considered in Fig. 3.3 being less than 3 meV for a given energy E. The insensitivity of the electron-phonon coupling strength $\lambda_{\mathbf{k}}$ to the wavevector $\mathbf{k}$ [see Fig. 3.2(b)] is fully consistent with the finding on the self-energy. Figure 3.3 also shows that, while the self-energy is highly isotropic, the corresponding spectral function exhibits significant angular dependence due to the anisotropic dispersion of the energy bands in graphene.

Recently, the observed anisotropy [55] in the apparent electron-phonon coupling strength has been related to foreign atoms based on calculations of CaC_6 layers with the dopants arranged periodically in atop sites on the graphene plane [61]. Our calculations clearly show that the anisotropy in the apparent strength $\lambda^{\rm app}$ is already present without invoking the possible effect of the dopants.

3.3.3 The effect of bare electron band curvature

Our investigation of doped graphene allows us to discuss some general aspects of the extraction of the electron-phonon coupling parameters from angle-resolved photoemission data. By expanding the energy dependence of the velocity to first order, we can rewrite approximately the apparent electron-phonon coupling strength in Eq. (3.4) as:

$$\lambda_{\mathbf{k}}^{\mathrm{app}} \approx \lambda_{\mathbf{k}} - \frac{v_{\mathbf{k}}'^{0}(E_{\mathrm{F}})}{v_{\mathbf{k}}(E_{\mathrm{F}})}\Delta E \ . \tag{3.5}$$

In Eq. (3.5), $v_{\mathbf{k}}'^{0}(E_{\mathrm{F}})$ is the energy derivative of the bare velocity, and we assumed that well below the phonon kink the bare and the renormalized velocities coincide. Equation (3.5) shows that, whenever the band velocity decreases with decreasing binding energy (i.e., $v_{\mathbf{k}}'^{0} < 0$) as is the case for graphene along the KM direction, the apparent electron-phonon coupling strength always exceeds the actual strength.

To illustrate this point, we consider in Fig. 3.4 the quasiparticle bandstructure for a model system obtained by assuming an Einstein phonon spectrum with phonon energy $\omega_{\mathrm{ph}} = 0.2$ eV, a constant density of states near the Fermi level, and a constant electron-phonon coupling strength λ=0.2. Within this model, the real part of the electron self-energy due to electron-phonon interaction reads [64]:

$$\mathrm{Re}\ \Sigma(E) = -\frac{\lambda\omega_{\mathrm{ph}}}{4}\log\left|\frac{(E+\omega_{\mathrm{ph}})^2+\Gamma^2}{(E-\omega_{\mathrm{ph}})^2+\Gamma^2}\right|, \tag{3.6}$$

having included broadening $\Gamma = 10$ meV for convenience. As shown in Fig. 3.4(a), the apparent strength $\lambda^{\mathrm{app}} = 0.21$ constitutes a good approximation to the actual strength $\lambda = 0.2$ when the slope of the bare electronic band does not change appreciably within the phonon energy scale, i.e. $v_{\mathbf{k}}'^{0}(E_{\mathrm{F}})\Delta E \ll v_{\mathbf{k}}(E_{\mathrm{F}})$. However, in the case where the bare velocity decreases with decreasing binding energy, the apparent strength $\lambda^{\mathrm{app}} = 1.8$ differs significantly from the actual electron-phonon coupling strength $\lambda = 0.2$, consistent with Eq. (3.5) [Fig. 3.4(b)]. In the limiting situation where the Fermi level is aligned with the van Hove singularity (as in heavily doped graphene), the velocity at the Fermi level vanishes while the velocity below the phonon kink energy remains finite. As a result, the apparent strength obtained through Eq. (3.4) becomes exceedingly large.

3.4 Conclusion

In conclusion, we have shown that while the phonon-induced electronic self-energy of graphene is isotropic and consequently the angular dependence of the electron-phonon coupling strength is negligible, the apparent electron-phonon coupling strength extracted from the experimental angle-resolved photoemission spectra using Eq. (3.4) exhibits significant anisotropy due to the curvature of the underlying bare electronic bands. Our analysis indicates that the band curvature is a crucial ingredient for the interpretation of angle-resolved

photoemission spectra. For example, the present result may carry implications in the interpretation of many-body renormalization effects along the antinodal cuts in the photoemission spectra of cuprate superconductors, due to the presence of a saddle-point van Hove singularity along the Cu-O bond directions [75, 76].

Chapter 4

First-principles study of electron linewidths in graphene

4.1 Introduction

Graphene [35, 36, 71], a single layer of carbon atoms in a hexagonal honeycomb structure, is a unique system whose carrier dynamics can be described by a massless Dirac equation [77]. Within the quasiparticle picture, carriers in graphene exhibit a linear energy dispersion relation and chiral behavior resulting in a half-integer quantum Hall effect [35, 36], absence of backscattering [78, 79], Klein tunneling [80], and novel phenomena such as electron supercollimation in superlattices [81, 82, 83].

Graphene is considered a promising candidate for electronic and spintronic devices [72]. For these applications it is important to understand the effects of many-body interactions on carrier dynamics. In particular, the scattering rate of charge carriers, manifested in their linewidths, affects the transport properties of actual devices.

The scattering of charge carriers in solids can arise from several different mechanisms, among which electron-hole pair generation, electron-plasmon interaction, and electron-phonon (e-ph) interaction are generally important. Scattering by impurities, defects and interactions with the substrate also affects the carrier dynamics. The contribution to the electron linewidths arising from the e-ph interaction has been studied with first-principles calculations [60, 5] and through the use of analytical and numerical calculations based on the massless Dirac equation [49, 84]. The linewidth contribution originating from electron-electron (e-e) interactions, which includes both the electron-hole pair generation process and the electron-plasmon interaction, has only been studied within the massless Dirac equation formalism [85, 86, 38].

A recent angle-resolved photoemission experiment on n-doped graphene epitaxially grown on silicon carbide (SiC) [2] has stimulated experimental [53, 55, 58] and theoretical [85, 86, 38, 60, 49, 84] studies on this topic. In Ref. [2], the width of the momentum distribution curve (MDC) from photoemission data is presented. The MDC of the graphene photoemission

spectra is observed to resemble a simple Lorentzian whose width may be interpreted to be directly proportional to the scattering rate [2].

We draw the attention to the well-known controversy in the different interpretations of the angle-resolved photoemission spectra of graphene. It is claimed in Ref. [2] that the spectral features can entirely be understood from many-body effects, including both *e*-*e* and *e*-ph interactions, in graphene. On the other hand, in Ref. [58], it is argued that many of those features are dominated by an energy gap of 0.2∼0.3 eV, which opens up at the Dirac point energy ($E_{\rm D}$) because of interactions between graphene and the reconstructed surface of SiC. This important problem in understanding the quasiparticle spectra of graphene (which also have implications in graphene-based electronics applications) has led to numerous additional experiments directly or indirectly addressing this discrepancy [56, 54, 87, 88, 59, 89]. On the theoretical side, several density functional theory calculations on the effect of substrates without considering many-body effects, along the line of Ref. [58], have been performed [90, 91, 92]. On the other hand, first-principles calculations on the effects of both *e*-*e* and *e*-ph interactions, along the line of Ref. [2], have been lacking up to now.

In this chapter, to fill in this missing part, we present *ab initio* calculations of the electron linewidth in *n*-doped graphene arising from *e*-*e* interactions employing the *GW* approximation [20, 93, 94]. In addition, we calculate the electron linewidth originating from the *e*-ph interaction following the method in Refs. [60, 95] and [31]. Combining both contributions, we provide a comprehensive view of the scattering rate originating from many-body effects. Our calculation indicates that the linewidth arising from *e*-*e* interactions is highly anisotropic. This is in contrast to the insensitivity to wavevector of the phonon-induced electron linewidth shown in Ref. [5]. The calculated linewidth arising from *e*-*e* interaction becomes comparable to that arising from *e*-ph interaction at a binding energy of ~ 0.2 eV (i. e. , the optical phonon energy). The combination of the two contributions accounts for most of the measured linewidth over the 0 eV $\sim$ 2.5 eV binding energy range.

4.2 Theory and computation

The electronic eigenstates $|n\mathbf{k}\rangle$ of graphene are obtained with *ab initio* pseudopotential density-functional calculations [96] in the local density approximation (LDA) [14, 40] in a supercell geometry. Electronic wavefunctions in a $72 \times 72 \times 1$ $\mathbf{k}$-point grid are expanded in a plane-waves basis [41] with a kinetic energy cutoff of 60 Ry. The core-valence interaction is treated by means of norm-conserving pseudopotentials [15]. Graphene layers between adjacent supercells are separated by 8.0 Å and the Coulomb interaction is truncated to prevent spurious interaction between periodic replicas [97]. Increasing the interlayer distance to 16.0 Å makes virtually no difference in the calculated electron self-energy. Doped graphene is modeled by an extra electron density with a neutralizing background.

We calculate the imaginary part of the electron self-energy induced by the *e*-*e* interaction within the *GW* approximation [20, 93]. The frequency dependent dielectric matrices $\epsilon_{\mathbf{G},\mathbf{G}'}(\mathbf{q},\omega)$ are calculated within the random phase approximation using the LDA wavefunc-

tions on a regular grid of ω with spacing $\Delta\omega$ =0.125 eV [98], and a linear interpolation is performed to obtain the dielectric matrices for energies in between the grid points. In the calculation of the polarizability, for numerical convergence, an imaginary component of magnitude $\Delta\omega$ of 0.125 eV as above is introduced in the energy denominator. Convergence tests showed that the dimension of $\epsilon_{\mathbf{G},\mathbf{G}'}$ may be truncated at a kinetic energy cutoff of $\hbar^2 G^2/2m$ =12 Ry. To take into account the screening of the SiC substrate, we have renormalized the bare Coulomb interaction by an effective background dielectric constant of $\varepsilon_{\rm b} = (1 + \varepsilon_{\rm SiC})/2 = 3.8$ [2, 85, 86, 38], where $\varepsilon_{\rm SiC}(= 6.6)$ is the optical dielectric constant of SiC [99, 100].

4.3 Results and discussion

4.3.1 The electron self energy arising from electron-electron interactions

Figure 4.1 shows the calculated imaginary part $\mathrm{Im}\,\Sigma^{e-e}_{n\mathbf{k}}(\varepsilon_{n\mathbf{k}}) = \langle n\mathbf{k}|\,\mathrm{Im}\,\Sigma^{e-e}(\mathbf{r},\mathbf{r}',\varepsilon_{n\mathbf{k}})\,|n\mathbf{k}\rangle$ of the electron self-energy arising from the *e*-*e* interaction with ω set at the LDA eigenvalue $\varepsilon_{n\mathbf{k}}$. The Fermi level $E_{\rm F}$ (= 0) is taken to be 1 eV above $E_{\rm D}$. In Fig. 4.1(a), $\mathrm{Im}\,\Sigma^{e-e}_{n\mathbf{k}}(\varepsilon_{n\mathbf{k}})$ for graphene without including substrate screening, appropriate for suspended graphene [101, 102], is plotted along the KΓ direction. Generally, the self-energy increases with increasing $|\varepsilon_{n\mathbf{k}}|$ as measured from $E_{\rm F}$. A notable feature is the peak around $\varepsilon_{n\mathbf{k}} = -1.5$ eV. To find the origin of this peak, we have decomposed the total electron self-energy into the contributions arising from transitions into the upper linear bands (above $E_{\rm D}$) and the lower linear bands (below $E_{\rm D}$). The former involves electron-plasmon interaction [85]. The peak structure comes from scattering processes of electrons into the upper linear bands, whereas those scattering processes into the lower linear bands result in a monotonic increase in the electron linewidth. When the background dielectric constant $\varepsilon_{\rm b}$ is changed from 1 to 3.8 [Fig. 4.1(b)], the position of this peak shifts toward lower-binding energy by ~ 0.3 eV, reflecting a decrease of the plasmon energy in graphene [Fig. 4.1(e)] [103, 104]. The height of the peak is further suppressed. At low energy ($|\varepsilon_{n\mathbf{k}}| < 1.0$ eV), the imaginary part of the self-energy is however not sensitive to the choice of $\varepsilon_{\rm b}$.

Comparing Figs. 4.1(a) and 4.1(b) with Figs. 4.1(c) and 4.1(d) shows that the electron self-energy arising from the *e*-*e* interaction calculated along the KM direction is very different from that along the KΓ direction. Below −1.5 eV, $\mathrm{Im}\,\Sigma^{e-e}_{n\mathbf{k}}(\varepsilon_{n\mathbf{k}})$ along K→M decreases with increasing $|\varepsilon_{n\mathbf{k}}|$, and it almost vanishes at the M point. This strong $\mathbf{k}$ anisotropy in the *e*-*e* contribution to the imaginary part of the self-energy is a band structure effect, and is absent in calculations based on the massless Dirac equation. This behavior is in contrast with the wavevector insensitivity of the phonon-induced electron self-energy [5] (Fig. 4.2). The calculated real part [105] and the imaginary part [93] of the electron self-energy in bulk graphite arising from the *e*-*e* interaction are also anisotropic, in line with the present findings.

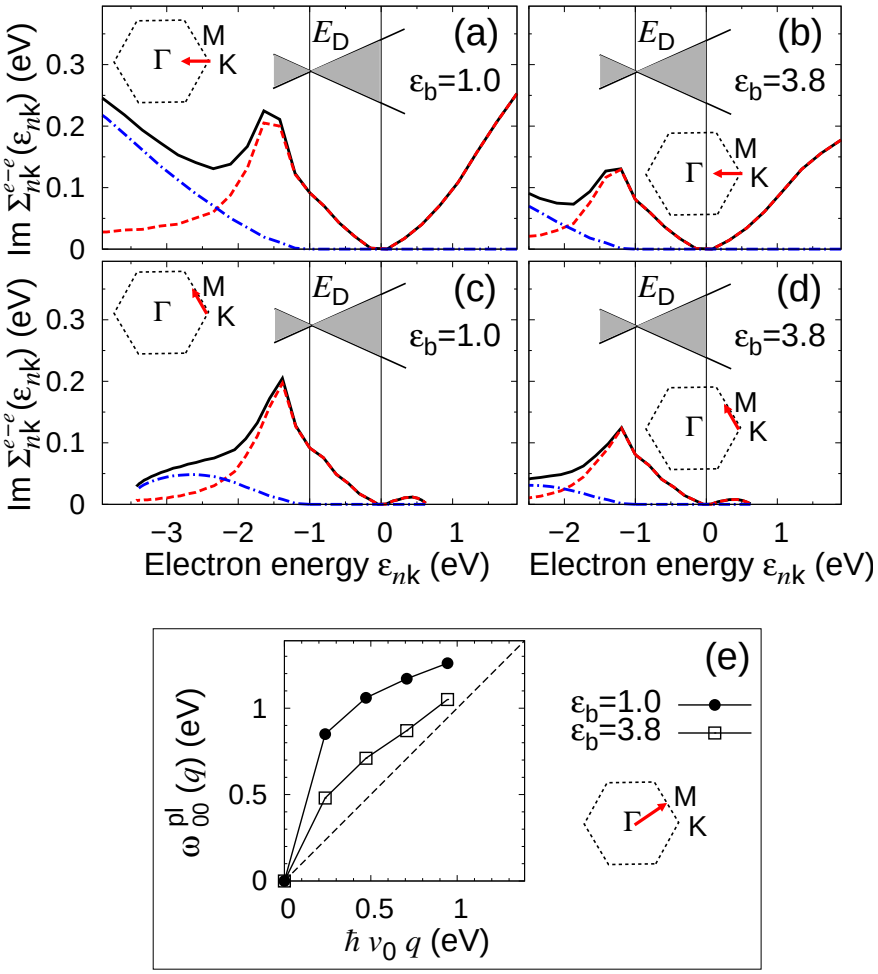

Figure 4.1: (a)-(d): Calculated imaginary part of the electron self-energy arising from the e-e interaction, $\mathrm{Im}\,\Sigma^{e-e}_{n\mathbf{k}}(\varepsilon_{n\mathbf{k}})$, versus the LDA energy $\varepsilon_{n\mathbf{k}}$ (solid lines) in n-doped graphene. The Dirac point energy E_D is 1.0 eV below the Fermi level. The contributions to $\mathrm{Im}\,\Sigma^{e-e}_{n\mathbf{k}}(\varepsilon_{n\mathbf{k}})$ coming from electronic transitions to the upper linear bands and to the lower linear bands are shown as dashed lines and dash-dotted lines, respectively. The self-energy is evaluated along the reciprocal space segments shown in the insets. (a) and (c) are results for suspended graphene with a background dielectric constant of $\varepsilon_\mathrm{b} = 1.0$, whereas (b) and (d) are results for graphene with a background dielectric constant of $\varepsilon_\mathrm{b} = (1 + \varepsilon_\mathrm{SiC})/2 = 3.8$. The Fermi level and E_D are indicated by vertical lines. (e): Calculated plasmon energy dispersion relation $\omega^\mathrm{pl}_{00}(\mathbf{q})$, given by $\epsilon_{\mathbf{G}=0,\mathbf{G}'=0}[\mathbf{q}, \omega^\mathrm{pl}_{00}(\mathbf{q})] = 0$, versus $\hbar v_0 |\mathbf{q}|$ along the ΓM direction. The solid lines are guides to the eye and the dashed line corresponds to $\omega(q) = \hbar v_0 q$.

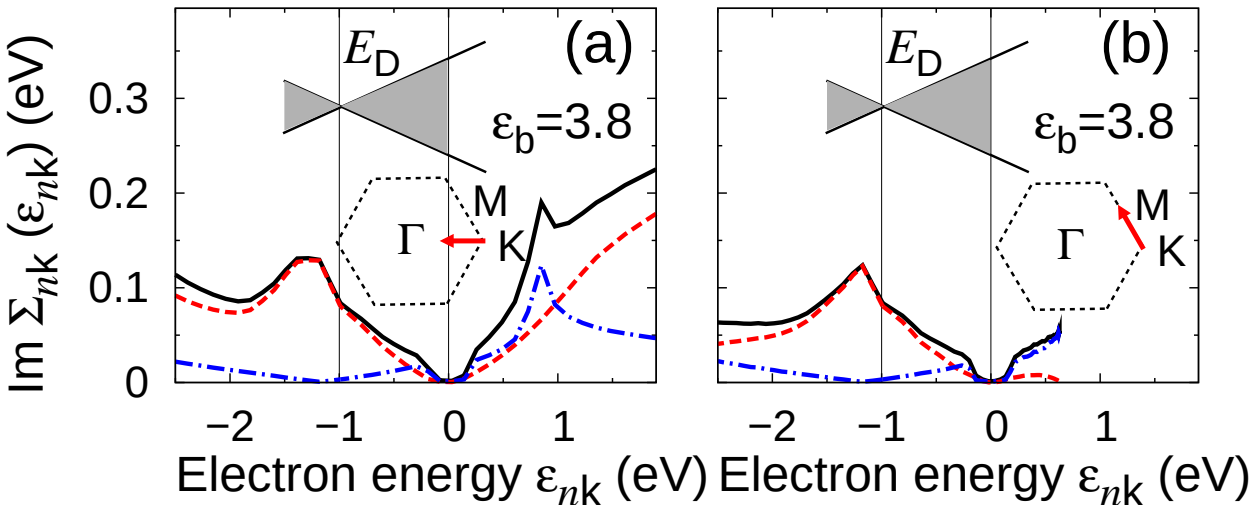

Figure 4.2: Calculated Im $\Sigma_{n\mathbf{k}}(\varepsilon_{n\mathbf{k}})$ versus the LDA energy eigenvalue $\varepsilon_{n\mathbf{k}}$ in n-doped graphene ($E_{\rm D} = -1.0$ eV) on a model substrate ($\varepsilon_{\rm b} = 3.8$). The total self-energy, the self-energy arising from the e-e interaction, and that arising from the e-ph interaction are shown in solid, dashed and dash-dotted lines, respectively. The self-energy is evaluated along the reciprocal space segments shown in the insets.

4.3.2 The total electron self energy

Figures 4.2(a) and 4.2(b) show the electron self-energy in n-doped graphene ($E_{\rm D} = -1.0$ eV) on a substrate (model with $\varepsilon_{\rm b} = 3.8$) arising both from the e-e and the e-ph interaction. The Im $\Sigma_{n\mathbf{k}}(\varepsilon_{n\mathbf{k}})$ along the two different directions KΓ and KM are qualitatively different at high binding energy. This anisotropy is due to the e-e interaction, and not the e-ph interaction [5]. It is noted that the total linewidth along the KM direction is almost constant for binding energies in the range 1.7 to 3.5 eV. These anisotropic features should be observable in photoemission experiments.

The e-e and the e-ph interactions give comparable contributions to the imaginary part of the electron self-energy, especially within a few tenths of an eV from the Fermi level (Fig. 4.2). This behavior is peculiar to graphene. In most metals the e-ph contribution to the electron self-energy near $E_{\rm F}$ is generally dominant over the e-e contribution at energies comparable to the relevant phonon energy scale [106]. Similarly large Im $\Sigma_{n\mathbf{k}}(\varepsilon_{n\mathbf{k}})$ due to e-e interactions are obtained in the Dirac Hamiltonian calculations in Refs. [85] and [86] if the same background dielectric constant $\varepsilon_{\rm b}$ is used. Because of this peculiar aspects of graphene, an e-ph coupling strength λ extracted from measured data could be overestimated if the e-e interaction is neglected. This may explain why the e-ph coupling strength λ extracted from photoemission spectra [55] is larger than the theoretical calculations [5, 49], together with the effects of bare band curvature [5] and dopants.

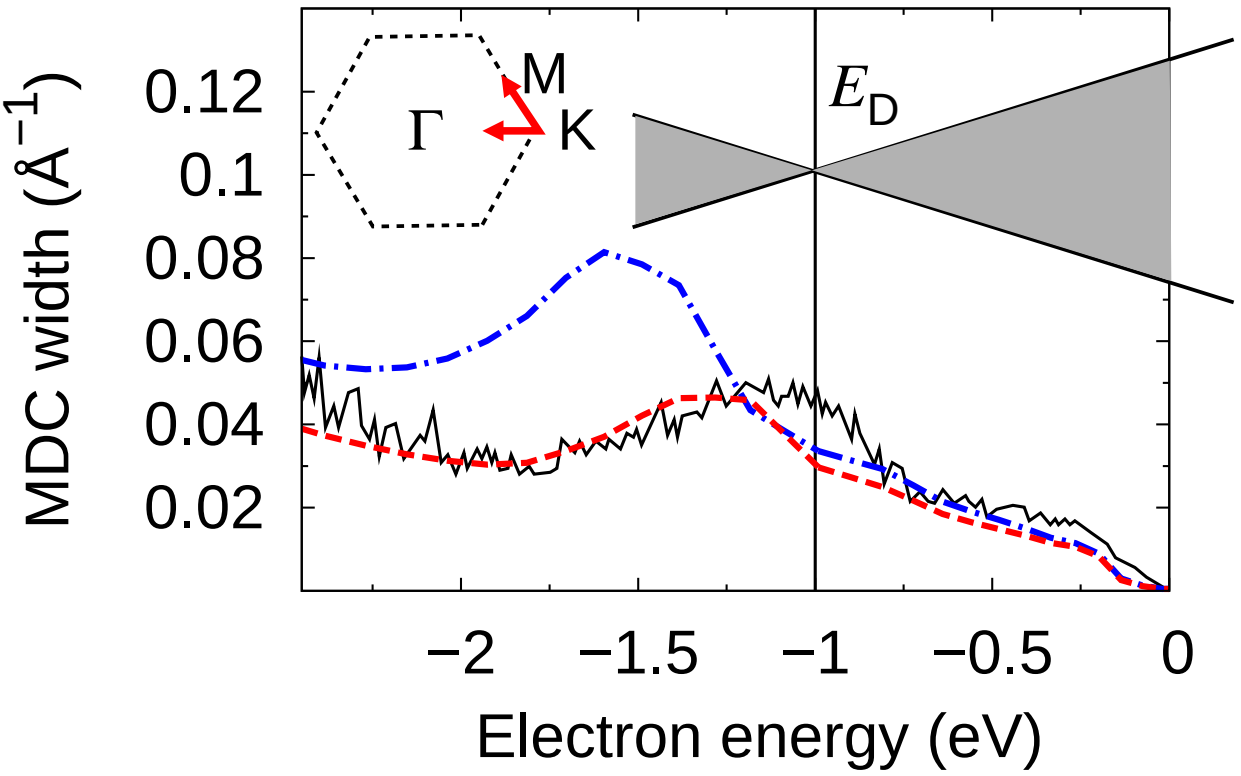

Figure 4.3: MDC width versus binding energy in n-doped graphene ($E_{\rm D} = -1.0$ eV). Calculated quantities for suspended graphene ($\varepsilon_{\rm b} = 1.0$) and for graphene on a model substrate ($\varepsilon_{\rm b} = 3.8$) are shown in dash-dotted and dashed lines, respectively. The experimental result measured for sample corresponding to the highest level of doping in Fig. 3 of Ref. [2] are shown as the solid line [3]. Both the experimental and the calculated results are along the KM and the KΓ direction of the Brillouin zone when the electron energy is above and below $E_{\rm D}$, respectively.

4.3.3 Comparison with experiment

We now compare the imaginary part of the electron self-energy obtained from our calculation with the MDC width obtained from measured photoemission spectra [2]. For a linear bare band energy dispersion, the spectral function at a fixed energy ω is a Lorentzian as a function of the wavevector measured from the **K** point [2]. Thus, the width of the MDC Δk at energy $\omega = \varepsilon_{n\mathbf{k}}$ can be identified as $\Delta k(\varepsilon_{n\mathbf{k}}) = 2{\rm Im}\,\Sigma_{n\mathbf{k}}(\varepsilon_{n\mathbf{k}})/\hbar v_0$ where v_0 is the LDA band velocity of low-energy charge carriers in graphene [2, 60]. (For the n-doped graphene with $E_{\rm D} = -1.0$ eV, the bare band dispersion is, to a good approximation, linear in the energy range considered in Fig. 4.3.)

Figure 4.3 shows the calculated MDC width for suspended graphene ($\varepsilon_{\rm b} = 1.0$) and for our model of graphene on SiC ($\varepsilon_{\rm b} = 3.8$). The substrate screening affects the position and the strength of the peak arising from the electron-plasmon interaction, while the low-

energy part is insensitive to the dielectric screening from the substrate. The calculated MDC width for graphene when substrate screening is accounted for is in agreement with the experimental data of Ref. [2] throughout the whole energy window shown in Fig. 4.3. However, the experimentally measured MDC width in a 0.4 eV energy window around $E_{\rm D}$ (=-1.0 eV) is larger than that from our calculation. This enhanced linewidth may possibly arise from the gap which opens up at $E_{\rm D}$ and midgap states originating from the interactions between graphene and SiC substrate with a carbon buffer layer [58, 90, 91, 92].

4.4 Conclusion

In conclusion, we have studied the electron linewidths of n-doped graphene including both the e-e and the e-ph interaction contributions, using first-principles calculations. The imaginary part of the electron self-energy arising from the e-e interaction is strongly anisotropic in $\mathbf{k}$-space. We have shown that for graphene, unlike in conventional metals, the e-e contribution is comparable to the e-ph contribution at low binding-energy. Our calculation explains most of the scattering rate observed in a recent photoemission experiment [2]; however, near the Dirac point energy, the calculated scattering rate is smaller than the measured one, suggesting the possibility of band gap opening and midgap states. These results contribute to the resolution of the important controversy introduced earlier in this chapter and encourages further theoretical studies including both many-body interactions and substrate effects at an atomistic level. More generally, our first-principles calculations convincingly demonstrate that multiple many-body interactions ought to be considered on the same footing in order to achieve a quantitative and comprehensive interpretation of high-resolution angle-resolved photoemission spectra.

Chapter 5

Angle-resolved photoemission spectra of graphene from first-principles calculations

5.1 Introduction

5.1.1 Angle-resolved photoemission spectroscopy

Angle-resolved photoemission spectroscopy (ARPES) is a powerful experimental technique for directly probing electron dynamics in solids. The energy vs. momentum dispersion relations and the associated spectral broadenings measured by ARPES provide a wealth of information on quantum many-body interaction effects. In particular, ARPES allows studies of the Coulomb interaction among electrons (electron-electron interactions) and the interaction between electrons and lattice vibrations (electron-phonon interactions).

In ARPES experiments a sample is illuminated by monochromatic photons, which can extract electrons from the sample if the photon energy exceeds the work function. Analysis of the kinetic energy and angular distribution of the emitted electrons yields the binding energy of the electron in the material and its crystal momentum parallel to the surface [37]. The measured intensity $I(\mathbf{k}, \omega)$, where $\mathbf{k}$ and ω are the momentum and the binding energy of electrons (usually referenced to the Fermi energy), can be written as [37]

$$I(\mathbf{k}, \omega, \hat{e}_\nu, \hbar\nu) = I_0(\mathbf{k}, \omega, \hat{e}_\nu, \hbar\nu) f(\omega) A(\mathbf{k}, \omega)\,, \tag{5.1}$$

where the function $I_0(\mathbf{k}, \omega, \hat{e}_\nu, \hbar\nu)$ takes into account the absorption cross section of the incident photon of energy $\hbar\nu$ and polarization $\hat{e}_\nu$. The function $f(\omega)$ is the Fermi-Dirac distribution, and $A(\mathbf{k}, \omega)$ is the electron spectral function [37]. In interpreting ARPES measurements in a narrow energy range, it is appropriate to assume that the absorption cross section of the photon is constant. Under these conditions, a measurement of the ARPES spectrum provides direct access to the electronic spectral function $A(\mathbf{k}, \omega)$. Within

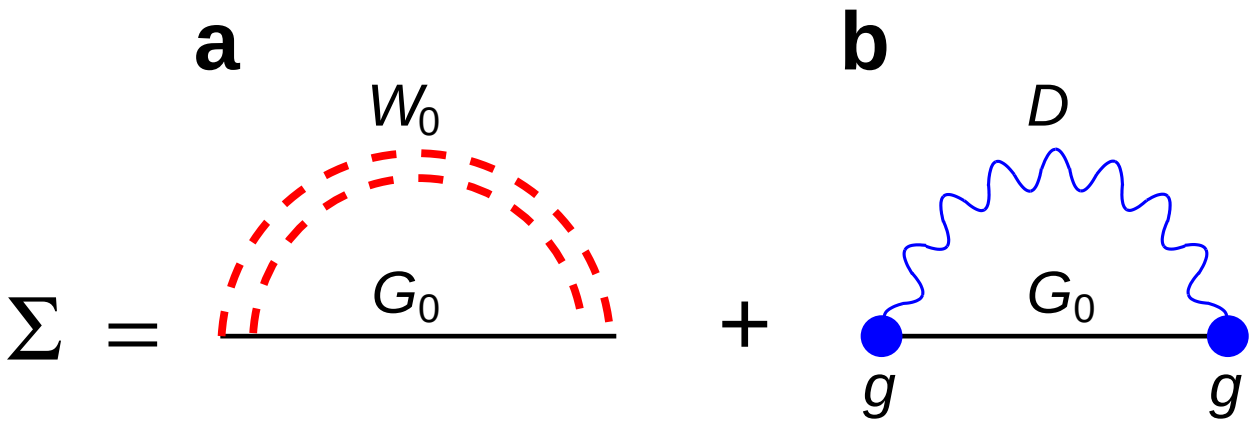

Figure 5.1: **Diagrams included in the calculated electron self-energy Σ. a**, Electron self-energy $\Sigma^{e-e} = iG_0W_0$ arising from e-e interactions within the G_0W_0 approximation. G_0 is the Green's function for bare electrons and W_0 is the screened Coulomb interaction. **b**, Self-energy $\Sigma^{e-ph} = ig^2G_0D$ arising from e-ph interactions within the Migdal approximation. Here, g is the e-ph interaction matrix element and D is the dressed phonon propagator.

quantum many-body theory the electronic spectral function can be expressed as

$$A(\mathbf{k},\omega) = \frac{2}{\pi}\frac{-\mathrm{Im}\Sigma(\mathbf{k},\omega)}{\left[\omega - \varepsilon_{\mathbf{k}} - \mathrm{Re}\Sigma(\mathbf{k},\omega)\right]^2 + \left[\mathrm{Im}\Sigma(\mathbf{k},\omega)\right]^2}\,, \tag{5.2}$$

where the $\varepsilon_{\mathbf{k}}$'s are the the single-particle energy eigenvalues of a reference mean-field system, and the self-energy $\Sigma(\mathbf{k},\omega)$ accounts for the many-body interactions going beyond the mean-field picture [37]. For simplicity of discussion, the band indices are dropped from Eq. (5.2) (see Methods).

5.1.2 Electron self energy

In our investigation, we use density-functional Kohn-Sham eigenstates to describe the mean-field or non-interacting electrons. The electron self-energy arising from the e-e interaction $\Sigma^{e-e}(\mathbf{k},\omega)$ is evaluated within the G_0W_0 approximation [20] (Fig. 5.1a). This corresponds to retaining the first diagram in the Feynman-Dyson perturbation expansion of the self-energy operator but in terms of the screened Coulomb interaction W_0 (Supplementary Discussion 3 for a comparison with previous first-principles calculations [107, 108]). In this work, G_0 is constructed from the Kohn-Sham eigenvalues and eigenfunctions of density-functional theory, and W_0 is the bare Coulomb interaction screened by the full frequency-dependent dielectric matrix $\epsilon(\mathbf{r},\mathbf{r}',\omega)$ calculated within the random phase approximation. The self-energy $\Sigma^{e-ph}(\mathbf{k},\omega)$ arising from the e-ph interaction is similarly evaluated within the Migdal approximation [31] (Fig. 5.1b). With these choices, the e-e interaction and the e-ph interaction are described consistently within the same level of approximation [19] (see

Methods). The total self energy is then obtained as

$$\Sigma(\mathbf{k},\omega) = \Sigma^{e-e}(\mathbf{k},\omega) + \Sigma^{e-ph}(\mathbf{k},\omega)\,. \tag{5.3}$$

5.1.3 ARPES of graphene

Graphene, a single layer of carbon atoms in a honeycomb structure, has recently become an active research area in physics, chemistry, and nanoscience not only because of its peculiar low-energy massless Dirac fermion band structure [35, 36, 71], but also because it holds promise for novel electronics and spintronics applications [109]. In particular, the epitaxial growth of graphene on silicon carbide (SiC) has emerged as one of the promising routes towards large-scale production of graphene [71, 109].

The interpretation of the measured ARPES spectra of epitaxial graphene grown on silicon-rich surface of SiC has been controversial. The spectral features observed in early ARPES measurements [4] were interpreted qualitatively in terms of *e*-*e* and *e*-ph interactions. On the other hand, experiments and analyses performed by a different group suggested that the low-energy ARPES spectrum is dominated by a quasiparticle energy gap of 0.2-0.3 eV at the Dirac point [58]. According to Ref. [58], this band gap likely arises from the coupling of the graphene layer with the reconstructed surface of the SiC substrate. Despite a number of subsequent studies to resolve this controversy [87, 88], the detailed nature of the low-energy quasiparticle dynamics in epitaxial graphene remains an open question.

The electronic structure and the photoemission spectra of graphene have also been explored in a number of theoretical investigations using density-functional theory approaches within a non-interacting single-particle picture [90, 91, 92]. The effects of many-body interactions have also been investigated in model calculations [85, 86]. However, first-principles calculations of the full **k**- and ω-dependent ARPES spectral function - which contains both the quasiparticle dispersions and their lifetimes - including the *e*-*e* and the *e*-ph interactions have not been reported. The lack of first-principles many-body investigations can partly be ascribed to the extremely demanding computational efforts required to evaluate the real part of the electron self-energy, both for the *e*-*e* and for the *e*-ph contributions.

In dealing with effects of *e*-*e* interactions, first-principles calculations have advantages over model calculations based on the two-dimensional massless Dirac equation [85, 86]. First, the scattering rate of even the low-energy charge carriers, whose non-interacting dispersion relation can be well approximated by the two-dimensional massless Dirac equation, shows strong wavevector-anisotropic behaviors [110]. This is because the carrier scattering rate in graphene depends sensitively on the sign of the band curvature [111]. Therefore, the significant wavevector anisotropy in the electron scattering rate is not captured by the model calculations. Second, the model calculations require a cutoff of the high-energy states and an adjustable parameter mimicking effects of internal screening arising from the high-energy states (including the π states higher in energy than the cutoff and the σ states), in addition to the external screening due to the environment. The first-principles approach employing the full bandstructure accounts for these processes explicitly and requires neither a high-energy

cutoff nor an empirical parameter to describe the internal screening.

5.2 Results and discussion

5.2.1 Energy distribution curves

To determine the quasiparticle energy vs. momentum dispersion relations from the calculated ARPES intensity maps for graphene (Figs. 5.2a, d, and g), we follow the standard procedure adopted in analyzing ARPES experiments [37]. First, the energy distribution curves (EDCs) are obtained by performing cuts of the intensity maps at fixed photoelectron momentum (vertical cuts in Figs. 5.2a, d, and g). Subsequently, the quasiparticle band structures are generated by connecting the locations of the maxima in the EDCs for each photoelectron momentum (Figs. 5.2b, e, and h). This procedure ensures that the calculated and the measured dispersion relations are obtained from the corresponding intensity maps using the same procedure.

5.2.2 Energy mismatch between the upper and lower bands

While the dispersion relations extracted from our spectral functions for an isolated graphene layer are linear at large binding energy, we observe a sizable kink for n-doped graphene near the Dirac point ($\mathbf{k} = 0$ in Fig. 5.2) at an energy below the Dirac point energy. Such kinks result in a mismatch between the linear extrapolations of the lower and the upper portions of the Dirac cone (Fig. 5.2). A similar phenomenon has been observed in the measured ARPES spectra [4, 58]. In order to quantify the size of the kinks and the associated energy mismatch, we have taken the energy difference between the two linear asymptotes of the upper and the lower bands (Δ_{kink} in Fig. 5.2f). This calculated energy offset Δ_{kink} is predominantly a result of many-body effects, which comes from the GW self-energy, and is found to increase with the doping level (see Fig. 5.3), consistent with the experimental trend [4]. We have checked that, if many-electron effects are not considered, the energy mismatch is several times smaller, with value ≤ 20 meV for the most heavily doped case considered here and even smaller for other cases. We note that, for the path along which the ARPES spectra are calculated (inset of Fig. 5.2c), the nonlinearity of the bare graphene band is smallest.

Although the calculated Δ_{kink} shows qualitative agreement with experiment, after taking into account the screening of the SiC substrate (Refs. [85, 86], see Methods), our calculated values underestimate the experimentally observed offsets in Ref. [4] consistently by 60-90 meV; this discrepancy, together with the comparison between theory and experiment of electron linewidths discussed in Ref. [110] and later in this chapter, suggests the possible opening up of a band gap at the Dirac point energy due to the interaction between graphene and a reconstructed silicon-rich surface of SiC [58, 90, 91, 92]. Our study shows the need of further first-principles studies, considering both the atomistic structure of the

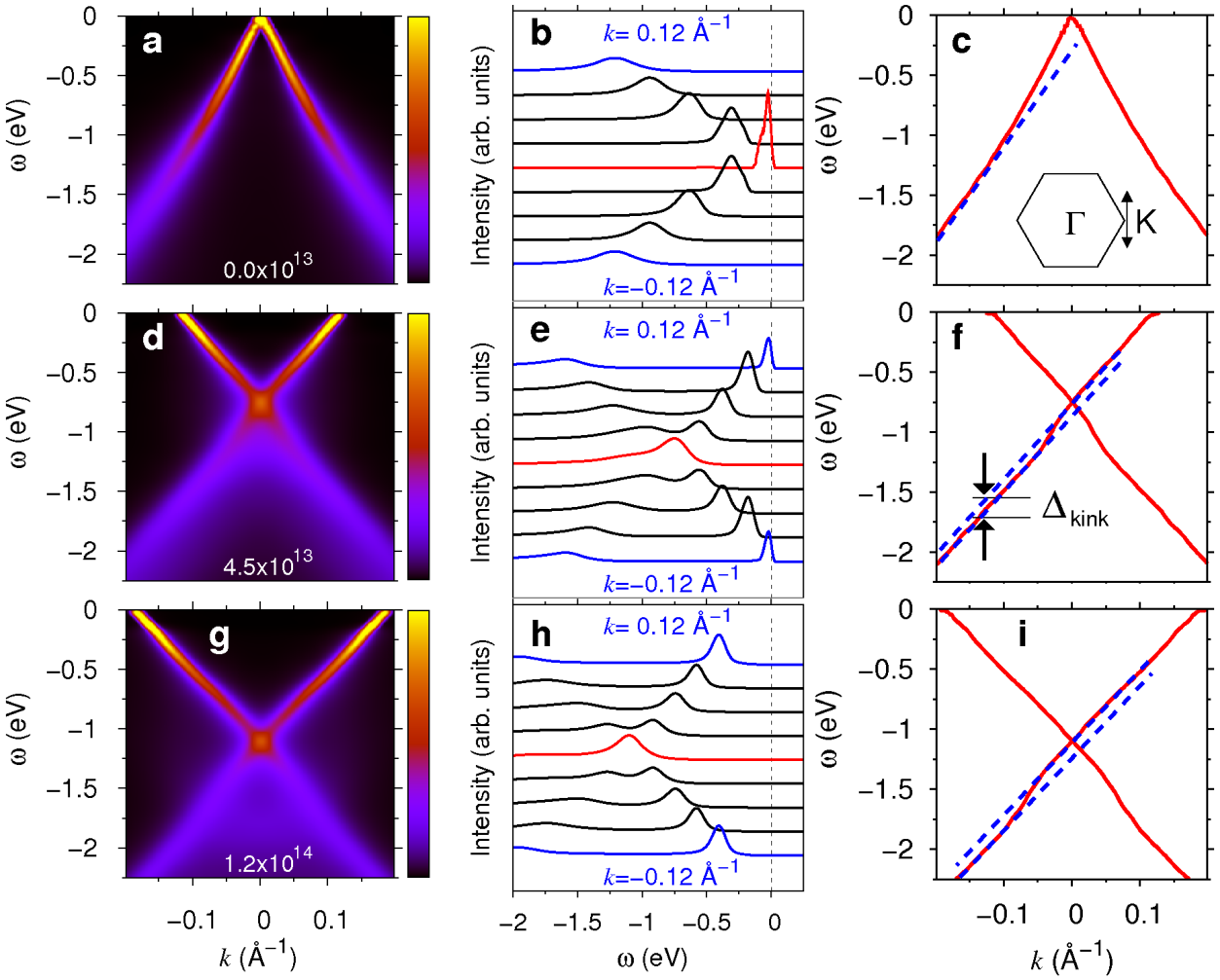

Figure 5.2: **Simulated ARPES spectra, energy distribution curves (EDCs) and quasiparticle band structures of suspended graphene including e-e and e-ph interactions.** **a**, Simulated ARPES spectrum of pristine graphene at $T = 25$ K taken along the Brillouin zone segment indicated in the inset of **c**. **b**, EDCs extracted from **a**. The central red curve corresponds to $k = 0$ (the K point). **c**, Quasiparticle band structure (solid red curve) obtained by connecting the peak positions of EDCs in **b**. **d** to **f**, and **g** to **i**, Same quantities as in **a** to **c** for n-doped graphene with charge densities of 4.5×10^{13} cm^{-2} and 1.2×10^{14} cm^{-2}, respectively. The dashed blue lines in **c**, **f**, and **i** indicate the asymptotes of the linear bands far from the Dirac point. The energy difference between the upper and the lower asymptotes close to the Dirac point is indicated by Δ_{kink}.

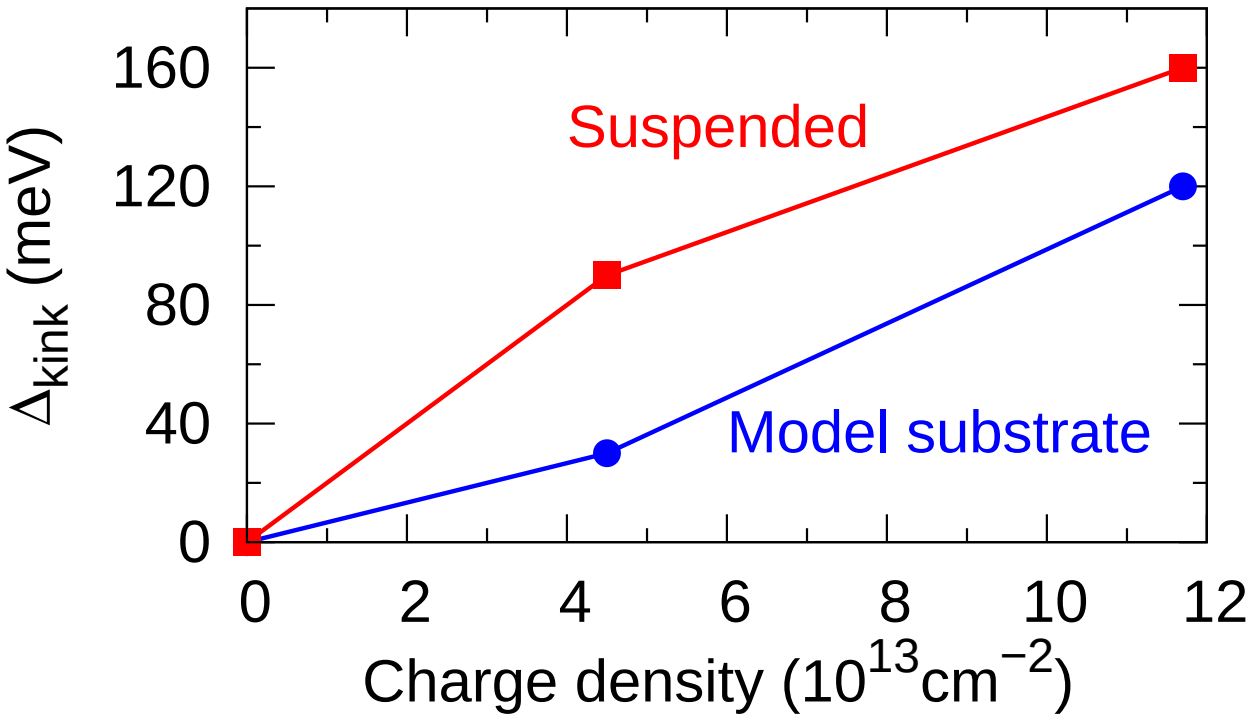

Figure 5.3: **Mismatch between the upper and lower bands of the Dirac cone.** Calculated energy difference Δ_{kink} between the asymptotic lines close to the Dirac point of the upper and the lower linear bands vs. doping for suspended graphene (squares) and for graphene with a model dielectric screening (circles) corresponding to the SiC substrate (see Methods). The lines are a guide to the eye.

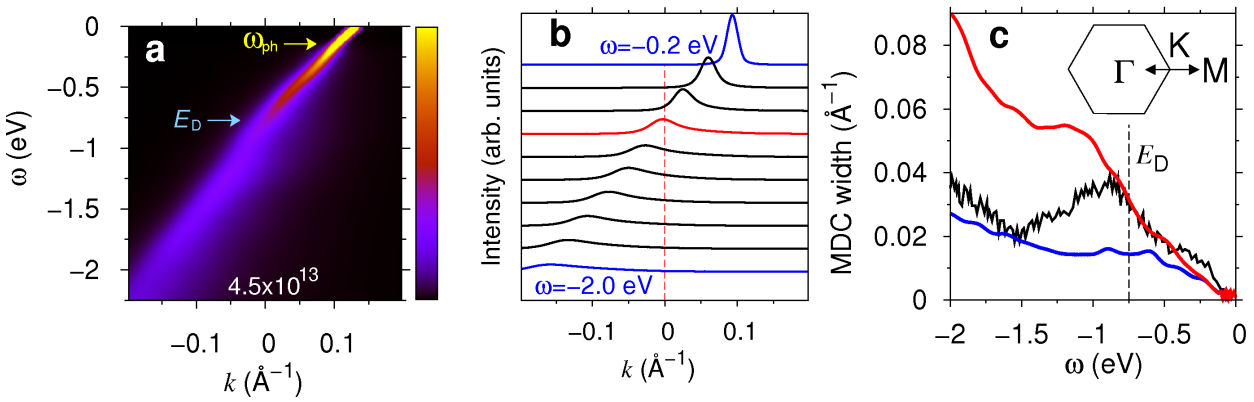

Figure 5.4: **Momentum distribution curves (MDCs) of graphene and associated linewidths.** **a**, Simulated ARPES spectrum of suspended n-doped graphene, for a doping level corresponding to a charge density of 4.5×10^{13} cm^{-2}, taken along the Brillouin zone segment indicated in the inset of **c**. **b**, MDCs obtained from **a**. **c**, Width of the MDCs obtained from **b** for suspended graphene (red curve) and that for graphene with a model dielectric screening corresponding to the SiC substrate (blue curve). The measured widths of the MDCs [4] are shown for comparison (black curve).

graphene-substrate interface and many-body effects.

The quasiparticle velocity can be extracted from the simulated spectral functions. We find that e-e interactions greatly enhance the band velocity by over 30 % compared to the density-functional theory value in pristine graphene, but dielectric screening from the SiC substrate (by weakening the e-e interaction) reduces the quasiparticle velocity by as much as ∼10 % (Supplementary discussion and Fig. 5.5). Moreover, the calculated velocity decreases with doping (Fig. 5.5) in agreement with previous calculations [108].

5.2.3 Momentum distribution curves and electron linewidths

Our calculations also reveal phonon-induced kinks near the Fermi energy at binding energies between 150 and 200 meV (e. g. , Fig. 5.4a) in good agreement with experimental photoemission maps [4, 58, 87, 88]. These signatures of the e-ph interaction in graphene have been analyzed thoroughly both experimentally and theoretically [60, 5, 49, 84].

A complementary and important piece of information provided by ARPES intensity maps is the linewidth of the electronic quasiparticle peaks. The linewidth $\Gamma_{n\mathbf{k}}$ is related to the lifetime $\tau_{n\mathbf{k}}$ of the electron in a given quasiparticle state through $\tau_{n\mathbf{k}} = 2\hbar/\Gamma_{n\mathbf{k}}$, and plays an important role in transport phenomena. The electron linewidths are extracted from the measured photoemission spectra by considering momentum distribution curves (MDCs), which are constant-energy cuts of the intensity maps. The width of the MDC at a given binding energy can subsequently be obtained using a Lorentzian fit [37]. From our simulated ARPES spectra of graphene along the ΓKM direction in wavevector space (Fig. 5.4a), we

obtained the MDCs (Fig. 5.4b) and their widths (Fig. 5.4c). Unlike previous methods [110], this procedure is direct and is not confined to materials having a linear electronic dispersion.

The widths extracted from the calculated MDCs in n-doped graphene after including the effect of the SiC substrate screening (see Methods) follow closely the experimental measurements on epitaxial graphene at large binding energies [4], although they underestimate the experimental data close to the Dirac point energy (Fig. 5.4c). The agreement between calculated and measured widths at large binding energy and the underestimation of the linewidths close to the Dirac point energy provide additional support to the proposed scenario of a band gap opening arising from the interaction with the SiC substrate [58, 90, 91, 92, 110]. That is, the opening of a band gap and the generation of midgap states near the Dirac point energy (not included in our calculations) would lead to increased linewidths in this energy regime [92]. However, from the view point of theory, a conclusive statement can be made only after first-principles calculations considering both the atomistic structure of the graphene-substrate interface and the many-body effects, which is beyond the scope of this work.

The widths extracted from the calculated full ARPES spectrum and those obtained by calculating the imaginary part of the on-shell electron self-energy Im $\Sigma(\mathbf{k}, \varepsilon_{\mathbf{k}})$ [110] are similar for n-doped graphene with the same charge density. (The charge density of n-doped graphene considered in Ref. [110] is different from that in Fig. 5.4.) However, it is important to note that the current method of using the full ARPES spectra, although involving heavier computations, is more powerful because it can be in general applied to systems whose bare electronic energy dispersion is not linear.

5.3 Conclusion

In this work, the effects of substrate optical phonons have not been considered. These substrate phonons contribute to the room-temperature transport properties of graphene [112]. However, over a 1.5 eV range around the Fermi level in doped graphene relevant to ARPES experiments [4, 58], the imaginary part of the electron self energy that arises from interactions with the substrate phonons is less than 1 meV [113], about two orders of magnitude smaller than the self-energy effects intrinsic to graphene itself [110].

The present work shows that first-principles simulation of ARPES spectra based on a quantum many-body theory approach treating e-e and e-ph interactions on the same footing holds great potential for the interpretation of complex ARPES spectra. In particular, a direct calculation of the quasiparticle spectral function is needed to obtain meaningful comparisons with experimental data (e. g. , the extraction of EDCs, MDCs, linewidths, and quasiparticle dispersion relations).

5.4 Methods

5.4.1 Computational setup

The Kohn-Sham eigenstates of graphene are obtained using density-functional theory calculations within the local density approximation (LDA) [14] in a supercell geometry [114]. Electronic wavefunctions in a $72 \times 72 \times 1$ k-grid are expanded in a plane-waves basis with a kinetic energy cutoff of 60 Ry. The core-valence interaction is treated by means of *ab initio* norm-conserving pseudopotentials [15]. Graphene layers are separated by 8.0 Å and the Coulomb interaction is truncated to prevent spurious interaction between periodic replicas [97]. We have checked that increasing the interlayer distance to 16.0 Å makes virtually no difference in the calculated self energy. Charge doping is modeled by an added electron density with a neutralizing background.

Extending the procedure presented in Ref. [110], where only the imaginary part of the on-shell electron self-energy $\mathrm{Im}\Sigma^{e-e}(\varepsilon_{\mathbf{k}})$ arising from electron-electron (e-e) interactions is calculated ($\varepsilon_{\mathbf{k}}$ being the LDA energy eigenvalue), we calculate the full frequency dependence of both the real and the imaginary parts of the dielectric matrix (within the random phase approximation) and the self-energy operator $\Sigma^{e-e}(\omega)$ within the G_0W_0 approximation in the present work. Thus our theory includes the two scattering mechanisms arising from e-e interaction effects discussed in previous model calculations performed within the massless Dirac equation formalism [85, 86], i. e. , electron-hole pair and plasmon excitations. Since our calculations are based on first-principles, they are parameter free for suspended graphene and can give information that depends on atomistic details, e. g. , the effects of trigonal warping. For convergence of the real part of $\Sigma^{e-e}(\omega)$, we have included conduction bands with kinetic energy up to 100 eV above the Fermi level. The frequency dependent dielectric matrix $\epsilon_{\mathbf{G},\mathbf{G}'}(\mathbf{q},\omega)$ is calculated within the random phase approximation using the LDA wavefunctions on a regular grid of ω with spacing $\Delta\omega$ =0.125 eV [98], and the dielectric matrix at energies in between frequency grid points is obtained by a linear interpolation. In the calculation of the polarizability, for numerical convergence, an imaginary component of magnitude $\Delta\omega$ of 0.125 eV is introduced in the energy denominator. Convergence tests showed that the dimension of the dielectric matrix may be truncated at a kinetic energy cutoff of $\hbar^2G^2/2m$ =12 Ry. Additionally, we obtain the electron self-energy arising from electron-phonon (e-ph) interactions $\Sigma^{e-ph}(\omega)$ following Ref. [5] for different levels of doping.

In our approach, we describe the e-e and the e-ph interactions within the same level of approximation. Previous studies suggested the use of the quasiparticle dispersions renormalized by the e-e interaction to compute the e-ph interaction [115]. This latter procedure (not adopted here) would correspond to including some of the higher order processes in $\Sigma^{e-ph}(\omega)$ whilst neglecting them in $\Sigma^{e-e}(\omega)$, and would result in an unbalanced evaluation of e-e and e-ph effects according to different levels of approximation. In any event, even if some e-ph matrix elements calculated after renormalizing the bands through the GW approximation were 20% to 40% larger than those used in this work [115], the band velocity would also be enhanced by a similar factor (this work and Refs. [107, 108]), and the two factors would

cancel out approximately in the calculation of $\Sigma^{e-ph}(\omega)$ [cf. Eq. (2) of Ref. [60]]. Therefore, we estimate that the effects of such alterations on our results are not significant.

5.4.2 Angle-resolved photoemission spectra

First, the trace of the spectral function with respect to band index n, i.e., $A(\mathbf{k},\omega) = c\sum_n A_{nn}(\mathbf{k},\omega)$, is calculated. Here, c is a normalization constant, $|n\rangle$ are the Kohn-Sham eigenstates, and

$$A_{nn}(\mathbf{k},\omega) = \frac{2}{\pi}\frac{-\mathrm{Im}\,\langle n\mathbf{k}|\Sigma(\omega)|n\mathbf{k}\rangle}{\left[\omega-\varepsilon_{\mathbf{k}}-\mathrm{Re}\,\langle n\mathbf{k}|\Sigma(\omega)|n\mathbf{k}\rangle\right]^2+\left[\mathrm{Im}\,\langle n\mathbf{k}|\Sigma(\omega)|n\mathbf{k}\rangle\right]^2}\,. \tag{5.4}$$

To simulate the measured angle-resolved photoemission spectra from the calculated spectral functions, we multiplied the spectral function by the Fermi-Dirac distribution $f(\omega)$ [Eq. (5.1)] with $T = 25$ K at which the experiments were performed [4, 58]. Then, to take into account the experimental resolutions in energy and momentum, we have convoluted the intensity maps with a two-dimensional Lorentzian mask with Δk=0.01 Å^{-1} and $\Delta\omega = 25$ meV, corresponding to the experimental resolution [4, 58]. (This convolution results in finite linewidths even for zero binding-energy states.) In simulating the photoemission spectra along the ΓKM direction (Fig. 5.4a), we have used only one branch of the two linear bands in order to simulate the matrix element effects in $I_0(\mathbf{k},\omega,\hat{e}_\nu,E_\nu)$ [Eq. (5.1)] (cf. Fig. 2 of Ref. [4]). In calculating the width of momentum distribution curves (the linewidths in Fig. 5.4c), we have arbitrarily subtracted off a constant from the simulated widths so that the width vanishes at zero binding energy, as also done in the analysis of experimental data in Ref. [4].

5.4.3 Substrate screening

To include the effects of the dielectric screening associated with the silicon carbide (SiC) substrate, we have, as done in previous studies [4, 85, 86] (Supplementary discussion and Fig. 5.6), renormalized the bare Coulomb interaction by an effective background dielectric constant $\epsilon_{\mathrm{b}} = (1+\epsilon_{\mathrm{SiC}})/2$, where ϵ_{SiC}=6.6 is the optical dielectric constant of silicon carbide [110]; one takes the average of the vacuum dielectric constant and the substrate dielectric constant because graphene is sandwiched in between the two media [116]. Along the lines of Ref. [4], we do not take into account atomistic interactions between graphene and the reconstructed surface of the silicon carbide substrate [90, 91, 92].

5.5 Supplementary discussion

5.5.1 Velocity renormalization

Our simulated spectral functions allow us to study the velocity of Dirac fermions in the linear regime (away from the Dirac point) as a function of dielectric screening of the substrate

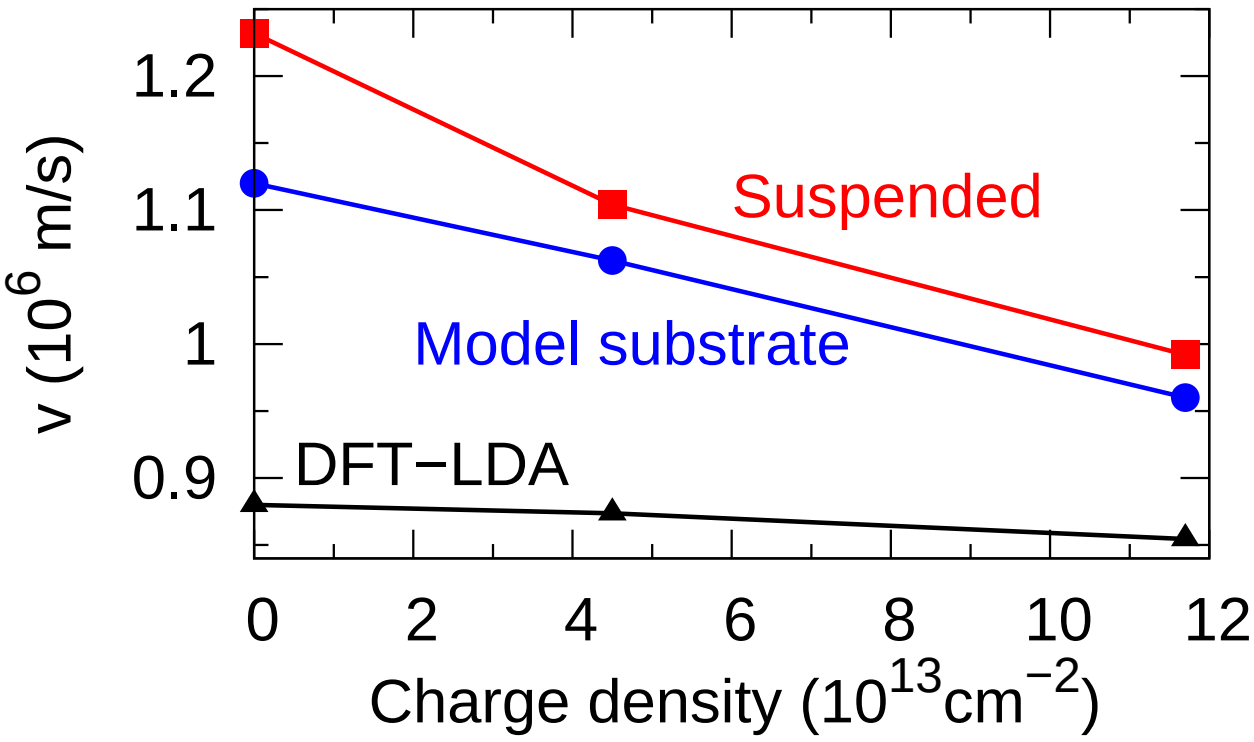

Figure 5.5: **Quasiparticle velocity in graphene.** The slopes (quasiparticle velocity) of the linear bands far from the Dirac point (indicated by the blue dashed lines in Figs. 5.1c, 5.1f, and 5.1i) vs. doping. Squares and circles are calculated quantities for suspended graphene and for graphene with a model silicon carbide (SiC) dielectric screening, respectively. Triangles are DFT results within the LDA. The lines are a guide to the eye.

and doping (Fig. 5.5). The band velocity of our model epitaxial graphene [$\epsilon_{\rm b} = (1+\epsilon_{\rm SiC})/2 = 3.8$] is found to be smaller than that of suspended graphene ($\epsilon_{\rm b} = 1$) by as much as $\sim$10% (Fig. 5.5). In addition, the velocity decreases as doping increases (Fig. 5.5), in agreement with the previous calculation [108]. Both trends are easily explained by observing that the polarizability of the substrate and the additional electrons in the graphene layer both lead to weaker e-e interactions.

5.5.2 Substrate Dielectric Function

In this section, we show that the dielectric function of silicon carbide (SiC) $\varepsilon^{\rm SiC}(\mathbf{q},\omega)$ is well represented by the value at $\mathbf{q} = 0$ and $\omega = 0$ (i. e. , the optical dielectric constant) as far as our calculation is concerned. We also estimate that an error in the electron self energy arising from this simplification is less than 10%.

In calculating the imaginary part of the self-energy, the relevant energy scale of the dielectric function of SiC is the quasiparticle energy measured from the Fermi surface, since the lifetime is determined by the real decay processes to lower energy states [see, e. g. , Eq. (5) of Ref. [38]]. The energy argument of the inverse dielectric function used in the calculation of the imaginary part of the self energy at energy ω varies between ω itself and the Fermi energy due to the two Heaviside functions. As long as the dielectric function is reasonably constant over this range, the results are valid. Since we are only interested in the value of the linewidth for states from the Fermi level down to about 2.5 eV below it (as measured by experiment and presented in Figs. 5.2 and 5.4), we have checked the validity of our approximation on substrate screening within this energy range and the corresponding wavevector range as discussed later. The real part of the self energy is affected by the dielectric screening involving large wavevectors; however, the contribution coming from larger wavevector scatterings is smaller because the Coulomb interaction decreases with q. The error in the real part of the self energy arising from the inaccuracy in the dielectric function for a larger wavevector would be smaller than that involving a smaller wavevector, which is estimated below.

In order to give a quantitative estimate of the possible error arising from the frequency and wavevector dependence of the dielectric function, we performed first-principles calculations of the dielectric function of 3C-SiC showing dielectric responses very similar to 6H-SiC [99], which is the substrate used in experiments [4, 58]. (The unit cell of 3C-SiC is much smaller than that of 6H-SiC though.)

Figure 5.6 shows that using the optical dielectric constant ($\omega = 0$, $\mathbf{q} = 0$) is a good approximation for the energy and wavevector regime considered in our work: the maximum variation in the dielectric function is 15%. (We have also checked that the inverse dielectric function shows similar behaviors.) Moreover, since (i) the self energy is an average of many contributions, and, (ii) the finite frequency and finite wavevector effects increase and decrease the value of the dielectric function, respectively, the combined error coming from our approximation will be less than 10%.

Figure 5.6 also shows (difference between solid and dashed lines) that in fact the maximum anisotropy in the dielectric function of SiC is $\sim$3%. (We have also checked that the

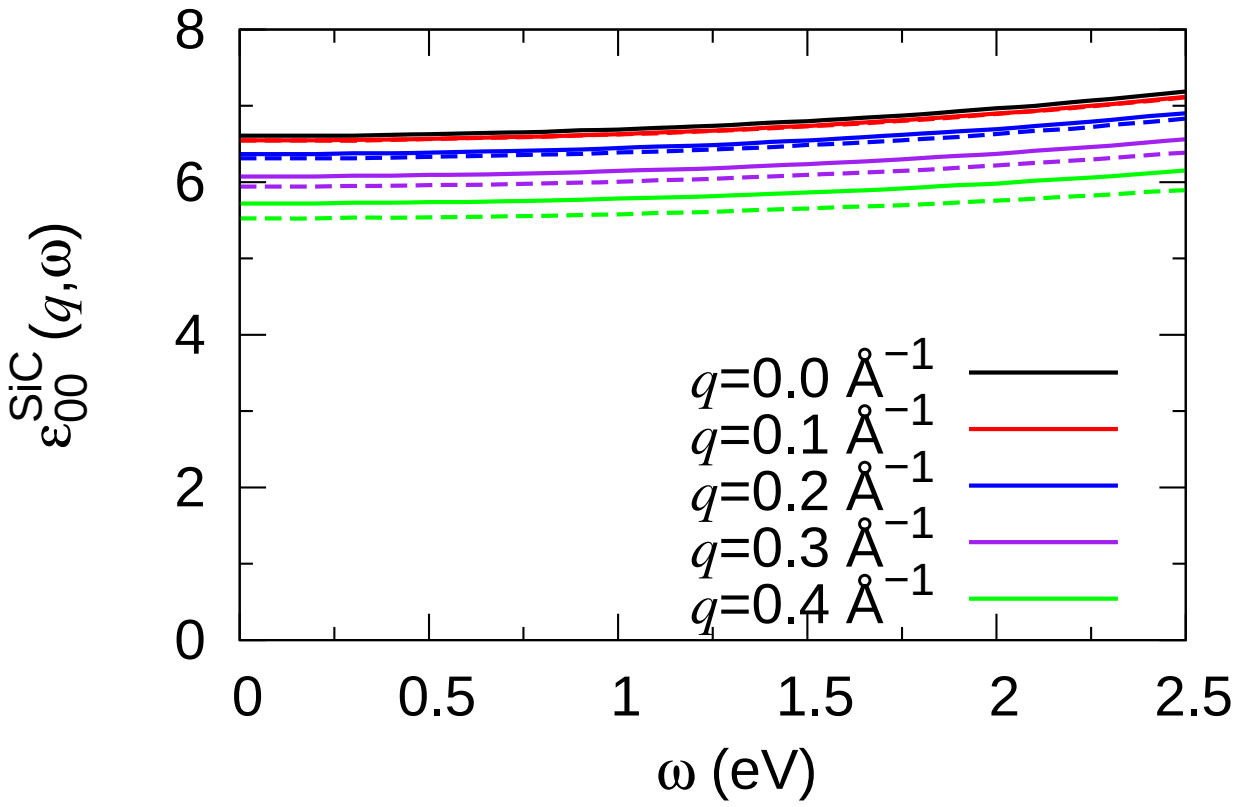

Figure 5.6: **Calculated dielectric functions of SiC versus energy.** Macroscopic dielectric function of 3C-SiC $\varepsilon^{\mathrm{SiC}}_{0,0}(\mathbf{q},\omega)$ versus energy ω. Quantities for different wavevectors are shown in different colors. Solid lines and dashed lines show quantities for the wavevector $\mathbf{q}$ in two representative directions in wavevector space: Γ-X and Γ-L, respectively.

inverse dielectric function shows similar behaviors.) Since the self energy is an average of all contributions, we expect that the anisotropy in the calculated electron self energy arising from that in the dielectric function of SiC will be even smaller than that.

5.5.3 Comments on other calculations

First-principles calculations of the real part of the self-energy in graphene arising from *e*-*e* interactions within the *GW* approximation have been reported previously [107, 108]. The authors of Ref. [108] calculated the frequency dependence of the dielectric matrices within the generalized plasmon-pole model. The authors of Ref. [107] calculated the full frequency dependence of the dielectric matrices using the random phase approximation as we did for the present work. For consistency we compare our calculations to the latter study.

Our calculated velocity (1.23×10^6 m/s) in suspended graphene is ∼9% larger than the one reported in Ref. [107] (1.12×10^6 m/s). Moreover, unlike the finding of Ref. [107], we do not observe a kink in the quasiparticle band structure of suspended pristine graphene at an energy $\omega \sim -0.15$ eV when *e*-ph interactions are not included. The fact that we observe a gradual increase in the band velocity when approaching the Dirac point energy, rather than a kink at a finite energy value is in line with results of model analytical calculations [111, 117]. To clarify this difference, we observe that, in the case of graphene, electronic states with wavevectors on nearest neighboring grid points of a discretized $N \times N$ mesh of the full Brillouin zone have an energy difference ΔE (eV) $\approx 20/N$. The Brillouin zone sampling adopted in Ref. [107] (10×10 points) corresponds to electronic eigenstates with minimal energy separation of approximately 2 eV. We find that this energy resolution is not sufficient to achieve convergence in the dielectric matrices needed for the GW self energy (we used instead a 72×72 grid, corresponding to energy separations of about 0.25 eV). Therefore we suggest that the difference between the band dispersions and velocities calculated here and those of Ref. [107] may arise from the insufficient Brillouin zone sampling adopted in that work.

Chapter 6

Electron-phonon interactions in graphene, bilayer graphene, and graphite

6.1 Introduction

Since the fabrication of crystalline graphitic films with a thickness of only a few atoms [70, 34, 35, 36, 71], single- and double-layer graphene have received considerable attention [72]. These materials are promising candidates for nanoelectronics applications because of the high mobility of charge carriers in these systems and the tunability of their electronic properties by gating [72]. Since electron-phonon (e-ph) interaction plays an important role in the dynamics of charge carriers [64, 39], understanding its effects in single- and double-layer graphene is of crucial importance for graphene-based electronics.

The e-ph interaction in metals modifies the dynamics of electrons with energy near the Fermi level by increasing their mass and reducing their lifetime. The mass renormalization can be described in terms of the e-ph coupling strength $\lambda_{n\mathbf{k}}$, defined as the energy derivative of the real part of the phonon-induced electronic self-energy $\Sigma_{n\mathbf{k}}(E)$ at the Fermi level E_F: $\lambda_{n\mathbf{k}} = -\partial\,\mathrm{Re}\Sigma_{n\mathbf{k}}(E)/\partial E|_{E=E_\mathrm{F}}$, where n, $\mathbf{k}$ and E are the band index, the wavevector and the energy of the electron, respectively [39]. The electron mass renormalization can be obtained from the e-ph coupling strength through $m^*/m = 1 + \lambda_{n\mathbf{k}}$ where m and m^* are the bare band mass and the renormalized mass, respectively. The e-ph interaction also gives rise to a phonon lifetime $\tau_{\nu\mathbf{q}} = \hbar/\Gamma_{\nu\mathbf{q}}$ [118], where $\Gamma_{\nu\mathbf{q}}$ is the phonon linewidth, i. e. , twice the imaginary part of the phonon self-energy arising from the e-ph interaction. Here ν, $\mathbf{q}$ and ω are the phonon branch index, the wavevector and the energy of the phonon, respectively [39].

These quantities can be calculated from first-principles within the Migdal approximation

as [39]

$$\lambda_{n\mathbf{k}} = \sum_{m,\nu} \int \frac{d\mathbf{q}}{A_{\rm BZ}} \, |g_{mn,\nu}(\mathbf{k},\mathbf{q})|^2 \times \left[\frac{n_{\mathbf{q}\nu} + 1 - f_{m\mathbf{k}+\mathbf{q}}}{(E_{\rm F} - \epsilon_{m\mathbf{k}+\mathbf{q}} - \omega_{\mathbf{q}\nu})^2} + \frac{n_{\mathbf{q}\nu} + f_{m\mathbf{k}+\mathbf{q}}}{(E_{\rm F} - \epsilon_{m\mathbf{k}+\mathbf{q}} + \omega_{\mathbf{q}\nu})^2} \right] , \tag{6.1}$$

and

$$\Gamma_{\mathbf{q}\nu} = 4\pi \sum_{m,n} \int \frac{d\mathbf{k}}{A_{\rm BZ}} \, |g_{mn,\nu}(\mathbf{k},\mathbf{q})|^2 \times (f_{n\mathbf{k}} - f_{m\mathbf{k}+\mathbf{q}}) \; \delta\left(\epsilon_{m\mathbf{k}+\mathbf{q}} - \epsilon_{n\mathbf{k}} - \omega_{\mathbf{q}\nu}\right) \; . \tag{6.2}$$

Here $\epsilon_{n\mathbf{k}}$ and $\omega_{\mathbf{q}\nu}$ are the energy eigenvalue of an electron with band index n and wavevector $\mathbf{k}$ and that of a phonon with branch index ν and wavevector $\mathbf{q}$, respectively. $A_{\rm BZ}$ is the area of the first Brillouin zone where the integration is performed. The quantities $f_{n\mathbf{k}}$ and $n_{\nu\mathbf{q}}$ are the Fermi-Dirac and the Bose-Einstein factors, respectively, and $g_{mn,\nu}(\mathbf{k},\mathbf{q}) \equiv \langle m\mathbf{k}+\mathbf{q}| \, \Delta V_{\nu\mathbf{q}}(\mathbf{r}) \, |n\mathbf{k}\rangle$ is the scattering amplitude of an electronic state $|n\mathbf{k}\rangle$ into another state $|m\mathbf{k}+\mathbf{q}\rangle$ resulting from the change in the self-consistent field potential $\Delta V_{\nu\mathbf{q}}(\mathbf{r})$ arising from a phonon with the branch index ν and the wavevector $\mathbf{q}$.

6.2 Theory and computation

Electron wavefunctions and energy eigenvalues are obtained using *ab initio* pseudopotential density functional theory calculations [96] within the local density approximation [14, 40]. Phonon frequencies and eigenstates are obtained through density functional perturbation theory [43]. We have used a planewave basis set [41] with a kinetic energy cutoff of 60 Ry. The core-valence interaction is handled using norm-conserving pseudopotentials [15, 42]. The integration in Eq. (6.1) for graphene and bilayer graphene is performed by summation over 300×300 points and for graphite it is performed with 90×90×30 points in the irreducible part of the Brillouin zone. The integration of Eq. (6.2) for graphene and bilayer graphene is done by summation over 1000×1000 points in the irreducible part of the Brillouin zone, and the δ function is replaced by a Lorentzian with 15 meV broadening for convergence. Electron and phonon wavefunctions, energy eigenvalues and the e-ph coupling matrix elements in these extremely dense grid sets are obtained by a recently developed interpolation scheme [45, 31] based on maximally localized Wannier functions [32, 33]. The Fermi-Dirac and Bose-Einstein factors are evaluated at the temperature $T = 15$ K in all the calculations. Charge doping is modelled by adding or removing electrons from the simulation cell and by using a neutralizing background. In this work we assume that the layers in bilayer graphene and in graphite are arranged according to the Bernal stacking sequence [Fig. 6.1(a)] [119].

6.3 Results and discussion

6.3.1 The electron-phonon coupling strength $\lambda_{n\mathbf{k}}$

Figure 6.1 shows the e-ph coupling strengths $\lambda_{n\mathbf{k}}$ in graphene, bilayer graphene and in graphite calculated along the reciprocal space path indicated by the double-head arrow in Fig. 6.1(b). As pointed out in Ref. [5] the e-ph coupling strength in graphene $\lambda_{n\mathbf{k}}$ is insensitive to the location of the wavevector $\mathbf{k}$ on the Fermi surface. This is also the case for bilayer graphene and for graphite. Therefore, we drop the index n and the wavevector $\mathbf{k}$ from now on. In bilayer graphene, the two electronic bands near the Dirac point energy exhibit almost identical e-ph coupling strengths [Fig. 6.1(c)].

The key factors determining the e-ph coupling strength are the density of states around the Dirac point energy and the e-ph matrix elements between the initial and the final electronic states close to the Fermi level [39]. The density of states of pristine graphene vanishes at the Fermi level, whereas bilayer graphene has a finite density of states. Despite this difference, at low doping with only one band occupied ($|E_\mathrm{F} - E_\mathrm{D}| < 0.2$ eV, E_D being the energy at the Dirac point and is set to $E_\mathrm{D} = 0$ in the following discussion), the e-ph coupling strengths in bilayer graphene and in graphite are similar (within 5%) to those of graphene. This indicates that, as in graphene, there is no significant scattering between low-energy electronic states in bilayer graphene and in graphite arising from the e-ph interaction. This behavior originates from the chiral nature of the charge carriers in bilayer graphene [120, 80] and in graphite [77], i. e. , it is a matrix-element effect. The difference in the e-ph coupling strength between graphene and bilayer graphene (or graphite) increases with doping. At the largest doping level considered [$E_\mathrm{F} = 1.5$ eV, Figs. 6.1(c) and 6.1(d)], the coupling strength in bilayer graphene and graphite ($\lambda = 0.28$) is 30% larger than in graphene ($\lambda = 0.21$). As we show in the following, these differences result from interlayer interaction.

In order to determine which phonon modes lead to the differences in the e-ph coupling strengths between monolayer and bilayer graphene, we decomposed the coupling strength $\lambda_{n\mathbf{k}}$ of both systems into contributions from each phonon branch and wavevector. Figures 6.2(b) and 6.2(e) show the Fermi surfaces of hole-doped graphene and bilayer graphene and the initial wavevector $\mathbf{k}$ of the electronic state considered. Figures 6.2(c) and 6.2(f) show the phonon dispersions of both pristine and hole-doped graphene and bilayer graphene, respectively. The size of the disks superimposed to the phonon dispersions is proportional to the contribution to the coupling strength $\lambda_{n\mathbf{k}}$ arising from the corresponding phonon mode. Figures 6.2(c) and 6.2(f) show that both in graphene and in bilayer graphene, the major contributions result from the highest-energy in-plane vibrations with wavevectors connecting the initial and final electronic states on the Fermi surface. However, in the case of bilayer graphene, the three low-energy optical branches with energy ~ 10 meV enhance the e-ph coupling strength with respect to graphene. The latter vibrations correspond to the compression mode (singly degenerate) and to the sliding mode of the two layers (doubly-degenerate).

Since, as in graphene, the e-ph coupling strength in bilayer graphene is rather small, even in the heavily doped case considered here, it appears unlikely for bilayer graphene to

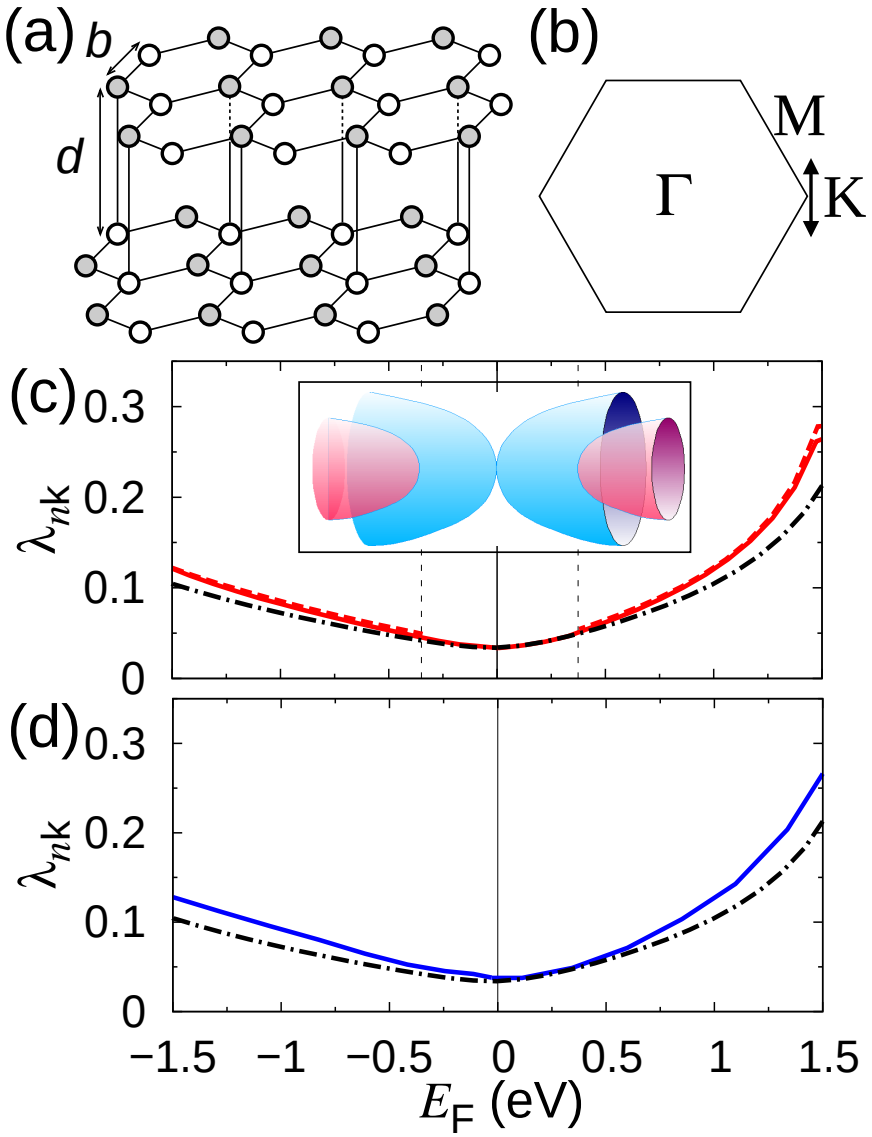

Figure 6.1: (a) Ball-and-stick model of bilayer graphene (Bernal stacking). (b) Brillouin zone of graphene and bilayer graphene. (c) The electron-phonon coupling strength $\lambda_{n\mathbf{k}}$ in bilayer graphene versus changing Fermi level $E_{\rm F}$ calculated along the path (double-head arrow) shown in (b). Solid and dashed red lines correspond to $\lambda_{n\mathbf{k}}$ of the individual blue and red parabolic band in the inset, respectively. The Fermi level of neutral bilayer graphene is set at zero. (d) As in (c), for each of the two electronic bands of *graphite* touching at the K point (solid blue line). In (c) and (d), we show for comparison the *e*-ph coupling strength in graphene [5] (indicated by the dash-dotted line).

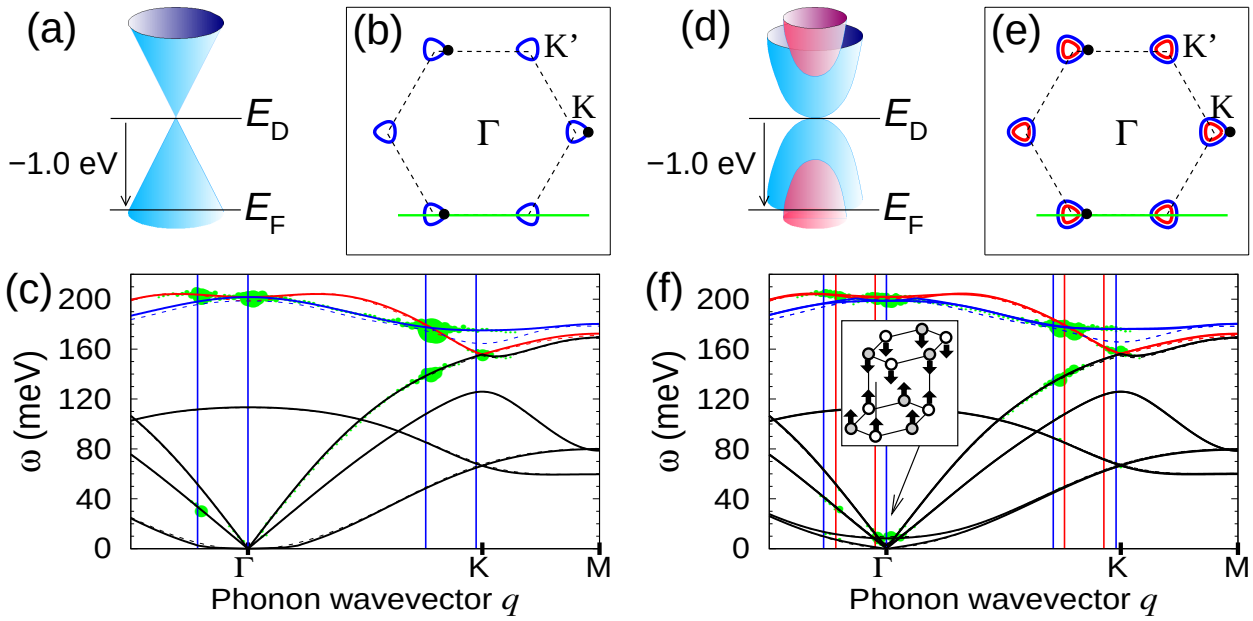

Figure 6.2: (a) The electronic energy dispersion and the Fermi level of hole-doped graphene. (b) The Fermi surface (contours) and the Brillouin zone (dashed hexagon) of hole-doped graphene. The black dots represent the wavevector $\mathbf{k}$ of the electronic state considered on the Fermi surface. (c) The phonon dispersion curves of undoped (dashed lines) and hole-doped (solid lines) graphene versus the wavevector $\mathbf{q}$ along the solid green line shown in (b). The vertical lines indicate the phonon wavevectors $\mathbf{q}$ such that the final electronic state with wavevector $\mathbf{k}+\mathbf{q}$ is also on the Fermi surface. The size of the disks on top of the phonon dispersions is proportional to the contribution of that phonon mode to $\lambda_{n\mathbf{k}}$. (d) to (f): Same quantities as in (a) to (c) for hole-doped bilayer graphene but including also interband coupling. The inset of (f) shows one of the three modes responsible for the enhancement of the e-ph coupling strength in bilayer graphene. The color (red and blue) and the type (solid and dashed) of the curves in (c) and (f) corresponds to the phonon branches in Figs. 6.4(a) and 6.4(b) and 6.4(c) and 6.4(d), respectively.

exhibit superconductivity with a transition temperature significantly higher than that one may expect for graphene.

Recent angle-resolved photoemission experiments on kish graphite [121] and on a single crystal of graphite [122] reported very different values of the *e*-ph renormalization, namely, $\lambda = 0.70$ along the KK direction [path indicated by the double-head arrow in Fig. 6.1(b)] [121] and $\lambda = 0.14$ along the KM direction [Fig. 6.1(b)] [122]. Our calculated *e*-ph coupling strength in undoped graphite ($\lambda = 0.034$) is closer to the estimate of Ref. [122]. In that work, the broadening of the energy distribution curve in the photoemission spectra was entirely assigned to the *e*-ph interaction. This assumption leads to an apparent *e*-ph coupling strength which is enhanced by the contributions arising from other interactions. In particular, it has been shown that the electronic linewidth in graphite arising from the electron-electron interaction is sizable [123]. A similar discrepancy has been pointed out for the case of graphene [124, 125]. However, recent calculations indicate that the effect of the electron-electron interaction in graphene is not negligible and must be taken into account in the analysis of the experimental data [110].

6.3.2 The phonon linewidth $\Gamma_{\nu\mathbf{q}}$

So far we have discussed the effect of the *e*-ph interaction on the Fermi velocity of the carriers. In what follows we focus on the effect of *e*-ph interaction on the phonon linewidths. Figure 6.3(a) shows the linewidth of the doubly-degenerate E_{2g} phonons at the Γ point and of the doubly-degenerate A'_1 mode at the K point for graphene. These phonons exhibit a finite and constant linewidth for $|E_\mathrm{F}| < \omega_\mathrm{ph}/2$, where $\omega_\mathrm{ph} \sim 0.2$ eV is the optical phonon energy, and a negligible linewidth otherwise. The dependence of the phonon linewidth on the doping level can be explained by considering that interband transitions through phonon absorption are forbidden whenever $|E_\mathrm{F}| > \omega_\mathrm{ph}/2$. Our calculated linewidth of the E_{2g} phonon is in good agreement with previous studies [126, 127].

In bilayer graphene, as a consequence of the interlayer coupling, the four highest-energy modes (originating from the E_{2g} modes of graphene) split into two sets of doubly-degenerate E_g and E_u modes [128], with the E_u modes 1.1 meV higher in energy than the E_g modes (cf. Fig. 6.3). Interestingly, at Γ, only the E_g modes exhibit a finite linewidth (1.1 meV) whereas the E_u modes are not broadened by the *e*-ph interaction. It can be shown that this difference results from (i) the chiral nature of the low-energy electronic states [77, 129] and (ii) from the fact that atoms in the same sublattice but different layers move in phase in the E_g modes, while they move out of phase in the E_u modes [130]. The calculated linewidths of the E_g and the E_u modes are in good agreement with a previous study based on a pseudospin effective Hamiltonian for the massive Dirac fermions of bilayer graphene [130].

Among the two sets of high-energy zone-center modes, only the E_g phonons are Raman active [128]. The calculated phonon linewidth of the E_g modes can therefore be compared directly with the measured broadening of the Raman lines. As shown in Fig. 6.3(b), our calculated linewidths are in excellent agreement with those reported in a recent experimental study [7]. For the purpose of comparison, we have downshifted the experimental

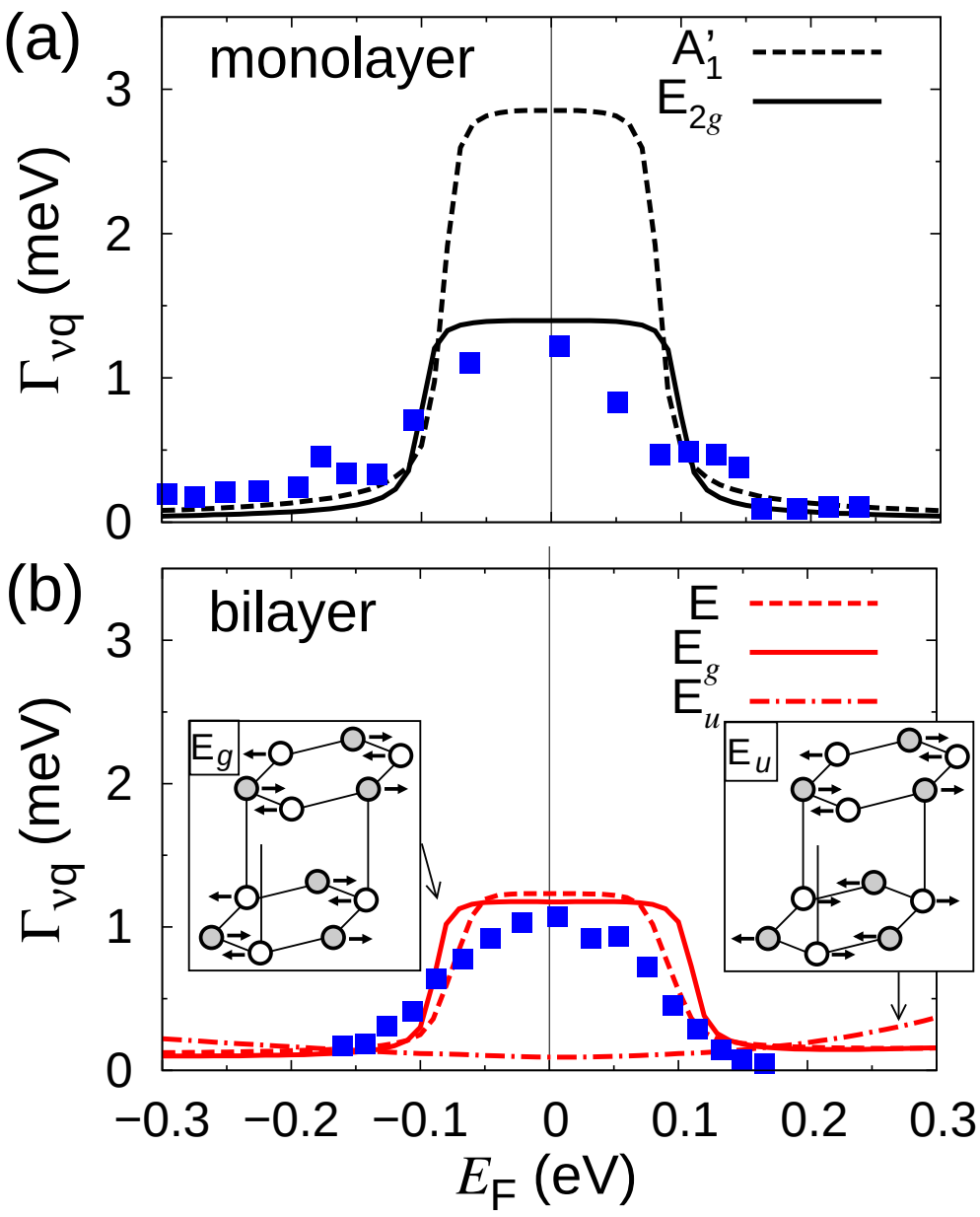

Figure 6.3: (a) Phonon linewidth in doped graphene for the E_{2g} mode at the Γ point (solid line) and the A'_1 mode at the K point (dashed line) versus the Fermi level E_F. The filled squares are the experimental data from Ref. [6] downshifted by 0.6 meV (to account for a uniform background). (b) Phonon linewidth in bilayer graphene for the E_g mode (solid line) and the E_u mode (dash-dotted line) at the Γ point, and for the E mode at the K point (dashed line). The insets show one of each of the two doubly-degenerate zone-center modes considered here. The filled squares are the experimental data from Ref. [7] downshifted by 0.6 meV (to account for a uniform background).

linewidths of the E_{2g} phonon in graphene [6, 131, 132] and of the E_g phonon mode in bilayer graphene [7, 133] by 0.6 meV. The agreement between our calculations and experiment after the subtraction of this uniform background indicates that defect-induced scattering and anharmonic effects are small and similar in magnitude in graphene and bilayer graphene.

We note that the linewidth of the E_{2g} phonons in graphene (1.1 meV) and that of the E_g phonons in bilayer graphene (1.4 meV) are very similar. This behavior originates from the cancellation of the effects of larger electron density of states and smaller e-ph matrix elements of bilayer graphene as compared to graphene. Because of their similar linewidths, the broadening of these modes is unlikely to be useful for determining the number of graphene layers using Raman spectroscopy. In contrast, the linewidth of the highest-energy mode at the K point in graphene (the A_1' mode) is reduced from 2.9 meV in graphene to 1.2 meV in bilayer graphene (the E mode). Therefore it should be possible, at least in principle, to exploit this difference in two-phonon Raman experiments to distinguish between graphene and bilayer graphene.

Figure 6.4(a) shows the linewidths of the two highest-energy phonon branches in pristine graphene. The phonon linewidths exhibit maxima at the K point and at or near the Γ point. At the Γ point, the highest-energy phonons decay through electronic transitions with no momentum transfer. Off the Γ point, because of the topology of the Dirac cone, non-vertical transitions can occur if the wavevector of the phonon is smaller than $k_0 = \omega_{\rm ph}/v_{\rm F} = 0.035$ Å^{-1} ($\omega_{\rm ph}$ being the phonon energy and $v_{\rm F}$ the Fermi velocity). These transitions are allowed since the phonon wavevectors connect electronic states of the same chirality [134]. The scattering of phonons with wavevector $k_0 = \omega_{\rm ph}/v_{\rm F}$ is enhanced because the phase velocity of the phonon matches the slope of the Dirac cone. Correspondingly, at this wavevector the transverse-optical phonon branch exhibits the largest linewidth. Unlike the case for the transverse-optical phonons, the longitudinal-optical phonons with wavevector k_0 cannot promote electronic transitions, as a consequence of the chiral symmetry [134], and the corresponding linewidth vanishes.

As shown in Fig. 6.4(b), in hole-doped graphene, the phonon linewidths in the highest energy branches with wavevector at the Γ point or at the K point are negligible. However, whenever the phonon wavevector exceeds k_0 in magnitude, intraband electronic transitions can occur through phonon absorption. In the case of phonons with wavevector close to the K point, this kind of electronic transition is suppressed due to chirality [134]. In hole-doped graphene, the Fermi surface consists of two contours centered around the two inequivalent Dirac points. Two maxima are found in the phonon linewidths near K, corresponding to the smallest and the largest wavevectors connecting electronic states on different contours.

Figures 6.4(c) and 6.4(d) show the linewidths of the E_g phonons for undoped as well as for hole-doped ($E_{\rm F} = -1.0$ eV) bilayer graphene, respectively. In the undoped case, the linewidths of transverse phonons with wavevector k_0 are not as large as in graphene since the low-energy electronic energy dispersions are nonlinear. In the case of hole-doped bilayer graphene, the profile of the phonon linewidths is almost identical to the one calculated for graphene. This can be explained by considering that the electronic density of states per carbon atom near the Fermi level in graphene and bilayer graphene are very similar.

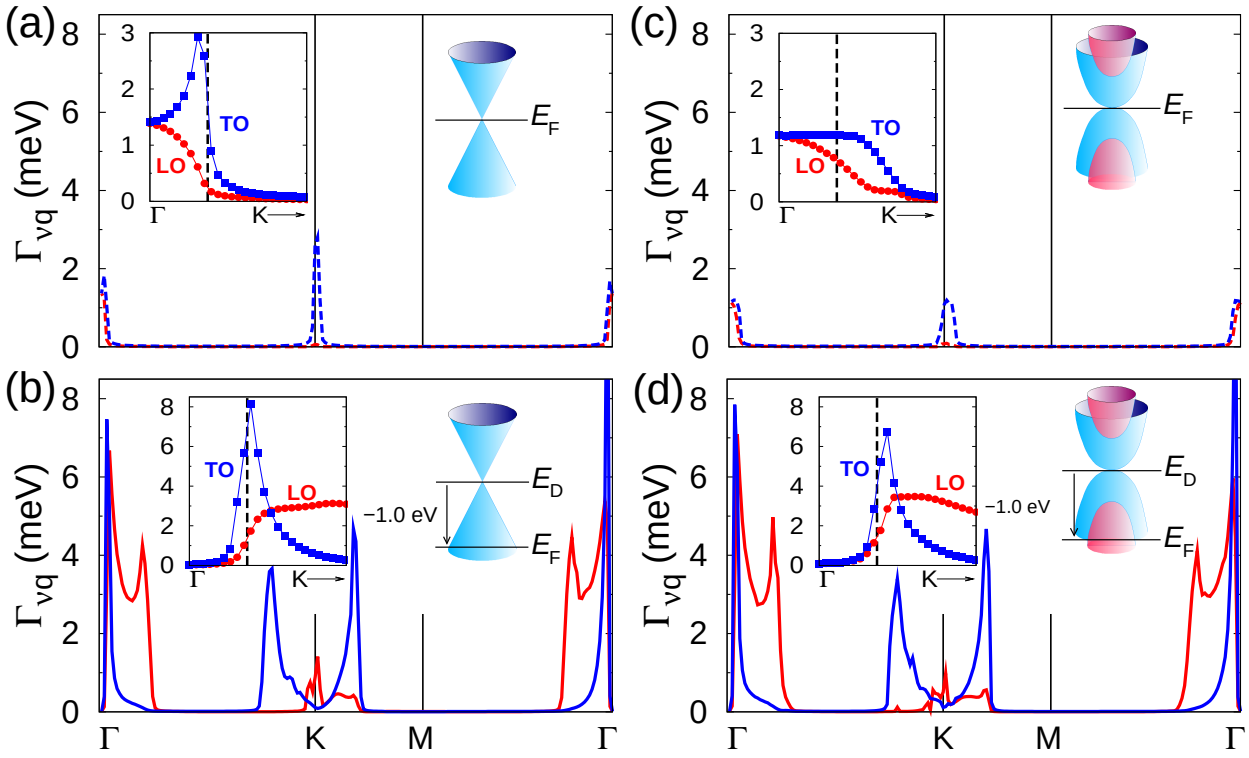

Figure 6.4: (a), (b): The phonon linewidth of the highest energy branches in undoped [(a)] and hole-doped [(b)] graphene. The color code (red and blue) and the type (solid and dashed) of the line correspond to the phonon branches shown in Fig. 6.2(c). (c), (d): Phonon linewidth of the second highest doubly-degenerate phonon branches at the Γ point in undoped [(c)] and hole-doped [(d)] bilayer graphene. The color code (red and blue) and the type (solid and dashed) of the line corresponds to the phonon branches shown in Fig. 6.2(f). The inset in each panel shows a magnified view of the region near the Γ point, where the symbols represent calculated data points and the lines are a guide to the eye. The vertical dashed line in the inset specifies the characteristic wavevector k_0 (see text).

The results of our calculations could be confirmed by performing detailed inelastic neutron scattering, electron energy loss spectroscopy, or inelastic x-ray scattering experiments. Measurements of this kind have been performed, for example, in the case of magnesium diboride, allowing for a direct comparison with theoretical calculations. [135].

6.4 Conclusion

In summary the Fermi velocity renormalization and the phonon line broadening arising from the *e*-ph interaction in bilayer graphene and in graphite are studied and compared with the corresponding quantities in graphene. In bilayer graphene and in graphite, the *e*-ph coupling strength is enhanced by up to 30% at high doping as compared to graphene. The calculated doping dependence of the phonon linewidth of the zone-center E_g mode in bilayer graphene is in excellent agreement with recent Raman measurements [6]. We discussed the similarities and the differences in the linewidths of the optical phonons in graphene and in bilayer graphene.

Chapter 7

Inelastic carrier lifetime in bilayer graphene

7.1 Introduction

The lifetime of charge carriers through inelastic scattering processes determines ballistic transport properties of electronic devices operating at a high source-drain bias voltage for which the inelastic carrier mean free path is much shorter than the elastic one [136]. Therefore, knowing the carrier lifetime arising from inelastic scattering processes is an important step towards the micro- or nano-meter scale electronic device applications. Inelastic scattering processes are induced by many-body interactions, two of the most important classes of which are electron-electron (e-e) and electron-phonon (e-ph) interactions [136].

Graphene holds a great promise for electronic and spintronic device applications [72]. Moreover, recent experimental manifestations of a band gap opening up in bilayer graphene [137, 8] show new possibilities in the application of bilayer graphene in electronics and optoelectronics applications. Although the carrier lifetime in electronic devices based on graphene in a low-bias regime is likely to be limited by charged impurities [138], in a high-bias regime, it is limited by many-body interactions [38].

The inelastic scattering rate of charge carriers in graphene arising from e-ph interactions have been studied from first-principles calculations [60, 49] as well as from the model calculations based on the two-dimensional massless Dirac equation [84, 139] and that arising from e-e interactions have also been studied from model calculations [38, 139] and from a first-principles approach [110]. However, a study on the inelastic carrier lifetime in bilayer graphene has been lacking up to now. In this chapter, we present a first-principles calculation of the inelastic carrier lifetime in pristine and charge-doped bilayer graphene arising from both e-e and e-ph interactions. (A model calculation study on monolayer graphene with similar spirit has recently been performed [139].)

We find that the scattering rate in bilayer graphene arising from e-e interactions varies highly anisotropically with the wavevector of electrons, as in graphene [110], even in a low-

energy regime. However, due to the enhanced screening and the bandstructure effects in bilayer graphene, this scattering rate is reduced by 20–40% depending on the charge density and the band index and wave vector of electrons than that in graphene. On the contrary, the scattering rate in bilayer graphene arising from *e*-ph interactions does not show band or wavevector dependence once the energy is the same, similar to the case of graphene [110]. We compare the results of our calculation with available experimental data and explain why the scattering rate measured from ultrafast optical pump-probe spectroscopy measurements [140] could be much smaller than that obtained from angle-resolved photoemission spectroscopy measurements [4, 58].

7.2 Theory and computation

The scattering rate of charge carriers arising from *e*-*e* and *e*-ph interactions are given by $\tau^{-1}_{e-e,n\mathbf{k}} = \hbar/2\Sigma^{e-e}_{n\mathbf{k}}(\varepsilon_{n\mathbf{k}})$ and $\tau^{-1}_{e-ph,n\mathbf{k}} = \hbar/2\Sigma^{e-ph}_{n\mathbf{k}}(\varepsilon_{n\mathbf{k}})$, respectively, where $\Sigma^{e-e}_{n\mathbf{k}}(\varepsilon_{n\mathbf{k}})$ and $\Sigma^{e-ph}_{n\mathbf{k}}(\varepsilon_{n\mathbf{k}})$ are the corresponding electron self energies of charge carriers having band index n, wavevector $\mathbf{k}$, and, energy $\varepsilon_{n\mathbf{k}}$ obtained from the density-functional calculations within the local density approximation (LDA). We evaluate $\Sigma^{e-e}_{n\mathbf{k}}(\varepsilon_{n\mathbf{k}})$ within the G_0W_0 approximation [20] by taking into account the full-frequency dependence of the dielectric function within the random-phase approximation [98], and $\Sigma^{e-ph}_{n\mathbf{k}}(\varepsilon_{n\mathbf{k}})$ within the Migdal approximation [31]. The computational setup for evaluating these self energies is the same as that of our previous work on graphene [110]. We set the interlayer distance in one unit cell of bilayer graphene to 3.33 Å.

7.3 Results and discussion

7.3.1 Carrier lifetime limited by electron-electron interactions

Figure 7.1(a) shows that the scattering rate $\tau^{-1}_{e-e,n\mathbf{k}}$ arising from *e*-*e* interactions in pristine suspended bilayer graphene is smaller than that in graphene by 20–40% on average. This decrease is partly due to the stronger screening in bilayer graphene. Another factor is the bandstructure effect: the scattering rate for electrons in the outer parabolic bands (dashed curve) are in general higher than that for the inner parabolic bands (solid curve). The electrons in outer parabolic bands require, on average, a larger momentum transfer to decay into lower-energy states than those in the inner parabolic bands. This bandstructure effect could be directly confirmed by angle-resolved photoemission experiments.

Figure 7.1(b) shows that the scattering rate $\tau^{-1}_{e-e,n\mathbf{k}}$ of charge carriers in bilayer graphene with wavevector on the KM line is much lower than that on the KΓ line, similar as in graphene [110] or in graphite [93, 141]. Because the scattering rate is not well defined in systems with a linear energy dispersion, it depends critically on the sign of the band curvature of the additional non-linear energy dispersion [111]. This effect is important even for low-energy carriers [Figs. 7.1(a) and 7.1(b)]. However, model calculations based on

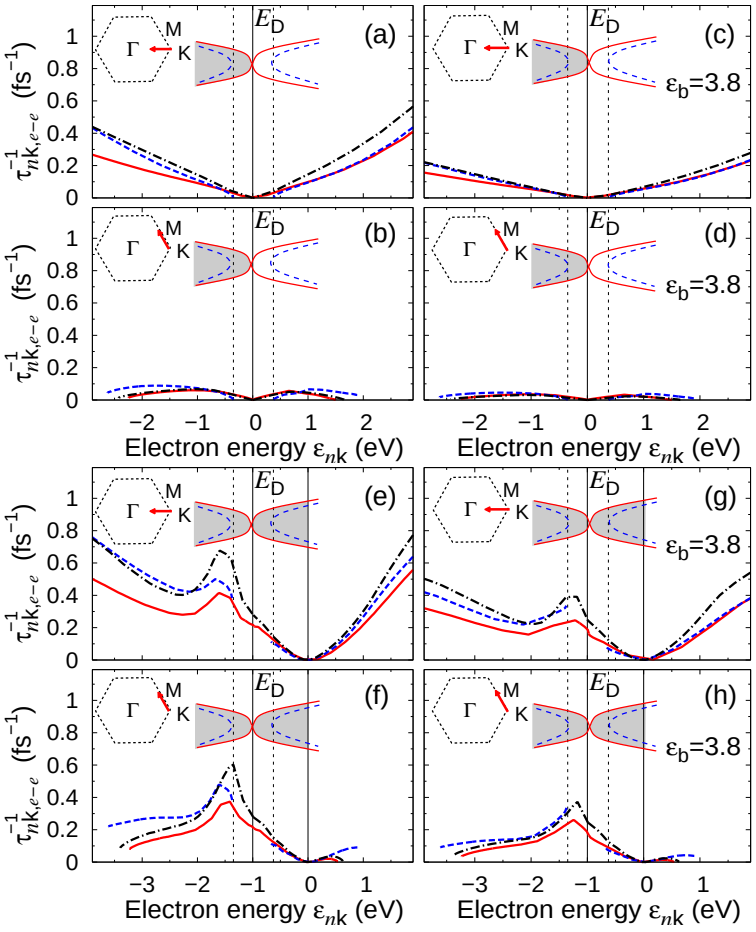

Figure 7.1: Calculated inelastic scattering rate of charge carriers arising from e-e interactions, $\tau^{-1}_{n\mathbf{k},e-e}$, versus the LDA energy $\varepsilon_{n\mathbf{k}}$. The solid, dashed, and dash-dotted lines are results, calculated along the reciprocal space segment shown in the inset of each panel, for the inner parabolic bands and outer parabolic bands in bilayer graphene and for the linear bands in graphene, respectively. (a)-(d) and (e)-(h) are results for undoped system and n-doped system where the Fermi level is 1.0 eV above the Dirac point energy $E_{\rm D}$, respectively. (a), (b), (e), and (f) are results for suspended systems, whereas (c), (d), (g), and (h) are results for systems with a background dielectric constant of $\varepsilon_{\rm b} = (1 + \varepsilon_{\rm SiC})/2 = 3.8$. The Fermi level and $E_{\rm D}$ are indicated by vertical lines.

the two-dimensional massless Dirac equation cannot describe this anisotropy, because of which, together with the ability to capture high-energy virtual scattering processes without a tunable fitting parameter, first-principles calculations are very important in discussing the carrier lifetime of graphitic systems.

Figures 7.1(c) and 7.1(d) show that the scattering rate $\tau^{-1}_{e-e,n\mathbf{k}}$ arising from e-e interactions is reduced by the dielectric screening from the substrate. We arbitrarily set the effective background dielectric constant $\varepsilon_{\rm b} = (1 + \varepsilon_{\rm SiC})/2 = 3.8$ to be that of interface between vacuum and silicon carbide (SiC) to see the effects of screening [104, 110]. We neglect the atomistic interaction between bilayer graphene and the substrate which affects the inelastic carrier lifetime near the Dirac point energy [58]. Also, for intrinsic systems, the interaction between bilayer graphene and the optical phonon modes of the substrate could affect the lifetime [142], although this effect is suppressed in real systems which are usually doped.

Figures 7.1(e)-7.1(h) show that in doped bilayer graphene, the inelastic scattering rate $\tau^{-1}_{e-e,n\mathbf{k}}$ shows the signature of electron-plasmon interactions (the peaks near $\varepsilon_{n\mathbf{k}} = -1.5$ eV) as in graphene [85, 86, 110]. Moreover, the lifetime of electrons with wavevector in the KM line in reciprocal space [Figs. 7.1(f) and 7.1(h)] is comparable to that in the KΓ line [Figs. 7.1(e) and 7.1(g)], in contrast to the case of pristine system [Figs. 7.1(a)-7.1(d)]. This increase in the scattering rate with doping has the origin in that the doped graphitic systems no longer show the bandstructure effect [111]. However, still, the scattering rate of electrons with wavevector in the KΓ line is higher than that in the KM line even for low-energy charge carriers.

7.3.2 Carrier lifetime limited by electron-phonon interactions

Figure 7.2 shows that the scattering rate $\tau^{-1}_{e-ph,n\mathbf{k}}$ arising from e-ph interactions in bilayer graphene is almost the same as that in graphene and that there is virtually no difference in $\tau^{-1}_{e-ph,n\mathbf{k}}$ between electrons in different bands with the same energy (solid and dashed curves). Moreover, $\tau^{-1}_{e-ph,n\mathbf{k}}$ does not depend sensitively on the wavevector $\mathbf{k}$ (not shown), consistent with the isotropic variation of the e-ph coupling constant in graphene [5] and in bilayer graphene [95]. Previous studies, using the quasiparticle dispersions renormalized by the e-e interaction to compute the e-ph interaction [115], reported anisotropy in the e-ph interaction in graphene. This latter procedure, which might give a better estimate for the e-ph interaction matrix element, would correspond to including some of the higher order processes in $\tau^{-1}_{e-ph,n\mathbf{k}}$ whilst neglecting them in $\tau^{-1}_{e-e,n\mathbf{k}}$, and would result in an unbalanced evaluation of e-e and e-ph effects according to different levels of approximation. Finally, the calculated carrier scattering rate $\tau^{-1}_{e-ph,n\mathbf{k}}$ in graphene (Fig. 7.2) agrees well with one of the previous theoretical studies [49] and is 5 times larger than the other [84].

The calculated total scattering rate $\tau^{-1}_{n\mathbf{k}} = \tau^{-1}_{e-e,n\mathbf{k}} + \tau^{-1}_{e-ph,n\mathbf{k}}$ in charge-doped graphene [110] is in good agreement with recent angle-resolved photoemission measurements on graphene epitaxially grown on SiC [4]. On the contrary, an ultrafast optical pump-probe spectroscopy study on similar samples has reported a carrier scattering rate of 0.014 fs^{-1} when the energy of the carrier is 0.8 eV, an order of magnitude smaller value than the one extracted from the

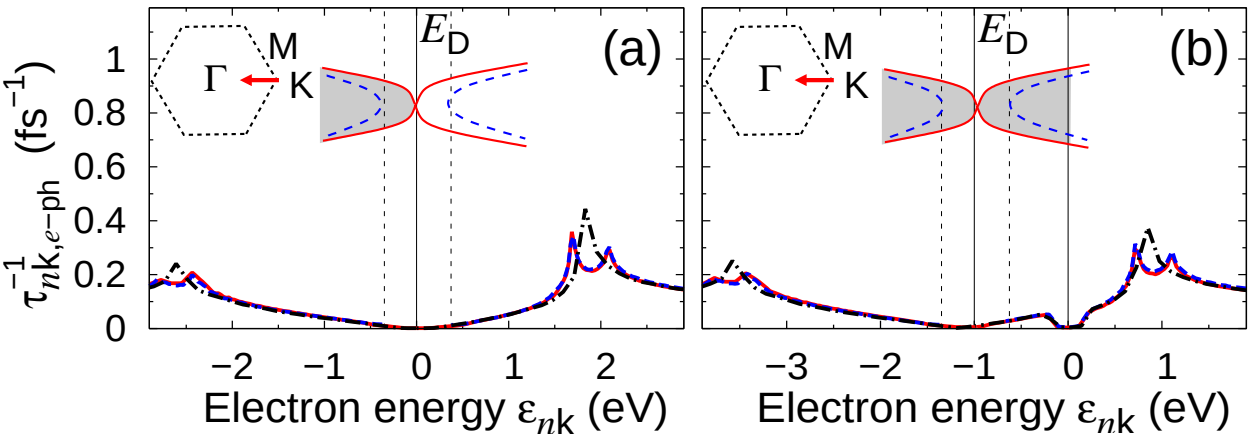

Figure 7.2: Calculated inelastic scattering rate of charge carriers arising from e-ph interactions, $\tau^{-1}_{n\mathbf{k},e-ph}$, versus the LDA energy $\varepsilon_{n\mathbf{k}}$. The solid, dashed, and dash-dotted lines are results, calculated along the KΓ reciprocal space segment, for the inner parabolic bands and outer parabolic bands in bilayer graphene and for the linear bands in graphene, respectively. (a) and (b) are results for undoped system and n-doped system where the Fermi level is 1.0 eV above the Dirac point energy $E_{\rm D}$, respectively. The Fermi level and $E_{\rm D}$ are indicated by vertical lines.

angle-resolved photoemission spectroscopy [4]. However, due to a finite duration ($\sim$ 85 fs) of the pump pulse, a scattering rate higher than 0.012 fs^{-1} cannot be accurately measured by this pump-probe study [140]. Moreover, the time-resolved measurements are likely to be dominated by the carriers having longer lifetimes. Therefore, our finding that the inelastic carrier lifetime varies significantly with the wavevector (Fig. 7.1) should be considered in the interpretation of future time-resolved experiments on graphitic systems.

7.4 Conclusion

In summary, we have studied the inelastic carrier lifetime in bilayer graphene from first-principles calculations. In particular, the scattering rate arising from e-e interactions is highly anisotropic and is reduced by 20–40% on average from that of graphene. Our findings could be useful in the electronic and spintronic device applications of bilayer graphene in a high-bias regime.

Chapter 8

Tunable excitons in biased bilayer graphene

8.1 Introduction

The low-energy electronic states of graphene are described by a massless Dirac equation [35, 36, 138]. If an extra layer is added [Fig. 8.1(a)], the electronic properties change drastically and the charge carriers become massive [Fig. 8.1(b)] [120]. There have been a number of theoretical studies on the possibility of opening up a bandgap in the gapless bilayer graphene if an electric field is applied perpendicularly [Figs. 8.1(c) and 1(d)] [143, 144, 145, 146, 147, 148, 149, 150, 151]. Indeed, a bandgap has been observed in the case of an internal perpendicular electric field generated by an imbalance of doped charge between the two graphene layers [152]. Also, bandgap opening in bilayer graphene under an electric field from a single gate has been observed by infra-red spectroscopy [153, 154, 155, 156, 157] and quantum Hall measurement [158].

A bandgap opening up in bilayer graphene under an electric field from a double-gate configuration has further been observed in transport experiments [137]. Very recently, infra-red measurements showed that the bandgap of bilayer graphene in a double-gate geometry is continuously tunable up to 250 meV, an order of magnitude higher than the thermal energy at room temperature [8]. This discovery provides exciting new possibilities for the nanoelectronic and nanophotonic device applications of bilayer graphene at room temperature.

Theoretical studies on the optical response of *intrinsic* bilayer graphene within a single-particle picture [159, 160] as well as including electron-hole () interactions [161, 162] have been performed. It is found that there are negligible many-electron effects on the low-energy ($\leq$ 1 eV) optical response of graphene and bilayer graphene [161]. There have also been theoretical studies within a single-particle picture on the electronic and optical properties of biased bilayer graphene (BBG) [163, 164, 165, 166]. However, theoretical investigation of excitonic effects on the optical response of this novel tunable bandgap system has yet to be performed up to now. It is known that interactions play a crucial role in the optical re-

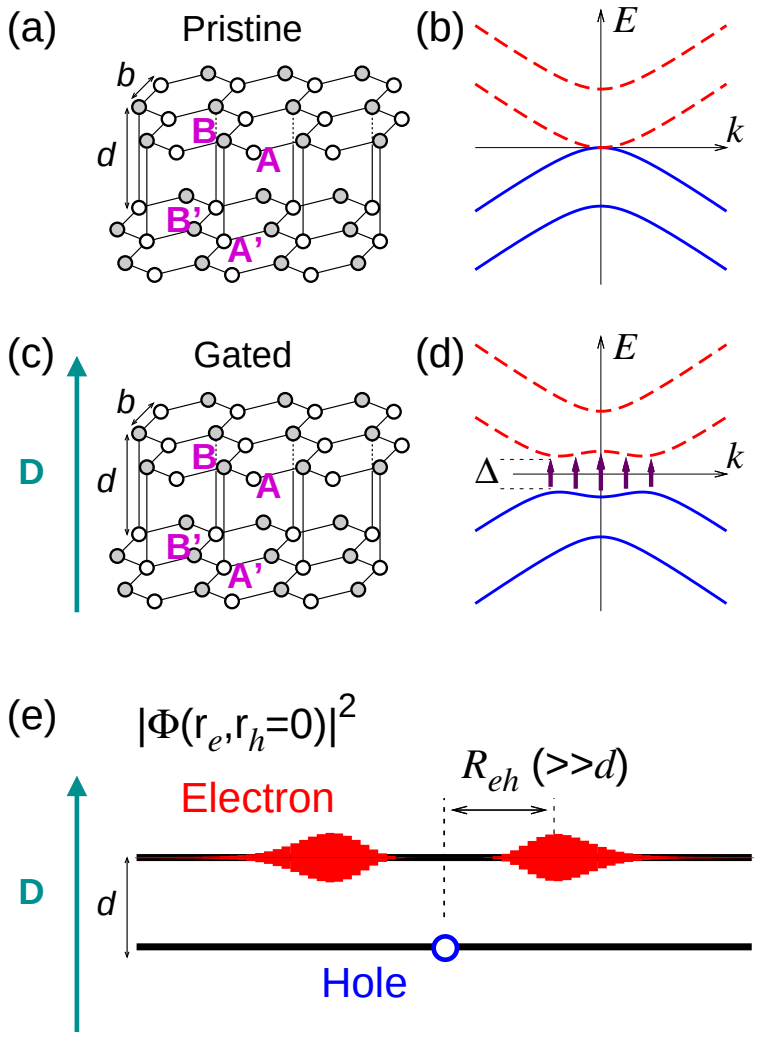

Figure 8.1: (a) Schematic diagram showing the structure of pristine bilayer graphene whose unit cell is composed of four different sublattices (A, B, A′, and B′). (b) Schematic band-structure of pristine bilayer graphene (origin is the Dirac point). Solid blue and dashed red lines represent valence bands and conduction bands, respectively. (c) and (d): Same schematic diagrams as in (a) and (b) for bilayer graphene under a displacement field **D** generated through a double-gate. In (d), Δ is the energy bandgap and vertical arrows represent interband transitions responsible for the formation of excitons. (e) Schematic diagram showing the probability density that a photo-excited electron is found at $\mathbf{r}_e$ when the hole (blue empty circle) is fixed at the origin, $|\Phi(\mathbf{r}_e, \mathbf{r}_h = 0)|^2$ (see text). For visualization purposes, we show the quantities in a vertical plane that includes the hole. The fake thickness of the plotted profile (red) is proportional to the probability density. The interlayer distance d is extremely exaggerated in (e). The size of the exciton R_{eh} is much larger than d [Fig. 8.4(b)].

sponse of semiconductors [28], especially, semiconducting nanostructures [167, 168, 169, 170]. Excitonic effects in BBG with a finite bandgap are expected to be important, considering that the lowest-energy van Hove singularity in its joint electronic density of states exhibits a one-dimensional (1D), and not a two-dimensional (2D), behavior (i. e. , it diverges as inverse of the energy difference from the bandgap) [165].

8.2 Theory and computation

Here, we obtain the optical response of a BBG including interactions by solving the Bethe-Salpeter equation (BSE):

$$(E_{c\mathbf{k}} - E_{v\mathbf{k}})\, A^S_{cv\mathbf{k}} + \sum_{c'v'\mathbf{k}'} \langle cv\mathbf{k}|K^{eh}|c'v'\mathbf{k}'\rangle A^S_{c'v'\mathbf{k}'} = \Omega^S A^S_{cv\mathbf{k}} \ , \tag{8.1}$$

where $A^S_{cv\mathbf{k}}$ is the amplitude of a free pair configuration composed of the electron state $|c\mathbf{k}\rangle$ and the hole state $|v\mathbf{k}\rangle$, Ω^S is the exciton excitation energy, $E_{c\mathbf{k}}$ and $E_{v\mathbf{k}}$ are quasiparticle energies, and K^{eh} is the interaction kernel [28]. The absorption spectrum is calculated by evaluating the optical matrix elements [28] using the eigenstates and eigenvalues of the BSE.

As in recent experiments [8, 171], we focus here on the case in which the net charge on the BBG is zero, or, the displacement fields $\mathbf{D}$ above and below the bilayer graphene are the same [Fig. 8.1(c)]. We find that the optical response of BBG is dominated by low-energy bound excitons with huge oscillator strength due to the 1D nature in the joint density of states. As a consequence, the main peak of the absorbance profile becomes highly symmetric. The binding energy and oscillator strength of the excitons increase with the bandgap. We find a very rich electronic structure for the excitons in a BBG. Especially, we discover a symmetry breaking of excitons having angular momenta of equal magnitude but of opposite sign which leads to an unusual selection rule in the optical absorption. This phenomenon is explained in terms of the pseudospin, a degree of freedom describing the bonding character between neighboring carbon atoms [138], in a BBG.

In this study, we make use of the $k\cdot p$ based method developed by Ando and coworkers for the excitonic spectra of graphene and carbon nanotubes [172, 173, 174, 175, 176]. Although, unlike the first-principles *GW*-BSE approach [28] that is parameter free, the current method is based on a tight-binding formalism and treats electron-electron interactions within the screened Hartree-Fock approximation, it does provide excitonic features of the absorption profile that may be compared with experiments for complex structures and applied fields [174, 177]. For the kernel K^{eh}, we consider only the attractive direct term, which is by far dominant and describes the screened interaction between electrons and holes, and neglect the repulsive exchange term. The exchange kernel is responsible for singlet-triplet splitting and the splitting among states within individual singlet and triplet complexes, but is usually only a few percent in magnitude of the direct term [167].

The quasiparticle energies $E_{c\mathbf{k}} = \varepsilon_{c\mathbf{k}} + \Sigma_{c\mathbf{k}}$ and $E_{v\mathbf{k}} = \varepsilon_{v\mathbf{k}} + \Sigma_{v\mathbf{k}}$ are obtained by first calculating the bare energy $\varepsilon_{\mathbf{k}}$ within the $k\cdot p$ formalism [174] using a tight-binding Hamilto-

nian where we set the intralayer hopping parameter between the nearest-neighboring atoms $\gamma_0 = 2.6$ eV and the interlayer hopping parameter $\gamma_1 = 0.37$ eV. These parameters reproduce well the bandstructure of pristine bilayer graphene obtained from density-functional calculations within the local density approximation (LDA) [161]. The self energy $\Sigma_{\mathbf{k}}$ is calculated within the screened Hartree-Fock approximation, using the static random-phase dielectric function [172, 173, 174, 177]. We calculate the static polarizability within the random-phase approximation [172, 173, 174, 177] by including the four electronic bands closest to the bandgap arising from the π states with an energy cutoff of 5 eV (we have checked that the resulting quasiparticle energies are insensitive to this cutoff), and incorporate the effects of screening from higher-energy states (including the π bands away from the Dirac points and the σ bands) by an additional effective static dielectric constant $\epsilon_{\rm int} = 2.0$ as done in previous graphene and nanotube studies [175, 176, 177]. The total dielectric function $\epsilon(q)$ is given by $\epsilon(q) = 1 - v(q)\ [P_{\rm int}(q) + P(q)]$ where $v(q) = 2\pi e^2/q$ is the bare Coulomb interaction and $P_{\rm int}(q)$ and $P(q)$ are the static polarizabilities coming from excitations involving higher-energy states and those involving only the low-energy π states, respectively. Using the relation $\epsilon_{\rm int}(q) = 1 - v(q)\ P_{\rm int}(q) \approx \epsilon_{\rm int}$ for screening with low-momentum transfer, we obtain $\epsilon(q) \approx \epsilon_{\rm int} - v(q)\ P(q)$ [172, 173, 174, 177]. The calculated self energy is then added to the LDA band energy to form the quasiparticle energy. Although in this scheme, the LDA exchange-correlation energy is not subtracted from the LDA band energy, it should be a reasonable approximation because the LDA exchange-correlation energy is nearly the same for all the π states giving rise to a constant shift to both occupied and unoccupied states.

We use in all the calculations a very dense grid for electronic state sampling corresponding to 1500×1500 **k**-points in the *irreducible* wedge of the Brillouin zone of bilayer graphene in order to describe the extended wavefunction (correlation length) of the excitons in real space, in particular at small bias voltage when the bandgap is small.

The external displacement field **D** induces an imbalance between the charge densities on the two graphene layers of the BBG, which creates an internal depolarization electric field. This depolarization field induces additional charge changes, which in turn induce further adjustments in the internal electric field, and so on. We obtain the resulting internal electric field and the charge imbalance between the layers by solving Poisson's equation [8].

8.3 Results and discussion

8.3.1 The wavefunctions and binding energies of bound excitons

Figure 8.1(e) is a schematic diagram showing the squared amplitude (wavefunction) of the lowest-energy optically active (bright) exciton for incident light with in-plane polarization, $|\Phi(\mathbf{r}_e, \mathbf{r}_h = 0)|^2 = \left|\sum_{cv\mathbf{k}} A^S_{cv\mathbf{k}} \langle \mathbf{r}_e|c\mathbf{k}\rangle \langle v\mathbf{k}|\mathbf{r}_h = 0\rangle\right|^2$ where the hole is fixed at a carbon atom belonging to the B′ sublattice. The bound excitons [Fig. 8.2(a)] are comprised of interband transitions forming the bandgap [Fig. 8.1(d)]. The electronic states in those two bands are localized at A and B′ sublattices for the conduction and valence band, respectively, i.e.,

Table 8.1: Calculated quantities of bound excitons in a BBG: the binding energy ($E_{\rm b}$), the radial quantum number n, the angular momentum quantum number m, and the integrated absorbance (IA), the absorbance integrated over energy, of the exciton $X_{n,m}$ made from free pairs near the K point. The IA is for incident light with in-plane polarization. The quantities are the same for the exciton $X'_{n,-m}$ made from pairs near the K′ point. Here, we consider the BBG with $V_{\rm ext} = eDd$ equal to 0.56 eV.

Index	$E_{\rm b}$ (meV)	n	m	$n + \|m\|$	IA (meV)
1	55.6	0	0	0	0.000
(bright) 2	40.6	0	-1	1	1.240
3	35.0	0	1	1	0.000
4	32.7	0	-2	2	0.000
5	27.0	0	2	2	0.000
6	25.5	0	-3	3	0.000
7	22.8	1	0	1	0.000
8	22.0	0	3	3	0.000
9	20.9	0	-4	4	0.000
(bright) 10	19.5	1	-1	2	0.146
11	18.5	0	4	4	0.000
12	18.2	1	1	2	0.000
13	17.7	0	-5	5	0.000
14	17.0	1	-2	3	0.000
⋮	⋮	⋮	⋮	⋮	⋮

the electron and hole are localized on two different graphene layers. As shown schematically in Fig. 8.1(e), the position of the maximum in the electron density is not on top of the hole, but is on a ring with a radius R_{eh} from the hole that is about two orders of magnitude larger than the interlayer distance d. The radius of the exciton in real space is related to that in $\mathbf{k}$ space by $R_{eh} \approx 2\pi/R_{cv\mathbf{k}}$ [see, e. g. , Fig. 8.2(e) and Fig. 8.2(f)].

8.3.2 Optical selection rules

Figure 8.2(a) shows the bound exciton levels for a particular BBG ($eDd = 0.56$ eV), in which we label an exciton by the radial quantum number n and the angular momentum quantum number m of its wavefunction. The wavefunction of an exciton $X_{n,m}$ formed from the free pairs near the K point is approximately of the form $\Phi(\mathbf{r}_e, \mathbf{r}_h = 0) \approx e^{im\theta_{\mathbf{r}_e}} r_e^{|m|} f_{n,m}(r_e)$ near the origin ($\mathbf{r}_e = 0$) where $f_{n,m}(r_e)$ has n zeros like the wavefunctions in the 2D quantum well problem having the angular symmetry [178]. However, in our system, the angular symmetry is broken, i. e. , the binding energy of $X_{n,m}$ and that of $X_{n,-m}$ are different (see Table 8.1). The origin of this symmetry breaking lies in the pseudospin of BBG. The elec-

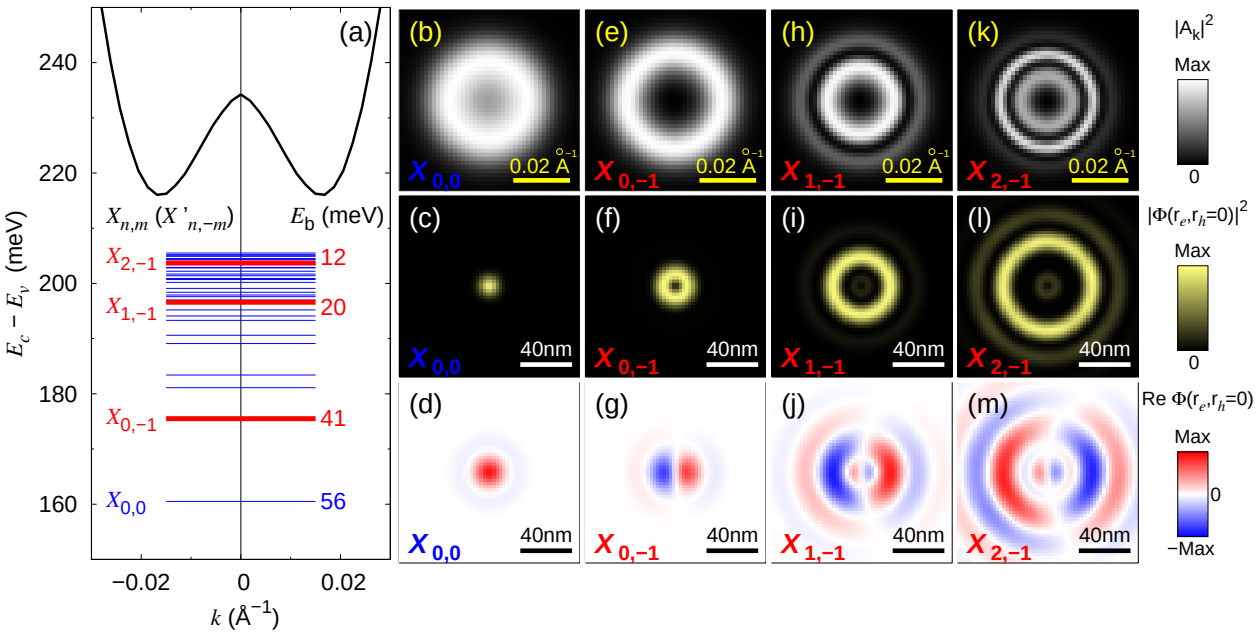

Figure 8.2: (a) Calculated free pair excitation dispersion ($E_{c\mathbf{k}} - E_{v\mathbf{k}}$ versus $\mathbf{k}$) and exciton levels of a BBG with an *external* electrostatic potential between the two graphene layers $V_{\text{ext}} = eDd$ equal to 0.56 eV (Fig. 8.1). Thick red lines and thin blue lines show optically active (bright) and inactive (dark) exciton levels, respectively, for incident light with in-plane polarization. The exciton $X_{n,m}$ ($X'_{n,-m}$) formed by pairs near the K (K′) point is denoted by its radial quantum number n, angular momentum quantum number m (see text), and binding energy E_{b}. Each exciton level is four-fold degenerate due to the spin and valley degeneracy (see text). There are many other higher-energy bound excitons not shown here whose energy is below the bandgap. (b) The squared amplitude of the lowest-energy exciton [exciton $X_{0,0}$ in (a)] in momentum space $\left|A^S_{cv\mathbf{k}}\right|^2$. (c) Squared wavefunction in real space of the corresponding exciton in (b). The plotted quantity is the probability density $|\Phi(\mathbf{r}_e, \mathbf{r}_h = 0)|^2$ of finding an electron at $\mathbf{r}_e$ given that the hole is fixed at one of the carbon atoms (at the center of the figure) in sublattice B′ (Fig. 8.1). (d) Real part of the exciton wavefunction Re $\Phi(\mathbf{r}_e, \mathbf{r}_h = 0)$ for the corresponding exciton in (b). (e)-(g), (h)-(j), and (k)-(m): Similar quantities as in (b)-(d) for the first, the second and the third bright excitons [excitons $X_{0,-1}$, $X_{1,-1}$, and $X_{2,-1}$ in (a), respectively].

tronic states in in the conduction and valence bands forming the bandgap of a BBG, in the basis of amplitudes on the four sublattices (A, B, A′ and B′), are

$$|c\mathbf{k}\rangle \propto \left(a_1, a_2\, e^{i\theta_{\mathbf{k}}}, a_3\, e^{i\theta_{\mathbf{k}}}, a_4\, e^{2i\theta_{\mathbf{k}}}\right)^{\mathrm{T}} \tag{8.2}$$

and

$$|v\mathbf{k}\rangle \propto \left(-a_4, a_3\, e^{i\theta_{\mathbf{k}}}, -a_2\, e^{i\theta_{\mathbf{k}}}, a_1\, e^{2i\theta_{\mathbf{k}}}\right)^{\mathrm{T}}, \tag{8.3}$$

respectively, where a_i's ($i = 1$, 2, 3, and 4) are real constants [176]. As discussed above, the band edge states that form the bound excitons have $|a_1| \approx 1$ and $|a_2|, |a_3|, |a_4| \ll 1$, i. e. , the electron and hole are localized at the A and B′ sublattices, respectively. Therefore, the pseudospin of the states in a BBG imposes *approximately* an extra phase of $e^{-2i\theta_{\mathbf{k}}}$ to the pair state $|c\mathbf{k}\rangle\langle v\mathbf{k}|$, resulting in an extra pseudospin angular momentum $m_{\mathrm{ps}} = -2$. This behavior is unique in BBG. In pristine bilayer graphene, $|a_1|$ and $|a_4|$ are the same [175, 176], and hence we cannot define a single extra phase.

If we denote the angular momentum of an exciton coming from the envelope function $A^S_{cv\mathbf{k}}$ by m_{env}, then the total angular momentum quantum number (which is the approximate good quantum number) is given by $m = m_{\mathrm{env}} + m_{\mathrm{ps}}$. Because of the extra pseudospin angular momentum, two exciton states having m_{env} of the same magnitude but of opposite sign are no longer degenerate since m would be different. Rather, two states having total angular momentum quantum number m and m will be degenerate if the extra phase imposition by the pseudospin is perfect. In fact, the extra phase imposition of $e^{-2i\theta_{\mathbf{k}}}$ is not perfect because the coefficients $|a_2 2|$, $|a_3|$, and $|a_4|$ are non-zero, resulting in the degeneracy breaking shown in Table 8.1. [The broken angular symmetry shown, e. g. , in Fig. 8.2(m) has the same origin.] On the contrary, due to time-reversal symmetry, the exciton $X_{n,m}$ (formed by states near K) is degenerate in binding energy with $X'_{n,-m}$, which is an exciton made from the free pairs near the K′ point with radial and angular momentum quantum numbers n and m, respectively. Therefore, considering the spin and valley degeneracy and neglecting possible intervalley coupling, each bound exciton shown in Fig. 8.2(a) is four-fold degenerate.

The extra phase $e^{-2i\theta_{\mathbf{k}}}$ arising from the pseudospin in a BBG qualitatively changes the selection rule for optical absorption as follows. The oscillator strength O^S of an exciton S of a BBG is given by $O^S = \sum_{cv\mathbf{k}} A^S_{cv\mathbf{k}} \langle v\mathbf{k}|\, \hat{O}\, |c\mathbf{k}\rangle$ in which $\hat{O}$ is proportional to the electron-photon interaction Hamiltonian. If the exciting photons are polarized along the x direction (i. e. , parallel to the graphene planes), then $\hat{O} \propto \begin{pmatrix} \sigma_x & 0 \\ 0 & \sigma_x \end{pmatrix}$ where σ_x is the Pauli matrix [175]. Using Eqs. (8.2) and (8.3), we obtain $O^S \propto \sum_{cv\mathbf{k}} A^S_{cv\mathbf{k}} \left(a_1 a_3\, e^{-i\theta_{\mathbf{k}}} - a_2 a_4\, e^{i\theta_{\mathbf{k}}}\right)$. In order to have a non-vanishing oscillator strength, we should have $A^S_{cv\mathbf{k}} \propto e^{i\theta_{\mathbf{k}}}$ or $A^S_{cv\mathbf{k}} \propto e^{-i\theta_{\mathbf{k}}}$, i. e. , the envelope angular momentum quantum number m_{env} should be 1 or -1. Therefore, the total angular momentum quantum number m (which is equal to $m_{\mathrm{env}} - 2$) for the optically active excitons is either -1 or -3. However, since $|a_1|$ is by far the largest among the four $|a_i|$'s and $|a_1 a_3| \gg |a_2 a_4|$ [176], effectively, only the excitons $X_{n,-1}$ or $X'_{n,1}$ are optically active (Table 8.1). This unusual optical selection rule in a BBG, hence, originates from the unique pseudospin physics.

8.3.3 Optical absorbance

In the discussion below on the optical absorbance, for concreteness, we shall assume that the polarization of the incident light is linear and is parallel to the graphene planes. Accordingly, the lowest-energy exciton $X_{0,0}$ [Figs. 8.2(b)-8.2(d)] is dark and the second lowest-energy exciton $X_{0,-1}$ [Figs. 8.2(e)-8.2(g)] is bright. As seen from the calculated oscillator strength in Table 8.1, the lowest-energy bright excitons by far dominate the absorbance spectrum. The first, second and third bright excitons have zero, one, and two nodes in the exciton wavefunction along the radial direction, respectively, in both momentum and real space (Fig. 8.2). Also, there are many dark exciton levels between the bright exciton ones as shown in Fig. 8.2(a). A change in the polarization direction of the incident light away from the graphene plane would alter the optical strength of the levels from those given in Fig. 8.2(a).

In a 2D hydrogen atom, the binding energy is proportional to $(n + |m| + 1/2)^{-2}$ resulting in a $2N + 1$-fold degeneracy with $N = n + |m|$ [178]. As shown in Table 8.1, however, this degeneracy in the binding energy of the excitons in a BBG is broken, and, further, the order of the binding energies largely deviates from the case for a 2D hydrogenic model. Also, we have checked that the detailed order of exciton levels changes with the external displacement field.

8.3.4 Tunable exciton binding energy

Figure 8.3 shows the calculated absorbance spectrum of BBG (for in-plane linearly polarized incident light) near the bandgap energy and the wavefunction of the lowest-energy bright exciton that forms the main peak for several bias voltages. Remarkably, when interactions are accounted for, the absorbance profile is dominated by a single four-fold degenerate excitonic level with huge oscillator strength. Accordingly, the dominant feature of the absorbance profile near the bandgap energy becomes symmetric when excitonic effects are considered – as in carbon nanotubes [167, 179]; whereas, if these effects are neglected, highly asymmetric absorbance spectra are obtained reflecting the "effective" 1D van Hove singularity in the joint density of quasiparticle states discussed above. The huge excitonic effects observed here in fact originate from this 1D singularity [167] which becomes more and more dominant as the bandgap increases. On the contrary, excitonic effects on the low-energy ($\leq$ 1 eV) optical response of *pristine* bilayer graphene are negligible since its joint density of states is characteristic of a 2D system [161]. The enhancement of excitonic effects with the bandgap is reflected in the increase in the exciton binding energy [Fig. 8.4(a)] and the decrease in the exciton radius [Fig. 8.3 and Fig. 8.4(b)].

In a previous study [171], we have shown that when the photo-excitation energy is close to the energy of the zone-center optical phonons in BBG ($\sim$0.2 eV), Fano lineshapes in the absorbance profile develop due to the coupling of pair excitations with the phonons. We expect that similar exciton-phonon coupling behavior, whose effects on the optical response is large when the optical energy gap is around 0.2 eV, would arise if electron-phonon

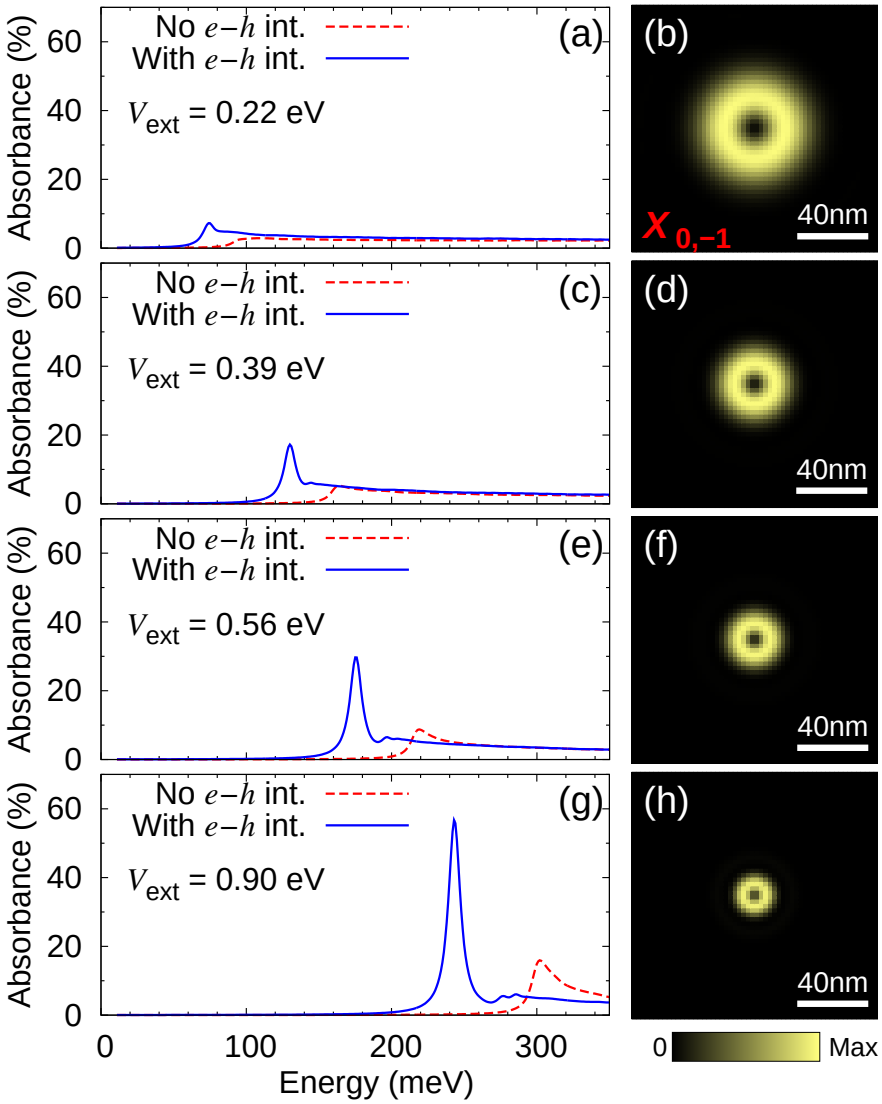

Figure 8.3: (a) Calculated absorbance spectra of BBG (with an arbitrary energy broadening of 5 meV and in-plane polarization) where $V_{\text{ext}} = eDd$ (see Fig. 8.1) is 0.22 eV. Results with (blue or solid line) and without (red or dashed line) interaction effects are shown. (b) Wavefunction of the lowest-energy bright exciton ($X_{0,-1}$ or $X'_{0,1}$) that forms the dominant peak in the absorbance spectrum. The plotted quantity is the probability density $|\Phi(\mathbf{r}_e, \mathbf{r}_h = 0)|^2$ of finding an electron at $\mathbf{r}_e$ given that the hole is fixed at one of the carbon atoms (at the center of the figure) in sublattice B′ (see Fig. 8.1). (c) and (d), (e) and (f), and (g) and (h): Same quantities as in (a) and (b) for $V_{\text{ext}} = 0.39$ eV, 0.56 eV, and 0.90 eV, respectively.

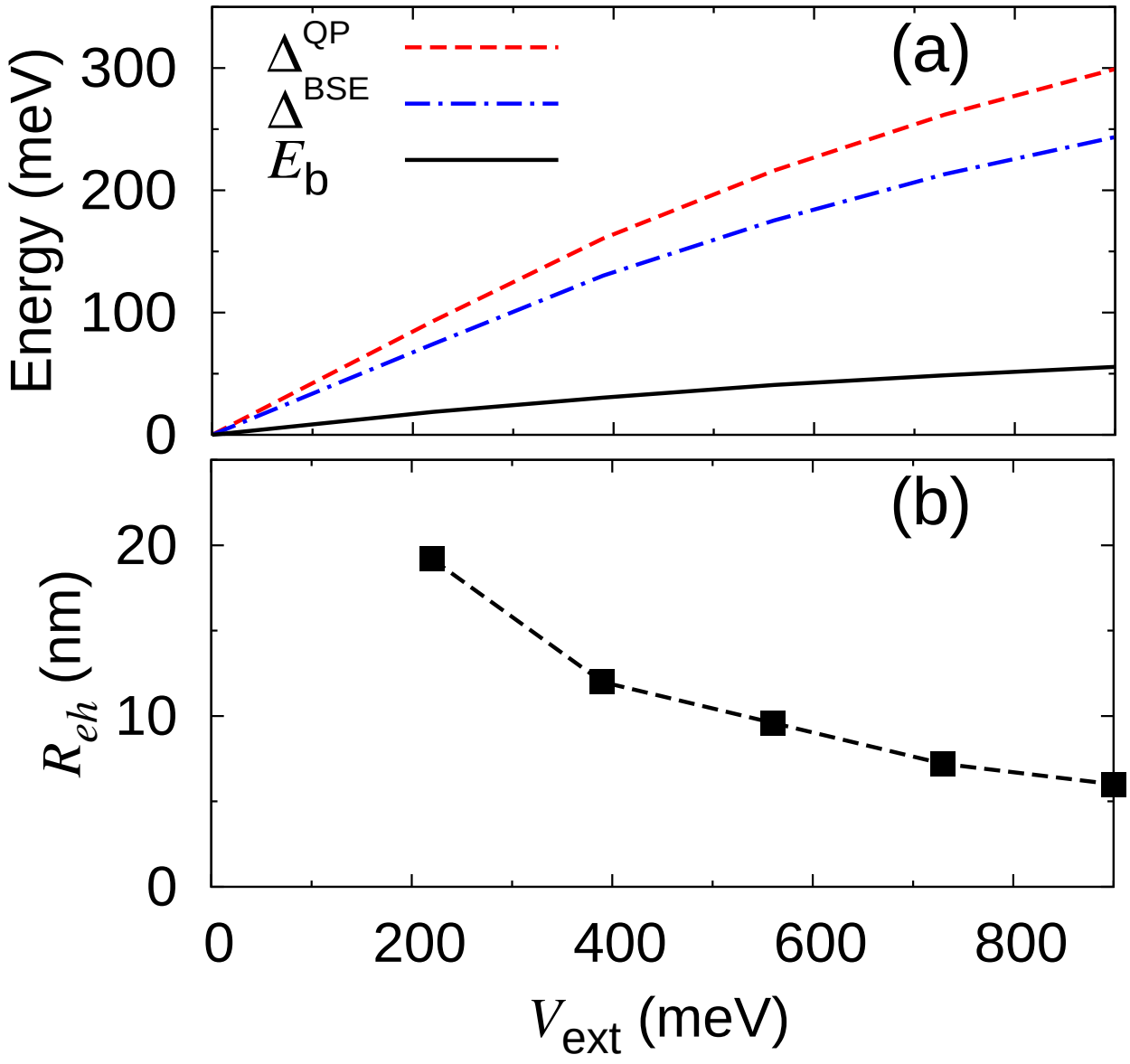

Figure 8.4: (a) The quasiparticle bandgap Δ^{QP}, the optical bandgap Δ^{BSE}, and the binding energy E_{b} ($= \Delta^{\mathrm{QP}} - \Delta^{\mathrm{BSE}}$) of BBG versus $V_{\mathrm{ext}} = eDd$. (b) The size R_{eh}, defined in Fig. 8.1(e), of the lowest-energy bright exciton ($X_{0,-1}$ or $X'_{0,1}$) versus V_{ext}. The line is a guide to the eye.

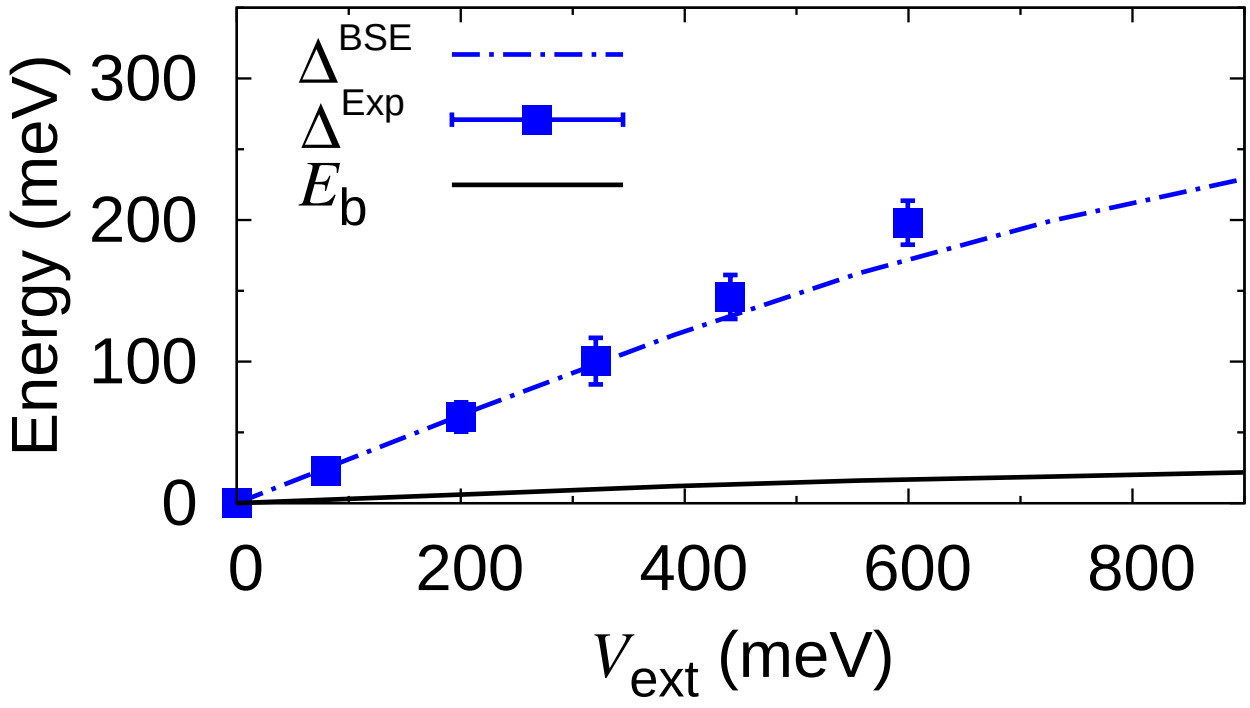

Figure 8.5: The optical bandgap $\Delta^{\rm BSE}$ and the binding energy $E_{\rm b}$ ($=\Delta^{\rm QP}-\Delta^{\rm BSE}$) of BBG under background screening ($\epsilon_{\rm BG}=5.7$) versus $V_{\rm ext}=eDd$. Measured data $\Delta^{\rm Exp}$ are taken from Ref. [8].

interactions are taken into account [180].

8.3.5 Effects of substrate dielectric screening

The above results are applicable to suspended BBG [181]. However, for BBG on substrates, excitonic effects are altered due to enhanced screening from the substrate. As an example, we consider the effect of background screening due to the substrate on the optical response of BBG relevant for the experimental setup in Refs. [8] and [171]. For substrates above and below the BBG having dielectric constants ϵ_1 and ϵ_2, respectively, their effect can effectively be replaced by a single material having a dielectric constant of $\epsilon_{\rm BG}=(\epsilon_1+\epsilon_2)/2$ [116]. Using the static dielectric constant of SiO_2 (=3.9) and that of amorphous Al_2O_3 (=7.5), we may roughly set the external background dielectric screening as $\epsilon_{\rm BG}=(3.9+7.5)/2=5.7$. Figure 8.5 shows similarly calculated quantities as in Fig. 8.4(a), but now for BBG with added substrate screening as discussed above. The exciton binding energy $E_{\rm b}=\Delta^{\rm QP}-\Delta^{\rm BSE}$ is smaller than the case without substrate screening. The calculated optical gap $\Delta^{\rm BSE}$ is in reasonable agreement with the experiment $\Delta^{\rm Exp}$ [8].

8.4 Conclusion

In conclusion, we have shown that excitons in biased bilayer graphene dramatically change the optical response because of the 1D nature of the joint density of quasiparticle states in this system. These excitonic effects are remarkably tunable by the external electric field. Also, we have shown that the pseudospin character of the electronic states dramatically alters the excitonic structure (energy level degeneracy, optical selection rule, etc.) of this system. These results illustrate the richness in the photophysics of biased bilayer graphene and their promise for potential applications in nanoelectronic and nanophotonic devices at room temperature [8].

Chapter 9

Anisotropic behaviors of massless Dirac fermions in graphene under periodic potentials

9.1 Introduction

Charge carriers of graphene show neutrino-like linear energy dispersions as well as chiral behavior near the Dirac point [77, 34, 35, 36, 182, 72]. Here we report highly unusual and unexpected behaviors of these carriers in applied external periodic potentials, i.e., in graphene superlattices. The group velocity renormalizes highly anisotropically even to a degree that it is not changed at all for states with wavevector in one direction but is reduced to zero in another, implying the possibility that one can make nanoscale electronic circuits out of graphene not by cutting it [183, 184, 185, 186] but by drawing on it in a non-destructive way. Also, the type of charge carrier species (e.g. electron, hole or open orbit) and their density of states vary drastically with the Fermi energy, enabling one to tune the Fermi surface-dominant properties significantly with gate voltage. These results address the fundamental question of how chiral massless Dirac fermions propagate in periodic potentials and point to a new possible path for nanoscale electronics.

Since the pioneering work by Esaki and Tsu [187], superlattices have been studied extensively and have had a huge impact on semiconductor physics [188, 189]. Superlattices demonstrate interesting phenomena such as negative differential conductivity, Bloch oscillations, gap openings at the mini Brillouin zone boundary formed by the additional periodic potential, etc [188, 189]. Conventional semiconducting superlattices are mainly produced by molecular-beam epitaxy and metallo-organic chemical vapour-phase deposition while metallic superlattices are made by sputtering procedures [188, 189]. We expect that, by modulating the potential seen by the electrons, graphene superlattices may be fabricated by adsorbing adatoms on graphene surface through similar techniques, by positioning and aligning impurities with scanning tunneling microscopy [190, 191, 192], by using hydrocarbon lithography

technique [193] or by applying a local top-gate voltage to graphene [194, 195, 196]. Epitaxial growth of graphene [182] on top of pre-patterned substrate is also a possible route to graphene superlattice. Recently, periodic pattern in the scanning tunneling microscope image has been demonstrated on a graphene monolayer on top of a metallic substrate [197, 198, 199] as well.

9.2 Theory and computation

The low energy charge carriers in pristine graphene are described by a massless Dirac equation and have a linear energy dispersion which is isotropic near the Dirac points K and K' in the Brillouin zone [77, 78, 200, 35, 36, 201] (Fig. 9.1a). It is shown experimentally that the carriers have a group velocity of $v_0 \approx 10^6$ m/s which plays the role of an effective speed of light in (2+1) dimensional quantum electrodynamics [35, 36]. Within the effective-Hamiltonian approximation,

$$H = \hbar v_0 \begin{pmatrix} 0 & -ik_x - k_y \\ ik_x - k_y & 0 \end{pmatrix} ,$$

where k_x and k_y are the x and y components of the wavevector $\mathbf{k}$ of the Bloch state defined with respect to the Dirac point, the wavefunction of the quasiparticles in graphene has two components corresponding to the amplitude on the two different trigonal sublattices of graphene and can be represented by a two component spinor [201, 78, 200]. This spinor structure of the wavefunction is called a pseudospin (because it is not related to a real spin) or chirality [201, 78, 200, 79, 80], which is of central importance to the novel physical properties of graphene superlattices discussed below.

Let us now consider the situation that an additional periodic potential is applied to graphene. If the spatial period of the superlattice potential is much larger than the nearest neighbor carbon-carbon distance in graphene (~ 1.42 Å), the scattering of a state close to one Dirac point to another one does not occur [78, 200, 79]. Therefore, even though there are two nonequivalent Dirac cones for the energy dispersion surface of graphene, focusing on a single cone is sufficient. This condition also implies that, in the graphene superlattices discussed here, there is no gap opening at the Dirac point [78, 200, 79].

To investigate the physics of charge carriers in graphene superlattices, we have calculated the energy dispersions, the group velocities, and energy gap openings at the minizone boundaries (MB) within the effective-Hamiltonian formalism [77]. Effects of the external periodic potential are incorporated into our calculation through the scattering matrix elements between pseudospin states, or chiral eigenstates, of the electrons in graphene:

$$\langle s, \mathbf{k} \left| U(\mathbf{r}) \right| s', \mathbf{k}' \rangle = \sum_{\mathbf{G}} \frac{1}{2} \left(1 + ss' e^{-i\theta_{\mathbf{k},\mathbf{k}-\mathbf{G}}} \right) U(\mathbf{G}) \; \delta_{\mathbf{k}',\mathbf{k}-\mathbf{G}} \; .$$

Here, $\mathbf{G}$'s are reciprocal lattice vectors of the superlattice and $\theta_{\mathbf{k},\mathbf{k}-\mathbf{G}}$ is the angle between $\mathbf{k}$ and $\mathbf{k}-\mathbf{G}$. $U(\mathbf{r})$ and $U(\mathbf{G})$ are external potential in real and wavevector space, respectively.

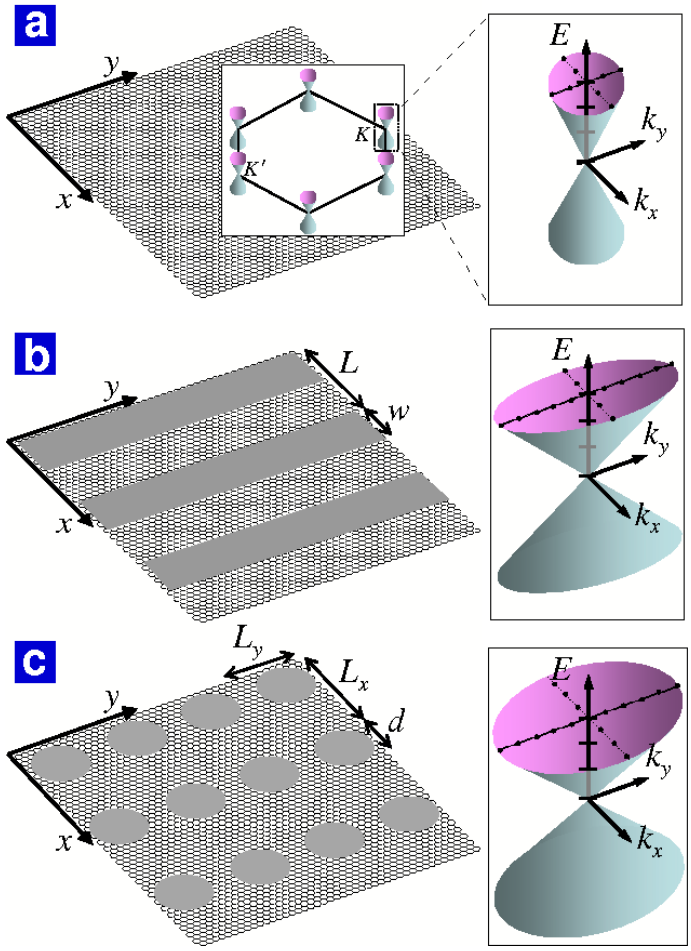

Figure 9.1: Graphene superlattices and anisotropic Dirac cones. (a) Schematic diagram of graphene. Inset: the Brillouin zone of graphene and Dirac cones centered at Dirac points among which two (K and K') are nonequivalent (left) and the linear and isotropic energy dispersion near one of the Dirac points of charge carriers in graphene (right). (b) One-dimensional (1D) graphene superlattice formed by Kronig-Penney type of potential periodic along $\hat{x}$ direction with spatial period L and barrier width w. The potential is U_{1D} in the grey regions and zero outside. Inset: energy dispersion of charge carriers in 1D graphene superlattice. The energy dispersion along any line in two-dimensional (2D) wavevector space from the Dirac point is linear but with different group velocity. For a particle moving parallel to the periodic direction, the group velocity ($v_{\parallel}$) is not renormalized at all whereas that for a particle moving perpendicular to the periodic direction ($v_{\perp}$) it is reduced most. (c) 2D graphene superlattice with muffin-tin type of potential periodic along both $\hat{x}$ and $\hat{y}$ directions with spatial periods L_x and L_y, respectively. The potential is U_{2D} inside the grey disks with diameter d and zero outside. Inset: energy dispersions of charge carriers in 2D graphene superlattice.

s and s' are either $+1$ or -1 depending on whether the energy of the state is above or below the energy at the Dirac point, respectively. We have also carried out a tight-binding formulation and obtained identical results as those discussed below.

9.3 Results and discussion

9.3.1 Velocity renormalization

First, for a one-dimensional (1D) graphene superlattice (Fig. 9.1b), we find that the group velocity for states with wavevector $\mathbf{k}$ is anisotropically renormalized, i.e., it is a strong function of the direction of $\mathbf{k}$. For pristine graphene, the group velocity of states near the Dirac point is parallel to $\mathbf{k}$ and of constant magnitude (v_0). For example, in a 1D superlattice of Kronig-Penny type of periodic potential with potential barrier height (U_{1D}) of 0.5 eV and spatial period (L) and barrier width (w) of 10 nm and 5 nm, respectively, the group velocity of the charge carriers when $\mathbf{k}$ is along certain direction is renormalized to be slower than 40 % of its original value v_0 but is the same as v_0 along some other direction. [Fig. 9.2a: the plotted quantity $v_{\hat{k}} \equiv \mathbf{v}(\mathbf{k}) \cdot \hat{k}$ is the component of the group velocity parallel to the wavevector $\mathbf{k}$ in units of v_0. We note that this quantity which depends only on the direction of $\mathbf{k}$ (Supplementary Discussion 2) is exactly equal to the absolute value of the group velocity v_g when $\mathbf{k}$ is at 0, 90, 180 or 270 degrees from the periodic direction of the applied potential and, when the applied potential is weak, is only slightly different from v_g at other angles (Supplementary Discussion 3).] Thus, the group velocity of charge carriers can be tailored highly anisotropically in graphene superlattices. More interestingly, the group velocity when $\mathbf{k}$ is along the direction perpendicular to the periodic direction of the potential ($v_\perp$) is reduced the most, whereas when $\mathbf{k}$ is in the parallel direction, it is not renormalized at all (Fig. 9.1b). This result is counter-intuitive since the velocity is strongly reduced when the charge carrier is moving parallel to the hurdles, but is not modulated when it is crossing them.

To understand the physics behind this phenomenon, we have performed the same calculation for a fictitious system with carriers that have no chirality but otherwise identical to those in graphene including the linear energy dispersion. The group velocity in this system is reduced isotropically and the renormalized group velocity is close to $v_\perp$, i.e., the maximally renormalized one, in 1D graphene superlattices (Fig. 9.2a). Thus, it is clear that the absence of velocity renormalization in the direction parallel to the periodicity of the external potential originates from the chiral nature of the electronic states of graphene. This behavior can be demonstrated more clearly by second order perturbation theory in the case of the 1D periodic potential with weak amplitudes (Supplementary Discussion 2). We note that the chirality discussed here is also important in tunneling phenomenon in graphene through a single barrier [80] or a finite number of barriers [202].

In the case of two-dimensional (2D) graphene superlattices, the group velocity is renormalized for $\mathbf{k}$ states along every direction, but anisotropically (Fig. 9.1c). As the amplitude of the potential increases the overall group velocity is reduced and the ratio of the maximum

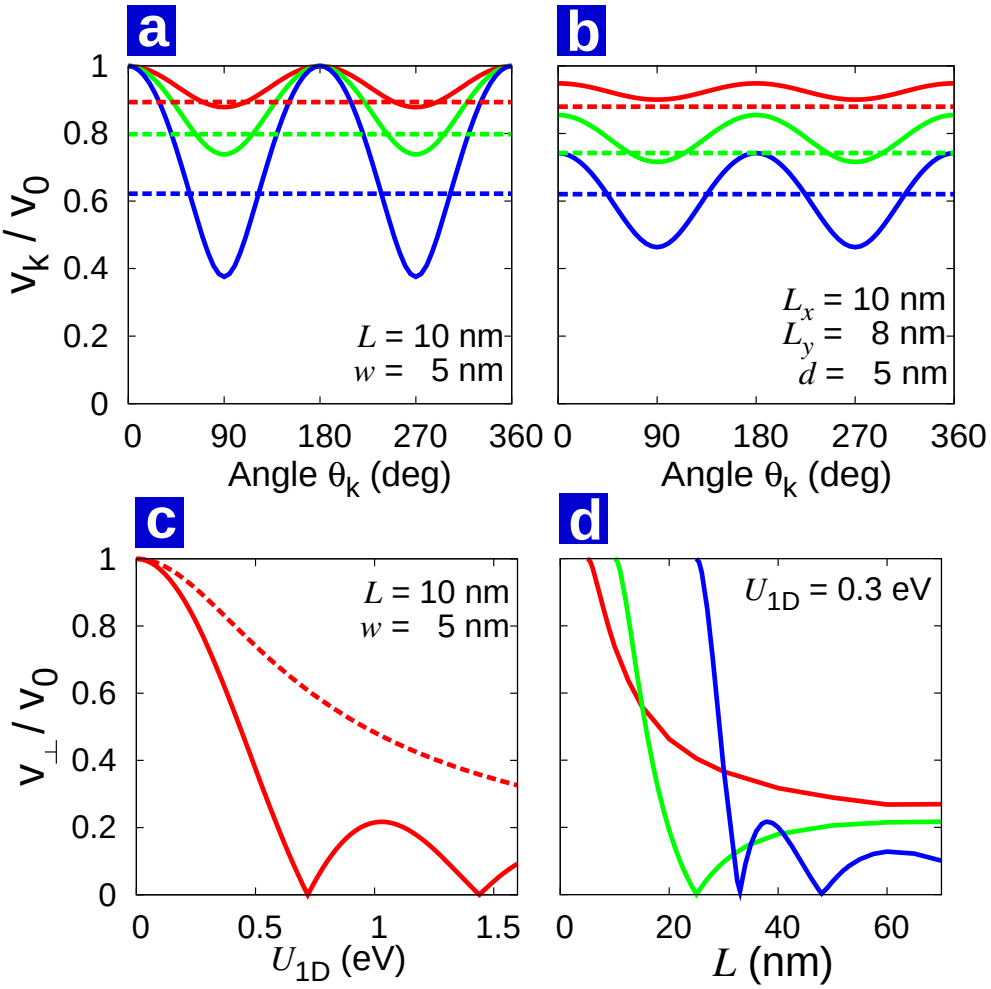

Figure 9.2: Anisotropic velocity renormalization in graphene superlattices. (a) The component of the group velocity parallel to the $\mathbf{k}$ vector [$v_{\hat{k}} \equiv \mathbf{v}(\mathbf{k}) \cdot \hat{k}$ with $\mathbf{k}$ measured from the Dirac point] of charge carriers in a 1D graphene superlattice in units of the Fermi velocity in graphene (v_0) versus the angle ($\theta_\mathbf{k}$) of the $\mathbf{k}$-vector from the periodic potential direction $\hat{x}$ (solid lines) and that in a superlattice made from a fictitious system of nonchiral fermions with properties otherwise identical to those in graphene (dashed lines). Red, green and blue lines correspond to U_{1D} being 0.2 eV, 0.3 eV and 0.5 eV, respectively. (b) Similar quantities as in (a) for a rectangular 2D graphene superlattice. Red, green and blue lines correspond to U_{2D} being 0.3 eV, 0.5 eV and 0.7 eV, respectively. (c) The group velocity of charge carriers in a 1D graphene superlattice (solid line) with $\mathbf{k}$ perpendicular to the periodic direction, $v_\perp$, in units of v_0 versus U_{1D} (solid line) and that in a superlattice made from a fictitious system of nonchiral fermions with properties otherwise identical to those in graphene (dashed line). (d) $v_\perp$ versus the potential spatial period (L) of charge carriers in a 1D graphene superlattice. Red, green and blue lines correspond to a fixed potential barrier height but with width (w) being 5 nm, 10 nm and 25 nm, respectively.

group velocity to the minimum one is enhanced (Fig. 9.2b). Here, again, the anisotropy disappears if the chiral nature of the states in graphene is arbitrarily removed. As was demonstrated for the 1D superlattice, the sinusoidal dependence on the angle of propagation as well as the overall shift in the case of 2D graphene superlattice of the component of the renormalized group velocity parallel to $\mathbf{k}$ in the weak potential limit is well explained and reproduced by second order perturbation theory (Supplementary Discussion 2).

Remarkably, the anisotropy in energy dispersions of the 1D superlattices can be tuned by changing the applied potential in such a way that $v_\perp$ is reduced completely to zero (Fig. 9.2c). Hence, we can achieve extremely low mobility in one direction and normal conduction in another one simultaneously. This enables one to control the flow of electrons dramatically. It also provides a novel non-destructive pathway to make graphene nanoribbons [183, 184, 185, 186] which have been actively pursued by way of cutting graphene sheets [185, 186]. The chiral nature of the states in graphene also plays a decisive role here. In the model without chirality as discussed before the (isotropic) group velocity of charge carriers is reduced monotonically and never reaches zero within a conceivable range of the potential amplitude (Fig. 9.2c). We can also achieve vanishing group velocity in one direction by changing the length parameters of the superlattice (Fig. 9.2d).

9.3.2 Gap opening at the mini Brillouin zone boundary

Graphene superlattices show peculiar behavior of gap openings at the MB formed by the external periodic potential (Fig. 9.3). In conventional layer-structured 1D superlattices, gap opening at the MBs is considered to be nearly constant, independent of $\mathbf{k}$. 1D graphene superlattices, however, are different in that the gap (ΔE) vanishes when $\mathbf{k}$ is along the direction of the periodic potential, i.e., at the centre of the MB (Fig. 9.3a and 4a). Moreover, the size of the gap depends strongly on where it is on the MB (Fig. 9.3b). These strong anisotropies in the gap opening do not happen in superlattices made from a system having linear energy dispersions but no chirality (Fig. 9.3b). Hence, again, the chiral nature of charge carriers in graphene is key in generating these anisotropies in the gap opening as it does in the velocity renormalization. In particular, the gap closure at the centre of the MB is directly related to the absence of back-scattering of charge carriers from a scattering potential when the size of the scatterer is several times larger than the inter-carbon distance [78, 200, 79]. In 1D graphene superlattices, the important length-scale is L, which is much larger than the inter-carbon distance, and hence the gap does not open at the centre of the MB.

The largest gap at the MB in a graphene superlattice is proportional to the amplitude of the applied potential if the potential is weak (i.e., small compared to the band width) and the size of which thus can be made to be a few tenths of an electron volt with appropriate perturbation and much larger than room temperature (Fig. 9.3b, Supplementary Discussion 5). We have also investigated the gap opening in 1D graphene superlattices with different values of length parameters (L and w). We find that, by changing these parameters, the anisotropy in the gap at the MB can also be controlled (Supplementary Discussion 5).

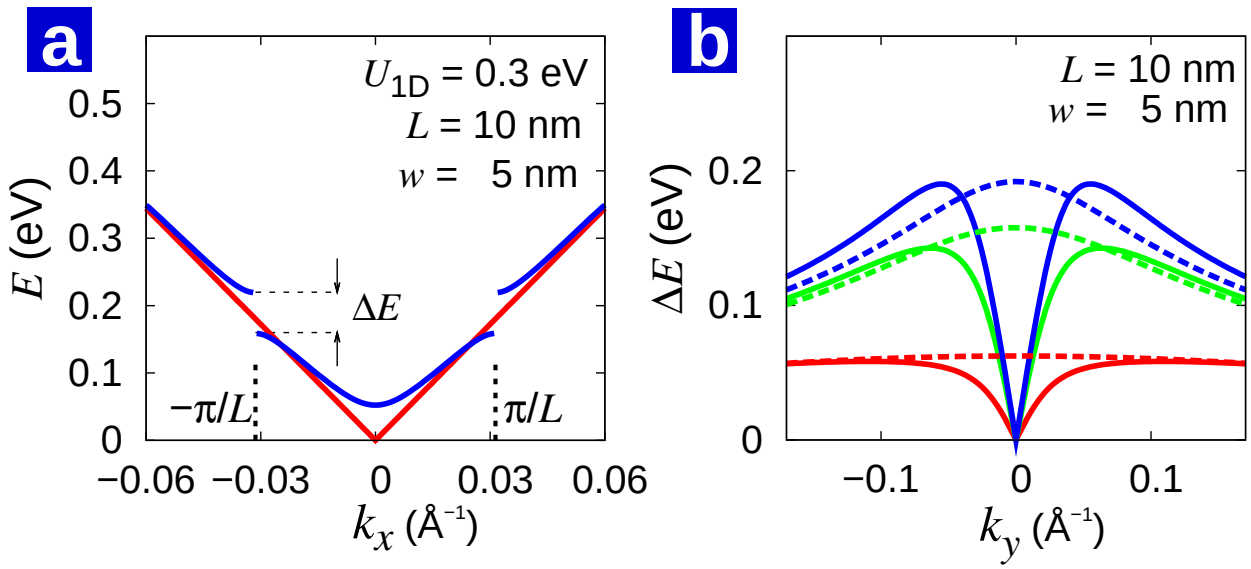

Figure 9.3: Energy gap at the superlattice Brillouin zone or minizone boundary of a 1D graphene superlattice. (a) Energy of charge carriers in 1D graphene superlattice versus the component of the wavevector **k** parallel to the periodic potential direction (k_x) at a fixed k_y. Dashed vertical lines indicate minizone boundaries ($k_x = \pm\pi/L$). ΔE is the energy gap at the minizone boundary for a given k_y. Red and blue lines correspond to k_y being zero and 0.012 Å^{-1}, respectively. (b) ΔE versus k_y for charge carriers in 1D graphene superlattice (solid lines) and that in a superlattice made from a fictitious system with states without chirality but otherwise identical to graphene (dashed lines). Red, green and blue lines correspond to U_{1D} being 0.1 eV, 0.3 eV and 0.5 eV, respectively.

9.3.3 Charge carriers in graphene superlattices

Due to the velocity renormalization near the Dirac point and the strong anisotropy in energy dispersion close to the MB, the type and the density of states (DOS) of charge carriers vary drastically from those in graphene as one varies the Fermi energy (Fig. 9.4). As the Fermi level changes, the topology of the Fermi surface also exhibits a dramatic variation (Supplementary Discussion 6). For example, as the Fermi level increases from the energy at the Dirac point, the charge carriers of a 1D graphene superlattice fill electron orbits and show a linear increase in the DOS with slope larger than that of graphene; but above certain value, the DOS of electron orbits vanishes and charge carriers suddenly fill open orbits and hole pockets. When the Fermi level increases further, charge carriers are in purely open orbits and then the DOS of electron orbits starts to reappear and increases again (Fig. 9.4b). We expect that the Fermi level in a graphene superlattice can be tuned as in graphene by applying a gate voltage [35, 36, 195, 196]. Hence, by exploiting the various characteristics of charge carriers and the Fermi surface topology, one can manipulate a variety of physical properties dominated by the Fermi surface, such as conductance or magnetoresistance, significantly.

The anisotropic gap opening at the MB and the dramatic variation of the characters of charge carriers with the Fermi energy are also common in 2D graphene superlattices. The gap at the centres of the zone boundaries closes as in 1D graphene superlattice (Fig. 9.4c). However, the gap at the corners of the 2D MB also disappears. This behavior, which occurs in rectangular 2D graphene superlattices in general, has again its origin in the chiral nature of charge carriers in graphene (Supplementary Discussion 4). In a square 2D graphene superlattice, charge carriers are electrons, holes or a mixture of the two depending on the Fermi level (Fig. 9.4d). For general rectangular 2D graphene superlattices, charge carriers can also be in open orbits.

9.4 Conclusion

Here we have presented several novel physical properties of graphene superlattices with Kronig-Penney type 1D and muffin-tin type 2D potentials. Through additional calculations, we have confirmed that all the salient features of our findings are the same in sinusoidal or Gaussian types of graphene superlattices in general as well. The novel properties discovered in the present study thus should be of interest to the fundamental study and practical applications of graphene systems in general.

Finally, since the massless Dirac fermions in graphene superlattices have some features in common with high-energy relativistic particles propagating in anisotropic space (like the anisotropy in the group velocity [203]), interesting physics of the latter may also be investigated by table-top experiments based on our theoretical findings.

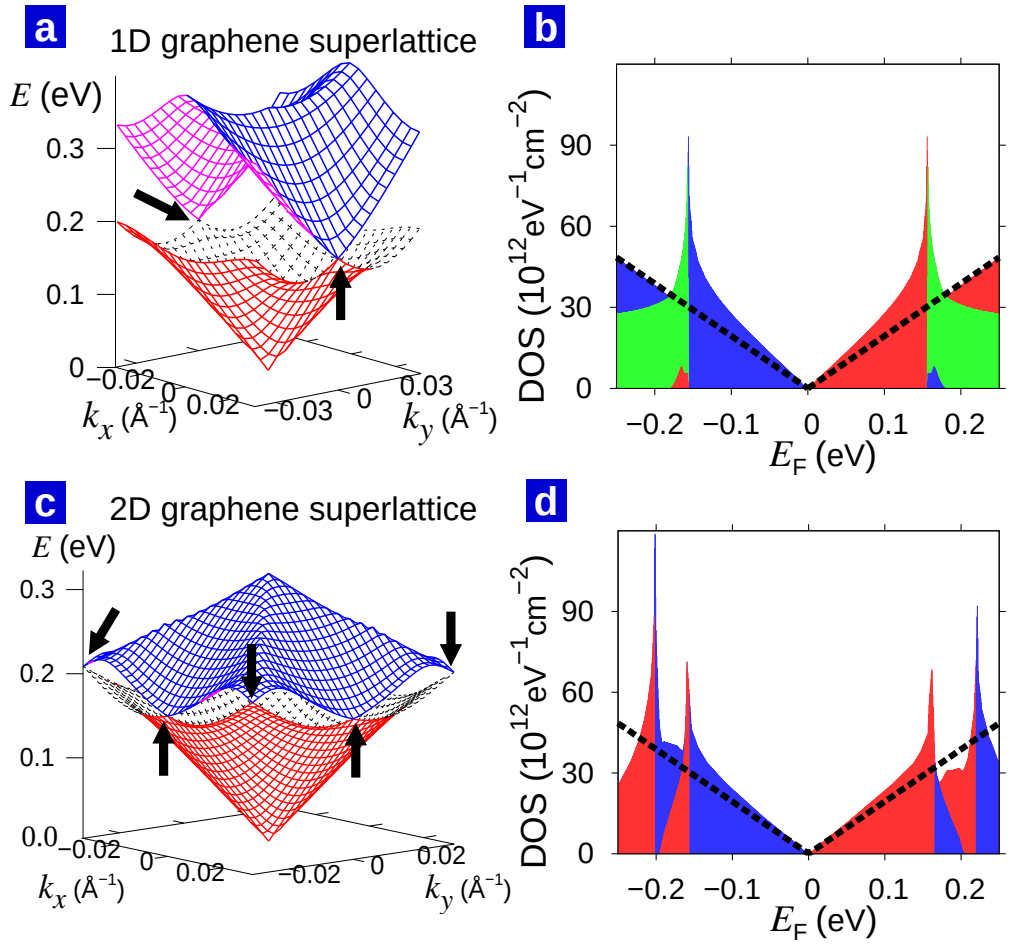

Figure 9.4: Energy dispersions and densities of states of charge carriers in graphene superlattices. (a) Energy of charge carriers in 1D graphene superlattice with $U_{1D} = 0.3$ eV, $L = 10$ nm and $w = 5$ nm in the first (red and black) and the second (blue and pink) band above the vertex of the Dirac cone versus 2D wavevector $\mathbf{k}$ away from the Dirac point. Minizone boundaries are at $k_x = \pm 0.031$ Å^{-1}. Arrows indicate points on the minizone boundary where the gap closes. (b) Density of states (DOS) of charge carriers in electron orbits (red), open orbits (green) and hole orbits (blue) in the 1D graphene superlattice characterized in (a) versus the Fermi energy (E_F). The origin of the energy scale is set at the energy of the Dirac point. The DOS of each species is the height of the corresponding colored region. Dashed black line shows the DOS of pristine graphene for comparison. (c) Similar quantities as in (a) for a 2D graphene superlattice with $U_{2D} = 0.3$ eV, $L_x = L_y = 10$ nm and $d = 5$ nm. (d) Similar quantities as in (b) for the 2D graphene superlattice specified in (c).

9.5 Supplementary discussion

9.5.1 Effective-Hamiltonian formalism

There are two carbon atoms per unit cell in graphene, forming two different sublattices, and hence the eigenstate of charge carriers in graphene can be represented by a two component basis vector. The Brillouin zone of graphene is a hexagon which has two inequivalent vertices, so-called the Dirac points, $\mathbf{K}$ and $\mathbf{K}'$, that cannot be connected by reciprocal lattice vectors. In this work, we are considering eigenstates near $\mathbf{K}$ only as discussed in the paper. The effective Hamiltonian for low-energy quasiparticles of graphene in this basis is given by

$$H_0(\mathbf{k}) = \hbar v_0 \begin{pmatrix} 0 & -ik_x - k_y \\ ik_x - k_y & 0 \end{pmatrix} , \tag{9.1}$$

where v_0 is the Fermi velocity and $\mathbf{k}$ the small wavevector of the quasiparticle from the $\mathbf{K}$ point in the Brillouin zone of graphene. The energy spectrum of this Hamiltonian is $E = s\hbar v_0 k$ where s is $+1$ or -1 for an eigenstate above or below the Dirac point energy which is defined to be the energy zero, respectively. Eigenstates of this Hamiltonian is given by

$$\langle \mathbf{r}|s, \mathbf{k}\rangle = \frac{1}{\sqrt{2}} e^{i(\mathbf{K}+\mathbf{k})\cdot\mathbf{r}} \begin{pmatrix} 1 \\ ise^{i\theta_{\mathbf{k}}} \end{pmatrix} , \tag{9.2}$$

where $\theta_{\mathbf{k}}$ is the angle of vector $\mathbf{k}$ with respect to the $\hat{k}_x$ direction. Now, when an additional periodic potential $U(\mathbf{r})$ is applied to graphene, the scattering amplitude between states are given by

$$\langle s, \mathbf{k}\,|U(\mathbf{r})|\,s', \mathbf{k}'\rangle = \sum_{\mathbf{G}} \frac{1}{2}\left(1 + ss'e^{-i\theta_{\mathbf{k},\mathbf{k}-\mathbf{G}}}\right) U(\mathbf{G})\ \delta_{\mathbf{k}',\mathbf{k}-\mathbf{G}} , \tag{9.3}$$

where $\mathbf{G}$ and $U(\mathbf{G})$ are the reciprocal lattice vector and the corresponding Fourier component of the external periodic potential, respectively, and $\theta_{\mathbf{k},\mathbf{k}-\mathbf{G}}$ the angle from $\mathbf{k}-\mathbf{G}$ to $\mathbf{k}$. The energy dispersions and eigenstates of the quasiparticles in a graphene superlattice are obtained non-perturbatively within the single-particle picture by solving the following set of linear equations:

$$(E - \varepsilon_{s,k})\ c(s, \mathbf{k}) = \sum_{s',\mathbf{G}} \frac{1}{2}\left(1 + ss'e^{-i\theta_{\mathbf{k},\mathbf{k}-\mathbf{G}}}\right) U(\mathbf{G})\ c(s', \mathbf{k}-\mathbf{G}) , \tag{9.4}$$

where E is the superlattice energy eigenvalue and $\varepsilon_{s,\mathbf{k}} = s\hbar v_0 k$ the energy of the quasiparticles before applying the periodic potential. $c(s, \mathbf{k})$ and $c(s', \mathbf{k}-\mathbf{G})$ are the amplitudes of mixing among different unperturbed quasiparticle states.

9.5.2 Velocity renormalization near the Dirac point from second order perturbation theory

When the external potential is weak, perturbative calculations can give results in good agreement with the full calculation and also in physically more intuitive forms. For pristine

graphene, the group velocity of states near the Dirac point is parallel to $\mathbf{k}$ and of constant magnitude (v_0). For a graphene superlattice, the renormalization in the component of the group velocity of quasiparticles parallel to the wavevector $\mathbf{k}$ [$v_{\hat{k}} \equiv \mathbf{v}(\mathbf{k}) \cdot \hat{k}$] around the Dirac point can be obtained within second order perturbation approximation as

$$\frac{v_{\hat{k}} - v_0}{v_0} = -\sum_{\mathbf{G}\neq\mathbf{0}} \frac{2|U(\mathbf{G})|^2}{v_0^2|\mathbf{G}|^2} \sin^2 \theta_{\mathbf{k},\mathbf{G}} \ , \tag{9.5}$$

where $\theta_{\mathbf{k},\mathbf{G}}$ is the angle from $\mathbf{G}$ to $\mathbf{k}$. From Eq. (9.5), it is clear that for weak potentials, the velocity renormalization grows as square of the amplitude of the external potential and $v_{\hat{k}}$ depends only on the direction of $\mathbf{k}$. Throughout this document, by weak potential we mean that the condition,

$$\frac{|U(\mathbf{G})|}{v_0|\mathbf{G}|} \ll 1 \ , \tag{9.6}$$

is satisfied for all the $U(\mathbf{G})$ components. In the absence of chirality of the states, the scattering matrix element [Eq. (9.3)] should be changed into

$$\langle s, \mathbf{k} \left| U(\mathbf{r}) \right| s', \mathbf{k}' \rangle = \sum_{\mathbf{G}} U(\mathbf{G}) \ \delta_{\mathbf{k}',\mathbf{k}-\mathbf{G}} \ . \tag{9.7}$$

Using Eq. (9.7), the similar quantity as in Eq. (9.5) for nonchiral massless Dirac fermions is now given by

$$\left(\frac{v_{\hat{k}} - v_0}{v_0}\right)_{\text{non}-\text{chiral}} = -\sum_{\mathbf{G}\neq\mathbf{0}} \frac{2|U(\mathbf{G})|^2}{v_0^2|\mathbf{G}|^2} \ , \tag{9.8}$$

which is isotropic independent of the direction of $\mathbf{k}$. Comparing Eq. (9.5) and Eq. (9.8), the renormalization of group velocity in a one-dimensional (1D) superlattice for a fictitious graphene with states without chirality corresponds to the maximum renormalization in the corresponding 1D graphene superlattice. This trend agrees with the results from the full calculation when the potential is weak (Fig. 9.2).

If Eq. (9.5) is applied to the Kronig-Penney type of 1D graphene superlattice periodic along the $\hat{x}$ direction as discussed in the paper (Fig. 9.1b),

$$\frac{v_{\hat{k}} - v_0}{v_0} = -\left\{\frac{U_{1\text{D}}^2 L^2}{\pi^4 v_0^2} \sum_{n>0} \frac{1}{n^4} \sin^2 \left(\frac{\pi w}{L} n\right)\right\} \sin^2 \theta_{\mathbf{k},\hat{x}} \ , \tag{9.9}$$

where L is the spatial period of the potential, and $U_{1\text{D}}$ and w are the height and the width of the rectangular potential barrier, respectively. Equation (9.9) is in good agreement with the full calculation when the potential is weak (Fig. 9.5) and also shows sinusoidal behavior with respect to the polar angle of $\mathbf{k}$ with respect to the periodic direction of the potential as well as the absence of renormalization for a particle moving across the potential barriers.

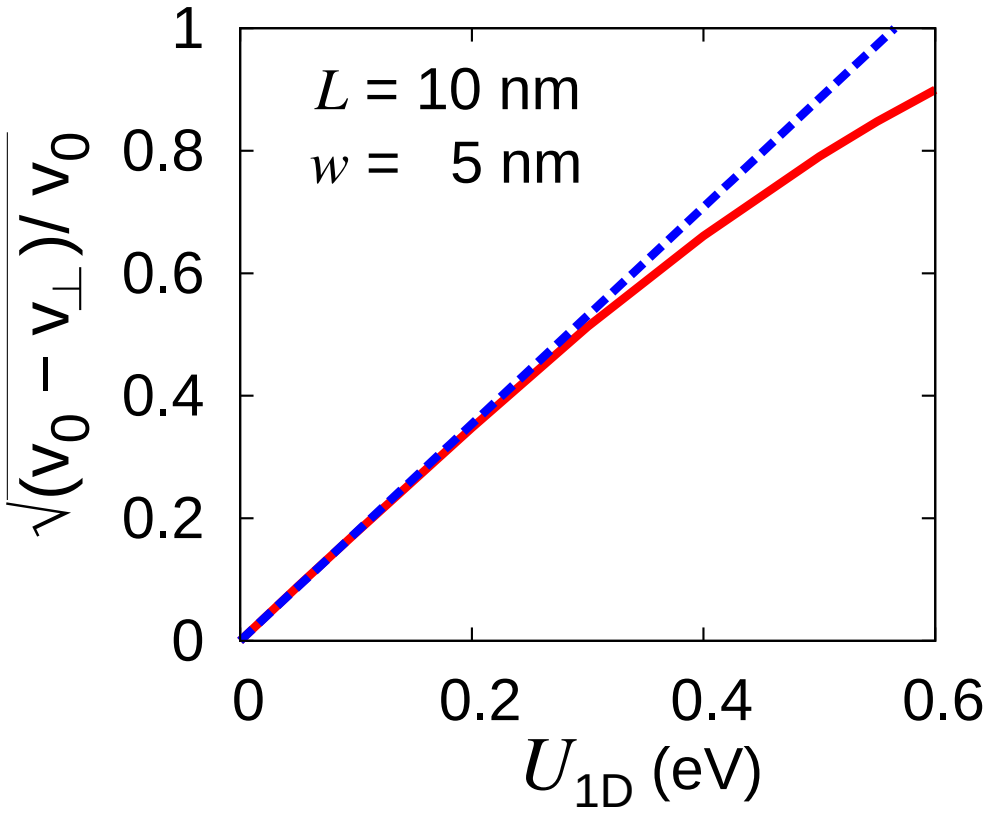

Figure 9.5: Dependence of the velocity renormalization on the amplitude of periodic potential in a 1D graphene superlattice. Square root of the difference between the group velocity for state with **k** along the direction perpendicular to the periodic direction of the potential ($v_\perp$) and the unrenormalized one (v_0) divided by v_0 versus the potential amplitude U_{1D}. Solid red line and dashed blue line are results of the full calculation and second order perturbation theory, respectively.

For the case of muffin-tin type of two-dimensional (2D) graphene superlattice (Fig. 9.1c) periodic along both $\hat{x}$ and $\hat{y}$ directions, with periods L_x and L_y, respectively,

$$\frac{v_{\hat{k}} - v_0}{v_0} = -\frac{2\pi^2 U_{2\mathrm{D}}^2\, d^2}{v_0^2 L_x^2 L_y^2} \sum_{\mathbf{G}\neq\mathbf{0}} \frac{1}{G^4}\; J_1^2\left(\frac{Gd}{2}\right) \sin^2\,\theta_{\mathbf{k},\mathbf{G}}\;, \tag{9.10}$$

where $U_{2\mathrm{D}}$ is the height of the circular potential barrier with diameter d and $\mathbf{G} = \left(\frac{2\pi}{L_x}m, \frac{2\pi}{L_y}n\right)$ the reciprocal lattice vector with integers m and n and $J_1(x)$ is the first order Bessel function of the first kind. When $L_x \approx L_y$ (as in Fig. 9.2b), the dominant contribution in the sum comes from the terms with $|m| = 1, n = 0$ and $m = 0, |n| = 1$. Counting only these four terms,

$$\begin{aligned}
\frac{v_{\hat{k}} - v_0}{v_0} &\approx -\frac{U_{2\mathrm{D}}^2\, d^2}{4\pi^2 v_0^2}\left\{\left(\frac{L_x}{L_y}\right)^2\; J_1^2\left(\frac{\pi d}{L_x}\right)\sin^2\,\theta_{\mathbf{k},\hat{x}} + \left(\frac{L_y}{L_x}\right)^2\; J_1^2\left(\frac{\pi d}{L_y}\right)\sin^2\,\theta_{\mathbf{k},\hat{y}}\right\} \\
&= -\frac{U_{2\mathrm{D}}^2\, d^2}{4\pi^2 v_0^2}\left\{\left[\left(\frac{L_x}{L_y}\right)^2\; J_1^2\left(\frac{\pi d}{L_x}\right) - \left(\frac{L_y}{L_x}\right)^2\; J_1^2\left(\frac{\pi d}{L_y}\right)\right]\sin^2\,\theta_{\mathbf{k},\hat{x}}\right. \\
&\qquad \left. + \left(\frac{L_y}{L_x}\right)^2\; J_1^2\left(\frac{\pi d}{L_y}\right)\right\}
\end{aligned} \tag{9.11}$$

where the relation $\sin^2\,\theta_{\mathbf{k},\hat{y}} = 1 - \sin^2\,\theta_{\mathbf{k},\hat{x}}$ has been used in the second line. Now the group velocity $v_{\hat{k}}$ is renormalized in every direction. Equation (9.11) reproduces the sinusoidal variation of the velocity renormalization as well as the constant shift as obtained in the full calculation quite well when the potential is weak (Fig. 9.2b).

9.5.3 The magnitude and the component parallel to the wavevector k of the group velocity

The component of the group velocity $v_{\hat{k}}$ parallel to the wavevector $\mathbf{k}$ above is exactly equal to the absolute value of the group velocity v_g when $\mathbf{k}$ is at 0, 90, 180 or 270 degrees from the periodic direction of the applied potential and, when the applied potential is weak, is only slightly different from v_g at other angles (Fig. 9.6).

9.5.4 Band gap at the minizone boundary from degenerate perturbation theory

When the wavevector $\mathbf{k}$ is on the minizone boundary (MB) of the 1D graphene superlattice, $k_x = \pm\pi/L$, two states $|s, \mathbf{k}\rangle$ and $|s, \mathbf{k} - (2\pi/L, 0)\rangle$ are degenerate before applying the periodic potential. The largest contribution to the energy eigenvalues at the MB comes from these two degenerate states. Scattering amplitude between these two states is given by Eq. (9.3). By choosing the origin at the centre of a potential barrier, we can make all

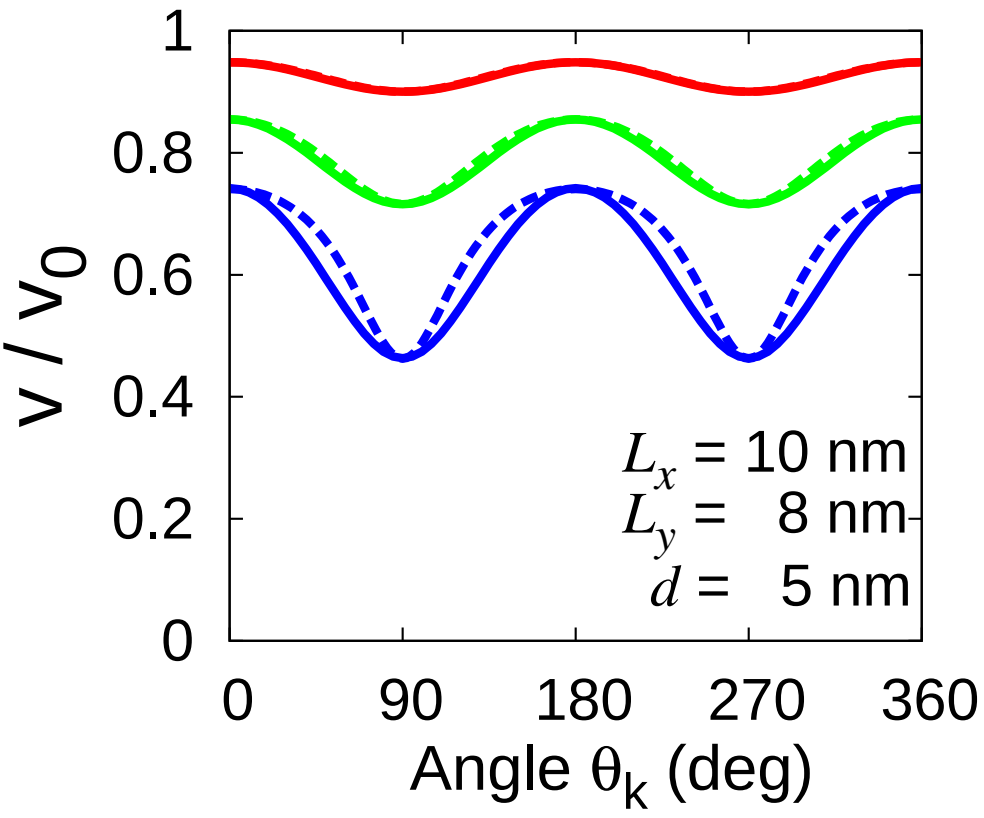

Figure 9.6: The magnitude and the component parallel to the wavevector $\mathbf{k}$ of the renormalized group velocity in a 2D graphene superlattice. The component of the group velocity parallel to the $\mathbf{k}$ vector [$v_{\hat{k}} \equiv \mathbf{v}(\mathbf{k}) \cdot \hat{k}$ with $\mathbf{k}$ measured from the Dirac point] of charge carriers in a 2D graphene superlattice (solid lines) and the absolute value of the group velocity (dashed lines) in units of the Fermi velocity in graphene (v_0) versus the angle ($\theta_{\mathbf{k}}$) of the $\mathbf{k}$-vector from the periodic potential direction $\hat{x}$. Red, green and blue lines correspond to the potential amplitude U_{2D} being 0.3 eV, 0.5 eV and 0.7 eV, respectively. Plotted quantities are obtained from the full calculation by solving Eq. (9.4).

the Fourier components of the periodic potential real without losing generality. Now the Hamiltonian for the two-state system is

$$H(\mathbf{k}) = \begin{pmatrix} \varepsilon_{s,\mathbf{k}} & \frac{1}{2}\left(1+e^{-i\theta_{\mathbf{k},\mathbf{k}-(2\pi/L,0)}}\right)\ U\left(2\pi/L\right) \\ \frac{1}{2}\left(1+e^{i\theta_{\mathbf{k},\mathbf{k}-(2\pi/L,0)}}\right)\ U\left(2\pi/L\right) & \varepsilon_{s,\mathbf{k}-(2\pi/L,0)} \end{pmatrix} , \tag{9.12}$$

where $\varepsilon_{s,\mathbf{k}} = \varepsilon_{s,\mathbf{k}-(2\pi/L,0)} = s\hbar v_0 k$ is the energy of the charge carrier before the external potential is applied and $U\left(2\pi/L\right)$ the Fourier component of the periodic potential whose wavevector connects the two MBs at $k_x = \pm\pi/L$. The energy separate of the eigenvalues of Eq. (9.12) (i.e., the energy gap) is given by

$$\Delta E = 2\ \left|U(2\pi/L)\ \sin\ \theta_{\mathbf{k},\hat{x}}\right|\ , \tag{9.13}$$

where $\theta_{\mathbf{k},\hat{x}}$ is the polar angle between $\mathbf{k}$ and $\hat{x}$. Equation (9.13) clearly shows that the gap opening depends on $\mathbf{k}$ and, in particular, is zero at the centre of the MB (Fig. 9.2), and that, as discussed in the paper, the maximum gap opening is proportional to the amplitude of the external potential in the weak potential regime.

If the chirality of the states in graphene is manually removed by using Eq. (9.7) for the scattering matrix element, the energy gap becomes

$$\Delta E_{\mathrm{non-chiral}} = 2\ \left|U(2\pi/L)\right|\ , \tag{9.14}$$

in which case the gap neither closes at the centre of the MB nor depends sensitively on the position along the MB in the weak potential limit (Fig. 9.2).

For a 2D rectangular graphene superlattice, in which the primitive translational lattice vectors are orthogonal, for the same reason as in the 1D case, the gap closes at the centres of MBs, i.e., when $\mathbf{k}$ is at $(\pm\pi/L_x, 0)$ or $(0, \pm\pi/L_y)$. The more interesting case is the corner of the minizone, where the four degenerate states $|s, (\pi/L_x, \pi/L_y)\rangle$, $|s, (-\pi/L_x, \pi/L_y)\rangle$, $|s, (\pi/L_x, -\pi/L_y)\rangle$ and $|s, (-\pi/L_x, -\pi/L_y)\rangle$ mix strongly among themselves by the applied periodic potential. If we set up a similar matrix for this case like Eq. (9.12) for the 1D graphene superlattice, the energy eigenvalues of the matrix are

$$E = \varepsilon_{s,\mathbf{k}} \pm \sqrt{\left|\left[U(2\pi/L_x, 0)\ \sin\ \theta_{\mathbf{k},\hat{x}}\right]^2 - \left[U(0, 2\pi/L_y)\cos\ \theta_{\mathbf{k},\hat{x}}\right]^2\right|}\ , \tag{9.15}$$

where $\mathbf{k} = (\pi/L_x, \pi/L_y)$ is at the minizone corner and each eigenvalue is doubly degenerate. The energy spectrum given by Eq. (9.15) clearly shows that there is no gap at the minizone corner between the first and the second band (Fig. 9.4c). This gap closure at the minizone corner is not obvious because a transition, which is not of a backscattering process, from one of the four $\mathbf{k}$ points at the zone corners to another can occur in the 2D rectangular graphene superlattice. For example, the state $|s, (\pi/L_x, \pi/L_y)\rangle$ can mix with another state $|s, (-\pi/L_x, \pi/L_y)\rangle$ by the reciprocal lattice vector $\mathbf{G} = (2\pi/L_x, 0)$ but the two $\mathbf{k}$ vectors are not anti-parallel. To understand the origin of the gap closure at the minizone corner,

we repeated a similar calculation for a 2D rectangular superlattice formed of a non-chiral system with linear energy dispersions. In this case, the energy eigenvalues are

$$\begin{aligned} E_{\text{non-chiral}} &= \varepsilon_{s,\mathbf{k}} + U(2\pi/L_x, 2\pi/L_y) \pm [U(2\pi/L_x, 0) - U(0, 2\pi/L_y)] \ , \\ &\quad \varepsilon_{s,\mathbf{k}} - U(2\pi/L_x, 2\pi/L_y) \pm [U(2\pi/L_x, 0) + U(0, 2\pi/L_y)] \ . \end{aligned} \tag{9.16}$$

According to Eq. (9.16), there is a finite energy gap between the first and the second band in general, other than in accidentally symmetric cases. Therefore, the gap closure at the minizone corner of a 2D rectangular graphene superlattice is a direct consequence of the chiral nature of the states in graphene.

9.5.5 Dependence of the band gap at the minizone boundary on length parameters and broken particle-hole symmetry

For a Kronig-Penney type rectangular potential barrier 1D graphene superlattice, the energy gap at the MB can be expressed with Eq. (9.13) in terms of superlattice parameters as

$$\Delta E = \frac{2}{\pi} \left| U_{1\text{D}} \sin\left(\frac{\pi w}{L}\right) \sin\theta_{\mathbf{k},\hat{x}} \right| \ . \tag{9.17}$$

Thus, according to this simple degenerate perturbation theory result if the spatial period (L) becomes long for a constant barrier width (w) the gap should decrease, whereas if L is fixed and w is increased from zero, the gap should reach a maximum at $w = L/2$ and after that should decrease symmetrically. The former trend is observed in the full calculation (Fig. 9.7a); however, the latter seems not to hold in the full calculation (Fig. 9.7b). Moreover, the gap openings at the MB above and below the Dirac cone are different (Fig. 9.7), which shows the limitation of the simple degenerate perturbation theory because the potential is not so weak and possesses higher Fourier components. One thing to note is that the energy dispersion for states above the energy of the Dirac point, including the gap opening, for a 1D Kronig-Penney type superlattice with width $w = w_0$ is identical with that of states below the energy of the Dirac point for width $w = L - w_0$ (Fig. 9.7b, compare red and blue lines). This symmetry can be understood following a simple argument. If we start from a 1D Kronig-Penney superlattice with $w = w_0$ and then change w to be $w = L - w_0$ and at the same time invert the whole potential, the resulting periodic potential is identical to the original one other than a constant shift which may be ignored. Inverting the potential is effectively the same as exchanging particles with holes.

9.5.6 Fermi surfaces

In 1D and 2D graphene superlattices, the topology as well as the shape of the Fermi surface varies significantly with the Fermi energy (Figs. 9.8 and 9.9). This variation gives rise to a dramatic variation in the species and the density of states of charge carriers as a function of the position of the Fermi level (Fig. 9.4).

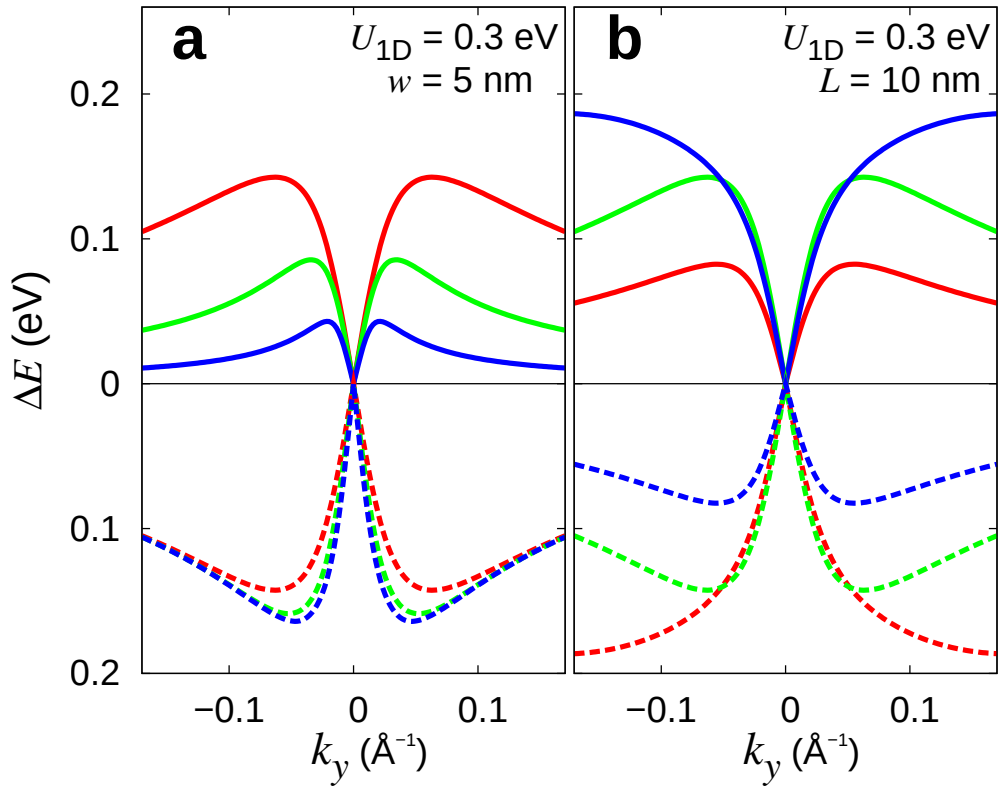

Figure 9.7: Dependence of the energy gap at the minizone boundary on the length parameters of 1D graphene superlattice. (a) The energy gap ΔE between the first and the second band at the minizone boundary versus k_y for charge carriers above (solid lines) and below (dashed lines) the energy at the Dirac point in a 1D graphene superlattice. Red, green and blue lines correspond to the spatial period (L) being 10 nm, 15 nm and 25 nm, respectively. (b) Similar quantities as in (a). Red, green and blue lines correspond to the potential barrier width (w) being 2.5 nm, 5 nm and 7.5 nm, respectively.

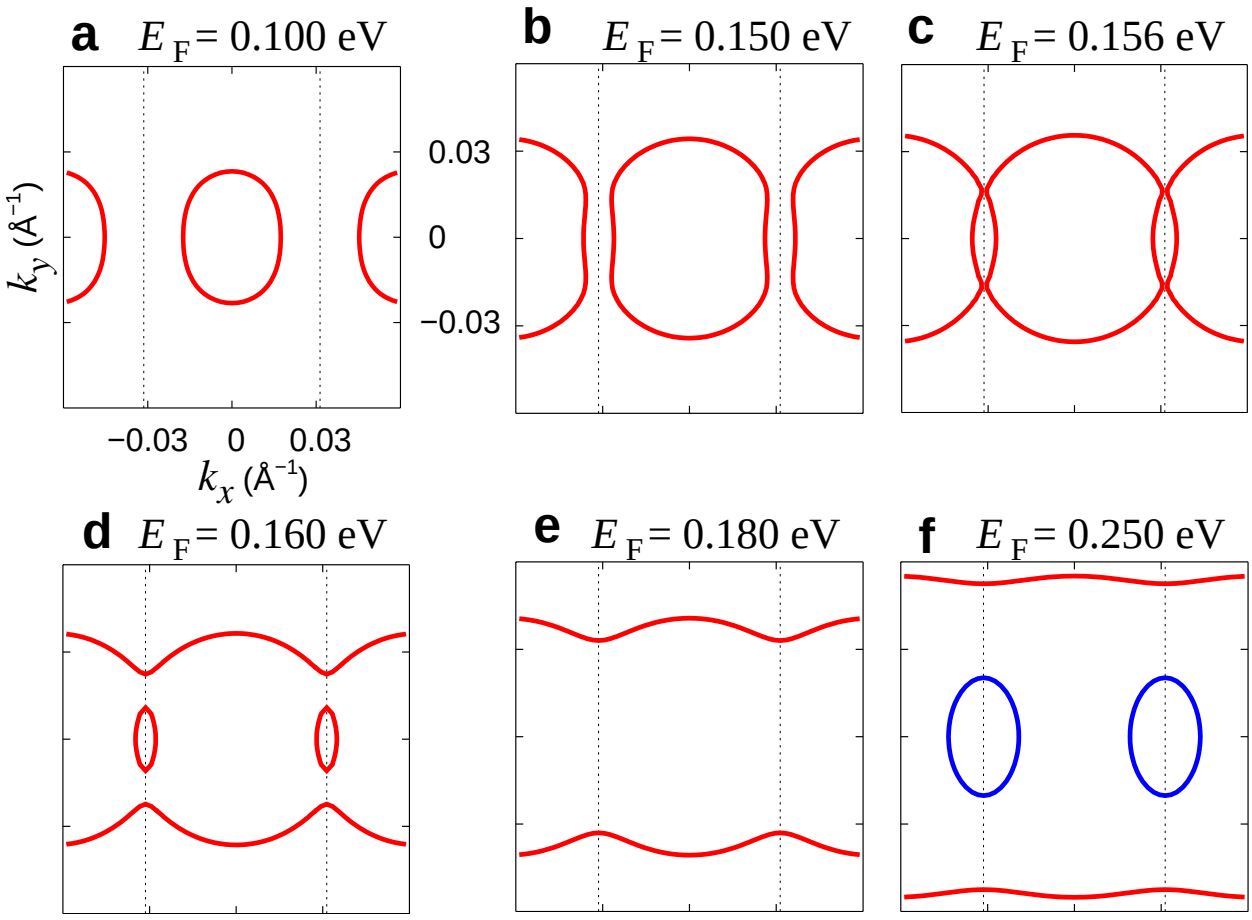

Figure 9.8: Fermi surfaces of a 1D graphene superlattice. (a)-(f) Fermi surfaces of 1D graphene superlattice with $U_{1D} = 0.3$ eV, $L = 10$ nm and $w = 5$ nm plotted in the repeated zone scheme for different values of the Fermi energy (E_F) with respect to that at the Dirac point. Dashed lines are minizone boundaries. Red and blue lines are parts coming from the first and the second band above the Dirac point energy, respectively.

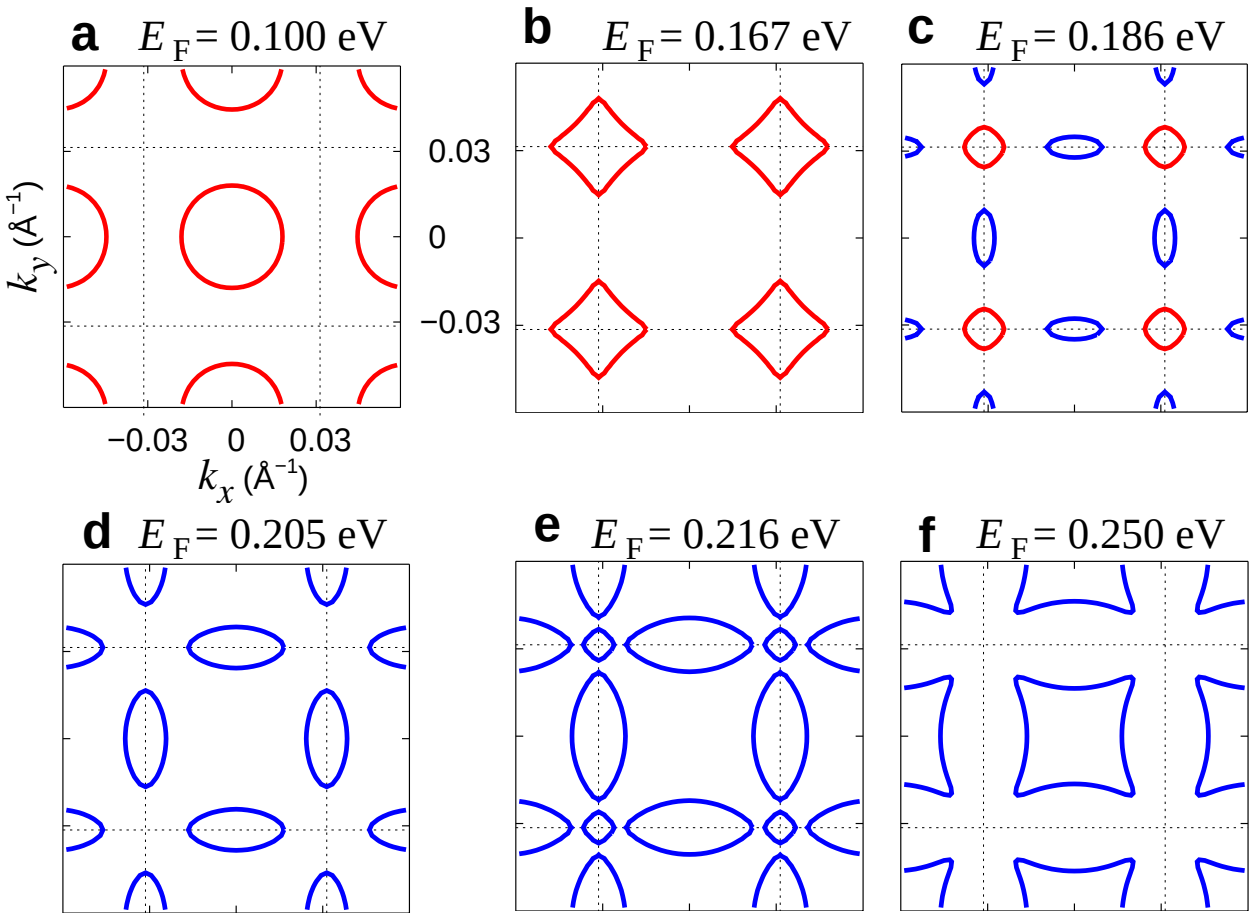

Figure 9.9: Fermi surfaces of a 2D rectangular graphene superlattice. (a)-(f) Fermi surfaces of a 2D rectangular graphene superlattice with $U_{2D} = 0.3$ eV, $L_x = L_y = 10$ nm and $d = 5$ nm plotted in the repeated zone scheme for different values of the Fermi energy (E_F) with respect to the Dirac point energy. Dashed lines are minizone boundaries. Red lines and blue line are parts coming from the first and the second band above the Dirac point energy, respectively.

Chapter 10

New generation of massless Dirac fermions in graphene under external periodic potentials

10.1 Introduction

Semiconducting and metallic superlattice structures are now routinely used in manipulating the electronic structure of materials [188]. These superlattices have additional electronic band gaps at the supercell Brillouin zone (SBZ) boundary, which often give rise to interesting phenomena.

Since the successful isolation of graphene [34, 35, 36, 182], numerous studies have been performed on this novel material [72]. In particular, there have been a number of interesting theoretical predictions on graphene superlattices (defined to be graphene under an external periodic potential or graphene with periodic defects). For example, for an one-dimensional (1D) or a two-dimensional (2D) rectangular graphene superlattice, the group velocity of the low-energy charge carriers is renormalized anisotropically [81]; a corrugated graphene sheet is expected to show charge inhomogeneity and localized states [204]; and arrays of anti-dots (missing carbon atoms) of specific design could induce band gaps [205] or magnetism [206].

Graphene superlattices are not only of theoretical interest, but have also been experimentally realized. Superlattice patterns with periodicity as small as 5 nm have been imprinted on graphene through electron-beam induced deposition of adatoms [193]. Also, triangular patterns with $\sim$10 nm lattice period have been observed for graphene on metal surfaces [197, 207, 199]. Using periodically patterned gates is another possible route to make graphene superlattices.

In this chapter, we show that when a periodic potential is applied to graphene, a new generation of massless Dirac fermions is formed at the SBZ boundaries. The electronic wavevector (measured from the new Dirac point), the group velocity and a *generalized* pseudospin vector, defined below, of the newly generated massless Dirac fermions are not collinear

anymore. In 1D or 2D rectangular graphene superlattices, the features of these new massless Dirac fermions are obscured by other states existing around the new Dirac point energy. We show however that, in triangular graphene superlattices (TGSs), there can be no states other than those of the new massless Dirac fermions around the energy of the new Dirac points. Therefore, doped or gated TGSs should provide a clear way to probe this new class of massless Dirac fermions that are absent in pristine graphene.

10.2 Analytical calculation

A physical requirement for the discussed phenomenon is that the variation of the external periodic potential is much slower than the inter-carbon distance so that inter-valley scattering (between $\mathbf{K}$ and $\mathbf{K}'$) may be neglected [78, 79], and we limit our discussion to the low-energy electronic states of graphene which have wavevectors close to the $\mathbf{K}$ point. The Hamiltonian of the low-energy quasiparticles in pristine graphene in a pseudospin basis, $\begin{pmatrix} 1 \\ 0 \end{pmatrix} e^{i\mathbf{k}\cdot\mathbf{r}}$ and $\begin{pmatrix} 0 \\ 1 \end{pmatrix} e^{i\mathbf{k}\cdot\mathbf{r}}$ (where $\begin{pmatrix} 1 \\ 0 \end{pmatrix}$ and $\begin{pmatrix} 0 \\ 1 \end{pmatrix}$ are Bloch sums of π-orbitals with wavevector $\mathbf{K}$ on the sublattices A and B, respectively, and $\mathbf{k}$ is the wavevector from the $\mathbf{K}$ point), is given by [77]

$$H_0 = \hbar v_0 \left(-i\sigma_x \partial_x - i\sigma_y \partial_y\right) , \tag{10.1}$$

where v_0 is the group velocity and σ's are the Pauli matrices. The eigenstates and the energy eigenvalues are given by

$$\psi^0_{s,\mathbf{k}}(\mathbf{r}) = \frac{1}{\sqrt{2}} \begin{pmatrix} 1 \\ s e^{i\theta_{\mathbf{k}}} \end{pmatrix} e^{i\mathbf{k}\cdot\mathbf{r}} \tag{10.2}$$

and

$$E^0_s(\mathbf{k}) = s\hbar v_0 k \,, \tag{10.3}$$

respectively, where $s = \pm 1$ is the band index and $\theta_{\mathbf{k}}$ is the polar angle of the wavevector $\mathbf{k}$. Equation (10.2) indicates that the pseudospin vector is parallel and anti-parallel to the wavevector $\mathbf{k}$ in the upper band ($s = 1$) and in the lower band ($s = -1$), respectively. Moreover, the pseudospin vector is always parallel to the group velocity.

Let us first consider the case that a 1D potential $V(x)$, periodic along the x direction with periodicity L, is applied to graphene. The Hamiltonian H then reads

$$H = \hbar v_0 \left(-i\sigma_x \partial_x - i\sigma_y \partial_y + I\, V(x)/\hbar v_0\right) , \tag{10.4}$$

where I is the 2×2 identity matrix. After a similarity transform, $H' = U_1^\dagger H U_1$, using the unitary matrix

$$U_1 = \frac{1}{\sqrt{2}} \begin{pmatrix} e^{-i\alpha(x)/2} & -e^{i\alpha(x)/2} \\ e^{-i\alpha(x)/2} & e^{i\alpha(x)/2} \end{pmatrix} \tag{10.5}$$

where $\alpha(x)$ is given by [208]

$$\alpha(x) = 2\int_0^x V(x')\,dx'/\hbar v_0\,, \tag{10.6}$$

we obtain [209]

$$H' = \hbar v_0 \begin{pmatrix} -i\partial_x & -e^{i\alpha(x)}\partial_y \\ e^{-i\alpha(x)}\partial_y & i\partial_x \end{pmatrix}. \tag{10.7}$$

To obtain the eigenstates and energy eigenspectrum of H' in general, using a plane wave spinor basis set, we need an infinite number of plane waves with wavevectors different from one another by the reciprocal lattice vectors of the superlattice. (A reciprocal vector of the superlattice is given by $\mathbf{G}_m = m\,(2\pi/L)\,\hat{x} \equiv m\,G_0\,\hat{x}$ where m is an integer.) However, if we are interested only in quasiparticle states whose wavevector $\mathbf{k} \equiv \mathbf{p} + \mathbf{G}_m/2$ is such that $|\mathbf{p}| \ll G_0$, we could treat the terms containing ∂_y in Eq. (10.7) as a perturbation since $\mathbf{G}_m$ is along $\hat{x}$. H' may be reduced to a 2×2 matrix using the following two states as basis functions

$$\begin{pmatrix} 1 \\ 0 \end{pmatrix}' e^{i(\mathbf{p}+\mathbf{G}_m/2)\cdot\mathbf{r}} \text{ and } \begin{pmatrix} 0 \\ 1 \end{pmatrix}' e^{i(\mathbf{p}-\mathbf{G}_m/2)\cdot\mathbf{r}}\,. \tag{10.8}$$

[Note that the spinors $\begin{pmatrix} 1 \\ 0 \end{pmatrix}'$ and $\begin{pmatrix} 0 \\ 1 \end{pmatrix}'$ now have a different meaning from $\begin{pmatrix} 1 \\ 0 \end{pmatrix}$ and $\begin{pmatrix} 0 \\ 1 \end{pmatrix}$ that were defined before because of the unitary transformation.]

In order to calculate these matrix elements, we expand $e^{i\alpha(x)}$ as

$$e^{i\alpha(x)} = \sum_{l=-\infty}^{\infty} f_l[V] e^{\,i\,l\,G_0\,x}, \tag{10.9}$$

where $f_l[V]$'s are coefficients determined by the periodic potential $V(x)$. One important thing to note is that in general

$$|f_l| < 1\,, \tag{10.10}$$

which can directly be deduced from Eq. (10.9). The physics simplifies when the external potential $V(x)$ is an even function. Then, $f_l[V]$'s are all real [210]. For states with wavevector $\mathbf{k}$ very close to $\mathbf{G}_m/2$, the 2×2 matrix M whose elements are calculated from the Hamiltonian H' with the basis given by Eq. (10.8) can be written as

$$M = \hbar v_0\,(p_x\sigma_z + f_m p_y \sigma_y) + \hbar v_0\,mG_0/2 \cdot I\,. \tag{10.11}$$

After performing yet another similarity transform $M' = U_2^\dagger M U_2$ with

$$U_2 = \frac{1}{\sqrt{2}} \begin{pmatrix} 1 & 1 \\ -1 & 1 \end{pmatrix}, \tag{10.12}$$

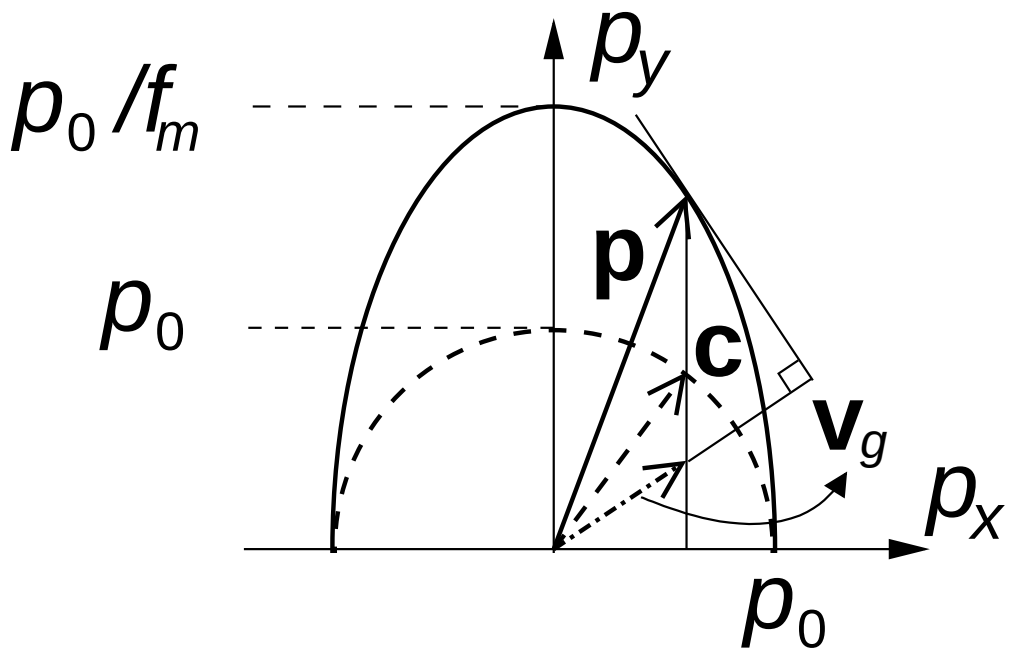

Figure 10.1: Schematic diagram showing an equi-energy contour (ellipse) with $E = \hbar v_0 k_0 + \hbar v_0\, m\, G_0/2$ of the newly generated massless Dirac fermions. The quasiparticle wavevector $\mathbf{k}$, the generalized pseudospin vector (see text) $\mathbf{c}$, and the group velocity vector $\mathbf{v}_g$ are represented by solid, dashed and dash-dotted arrows, respectively, for graphene in an even periodic potential.

we obtain the final result:

$$M' = \hbar v_0 \left(p_x \sigma_x + f_m\, p_y \sigma_y\right) + \hbar v_0\, m\, G_0/2 \cdot I\,. \tag{10.13}$$

The only difference of the Hamiltonian in Eq. (10.13) from that in Eq. (10.1), other than a constant energy term, is that the group velocity of quasiparticles moving along the y direction has been changed from v_0 to $f_m v_0$ [211]. Thus, the electronic states near $\mathbf{k} = \mathbf{G}_m/2$ are also those of massless Dirac fermions but having a group velocity varying *anisotropically* depending on the propagation direction. Moreover, the group velocity along the y direction is *always lower* than v_0 [Eq. (10.10)] regardless of the form or magnitude of the periodic potential $V(x)$.

The eigenstate and the energy eigenvalue of the matrix M' are given by

$$\varphi_{s,\mathbf{p}} = \frac{1}{\sqrt{2}} \begin{pmatrix} 1 \\ s e^{i\phi_{\mathbf{p}}} \end{pmatrix}'' \tag{10.14}$$

and

$$E_s(\mathbf{p}) = s\hbar v_0 \sqrt{p_x^2 + |f_m|^2 p_y^2} + \hbar v_0\, m\, G_0/2\,, \tag{10.15}$$

respectively, where $\phi_{\mathbf{p}}$ is the polar angle of the pseudospin vector $\mathbf{c}$ of $\varphi_{s,\mathbf{p}}$, which is parallel to $s(p_x\hat{x} + f_m\, p_y\hat{y})$. The spinor $\varphi_{s,\mathbf{p}}$, however, should not be confused with the one in Eq. (10.2) representing the sublattice degree of freedom, or with the one in Eq. (10.8). A double prime in Eq. (10.14) emphasizes this point.

The eigenstate $\psi_{s,\mathbf{k}}(\mathbf{r})$ of the original Hamiltonian H in Eq. (10.4) can be obtained by using Eqs. (10.5), (10.8), (10.12) and (10.14). Since the unitary transforms conserve the inner-product between eigenstates, if a *generalized* pseudospin vector for the original Hamiltonian H in Eq. (10.4) is defined as the pseudospin vector of the transformed Hamiltonian M', i. e. , $\mathbf{c}$, the scattering matrix elements between states of these new massless Dirac fermions due to long-wavelength perturbations are described by the generalized pseudospin in the same manner as those of the original massless Dirac fermions in pristine graphene are described with their pseudospin.

On the other hand, the group velocity vector $\mathbf{v}_g$ is parallel to $s\,(p_x\hat{x}+f_m^2\, p_y\hat{y})$ [Eq. (10.15)]. Therefore, in general, the three vectors $\mathbf{p}$, $\mathbf{c}$ and $\mathbf{v}_g$ are not collinear (Fig. 10.1). However, it is obvious that if the wavevectors ($\mathbf{p}$) of two electronic states are aligned or anti-aligned to each other, so are their generalized pseudospin vectors, as in pristine graphene, resulting in a maximum or a zero overlap between the two states, respectively. If $V(x)$ is not an even function, the dispersion relation of the new massless Dirac fermions remains the same as Eq. (10.15) but a generalized pseudospin vector may not be defined [212].

Similarly, for graphene in slowly varying 2D periodic potential, new massless Dirac fermions are generated centered around the wavevectors $\mathbf{k}_c = \mathbf{G}/2$ where the $\mathbf{G}$'s are the superlattice reciprocal vectors. A state with wavevector $\mathbf{k}$ around $\mathbf{k}_c$ mixes strongly with another state with wavevector $\mathbf{k}-\mathbf{G}$ by the superlattice potential. Applications of the same argument that we made use of in the case of 1D graphene superlattices result in linear band dispersions.

10.3 Triangular graphene superlattices

Even though new massless Dirac fermions are generated in 1D graphene superlattices, because there is no SBZ boundary perpendicular to the periodic direction, they are obscured by other states, and there is no new value of energy at which the density of states vanishes. In a 2D rectangular graphene superlattices, the SBZ is a rectangle. It turns out that the energy separation at the SBZ corners also vanishes due to the chiral nature of graphene [81]. Therefore, in 2D rectangular graphene superlattices, again, there are states other than the new massless Dirac fermions in the range of the new Dirac point energy. However, as we show below, in TGSs, there can exist an energy window within which the only available states are the newly generated massless Dirac fermions.

As an illustration, we consider a TGS shown in Fig. 10.2(a). The external potential is of a muffin-tin type with value U_0 in a triangular array of disks of diameter d and zero outside of the disks. The spatial period of the superlattice is L. Figure 10.2(b) shows the SBZ of a TGS.

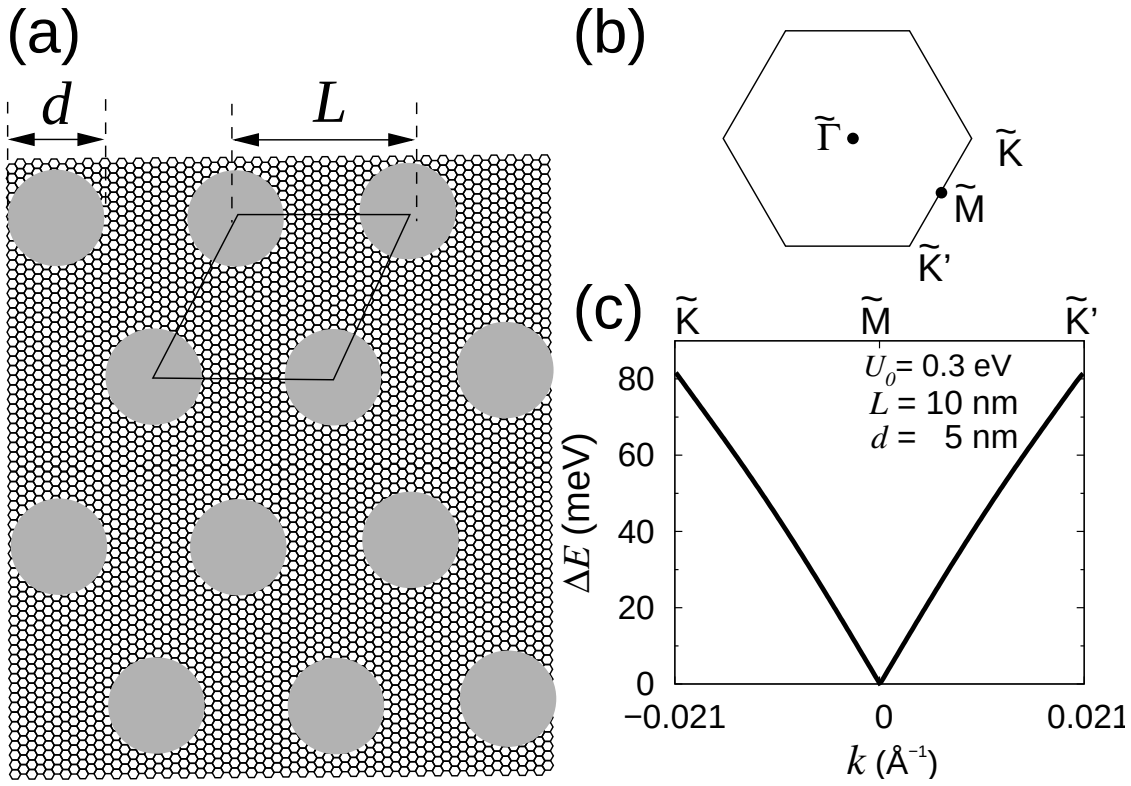

Figure 10.2: (a): A TGS with muffin-tin type of periodic potential with a spatial period L. The potential is U_0 inside the gray disks with diameter d and zero outside. (b) The SBZ of a TGS. (c) The energy separation ΔE between states in the first and the second band above the original Dirac point energy versus the wavevector k along the path $\tilde{\mathrm{K}}\tilde{\mathrm{M}}\tilde{\mathrm{K}}'$ in a TGS given by U_0 =0.5 eV, $L = 10$ nm, and $d = 5$ nm.

Figure 10.2(c) shows the electron energy separation between states in the first and the second band above the original Dirac point energy along the path $\tilde{\mathrm{K}}\tilde{\mathrm{M}}\tilde{\mathrm{K}}'$ in the SBZ [Fig. 10.2(b)] for a TGS. The energy separation at the corner, or the $\tilde{\mathrm{K}}$ point, of the SBZ is largest, contrary to that of the rectangular graphene superlattices where the energy separation closes at the SBZ corners [81]; but that at the $\tilde{\mathrm{M}}$ point is zero. New massless Dirac fermions are thus formed around the $\tilde{\mathrm{M}}$ points. With the set of potential parameters in Fig. 10.2 (U_0 =0.5 eV, L = 10 nm, and d = 5 nm), the energy separation at the $\tilde{\mathrm{K}}$ point is 82 meV, much larger than room-temperature thermal energy. This energy separation can be tuned by changing the superlattice parameters.

Figure 10.3(a) shows the energy dispersions of the first and the second band of the considered TGS. We can see the linear energy dispersion relation at the $\tilde{\mathrm{M}}$ points [Fig. 10.2(c)]. Close to the original Dirac point energy ($E = 0$), the density of states (DOS) varies linearly with energy, similar to that of pristine graphene, except that the slope is larger because of the reduced band velocity. At around $E = 0.16$ eV, there exists another energy value where the DOS vanishes also linearly.

10.4 Conclusion

In conclusion, we have shown that a new class of massless Dirac fermions are generated in graphene when a periodic potential is applied and we have studied the novel characteristics of these quasiparticles. Moreover, in triangular graphene superlattices, there can exist energy windows where there are no other states than these new quasiparticles. The triangular graphene superlattices thus should provide a good platform for experimental probing of the new massless Dirac fermions predicted here.

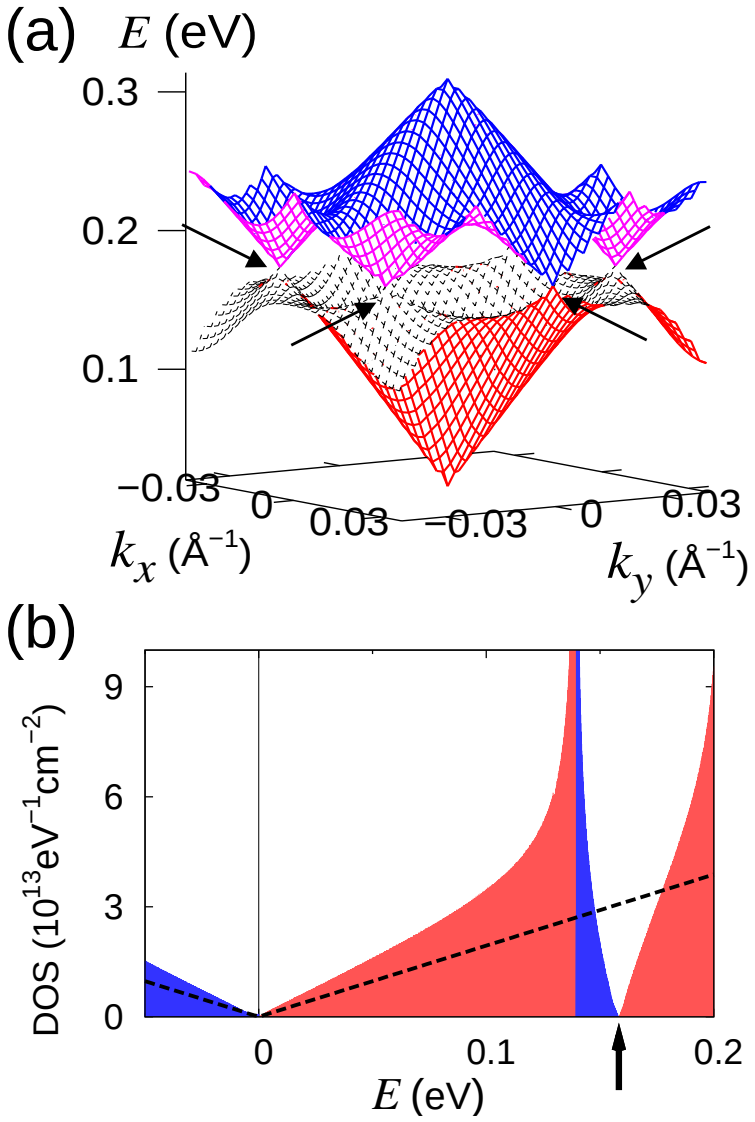

Figure 10.3: (a): Energy dispersion relation of a TGS with external potential with $U_0 = 0.5$ eV, $L = 10$ nm and $d = 5$ nm for the first and the second band above the original Dirac point energy as a function of wavevector $\mathbf{k}$ from the original Dirac point. Arrows indicate the $\tilde{\mathrm{M}}$ points of the SBZ around which new massless Dirac fermions are generated. (b): The DOS of charge carriers in electron orbits (bright) and hole orbits (dark) in the TGS characterized in (a). The original Dirac point energy is set at zero. Dashed black line shows the DOS of pristine graphene. The arrow indicates the new Dirac point energy.

Chapter 11

Electron beam supercollimation in graphene superlattices

11.1 Introduction

Although electrons and photons are intrinsically different, importing useful concepts in optics to electronics performing similar functions has been actively pursued over the last two decades. In particular, collimation of an electron beam is a long-standing goal. In this chapter, we show that ballistic propagation of an electron beam with virtual no spatial spreading or diffraction, without a waveguide or external magnetic field, can be achieved in graphene under an appropriate class of experimentally feasible one-dimensional external periodic potentials. The novel chiral quasi-one-dimensional metallic state that the charge carriers are in originates from a collapse of the intrinsic helical nature of the charge carriers in graphene owing to the superlattice potential. Beyond providing a new way to constructing chiral one-dimensional states in two dimensions, our findings should be useful in graphene-based electronic devices (e. g. , for information processing) utilizing some of the highly developed concepts in optics.

Electronic analogues of many optical behaviors such as focusing [213, 214, 215], collimation [216], and interference [217] have been achieved in two-dimensional electron gas (2DEG), enabling the system as a basic platform to study fundamental problems in quantum mechanics [218, 219, 220] as well as quantum information processing [221]. The close relationship between optics and electronics is been made possible due to the ballistic transport properties of a high-mobility 2DEG created in semiconductor heterostructures [222]. Among those electronics-optics analogues, the collimation or quasi-one-dimensional (quasi-1D) motion of electrons and photons are particularly important not only to achieve electronic quantum devices [219, 221] but also to realize ultracompact integrated light circuits [223, 224]. Usually, electrons originated from a point source may be controlled by electrostatics or geometrical constrictions [214, 215]. Quasi-1D electronic states and focusing have been achieved in a 2DEG with the help of external magnetic fields, e. g. , employing magnetic focusing [213]

and quantum Hall edge states [219, 225]. However, it would be difficult to integrate them into a single electronic device due to the external high magnetic field apparatus needed. In view of recent successful demonstrations of extreme anisotropic light propagation without diffraction, called supercollimation in photonic crystals [223, 224, 226, 227], an analogue of this effect in two-dimensional (2D) electron systems may also be possible. In this work, we demonstrate that graphene [35, 36, 182] in an external periodic potentials, or a graphene superlattice, is particularly suitable to realize electron supercollimation in two dimensions.

The isolation of graphene [35, 36, 182], a single layer of carbon atoms in a honeycomb structure composed of two equivalent sublattices, offers a new dimension to study electronics-optics analogues. Carriers in graphene exhibit ballistic transport on the submicron scale at room temperature [228] and with mobility up to $2 \times 10^5\,\mathrm{cm}^2\,\mathrm{V}^{-1}\,\mathrm{s}^{-1}$ [229]. Graphene electronic states have an internal quantum number, a pseudospin, that is not found in normal electronic systems and strongly influences the dynamics of the charge carriers. The pseudospin is of central importance to many of the novel physical properties of graphene [35, 36, 182, 228, 229, 80, 230], and it also plays a significant role in the present work.

11.2 Graphene: linear energy dispersion and pseudospin

The low-energy quasiparticles in graphene whose wavevectors are close to the Dirac point $\mathbf{K}$ in the Brillouin zone are described by a 2×2 Hamiltonian matrix $H_0(\mathbf{k}) = \hbar v_0\,(\sigma_x k_x + \sigma_y k_y)$, where $v_0 \approx 10^6$ m/s is the band velocity, $\mathbf{k}$ is the wavevector measured from the $\mathbf{K}$ point, and σ's are the Pauli matrices. The energy eigenvalues are given by $E_s^0(\mathbf{k}) = s\,\hbar\,v_0\,|\mathbf{k}|$ where $s = +1\,(-1)$ denotes the conical conduction (valence) band (Fig. 11.1b). The sublattice degree of freedom of the quasiparticles in graphene can conveniently be described with a pseudospin basis, or spinors, where the $|\uparrow\rangle$ and the $|\downarrow\rangle$ pseudospin states of σ_z represent π-electron orbital on the A and B sublattices of the structure of graphene, respectively. This Hamiltonian is very similar to the one used to model neutrinos as massless Dirac fermions [129, 79]. The corresponding wavefunction is given by

$$\psi^0_{s,\mathbf{k}}(\mathbf{r}) = \frac{1}{\sqrt{2}} \begin{pmatrix} 1 \\ s\,e^{i\theta_{\mathbf{k}}} \end{pmatrix} e^{i\mathbf{k}\cdot\mathbf{r}}\,, \tag{11.1}$$

where $\theta_{\mathbf{k}}$ is the angle of the wavevector $\mathbf{k}$ with respect to the x-axis. Equation (11.1) may be viewed as having the pseudospin vector being parallel and anti-parallel to the wavevector $\mathbf{k}$ for electronic states in the upper ($s = 1$) and the lower ($s = -1$) band, respectively (Fig. 11.1b) [129, 79]. As the spin plays a role in the dynamics of neutrinos, the present pseudospin is similarly important in the quasiparticle dynamics of graphene [129, 79].

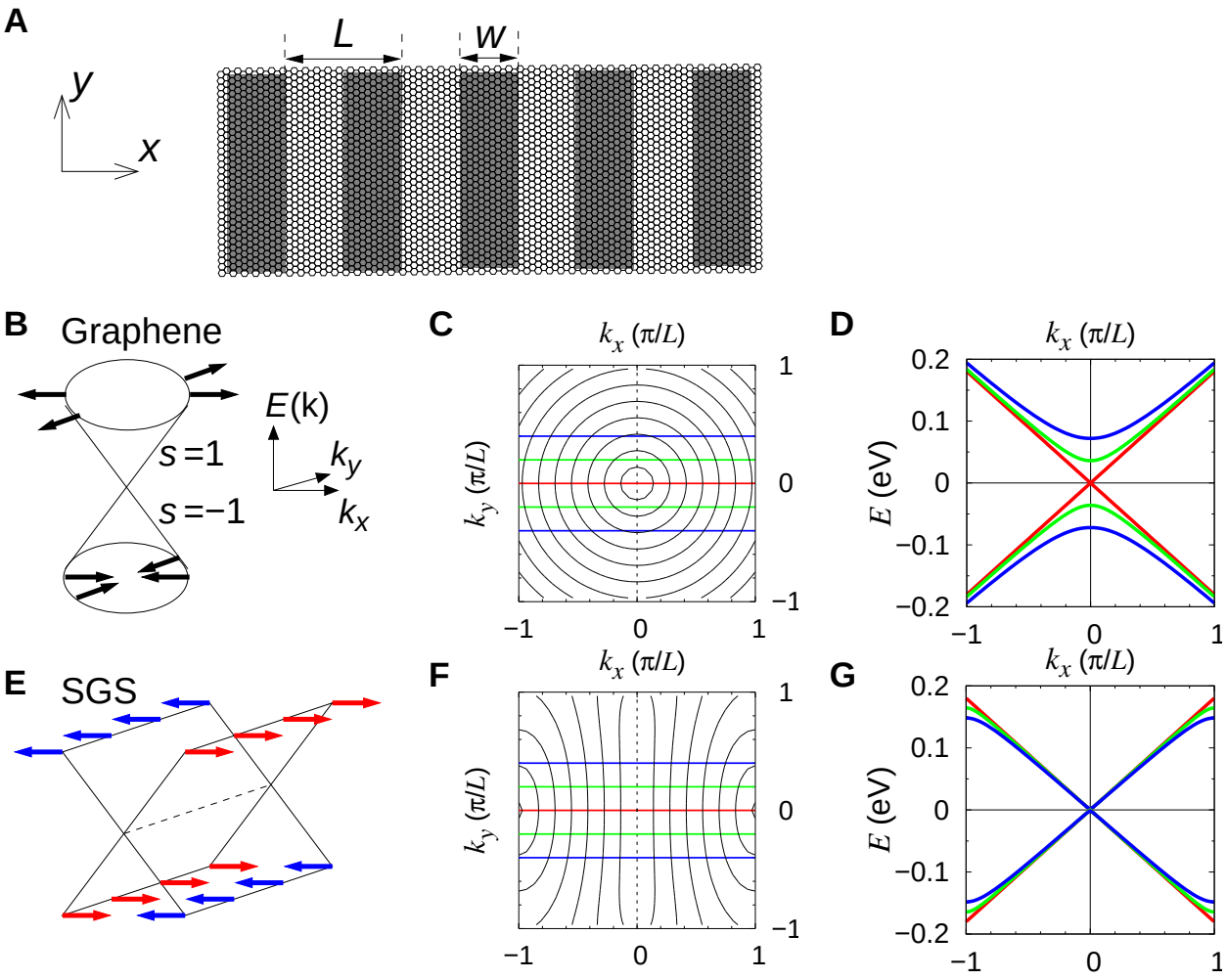

Figure 11.1: Electron energy dispersion relation in a special graphene superlattice. (a) Schematic diagram of a Kronnig-Penney type of potential applied to graphene with strength U_0 inside the gray regions and zero outside. The lattice period is L and the barrier width is w. (b) Schematic diagram showing the electronic energy dispersion relations and pseudospin vectors (black arrows) in graphene. (c) Contour plot of the first electronic band above the Dirac point energy in pristine graphene. The energy difference between neighbouring contours is 25 meV, with the lowest contour near the origin having a value of 25 meV. (d) The electronic energy dispersion relation E versus k_x with fixed k_y. Red, green and blue lines correspond to $k_y = 0$, $0.1\ \pi/L$ and $0.2\ \pi/L$, respectively, as indicated in (c). (e), (f) and (g) Same quantities as in (b), (c) and (d) for the considered SGS ($U_0 = 0.72$ eV, $L = 10$ nm and $w = 5$nm). Red and blue arrows in (e) represent the 'right' and the 'left' pseudospin state, respectively.

11.3 Graphene superlattices

Now, let us consider a 1D external periodic potential $V(x)$ applied to graphene. The potential is taken to vary much more slowly than the carbon-carbon distance so that inter-valley scattering can be neglected [129, 79]. Under this condition and for low-energy quasiparticle states whose wavevectors are close to the **K** point, the Hamiltonian reads

$$H = \hbar v_0 \left(-i\sigma_x \partial_x + \sigma_y k_y + I\ V(x)/\hbar v_0\right), \tag{11.2}$$

where I is the 2×2 identity matrix. The eigenstates and eigenenergies of the Hamiltonian H in Eq. (11.2) may be obtained numerically in the general case or analytically for small $\mathbf{k}$.

It has been predicted that, in a graphene superlattice with a slowly varying 1D periodic potential or a 2D periodic potential of rectangular symmetry, the group velocity of its low-energy charge carriers is renormalized anisotropically [81]. Unlike bare graphene which has an isotropic (zero mass) relativistic energy dispersion (Figs. 11.1b-11.11d), graphene under some specific superlattice potentials displays extremely anisotropic quasiparticle energy dispersion: the group velocity near the Dirac point along the direction perpendicular to the periodicity of the potential vanishes while the one parallel to the periodicity direction is intact [81].

We consider a Kronig-Penney type of potential with barrier height U_0, lattice period L, and barrier width w, periodic along the x direction (Fig. 11.1a). These potential parameters can be tuned so that the group velocity of the quasiparticles (with wavevector close to the Dirac point) along the y direction vanishes [81]. We shall focus on a graphene superlattice under one of these conditions ($U_0 = 0.72$ eV, $L = 10$ nm, and $w = 5$ nm) [81]. The parameters used here are experimentally feasible as shown in recent studies [193, 197, 207, 199]. Later, we will relax the special condition to confirm the robustness of the predicted supercollimation.

The quasiparticle energy dispersion of this superlattice (Figs. 11.1e-11.1g) shows that, not only the group velocity of quasiparticles at the Dirac point along the y direction vanishes, there is hardly any dispersion along the k_y direction within a good fraction of the supercell Brillouin zone (Figs. 11.1f and 11.1g). This portion of the energy dispersion in this superlattice thus is well described by the relation

$$E_s(\mathbf{k}) = s\hbar v_0 |k_x| \,. \tag{11.3}$$

The deviation of the actual energy dispersion from that of Eq. (11.3) is less than 5% for $\mathbf{k}$ vector as large as 40% of the supercell Brillouin zone considered (Figs. 11.1f and 11.1g). This is an equation for wedges. Thus, for some specific superlattice potentials, graphene turns from a zero-gap semiconductor into a quasi-1D metal with a finite and constant density of states about the Dirac point energy. We shall call this class of graphene superlattices as special graphene superlattices (SGSs).

Along with the quasiparticle energy dispersion, the internal pseudospin symmetry of the electronic states in SGSs also undergoes a dramatic alteration. We calculate numerically the overlap $\left|\left\langle \psi_{s',\mathbf{k}'} | e^{i(\mathbf{k}'-\mathbf{k})\cdot\mathbf{r}} | \psi_{s,\mathbf{k}} \right\rangle\right|^2$ of two quasiparticle states $\psi_{s,\mathbf{k}}(\mathbf{r})$ and $\psi_{s',\mathbf{k}'}(\mathbf{r})$. If there were no external periodic potential, this overlap would be simply $(1 + ss'\ \cos\ (\theta_{\mathbf{k}'} - \theta_{\mathbf{k}}))/2$

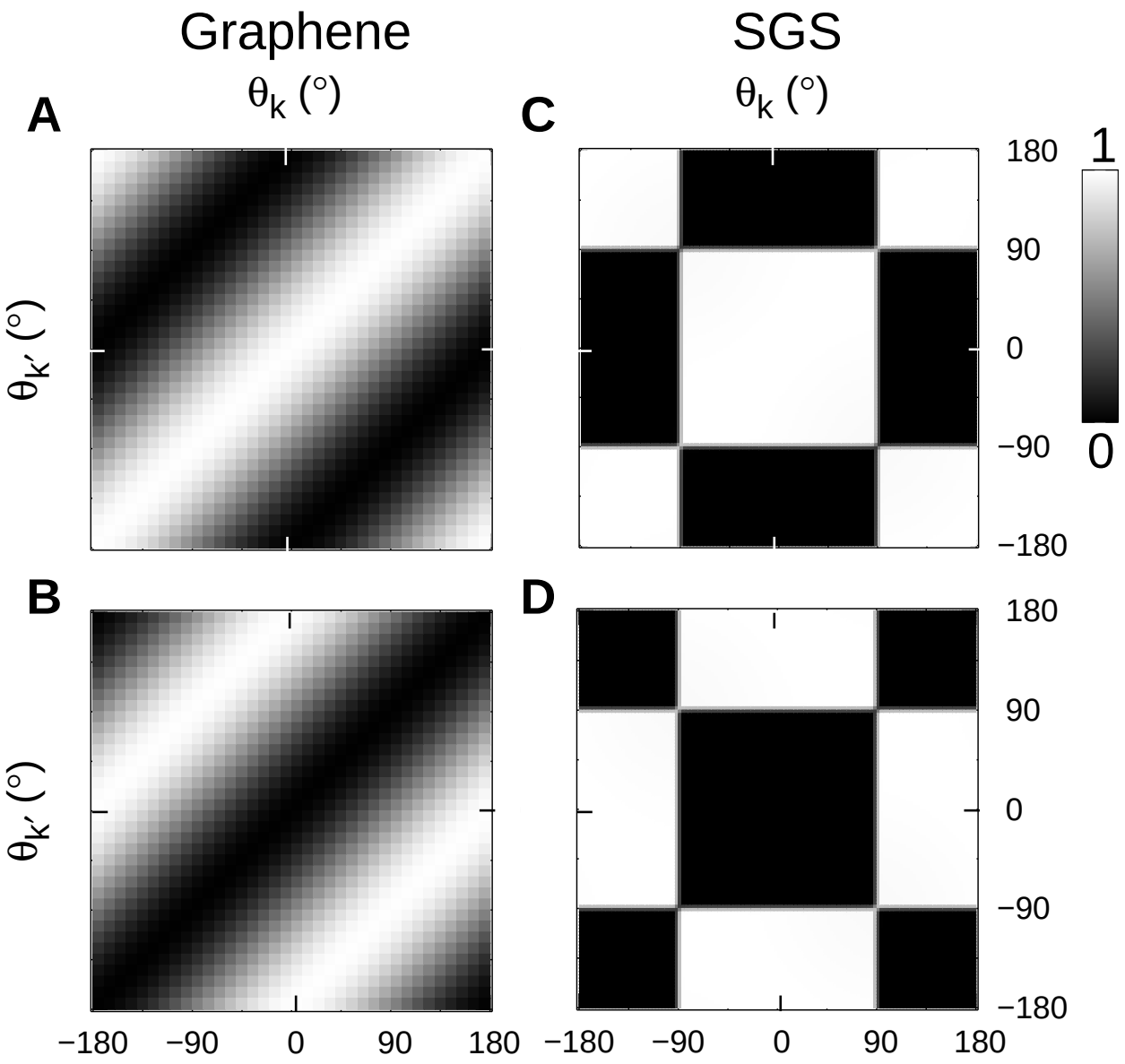

Figure 11.2: Pseudospin collapse in a special graphene superlattice. (a) and (b) Calculated overlap of two quasiparticle states $\psi^0_{s,\mathbf{k}}(\mathbf{r})$ and $\psi^0_{s',\mathbf{k}'}(\mathbf{r})$, $\left|\left\langle\psi^0_{s',\mathbf{k}'}|e^{i(\mathbf{k}'-\mathbf{k})\cdot\mathbf{r}}|\psi^0_{s,\mathbf{k}}\right\rangle\right|^2$, in graphene versus $\theta_{\mathbf{k}}$ and $\theta_{\mathbf{k}'}$ which are the angles between the x axis and wavevectors $\mathbf{k}$ and $\mathbf{k}'$ ($|\mathbf{k}| = |\mathbf{k}'| = 0.1\pi/L$), respectively. The overlap is shown in a gray scale (0 in black and 1 in white). The two states are in the same band ($s' = s$) in (a) and are in different bands ($s' = -s$) in (b). (c) and (d) Same quantities as in (a) and (b) for the considered SGS ($U_0 = 0.72$ eV, $L = 10$ nm and $w = 5$nm).

as seen from Eq. (11.1) (Figs. 11.2a and 11.22b). The same overlap in the SGS (Figs. 11.2c and 11.2d) is however dramatically different from that in graphene, and can be well described by $\left|\left\langle\psi_{s',\mathbf{k}'}|e^{i(\mathbf{k}'-\mathbf{k})\cdot\mathbf{r}}|\psi_{s,\mathbf{k}}\right\rangle\right|^2 = (1 + ss' \text{ sgn } (k_x) \text{ sgn } (k'_x))/2$. This behavior is robust for a wide range of the magnitudes of $\mathbf{k}$ and $\mathbf{k}'$, extending over a good fraction of the supercell Brillouin zone with a high degree of accuracy. The eigenfunctions of an SGS, for states with small $\mathbf{k}$, can be deduced from this result, together with results on the numerically obtained wavefunctions, (also from analytic calculation: see Supporting Information) as having the form of

$$\psi_{s,\mathbf{k}}(\mathbf{r}) = e^{if(x)}\frac{1}{\sqrt{2}}\begin{pmatrix} 1 \\ s \text{ sgn } (k_x) \end{pmatrix} e^{i\mathbf{k}\cdot\mathbf{r}}, \tag{11.4}$$

where $f(x)$ is a real function. Thus, the spinor in Eq. (11.4) is an eigenstate of σ_x. Therefore, the direction of the pseudospin is quantized so that it is either parallel or anti-parallel to the x direction, which is the direction of the periodicity of the superlattice potential (Fig. 11.1e), and not to the wavevector $\mathbf{k}$ as is the case in pristine graphene (Fig. 11.1b). In other words, the pseudospin in the SGS collapses into a backward ('left') or a forward ('right') state. The resulting quasi-one-dimensionality in the energy dispersion relation and in the pseudospin of quasiparticles in the SGS significantly changes the already unique properties of graphene.

11.4 Electron supercollimation

The quasi-one-dimensionality and specific chiral nature of the SGS makes it a natural candidate for electron supercollimation. It is indeed the case that, when a wavepacket of electron is injected into an SGS, the propagating packet exhibits essentially no spatial spreading, i. e. , electron beam supercollimation is realized (Fig. 11.3). We have calculated the time-evolution of a gaussian wave packet (with spatial extent along the x and the y direction given by $2\sigma_x = 40$ nm and $2\sigma_y = 200$ nm, respectively) composed of states in the first band above the Dirac point energy with a central wavevector $\mathbf{k}_c$ (Fig. 11.3). To provide a measure of the electron beam collimation, we compute the angle θ_c in which direction the beam intensity is maximum and the angular spread $\Delta\theta$ which gives half the maximum intensity when the angle is at $\theta_c \pm \Delta\theta$. For a central wavevector $\mathbf{k}_c$ parallel to the x direction with energy $E(\mathbf{k}_c) = E_0 = \hbar v_0\ 0.1\pi/L = 0.02$ eV, the angular spread $\Delta\theta$ in pristine graphene is $\Delta\theta = 55\ ^\circ$ (Fig. 11.3a), whereas in the SGS, $\Delta\theta = 0.3\ ^\circ$ (Fig. 11.3b), about 200 times smaller than in graphene. Specifically, in the SGS, the spread of the wave packet in the y direction after proceeding 0.1 mm along the x direction is only 500 nm. Therefore, supercollimation of currents of nanoscale width in the SGS can, in principle, be achieved and maintained as long as the ballistic transport occurs in the system.

Even when the experimental situation deviates from the ideal conditions for SGSs, supercollimation persists. Hence the phenomenon is quite robust. First, for example, if we consider an imperfection in making a superlattice potential such that the periodicity is slightly larger or smaller ($\Delta L/L = \pm 5\%$), the calculated time-evolution of a gaussian wave packet shows the angular spread $\Delta\theta = 0.007^\circ$ and 0.5°, respectively (Figs. 11.3c and 11.3d).

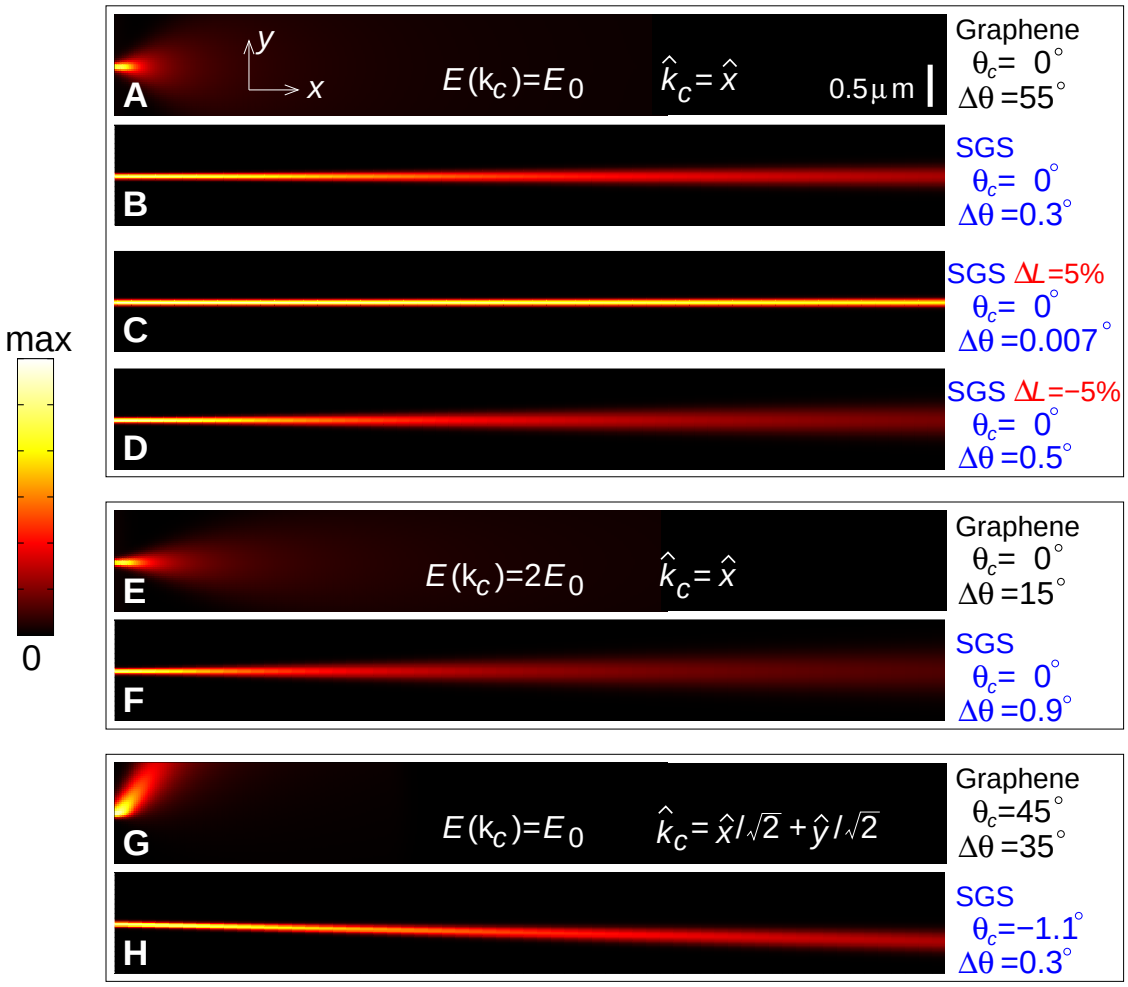

Figure 11.3: Special graphene superlattice as an electron supercollimator. (a), (e) and (g) Time-integrated probability density of an electron wave packet, $\int_0^\infty |\Psi(x,y,t)|^2 dt$, in graphene. The initial ($t = 0$) wave packet is a Gaussian localized at the coordinates origin (middle of the left edge of each panel) $|\Psi(x,y,0)|^2 \sim \exp\left[-\left(x^2/2\sigma_x^2 + y^2/2\sigma_y^2\right)\right]$ where $2\sigma_x = 200$ nm and $2\sigma_y = 40$ nm. The wave packet in wavevector space is set to be localized around a specific $\mathbf{k}_c$. In (a), $\mathbf{k}_c$ is set by $E(\mathbf{k}_c) = E_0 = \hbar v_0\, 0.1\pi/L = 0.02$ eV and $\hat{k}_c = \hat{x}$. In (e), $\mathbf{k}_c$ is set by $E(\mathbf{k}_c) = 2E_0$ and $\hat{k}_c = \hat{x}$. In (g), $\mathbf{k}_c$ is set by $E(\mathbf{k}_c) = E_0$ and $\hat{k}_c = \hat{x}/\sqrt{2} + \hat{y}/\sqrt{2}$. θ_c denotes the angle (defined with respect to the x-direction) along which direction the intensity is maximal and $\Delta\theta$ denotes the angular spread which gives half the maximum intensity when the angle is at $\theta_c \pm \Delta\theta$. (b), (f) and (h) Same quantities as in (a), (e) and (g) for the considered SGS ($U_0 = 0.72$ eV, $L = 10$ nm and $w = 5$ nm), respectively. (c) and (d), Same quantities as in (b) for graphene superlattices corresponding to a superlattice potential that is otherwise the same as the SGS studied but with a period L change of $\Delta L/L = 5\%$ and $\Delta L/L = -5\%$, respectively.

Second, when considering doped SGSs or high energy electron injection such that $E(\mathbf{k}_c)$ is doubled, the angular spread is still very small (Fig. 11.3f). Third, even when $\mathbf{k}_c$ is off from the collimation direction ($+x$) by 45 °, the angular deviation is still negligible ($\theta_c = -1.1$ °) (Fig. 11.3h). In graphene, on the other hand, the propagation direction and spread of the wave packet sensitively depends on the magnitude and the direction of the central wavevector $\mathbf{k}_c$ (Figs. 11.3e and 11.3g). This robustness here is quite contrary to the case in optics where the efficiency of supercollimator, superprism or superlens [231] depends sensitively on the magnitude and the direction of the light wavevector and in general provides a very narrow effective bandwidth [223, 224, 226, 227]. From our calculations, we expect that the predicted supercollimation be observable in SGSs over a wide operation range.

11.5 Electronic analogue of optics

Lastly, we consider the tunneling properties of injected electrons into SGSs from pristine graphene, which provides another measure of the efficiency of electronic devices based on SGSs. When an electron is injected into an SGS with an incidence angle θ from the graphene side, the wavevector of incident electron is given by $\mathbf{k}_i = k_0 \cos\theta \, \hat{x} + k_0 \sin\theta \, \hat{y}$ and those of the reflected and transmitted electrons by $\mathbf{k}_r = -k_0 \cos\theta \, \hat{x} + k_0 \sin\theta \, \hat{y}$ and $\mathbf{k}_t = k_0 \, \hat{x} + k_0 \sin\theta \, \hat{y}$, respectively (Fig. 11.4a). Here, we have made use of the continuity of the transverse component of the wavevector and conservation of energy, together with the novel dispersion relation given by Eq. (11.3). Using the continuity of the wavefunction in the system described by Eqs. (11.1) and (11.4), we find that the reflectance $R = |r|^2$ is

$$R(\theta) = \tan^2 \frac{\theta}{2} \, . \tag{11.5}$$

Interestingly, the reflectance is independent of the specific form of the external periodic potential of the SGS. Equation (11.5) indicates that the transmittance is large for most incidence angles. For example, even at $\theta = 45$ °, the reflectance is less than 20 % (Fig. 11.4b). Therefore, the SGS is not only an excellent electron supercollimator but also a good transmitter in a graphene-SGS-graphene junction (Fig. 11.4c). Utilizing this property, an immediate application could be made to demonstrate an electronic analogue of virtual imaging in this configuration (Fig. 11.4c).

11.6 Perspectives

Given the recent rapid progress in graphene superlattices fabrication [193, 197, 207, 199], the manipulation of electrons in ways similar to that of photons in optics by using the supercollimation effect discussed here together with other optics analogues [230, 80] is expected to soon be practicable. The SGSs have the promise of playing a unique role in devices based on the synergetic importing of concepts and techniques well developed in optics to electronics.

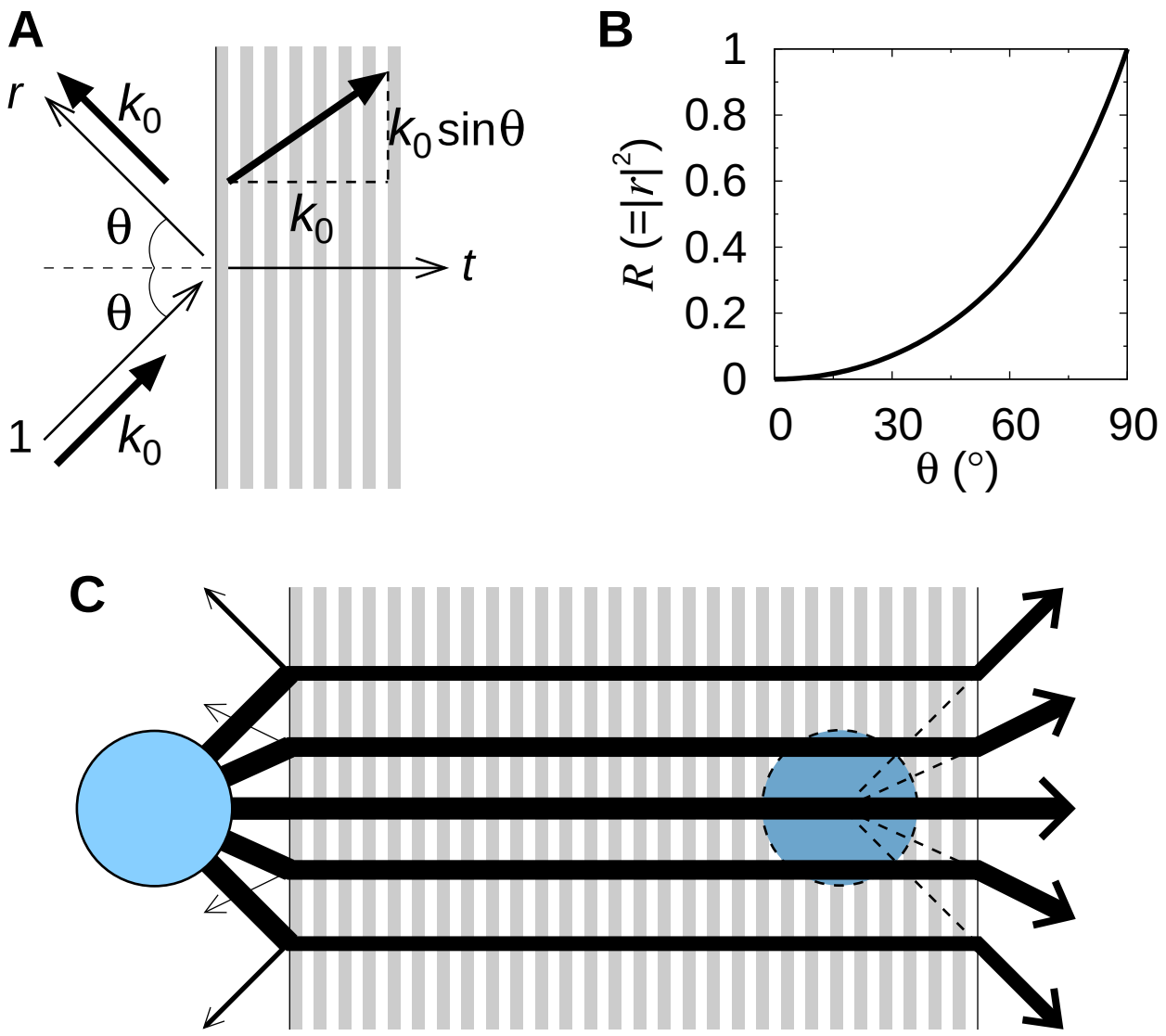

Figure 11.4: Reflection and transmission at a graphene − special graphene superlattice interface and virtual imaging. (a) Schematic diagram showing the incident, the reflected and the transmitted wave (the band index is set to $s = 1$) at a graphene − SGS interface, with the relative amplitudes being 1, r and t, respectively. Thick arrows represent the wavevectors of the corresponding waves. The incidence and reflection angle is θ. (b) Reflectance $R = |r|^2$ versus the incidence angle θ. (c) Schematic diagram showing the propagation of electron waves in graphene − SGS − graphene geometry. Thickness of each arrow is proportional to the actual intensity of the wave. A virtual image (dashed disk) is formed at a place far from the actual wave source (solid disk).

11.7 Supplementary discussion: Analytical solution of electronic states of special graphene superlattices

When graphene is in a 1D external periodic potential $V(x)$, the Hamiltonian for electrons whose wavevectors are close to the **K** pointreads

$$H = \hbar v_0 \left(-i\sigma_x \partial_x + \sigma_y k_y + I\ V(x)/\hbar v_0\right), \tag{11.6}$$

where I is the 2×2 identity matrix. In this case, we assume that the potential varies much more slowly than the carbon-carbon distance. So, the inter-valley scattering can be neglected safely [78, 79].

If a transform $H' = U^\dagger H U$ is applied to Eq. (11.6) with the unitary matrix $U = \exp\left(-i\sigma_x\ \alpha(x)/2\right)$, where $\alpha(x) = 2\int_0^x V(x')dx'/\hbar v_0$ (we assume that a constant is subtracted from $V(x)$ to set its average to zero), the resulting Hamiltonian H' reads

$$H' = \hbar v_0 \left(-i\sigma_x \partial_x + (\ \cos\alpha(x)\ \sigma_y - \sin\alpha(x)\ \sigma_z\ )\ k_y\right). \tag{11.7}$$

(A similar transform was applied to the Hamiltonian of a carbon nanotube under a sinusoidal potential for the specific case of finding the band gap opening behavior at the supercell Brillouin zone boundary [232, 233].) The terms having k_y could be treated as a perturbation if k_y is small. The eigenstate of the unperturbed Hamiltonian is given by

$$\psi'_{0\,s,\mathbf{k}}(\mathbf{r}) = \frac{1}{\sqrt{2}} \begin{pmatrix} 1 \\ s\ \mathrm{sgn}\ (k_x) \end{pmatrix} e^{i\mathbf{k}\cdot\mathbf{r}}. \tag{11.8}$$

Within second order perturbation theory, using Eqs. (11.7) and (11.8), the energy eigenvalue of the superlattice is

$$E_{s,\mathbf{k}} = s\ \hbar v_0 |k_x| + \hbar v_0 k_y^2 \sum_{s',\mathbf{G}} \frac{\left|\left\langle \psi'_{0\,s',\mathbf{k}+\mathbf{G}} \left|\cos\alpha(x)\ \sigma_y - \sin\alpha(x)\ \sigma_z\right| \psi'_{0\,s,\mathbf{k}} \right\rangle\right|^2}{s|k_x| - s'|k_x + G_x|}, \tag{11.9}$$

and the wavefunction is

$$\psi'_{s,\mathbf{k}}(\mathbf{r}) = \psi'_{0\,s,\mathbf{k}}(\mathbf{r}) + k_y \sum_{s',\mathbf{G}} \frac{\left\langle \psi'_{0\,s',\mathbf{k}+\mathbf{G}} \left|\cos\alpha(x)\ \sigma_y - \sin\alpha(x)\ \sigma_z\right| \psi'_{0\,s,\mathbf{k}} \right\rangle}{s|k_x| - s'|k_x + G_x|} \psi'_{0\,s,\mathbf{k}+\mathbf{G}}(\mathbf{r}). \tag{11.10}$$

Here, **G**'s are the superlattice reciprocal lattice vectors $\mathbf{G} = m\,\mathbf{G}_0$, where $\mathbf{G}_0 = (2\pi/L, 0)$ and m is an integer. Therefore, in order for the superlattice to be an SGS, in which there is negligible dispersion with respect to k_y, the energy shift arising from the perturbation (or k_y) should be negligible. Assuming that $\mathbf{k}$ is small, the dominant summand is the case when $s' = -s$ and $m = 0$. Thus, if

$$\left\langle \psi'_{-s,\mathbf{k}} \left|\cos\alpha(x)\ \sigma_y - \sin\alpha(x)\ \sigma_z\right| \psi'_{s,\mathbf{k}} \right\rangle = 0, \tag{11.11}$$

the superlattice would be an SGS. Under this condition, the relative deviation of the energy dispersion relation, Eq. (11.9), from $E_s(\mathbf{k}) = s\hbar v_0|k_x|$ (Eq. (11.3) in the paper) is $O\left(k_y^2/k_x G_x\right)$ and that of the wavefunction, Eq. (11.10), from Eq. (11.8) is $O\left(k_y/G_x\right)$. Similar quantities in a normal graphene superlattice are $O\left(k_y^2/k_x^2\right)$ and $O\left(k_y/k_x\right)$, respectively. The eigenfunction $\psi_{s,\mathbf{k}}(\mathbf{r})$ of the Hamiltonian H in Eq. (11.6) is, to a good approximation, obtained by $\psi_{s,\mathbf{k}}(\mathbf{r}) = U\psi'_{0\,s,\mathbf{k}}(\mathbf{r})$ and is still an eigenstate of σ_x because U commutes with σ_x.

Chapter 12

Landau levels and quantum Hall effect in graphene superlattices

12.1 Introduction

The physical properties of graphene [35, 36, 182] are currently among the most actively investigated topics in condensed matter physics. Graphene has the unique feature that the low-energy charge carriers are well described by the two-dimensional (2D) massless Dirac equation, used for massless neutrinos, rather than by the Schrödinger equation [35, 36]. Moreover, graphene is considered to be a promising candidate for electronics and spintronics applications [234].

It has been shown that, because of their gapless energy spectrum and chiral nature, the charge carriers in graphene are not hindered by a slowly varying electrostatic potential barrier at normal incidence [80], analogous to the Klein tunneling effect predicted in high-energy physics. Direct evidences of Klein tunneling through a single barrier in graphene [80] have been observed in recent experiments [235, 236].

Application of multiple barriers or periodic potentials, either electrostatic [202, 81, 237, 82, 83] or magnetic [238, 239, 240, 241], to graphene has been shown to modulate its electronic structure in unique ways and lead to fascinating new phenomena and possible applications. Periodic arrays of corrugations [204, 242, 243] have also been proposed as graphene superlattices (GSs).

Experimentally, different classes of GSs have been fabricated recently. Patterns with periodicity as small as 5 nm have been imprinted on graphene through electron-beam induced deposition of adsorbates [193]. Epitaxially grown graphene on the (0001) surface of ruthenium [197, 207, 199, 244, 245] and that on the (111) surface of iridium [246, 247, 248] also show superlattice patterns with $\sim$3 nm lattice period. The amplitude of the periodic potential applied to graphene in these surface systems has been estimated to be in the range of a few tenths of an electron volt [207]. Fabrication of periodically patterned gate electrodes is another possible way of making GSs with periodicity close to or larger than $\sim$20 nm.

The quantum Hall plateaus in graphene take on the unusual values of $4(l+1/2)\,e^2/h$ where l is a non-negative integer [249]. The factor 4 comes from the spin and valley degeneracies. In bilayer graphene, the quantum Hall plateaus are at $4l\,e^2/h$ with l a positive integer [120]. These unconventional quantum Hall effects have been experimentally verified [35, 36, 250], providing evidences for 2D massless particles in graphene and massive particles in bilayer graphene.

In this chapter, we investigate the LLs and the quantum Hall effect in GSs formed by the application of a one-dimensional (1D) electrostatic periodic potential and show that they exhibit additional unusual properties. We find that, for a range of potential shapes and parameters, new branches of massless fermions are generated with electron-hole crossing energy the same as that at the original Dirac point of pristine graphene. These additional massless fermions affect the LLs qualitatively. In particular, the LLs with energy corresponding to the Fermi energy at charge neutrality (i. e. , zero carrier density) become $4(2N+1)$-fold degenerate ($N = 0$, 1, 2, ...), depending on the strength and the spatial period of the potential (pristine graphene corresponds to $N = 0$). Accordingly, when sweeping the carrier density from electron-like to hole-like, the quantum Hall conductivity in such a GS is predicted to show an unconventional step size of $4(2N+1)\,e^2/h$ that may be tuned by adjusting the external periodic potential.

12.2 Computational details

In our study, the electronic structure of the GSs is evaluated using the methods developed in Ref. [81]; we evaluate the bandstructure of the GS numerically by solving the 2D massless Dirac equation with the external periodic potential included using a planewave basis. Similarly, to obtain the LLs, the eigenstates of the GSs under an external perpendicular magnetic field are expanded with planewaves. We work in a Landau gauge with the vector potential depending on the position coordinate along the direction of the periodicity of the GS, and a zigzag form for the vector potential with a very large artificial periodicity (large compared to the GS periodicity) is employed to mimic a constant magnetic field near the origin in position space [251]. We have checked that the LLs are converged in energy to within less than 1 % with respect to the size of the supercell for the vector potential and the kinetic energy cutoff for the planewaves. The size of the largest supercell and that of the smallest sampling distance in real space used are 400 and 0.05 in units of a single unit cell, respectively.

12.3 Results and discussion

12.3.1 Emerging zero-energy modes

Figure 12.1(a) shows a GS formed by a Kronig-Penney type of electrostatic potential periodic along the x direction, with lattice parameter L and barrier width $L/2$. Remarkably,

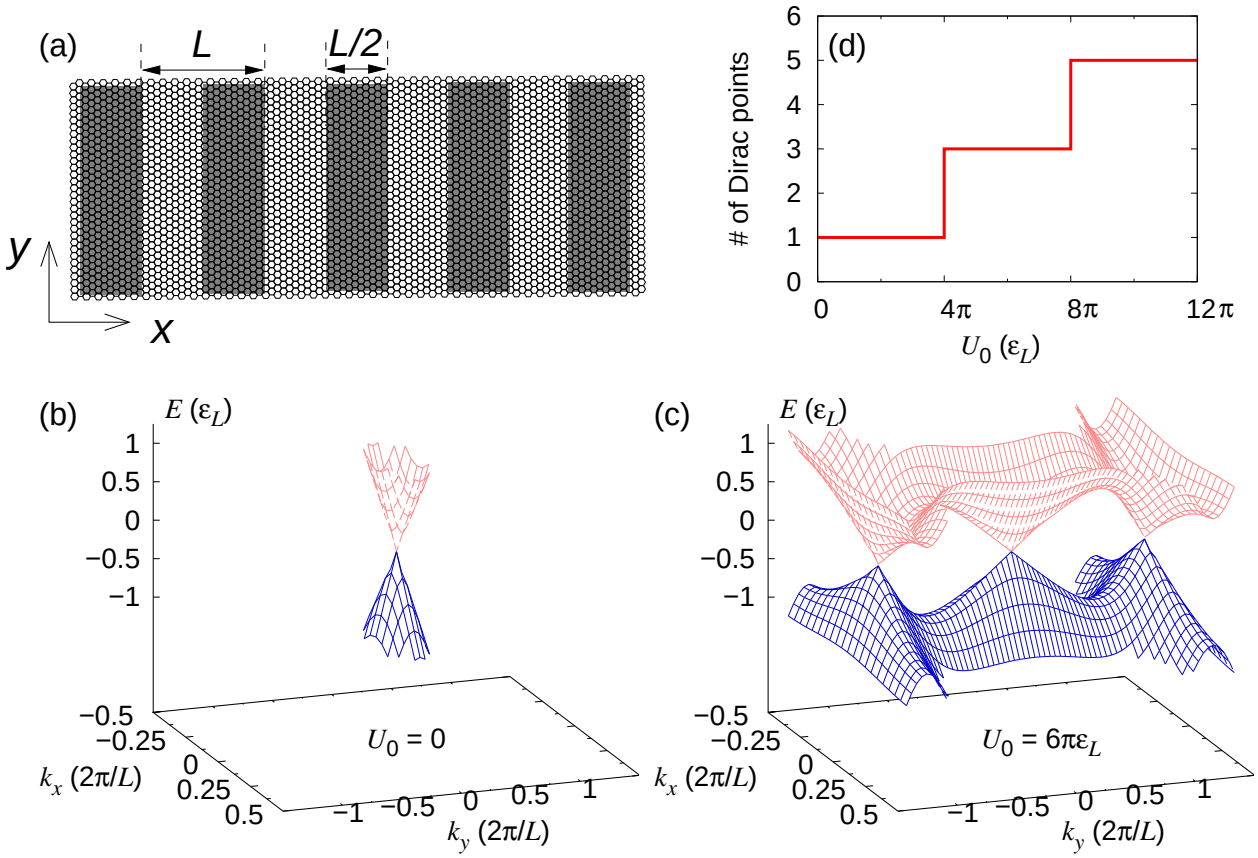

Figure 12.1: (a) Schematic diagram of a Kronig-Penney type of potential applied to graphene with strength $U_0/2$ inside the gray regions and $-U_0/2$ outside with lattice period L and barrier width $L/2$. (b) Electron energy in units of ε_L ($\equiv \hbar v_0/L$; for example, if $L = 20$ nm, $\varepsilon_L = 33$ meV) versus wavevector near the Dirac point in pristine graphene. (c) The same quantity as in (b) for a GS with $U_0 = 6\pi\varepsilon_L$. (d) Number of Dirac points (not including spin and valley degeneracies) in a GS versus U_0.

unlike that in graphene [Fig. 12.1(b)], the bandstructure in a GS [Fig. 12.1(c)] can have, depending on the potential barrier height U_0, more than one Dirac point with $k_x = 0$ having exactly the same electron-hole crossing energy [252]. As Fig. 12.1(c) shows, the number of Dirac points for this type of GSs increases by two (without considering the spin and valley degrees of freedom) whenever the potential amplitude exceeds a value of

$$U_0^N = 4\pi N \hbar v_0 / L \tag{12.1}$$

with N a positive integer. The value of the potential barrier given in Eq. (12.1) corresponds to special GSs in which the group velocity along the k_y direction vanishes for charge carriers whose wavevector is near the original Dirac cone [e. g. , the Dirac cone at the center in Fig. 12.1(c)] [253, 254]. All the findings in this study apply in general to GSs made from a periodic potential which has both even and odd symmetries, like a sinusoidal type of potential. The results for GSs whose odd or even symmetry is broken are discussed in the Supplementary discussion.

Figure 12.2 shows the evolution of the energy of the electronic states with $k_x = 0$ for a GS depicted in Fig. 12.1 for several different values of U_0. As stated above, the group velocity along the k_y direction becomes zero near $k_y = 0$ when the barrier height is given by Eq. (12.1) [Figs. 12.2(c) and 12.2(e)]. When U_0 has a value between those specific values, the position of the additional new Dirac points move away from the $k_y = 0$ point along the k_y direction with increasing U_0. The complex behavior of the zero-energy Dirac cones revealed by our numerical calculations cannot be derived using perturbation theory [83] because k_y is not small compared to the superlattice reciprocal lattice spacing $2\pi/L$. Moreover, the pseudospin character of these additional massless fermions [e. g. , the left and the right Dirac cones (not the center one) in Fig. 12.1(c)] are different from that of the original massless Dirac fermions. For example, backscattering amplitude due to a slowly varying potential within one of the new cones does not vanish (see the Supplementary discussion).

12.3.2 Landau levels and quantum Hall conductivity

A natural question arising from this peculiar behavior in the electronic structure of a GS, which is topologically different from that of pristine graphene, is how the LLs are distributed. Figure 12.3 shows the calculated LLs of the 1D Kronig-Penney GSs depicted in Fig. 12.1 for various values of U_0 [255]. When the superlattice potential modulation is moderate [Fig. 12.3(b)], the spacings between neighboring LLs become smaller than those in pristine graphene [Fig. 12.3(a)], owing to a reduction in the band velocity. Once U_0 becomes larger than $4\pi\hbar v_0/L$ (= 0.4 eV for $L = 20$ nm), the zero-energy LLs (corresponding to zero carrier density) become three-fold degenerate [Fig. 12.3(d)]. An important point to note is that this degeneracy is insensitive to U_0 over a range of U_0 near $6\pi\hbar v_0/L$ because the topology of the electron bands does not change with this variation [256, 257]. Moreover, even though the massless particles of the different Dirac cones may have different band velocities, the degeneracy of the zero-energy LLs is not affected.

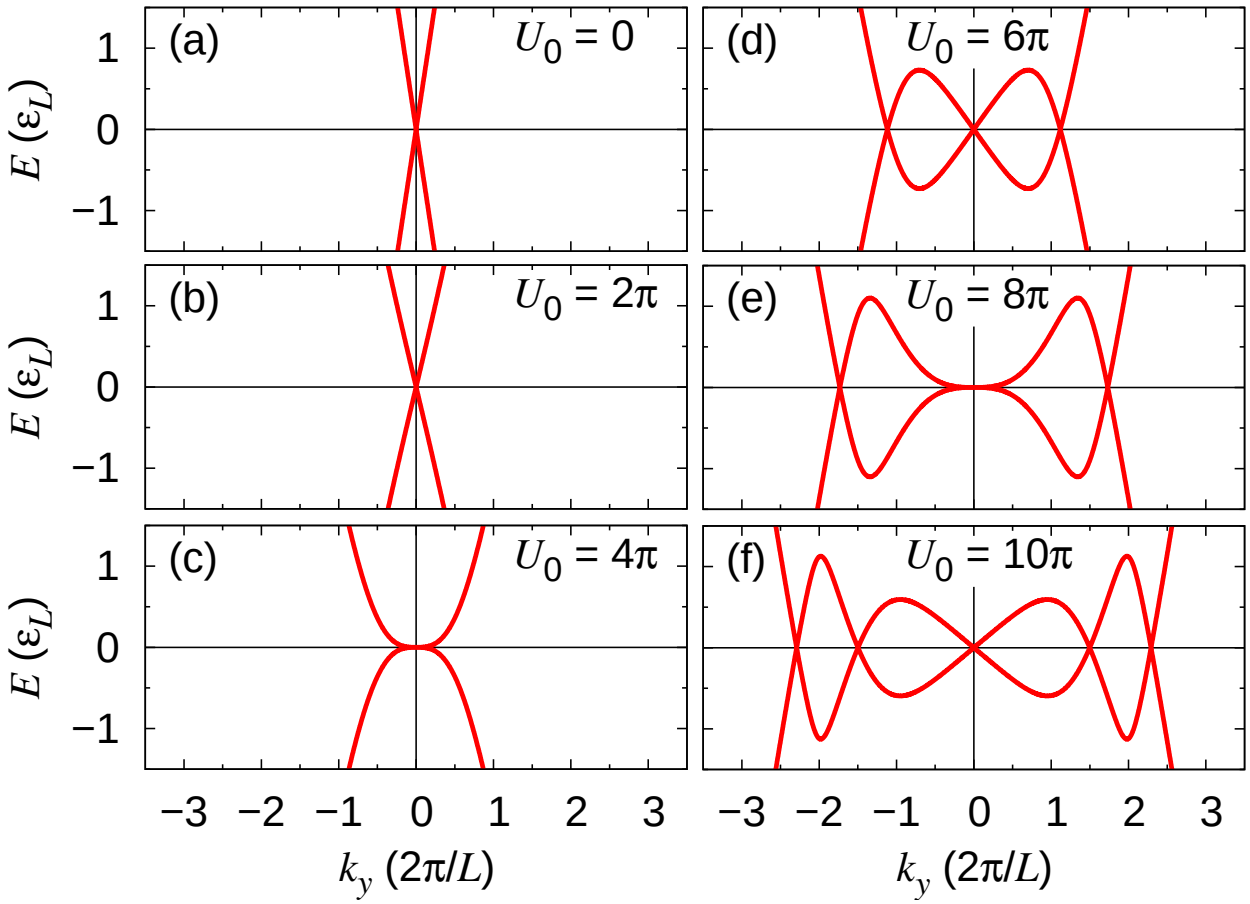

Figure 12.2: Electron energy (in units of $\varepsilon_L = \hbar v_0/L$) versus k_y with $k_x = 0$ in GSs shown in Fig. 12.1 for several different values of barrier height U_0 (specified in each panel in units of ε_L).

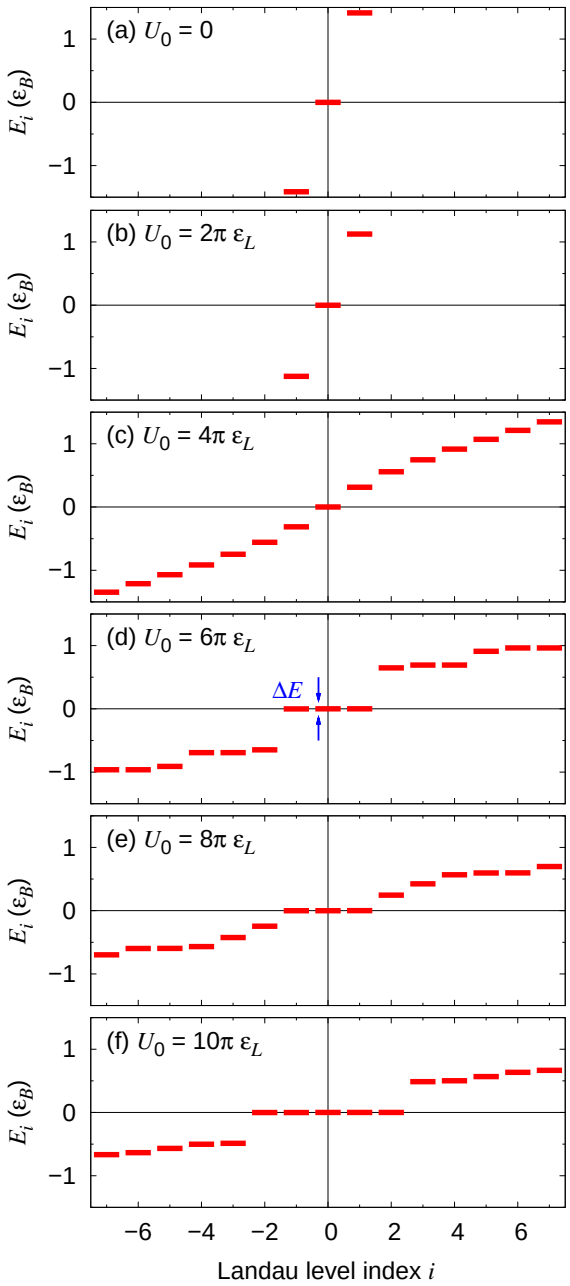

Figure 12.3: Landau level energy E_i (in units of $\varepsilon_B \equiv \hbar v_0/l_B$ with $l_B = \sqrt{\hbar c/eB}$) versus the Landau level index i ($i = 0, \pm 1, \pm 2, \ldots$) in GSs formed with a 1D Kronig-Penney potential for several different values of barrier height U_0, with lattice period $L = 0.5 l_B$. The LLs now have a finite width ΔE (shown not to scale and exaggerated in the figure) arising from the k_y dependence of the energy of the electronic states in a perpendicular magnetic field [9]. Note the 3-fold and the 5-fold degeneracies around $E_i = 0$ in (d) and (f), respectively. (If the spin and valley degeneracies are considered, those become 12-fold and 20-fold, respectively.)

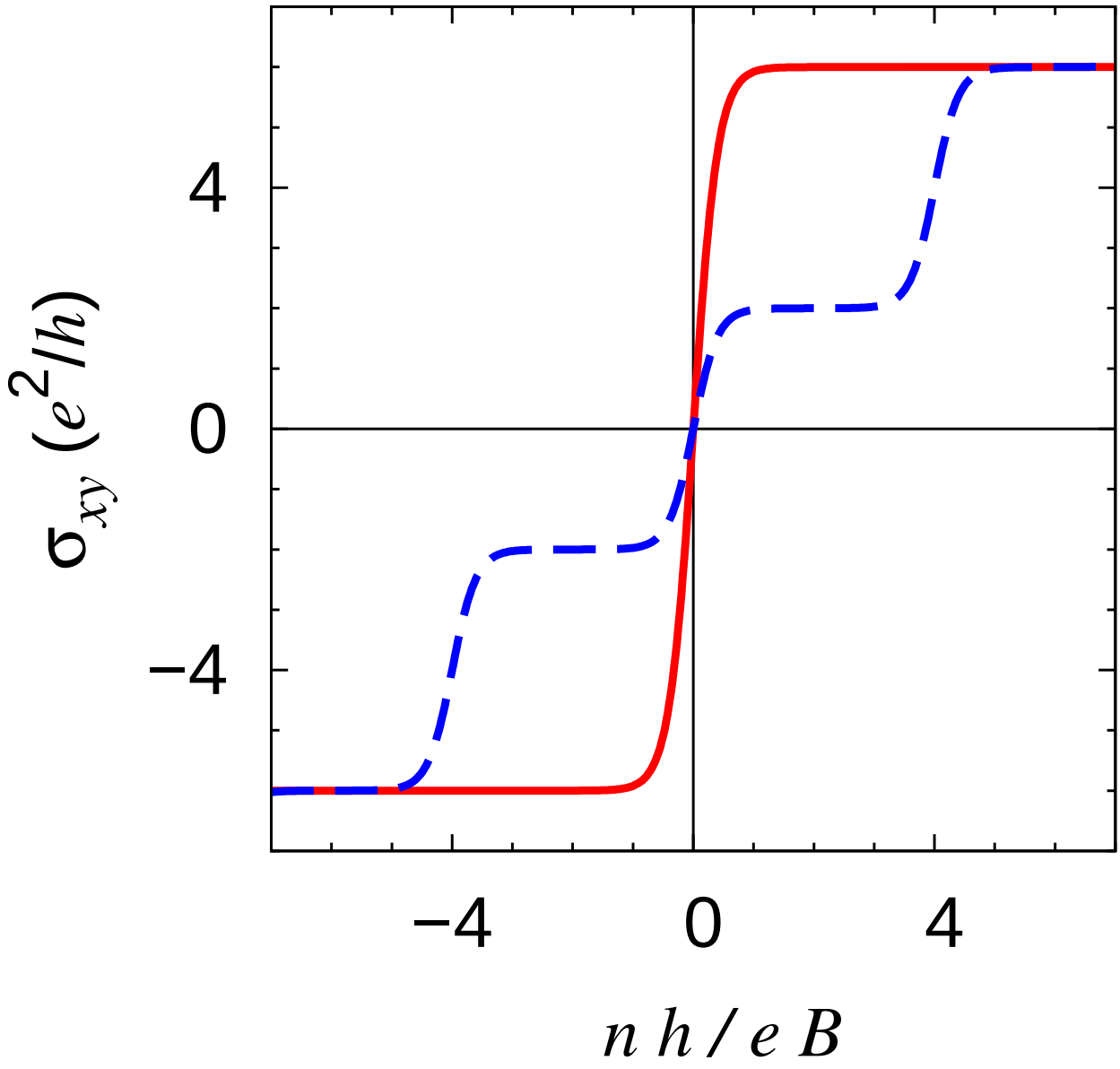

Figure 12.4: Hall conductivity σ_{xy} versus carrier density (with an artificial broadening for illustration) for a 1D Kronig-Penney GS with U_0 near $6\pi\hbar v_0/L$ (solid line) is compared to that of pristine graphene (dashed line).

The dependence of the Hall conductivity σ_{xy} on the charge carrier density n most directly reflects the degeneracy of the LLs. Figure 12.4 schematically shows that, depending on the superlattice potential parameters, σ_{xy} of the GSs considered has a $4(2N+1)\,e^2/h$ step as the density is scanned from hole-like to electron-like carriers. (We have put in the additional factor 4 coming from the spin and valley degeneracies in this discussion and in Fig. 12.4.) Because the degeneracy of the LLs in the 1D GSs is insensitive to a variation in U_0, this qualitative difference in σ_{xy} of the 1D GSs from that of pristine graphene (Fig. 12.4) is expected to be robust, and will provide a measurable signature of the unique electronic structure of the 1D GSs.

12.4 Conclusion

In conclusion, we have shown that the electronic structure of 1D graphene superlattices can have additional Dirac cones at the same energy as the original cones at the K and K' points of pristine graphene. These new massless particles contribute to a $4(2N+1)$-fold degeneracy in the zero-energy Landau levels, whose signature is reflected in a $4(2N+1)\,e^2/h$ Hall conductivity step where $N = 0$, 1, 2, ... depending on the superlattice potential parameters. This feature of the electronic structure of the 1D graphene superlattices gives rise to new properties for the quantum Hall effect. Equally importantly, these new phenomena may provide a direct way to characterize the peculiar electronic structure of these systems experimentally.

12.5 Supplementary discussion

12.5.1 Sinusoidal superlattice

In previous sections, we state that the essential features in the electronic structure of graphene superlattices (GSs) revealed by considering the Kronig-Penney type of potential remain valid for GSs made with different types of periodic potentials. In this section, we support this by showing the results for GSs with sinusoidal types of external periodic potentials [Fig. 12.5(a)].

The function $\alpha(x)$ defined by Eq. (6) in Ref. [83] for a sinusoidal type of external periodic potential $V(x) = V_0 \sin(2\pi x/L)$ is $\alpha(x) = -V_0 L/\pi\hbar v_0 \cdot \cos(2\pi x/L)$. Therefore, as shown in Eqs. (9) and (15) of Ref. [83], the group velocity at the original Dirac point perpendicular to the periodic direction is given by $v_y = f_0 v_0$, where v_0 is the group velocity in pristine graphene and $f_0 = J_0(LV_0/\pi\hbar v_0)$. Here, $J_0(x)$ is the zeroth order Bessel function of the first kind. Our calculations show that a new pair of massless Dirac points are generated whenever $f_0 = 0$, i.e., V_0 is equal to

$$V_0^N = \pi x_{0,N} \frac{\hbar v_0}{L}\,, \tag{12.2}$$

where $x_{0,N}$ is the N-th root of $J_0(x)$ (e.g., $x_{0,1} = 2.405$, $x_{0,2} = 5.520$, etc.) [Fig. 12.5(b)].

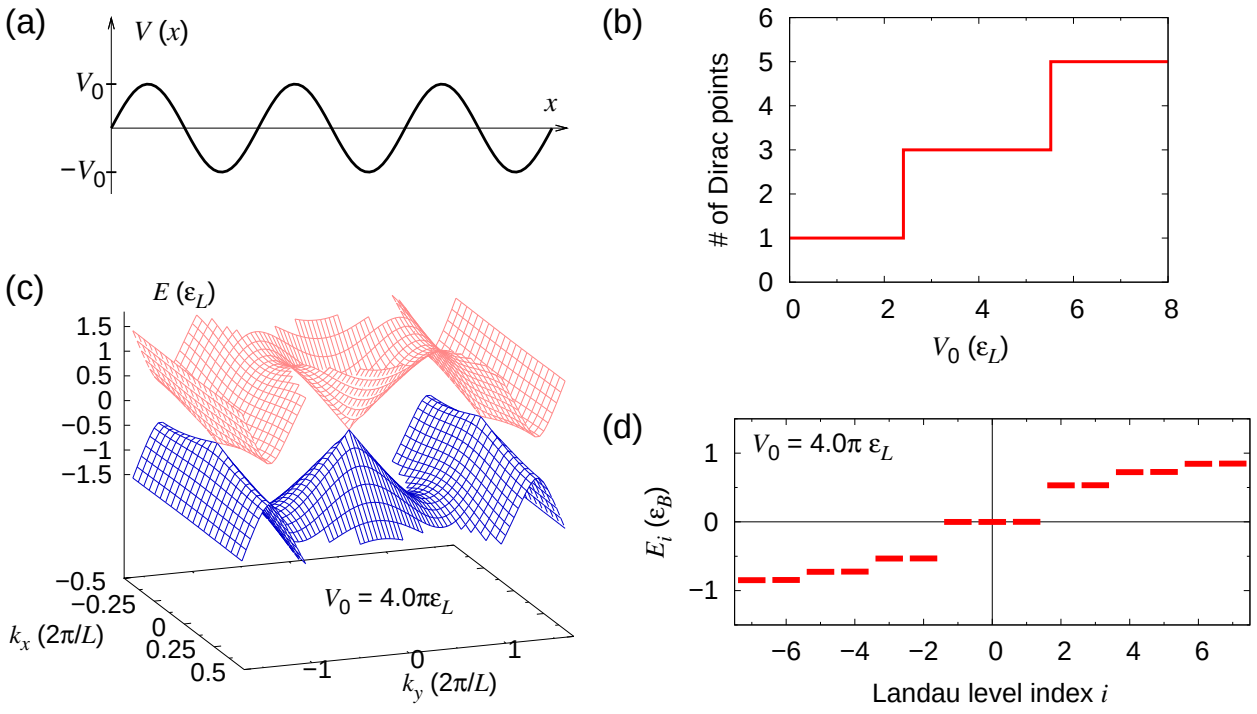

Figure 12.5: (a) Schematic diagram of a sinusoidal type of potential applied to graphene with lattice period L and potential amplitude V_0 [$V(x) = V_0 \sin(2\pi x/L)$]. (b) Number of Dirac points (not including the spin and valley degeneracies) in a GS versus V_0 in units of ε_L ($\equiv \hbar v_0/L$; for example, if $L = 20$ nm, $\varepsilon_L = 33$ meV). (c) Electron energy versus wavevector near the original Dirac point ($k_x = k_y = 0$) for a GS with $V_0 = 4.0\pi\varepsilon_L$. (d) Landau level energy E_i (in units of $\varepsilon_B \equiv \hbar v_0/l_B$ with $l_B = \sqrt{\hbar c/eB}$) versus the Landau level index i ($i = 0, \pm 1, \pm 2, \ldots$) in a GS formed with a sinusoidal potential with $V_0 = 4.0\pi\varepsilon_L$ and $L = 0.5 l_B$. Note the 3-fold degeneracy (becoming 12-fold degeneracy when the spin and valley degeneracies are considered) around $E_i = 0$.

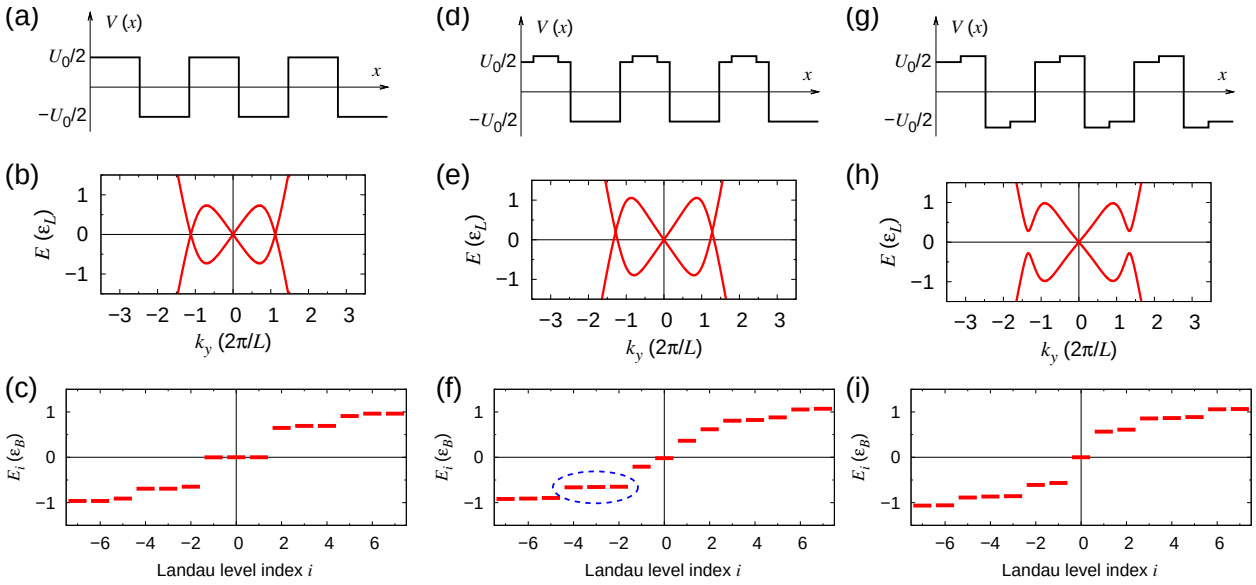

Figure 12.6: (a) Kronnig-Penney type of potential $V(x)$ given by $U_0/2$ for $0 < x < L/2$ and $-U_0/2$ for $L/2 < x < L$ with lattice period L. (b)Electron energy (in units of $\varepsilon_L = \hbar v_0/L$) versus k_y with $k_x = 0$ in a GS formed by the periodic potential in (a) with $U_0 = 6\pi\varepsilon_L$ (c) Landau level energy E_i (in units of $\varepsilon_B \equiv \hbar v_0/l_B$ with $l_B = \sqrt{\hbar c/eB}$) versus the Landau level index i ($i = 0, \pm 1, \pm 2, \ldots$) in a GS depicted in (b), with lattice period $L = 0.5 l_B$. (d) to (f): Same quantities as in (a) to (c) for a periodic potential $V(x)$ with a perturbation that breaks the odd symmetry. The perturbing potential $\Delta V(x)$ within one unit cell is given by +10 % of the potential amplitude $(U_0/2)$ for $L/8 < x < 3L/8$ and zero otherwise. Dashed circle in (f) shows a three-fold degenerate set of Landau levels. (g) to (i): Same quantities as in (a) to (c) for a periodic potential $V(x)$ with a perturbation that breaks the even symmetry. The perturbing potential $\Delta V(x)$ within one unit cell is given by +10 % and −10 % of the potential amplitude $(U_0/2)$ for $L/4 < x < L/2$ and for $L/2 < x < 3L/4$, respectively, and zero otherwise.

Figure 12.5(c) shows the energy bandstructure of a sinusoidal type of GS with $V_0 = 4.0\pi \cdot \frac{\hbar v_0}{L}$. Because this value of V_0 is between V_0^1 and V_0^2, a pair of new zero-energy massless Dirac cones are generated, and they clearly affect the Landau level degeneracy [Fig. 12.5(d)] in the same way as discussed in previous sections for a Kronig-Penney type of GS.

12.5.2 Effects of symmetry breaking on the newly generated massless fermions

In this section, we discuss the effect of symmetry breaking of the external periodic potential on the newly generated massless fermions. (The case of random perturbation is discussed in Ref. [256]. In this section, we focus on a periodic perturbing potential that breaks the

even or odd symmetry.)

Figure 12.6(a)-(c) repeats the results shown in previous sections for a Kronig-Penney type of periodic potential having both even and odd symmetries. If the odd symmetry is broken by adding an appropriate perturbation [Fig. 12.6(d)], new branches of massless fermions are still generated [Fig. 12.6(e)]. The energy at these new massless Dirac points however is different from that of the original Dirac point [Fig. 12.6(e)]. Even though $E_i = 0$ Landau level does not have the degeneracy coming from multiple Dirac points, some lower-index Landau levels still show this kind of degeneracy [Fig. 12.6(f)].

If the even symmetry is broken through a perturbing potential [Fig. 12.6(g)], new Dirac points are not generated [Fig. 12.6(h)]. However, the signature of newly generated states may still be probed with photoemission experiments or transport measurements [258].

12.5.3 Pseudospins of new massless fermions

The pseudospin character of the newly-generated massless states are different from that of the original Dirac fermions. In order to illustrate the pseudospin character of these states, we numerically calculate the overlap $\left|\left\langle \psi_{s',\mathbf{k}'} | e^{i(\mathbf{k}'-\mathbf{k})\cdot\mathbf{r}} | \psi_{s,\mathbf{k}} \right\rangle\right|^2$ of two quasiparticle states $\psi_{s,\mathbf{k}}(\mathbf{r})$ and $\psi_{s',\mathbf{k}'}(\mathbf{r})$ in a GS having wavevectors $\mathbf{k}$ and $\mathbf{k}'$ measured from the newly-generated Dirac point (appearing when $U_0 = 4\pi\varepsilon_L$ and moving along the k_y direction as U_0 is increased further). The behavior shown in Fig. 12.7, which corresponds to the overlap of the pseudospin part of the wavefunctions, is robust if the magnitudes of $\mathbf{k}$ and $\mathbf{k}'$ are smaller than $\sim 0.05 \times 2\pi/L$.

As mentioned in previous sections, the pseudospin character of these additional massless fermions [e. g. , the left and the right Dirac cones (not the center one) in Fig. 12.1(c)] are different from that of the original massless Dirac fermions. Backscattering amplitude due to a slowly varying potential within one of the new cones does not vanish (Fig. 12.7).

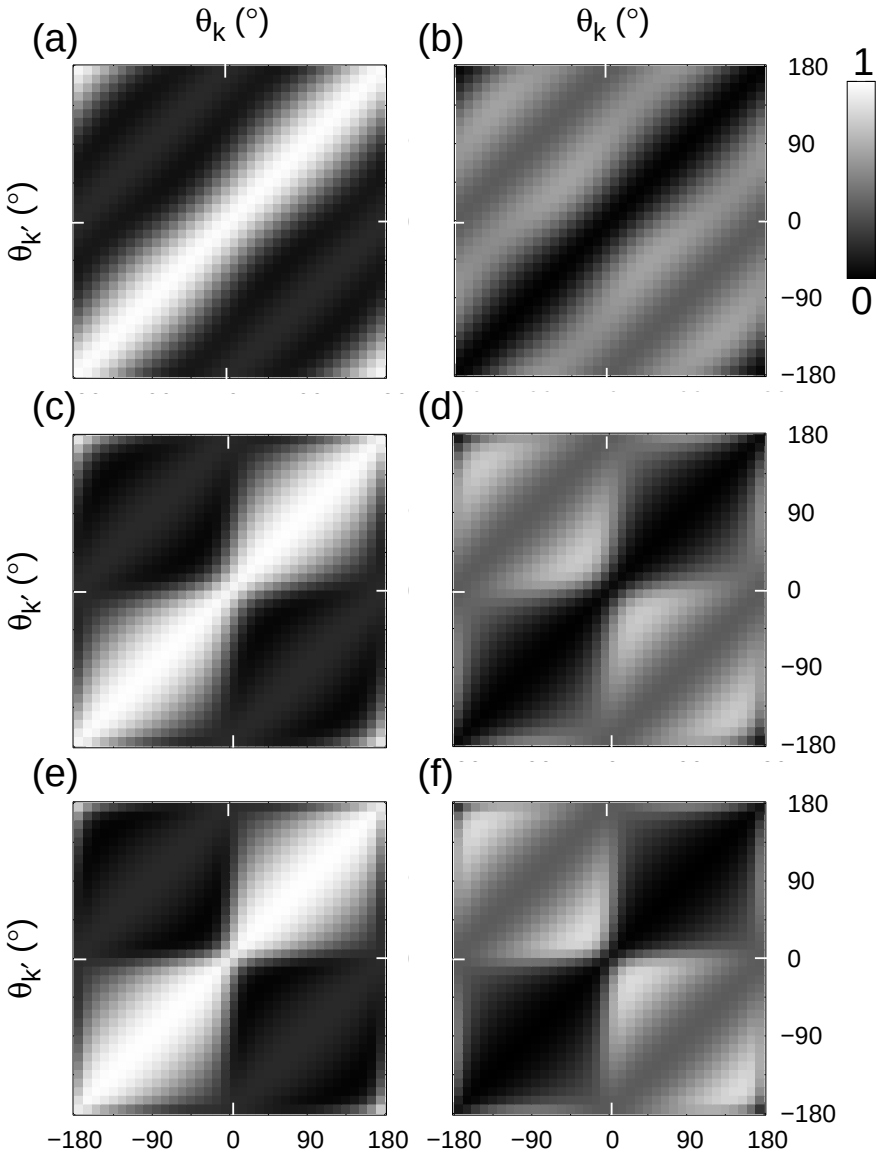

Figure 12.7: (a) and (b): Calculated overlap of two quasiparticle states $\psi^0_{s,\mathbf{k}}(\mathbf{r})$ and $\psi^0_{s',\mathbf{k}'}(\mathbf{r})$, $\left|\langle\psi^0_{s',\mathbf{k}'}|e^{i(\mathbf{k}'-\mathbf{k})\cdot\mathbf{r}}|\psi^0_{s,\mathbf{k}}\rangle\right|^2$, in a GS depicted in Fig. 12.5(a) with $U_0 = 6\pi\varepsilon_L$ versus $\theta_\mathbf{k}$ and $\theta_{\mathbf{k}'}$ which are the angles between the k_x axis and wavevectors $\mathbf{k}$ and $\mathbf{k}'$, measured from the newly-generated massless Dirac point (appearing when $U_0 = 4\pi\varepsilon_L$ and moving along the k_y direction as U_0 is increased further), respectively. The overlap is shown in a gray scale (0 in black and 1 in white). The results show negligible dependence on $|\mathbf{k}|$ and $|\mathbf{k}'|$ when they are smaller than $\sim 0.05 \times 2\pi/L$ (in the figures, $|\mathbf{k}| = |\mathbf{k}'| = 0.02 \times 2\pi/L$). The two states are in the same band ($s' = s$) in (a) and are in different bands ($s' = -s$) in (b). (c) and (d), and, (e) and (f): Same quantities as in (a) and (b) for GSs with $U_0 = 8\pi\varepsilon_L$ and $U_0 = 10\pi\varepsilon_L$, respectively.

Chapter 13

Making massless Dirac fermions from patterned two-dimensional electron gases

13.1 Introduction

Graphene [34, 35, 36, 182], a honeycomb lattice of carbon atoms, is composed of two equivalent sublattices of atoms. The dynamics of the low-energy charge carriers in graphene may be described to a high degree of accuracy by a massless Dirac equation with a two-component pseudospin basis which denotes the amplitudes of the electronic states on these two sublattices. The quasiparticles have a linear energy dispersion near the corners **K** and **K′** (the Dirac points) of the hexagonal Brillouin zone and an isotropic group velocity independent of the propagation direction [77, 259, 78, 200]. Consequently, the density of states (DOS) varies linearly and vanishes at the Dirac point energy. The sublattice degree of freedom of the wavefunctions is given by a pseudospin vector that is either parallel or anti-parallel to the wavevector measured from the Dirac point, giving rise to a chirality being 1 or -1, respectively [77, 78, 200]. These two fundamental properties of graphene, linear energy dispersion and the chiral nature of the quasiparticles, result in interesting phenomenon such as half-integer quantum Hall effect [35, 36], room temperature quantum Hall effect [260], Klein paradox [80], and suppression of backscattering [78, 200, 79], as well as some novel predicted properties such as electron supercollimation in graphene superlattices [81, 82].

As a possible realization of another two-dimensional (2D) massless Dirac particle system, theoretical studies on the physical properties of particles in optical honeycomb lattices [261] have been performed [262, 263, 264, 265, 266]. The behaviors of ultra-cold atoms in a honeycomb lattice potential were considered, in principle, to be equivalent to those of the low-energy charge carriers in graphene [262].

In this chapter, we propose a different practical scheme for generating massless Dirac fermions. We show through exact numerical calculations within an independent particle pic-

ture that applying an appropriate nanometer-scale periodic potential with hexagonal symmetry onto conventional two-dimensional electron gases (2DEGs) will generate massless Dirac fermions at the corners of the supercell Brillouin zone (SBZ). We find that the potential configurations needed should be within current laboratory capabilities, and this approach could benefit from the highly developed experimental techniques of 2DEG physics [267] including recent advances in self-assembly nanostructures [268, 269, 270].

We moreover find that the band velocity and the energy window within which the dispersion is linear may be varied by changing the superlattice parameters or the effective mass of the host 2DEG, thus providing a different class of massless Dirac fermion systems for study and application. Interestingly, the amplitude of the periodic potential does not affect the band velocity about the Dirac points. But, if the external periodic potential is too weak, there is no energy window within which the total DOS vanishes linearly. The linear energy dispersion and the chiral nature of states around the Dirac points of these 2DEG superlattices are found to be identical to those of graphene. Also, the associated up and down pseudospin states naturally correspond to states localizing, respectively, on two equivalent sublattice sites formed by the superlattice potential.

13.2 Numerical results

Let us consider a 2DEG with $E(\mathbf{p}) = p^2/2m^*$ where m^* is the electron effective mass. This is a good approximation to the energy dispersion of the lowest conduction band in diamond- or zinc-blende-type semiconductor quantum wells, which have effective masses ranging from $m^* = 0.02\ m_e \sim 0.17\ m_e$ where m_e is the free electron mass [271]. We shall consider explicitly two cases in the numerical calculations: $m^* = 0.05\ m_e$ and $m^* = 0.1\ m_e$.

Figure 13.1(a) shows the muffin-tin periodic potential considered in our numerical calculations, whose value is $U_0\,(> 0)$ in a triangular array of disks of diameter d and zero outside. Figure 13.1(b) is the corresponding Brillouin zone. The muffin-tin form is chosen for ease of discussion; the conclusions presented here are generally valid for any hexagonal potential.

We shall first discuss our numerical results and later consider the approximate analytic solutions. Figure 13.2 shows the calculated bandstructures of the lowest two bands for several hexagonal 2DEG superlattices with different effective mass m^*, lattice parameter L (with potential barrier diameter $d = 0.663\,L$ [272]), and barrier height U_0. As the barrier height is decreased, the energy window within which the energy dispersion is linear is reduced (Fig. 13.2). (The potential barrier heights used in our calculations are typical of values employed in confining 2DEGs [267].) However, the group velocity at the Dirac point is insensitive to the barrier height (Fig. 13.2). On the other hand, as the effective mass m^* of the 2DEG or the lattice parameter L is increased, the group velocity decreases (Fig. 13.2).

Figure 13.3 shows the DOS of a hexagonal 2DEG superlattice with $m^* = 0.05\,m_e$, $U_0 = 0.45$ eV, $L = 10$ nm and $d = 6.6$ nm. The DOS has a linear behavior around the Dirac point energy within a ~ 40 meV energy window. The charge density required to dope the system to reach the Dirac point energy is 2.3×10^{12} cm^{-2}, which is in the range of typical

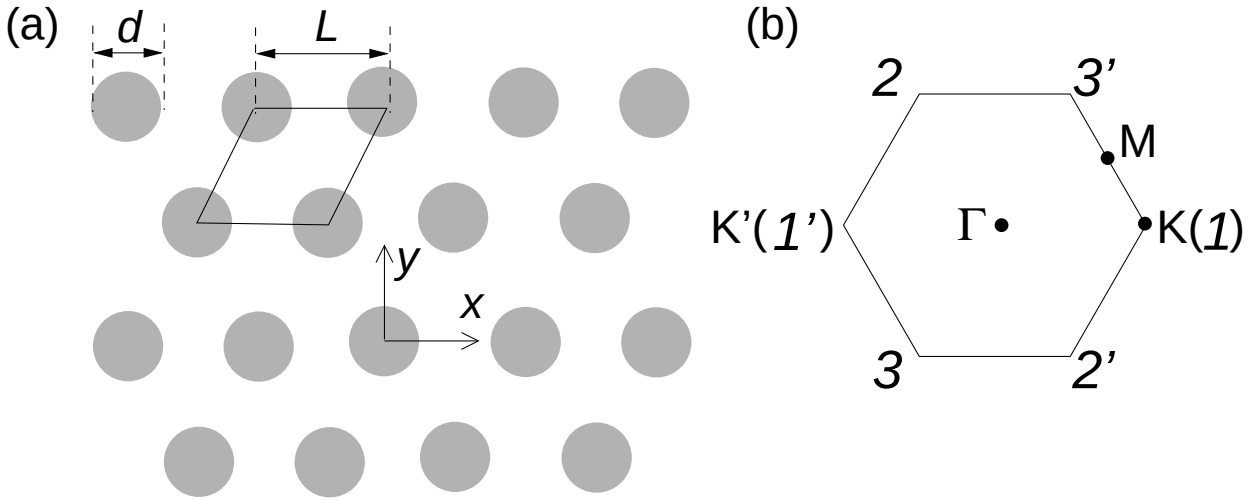

Figure 13.1: (a) A muffin-tin type of hexagonal periodic potential with a spatial period L. The potential is $U_0\,(>0)$ inside the gray disks with diameter d and zero outside. (b) The Brillouin zone of hexagonal lattice in (a).

value in 2DEG studies [267], and may be tuned by applying a gate voltage or by light illumination [273].

13.3 Analytical calculation

With the above results established from the numerical calculations, to gain further insight, we now present analytical expressions for the energy dispersion relation and wavefunctions around the SBZ corners obtained from degenerate perturbation theory. We concentrate on states with wavevector $\mathbf{k}+\mathbf{K}$ near the $\mathbf{K}$ point in the SBZ, i. e., $|\mathbf{k}| \ll |\mathbf{K}|$. Let us set the energy of the empty lattice bandstructure at the $\mathbf{K}$ point to zero, define W as the Fourier component of the periodic potential connecting $1 \to 2$, $2 \to 3$ and $3 \to 1$ in Fig. 13.1(b) [272], and denote v_0 as the group velocity of the electron state at the $\mathbf{K}$ point of the 2DEG before applying the periodic potential. [For $E(\mathbf{p}) = p^2/2m^*$, $v_0 = \hbar K/m^*$. However, the derivation below is not confined to a quadratic energy dispersion for the original 2DEG.] Due to the inversion symmetry of the system considered here, W is real. The wavefunction $\psi_{\mathbf{k}}(\mathbf{r})$ may be approximately expressed as a linear combination of three planewave states

$$\begin{aligned}\psi_{\mathbf{k}}(\mathbf{r}) = \frac{1}{\sqrt{3A_c}}\,[&c_1 \exp\left(i(\mathbf{K}_1+\mathbf{k})\cdot\mathbf{r}\right)\\ &+c_2 \exp\left(i(\mathbf{K}_2+\mathbf{k})\cdot\mathbf{r}\right) + c_3 \exp\left(i(\mathbf{K}_3+\mathbf{k})\cdot\mathbf{r}\right)]\ ,\end{aligned} \tag{13.1}$$

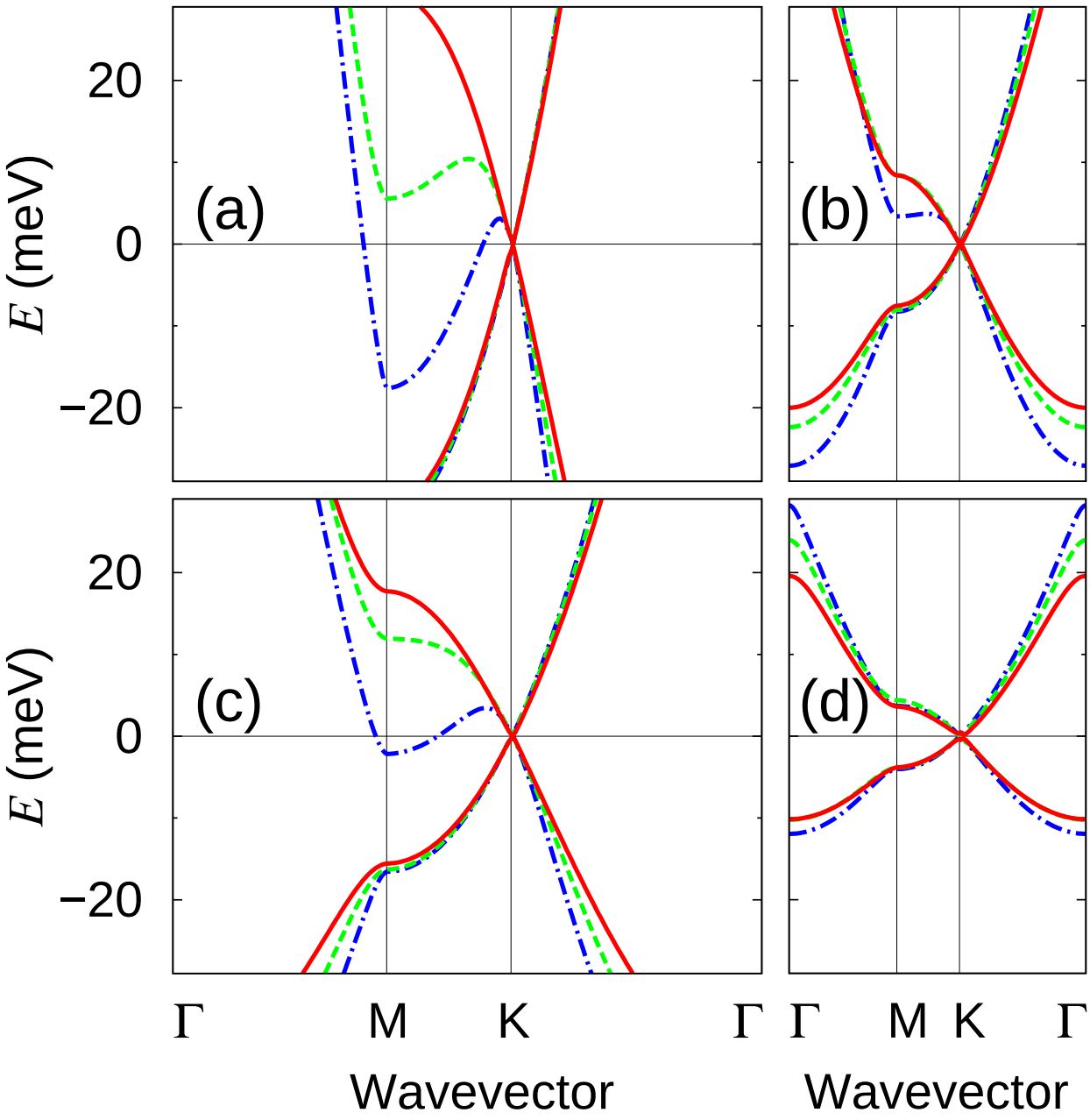

Figure 13.2: Calculated energy bandstructure of the lowest two bands of a hexagonal 2DEG superlattice shown in Fig. 13.1(a). (a) $m^* = 0.05\,m_e$ and $L = 10$ nm, (b) $m^* = 0.05\,m_e$ and $L = 20$ nm, (c) $m^* = 0.1\,m_e$ and $L = 10$ nm, and (d) $m^* = 0.1\,m_e$ and $L = 20$ nm. The diameter of the disks d is set to $d = 0.663\,L$ (see text). Solid, dashed, and dash-dotted lines show results for U_0 equal to 0.45 eV, 0.15 eV, and 0.05 eV, respectively. The Dirac point energy (i. e. , the energy at the crossing of the two bands at **K**) is set to zero.

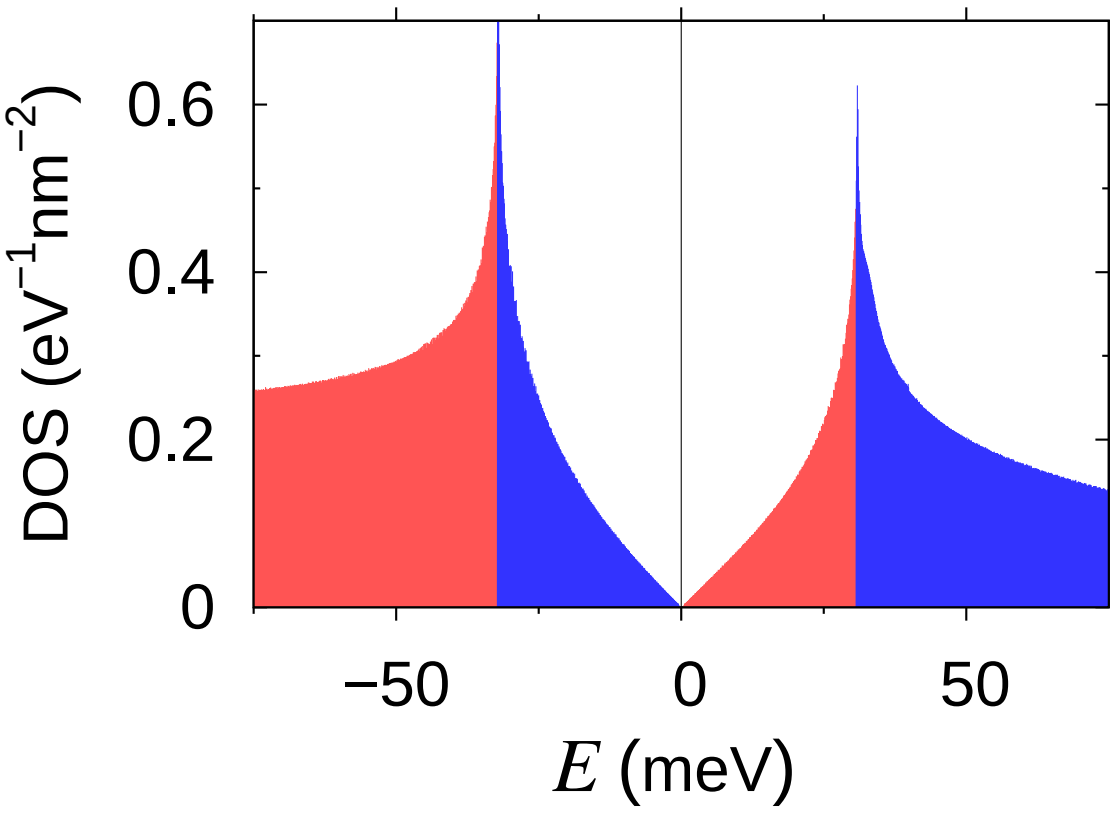

Figure 13.3: The DOS of a triangular 2DEG superlattice with $m^* = 0.05\, m_e$, $U_0 = 0.45$ eV, $L = 10$ nm and $d = 6.6$ nm. (The zero of energy is set at the Dirac point. Electron and hole orbits are indicated by bright and dark colors, respectively.) The charge density needed to fill the conduction band up to the Dirac point energy is 2.3×10^{12} cm^{-2}.

where A_c is the area of the 2DEG and $\mathbf{K}_1$, $\mathbf{K}_2$ and $\mathbf{K}_3$ represent wavevectors at the SBZ corners *1*, *2* and *3*, respectively, in Fig. 13.1(b). Equivalently, we could express the eigenstate as a three-component column vector $\mathbf{c} = (c_1, c_2, c_3)^{\mathrm{T}}$. Within this basis, the Hamiltonian H, up to first order in k, is given by $H = H_0 + H_1$, where

$$H_0 = W \begin{pmatrix} 0 & 1 & 1 \\ 1 & 0 & 1 \\ 1 & 1 & 0 \end{pmatrix} \tag{13.2}$$

and

$$H_1 = \hbar v_0 \, k \begin{pmatrix} \cos\theta_{\mathbf{k}} & 0 & 0 \\ 0 & \cos\left(\theta_{\mathbf{k}} - \frac{2\pi}{3}\right) & 0 \\ 0 & 0 & \cos\left(\theta_{\mathbf{k}} - \frac{4\pi}{3}\right) \end{pmatrix} . \tag{13.3}$$

Here $\theta_{\mathbf{k}}$ is the polar angle of the wavevector $\mathbf{k}$ from the $+x$ direction.

The eigenvalues of the unperturbed Hamiltonian H_0 are

$$E_0 = -W, \ -W, \ 2W \, , \tag{13.4}$$

which are also the energies of the states of the superlattice at $\mathbf{k} = 0$. We now focus on the doubly-degenerate eigenstates with eigenvalue $-W$. We shall find the $\mathbf{k}$-dependence of the eigenenergies and eigenvectors of H corresponding to these two states within degenerate perturbation theory by treating H_1 as a perturbation, which is approximate for $\hbar \, v_0 \, k < W$. Also, for a wavefunction in the form of Eq. (13.1) to give a good description of the actual wavefunction, the energy to the next planewave state [which is $\hbar^2(2K)^2/2m^* - \hbar^2K^2/2m^*$] should be smaller than W. Therefore, the approximation is valid within the regime $\hbar \, v_0 \, k < W < \frac{3\hbar^2K^2}{2m^*}$, or, equivalently,

$$\frac{4\pi\hbar^2}{3m^*L}k < W < \frac{8\pi^2\hbar^2}{3m^*L^2} \, , \tag{13.5}$$

where we have used $K = 4\pi/3L$.

The two eigenvectors of H_0 with eigenvalue $-W$ are

$$\mathbf{c}_1 = \frac{1}{\sqrt{2}} \begin{pmatrix} 0 \\ 1 \\ -1 \end{pmatrix} \quad \text{and} \quad \mathbf{c}_2 = \frac{1}{\sqrt{6}} \begin{pmatrix} 2 \\ -1 \\ -1 \end{pmatrix} . \tag{13.6}$$

The term H_1, when restricted to the sub-Hilbert-space spanned by the two vectors in Eq. (13.6), is represented by a 2×2 matrix $\tilde{H}_1$

$$\tilde{H}_1 = \hbar \frac{v_0}{2} \begin{pmatrix} -k_x & -k_y \\ -k_y & k_x \end{pmatrix} , \tag{13.7}$$

where $k_x = k \cos\theta_{\mathbf{k}}$ and $k_y = k \sin\theta_{\mathbf{k}}$. After a similarity transform $M = U^\dagger \tilde{H}_1 U$ with

$$U = \frac{1}{2} \begin{pmatrix} 1+i & -1-i \\ -1+i & -1+i \end{pmatrix} , \tag{13.8}$$

we obtain

$$M = \hbar \frac{v_0}{2} \left(k_x \sigma_x + k_y \sigma_y \right) . \tag{13.9}$$

Here, σ_x and σ_y are the Pauli matrices. Equation (13.9) is just the effective Hamiltonian of graphene [77] with a group velocity

$$v_g = v_0/2 = \frac{\hbar K}{2m^*} = \frac{2\pi\hbar}{3m^* L} . \tag{13.10}$$

Therefore, the group velocity is reduced if the effective mass is increased or the lattice parameter of the superlattice is increased, but it is insensitive to the amplitude of the external periodic potential, which explains the results of the numerical calculations shown in Fig. 13.2. Also, the size of the linear energy dispersion window [Eq. (13.5)] is dictated by the value of W, which for the muffin-tin potential in Fig. 13.1(a) with $d = 0.663\, L$ is $W = 0.172\, U_0$ [272] in agreement with the numerical calculations.

The eigenvalues and the eigenvectors of M are

$$E(s, \mathbf{k}) = s\, \hbar \frac{v_0}{2}\, k \,, \tag{13.11}$$

and

$$|s, \mathbf{k}\rangle = \frac{1}{\sqrt{2}} \begin{pmatrix} 1 \\ 0 \end{pmatrix} + \frac{1}{\sqrt{2}}\, s\, e^{i\theta_{\mathbf{k}}} \begin{pmatrix} 0 \\ 1 \end{pmatrix} , \tag{13.12}$$

respectively, where $s = \pm 1$ is a band index [77]. The vectors $\begin{pmatrix} 1 \\ 0 \end{pmatrix}$ and $\begin{pmatrix} 0 \\ 1 \end{pmatrix}$ are the up and the down pseudospin eigenstates of σ_z, respectively [274].

The up and the down pseudospin eigenstates may be expressed within the basis of the original Hamiltonian H using Eqs. (13.8) and (13.6) as

$$|\uparrow\rangle \;=\; \frac{1}{\sqrt{3}} e^{i\frac{3\pi}{4}} \left(1,\; e^{-i\frac{2\pi}{3}},\; e^{-i\frac{4\pi}{3}} \right)^{\mathrm{T}} \tag{13.13}$$

and

$$|\downarrow\rangle \;=\; \frac{1}{\sqrt{3}} e^{i\frac{3\pi}{4}} \left(1,\; e^{i\frac{2\pi}{3}},\; e^{i\frac{4\pi}{3}} \right)^{\mathrm{T}} , \tag{13.14}$$

respectively [275]. The real space pseudospin wavefunctions $\langle \mathbf{r}| \uparrow\rangle$ and $\langle \mathbf{r}| \downarrow\rangle$ are obtained by putting the coefficients in Eqs. (13.13) and (13.14) into Eq. (13.1). Figures 13.4(a) and 13.4(b) show $|\langle \mathbf{r}| \uparrow\rangle|^2$ and $|\langle \mathbf{r}| \downarrow\rangle|^2$, respectively. Note that the up and the down pseudospin states are seen as localized at the two equivalent sublattices formed by the external periodic potential, in perfect analogy with the behavior in graphene.

Let us now consider the Landau levels for the above hexagonal 2DEG superlattice in a magnetic field $\mathbf{B} = B\, \hat{z}$ when the Fermi level is at the Dirac point energy. In exact analogy with graphene, the low-energy Landau levels shifted by the energy W (i. e. , having the energy

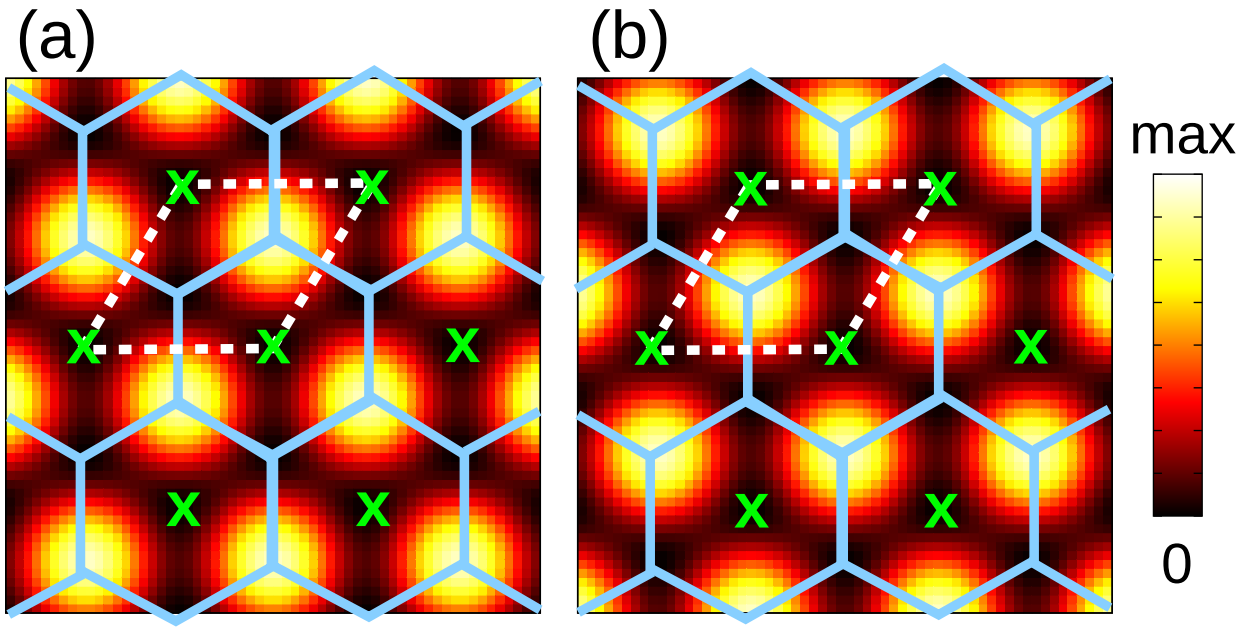

Figure 13.4: Probability densities of the pseudospin states in a hexagonal 2DEG superlattices (a) $|\langle \mathbf{r}| \uparrow\rangle|^2$ and (b) $|\langle \mathbf{r}| \downarrow\rangle|^2$. Note that the amplitudes of the states are localized at two different but equivalent sublattices. The centers of the potential barrier disks [Fig. 13.1(a)] are shown as 'x' marks, and the honeycomb structure is drawn to illustrate the connection to the superlattice structure.

zero at the Dirac point energy) are $E_n = \hbar\omega_c \,\mathrm{sgn}(n)\sqrt{|n|}$, where $\omega_c = v_0\sqrt{|e|B/2\hbar c}$ is the cyclotron frequency [259]. Here, for an appropriately constructed superlattice potential, the half-integer quantum Hall effect [35, 36] should be observable. Moreover, the spacing between quantum Hall plateaus is tunable by changing the lattice parameter of the potential or the effective mass of the original 2DEG.

13.4 Conclusion

In conclusion, we have shown that chiral massless Dirac fermions are generated if an appropriate nanometer-scale periodic potential with hexagonal symmetry is applied to a conventional 2DEG in semiconductors. These quasiparticles have a linear energy dispersion, with a group velocity half the value of the states before applying the periodic potential, and a wavefunction chiral structure exactly the same as that of graphene. The up and the down pseudospin states are shown to be localized at two different but equivalent sublattices formed by the superlattice potential. The quasiparticle group velocity moreover is tunable by changing the effective mass of the original 2DEG or the lattice parameter of the superlattice potential. Our findings thus provide a new class of systems for experimental investigations and practical applications of 2D massless Dirac quasiparticles.

Chapter 14

Energy gaps and Stark effect in boron nitride nanoribbons

14.1 Introduction

Two-dimensional crystals, including graphene and single layer of hexagonal boron nitride (BN), have recently been fabricated [34]. Among them, only graphene has been studied extensively [72]. Unlike graphene, a hexagonal BN sheet is a wide gap insulator like bulk hexagonal BN [276] and is a promising material in optics and opto-electronics [277].

Graphene nanoribbons (GNRs) [278] with width a few to a hundred nanometers have been produced by lithographical patterning [185, 279] or chemical processing [280] of graphene. We expect that boron nitride nanoribbons (BNNRs) could also be made using similar or other techniques. Figures 14.1(a) and 14.1(b) show the structures of an armchair BNNR with $N_{\rm a}$ dimer lines ($N_{\rm a}$-aBNNR) and a zigzag BNNR with $N_{\rm z}$ zigzag chains ($N_{\rm z}$-zBNNR), respectively. A tight-binding study of the bandstructures of 21-aBNNR and 13-zBNNR (corresponding to widths ~ 3 nm) [281] and first-principles investigations of the electronic properties of small width BNNRs [282, 283] have been reported. However, to our knowledge, first-principles calculations on the electronic properties of experimentally realizable size of BNNRs have not been performed.

Under a transverse electric field, carbon nanotubes with impurity atoms are expected to show novel band gap opening behaviors [284], whereas zigzag GNRs reveal half-metallicity [184]. On the other hand, single-walled boron nitride nanotubes (SW-BNNTs), which are rolled up BN sheets [285, 286, 287], have been predicted to show gigantic Stark effect in their band gaps in response to a transverse electric field [288], and this effect has been confirmed experimentally [289]. The effect becomes stronger in larger diameter SW-BNNTs [288]. A similar phenomenon is expected in BNNRs. Unlike SW-BNNTs, however, BNNRs can be arbitrarily wide. Therefore, the consequences of the Stark effect in BNNRs would be even more dramatic than in SW-BNNTs.

In this study, we report first-principles calculations on the electronic properties of arm-

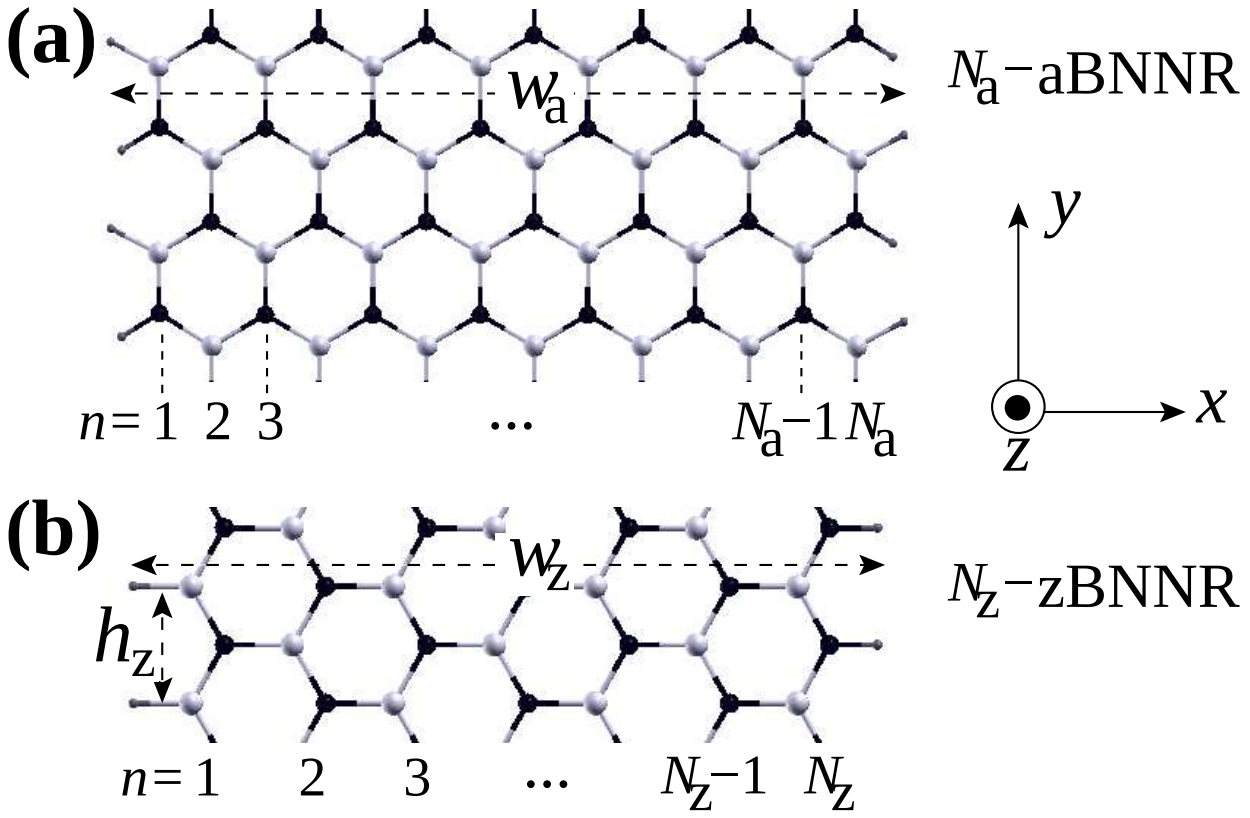

Figure 14.1: Schematic of (a) 14-aBNNR and (b) 7-zBNNR passivated by hydrogen atoms. Boron, nitrogen and hydrogen atoms are represented by white, black and grey spheres, respectively. BNNRs are periodic along the y direction.

chair and zigzag BNNRs up to width of 10 nm with hydrogen passivation of the edge carbon atoms. We show that the band gaps of armchair and zigzag BNNRs do not converge to the same value even when the ribbons are very wide. The band gap of armchair BNNRs, obtained by density functional theory (DFT) calculations within the local density approximation (LDA), converges to a value that is 0.02 eV smaller than the LDA band gap of 4.53 eV of a BN sheet [290]. Unlike armchair GNRs, the lowest unoccupied band of the armchair BNNRs is composed of edge states with energy position asymptote to a fixed value when the ribbon is wider than 3 nm, the decay length of the edge-state. The band gap of the zigzag BNNRs, also determined by edge states, is monotonically reduced as a function of increasing width and converges to a value that is 0.7 eV smaller than the LDA bulk gap because, as discussed below, of an additional edge polarization charge effect. The DFT Kohn-Sham eigenvalues within LDA in general underestimate the band gaps of materials; an accurate first-principles calculation of band gaps requires a quasiparticle approach [20]. The basic physics discovered here however should not be changed.

When a transverse electric field is applied, the highest occupied and the lowest empty states in armchair BNNRs become localized at the two different edges. Because of the external electrostatic potential difference between the two edges, the band gap is reduced with increased field strength. On the contrary, in zigzag BNNRs, depending on the field direction, the states near the band gap either become more localized at the edges or less so. Also, the band gaps and effective masses either decrease or increase depending on field strength and direction. These novel properties could be used in manipulating the transport properties of doped BNNRs.

14.2 Computational details

We performed *ab initio* pseudopotential DFT calculations within LDA in a supercell configuration using the SIESTA computer code [291]. A double-zeta plus polarization basis set was used and ghost orbitals were included to describe free-electron-like states [276, 288, 292]. A charge density cutoff of 300 Ry was used and atomic positions were relaxed so that the force on each atom is less than 0.04 eV/Å. To eliminate spurious interactions between periodic images, a supercell size of up to 20 nm×20 nm in the xz plane was used.

14.3 Results and discussion

14.3.1 Energy bandgaps and wavefunctions

The armchair BNNRs are found to have a direct gap at the zone center [left panel of Fig. 14.2(a)]. The highest occupied state, the valence band maximum (VBM), has a wavefunction which is localized at nitrogen atoms throughout the ribbon [right lower panel of Fig. 14.2(a)]. The lowest empty state, the conduction band minimum (CBM), is however an edge state with wavefunction localizing at the boron atoms on the edges [right upper panel

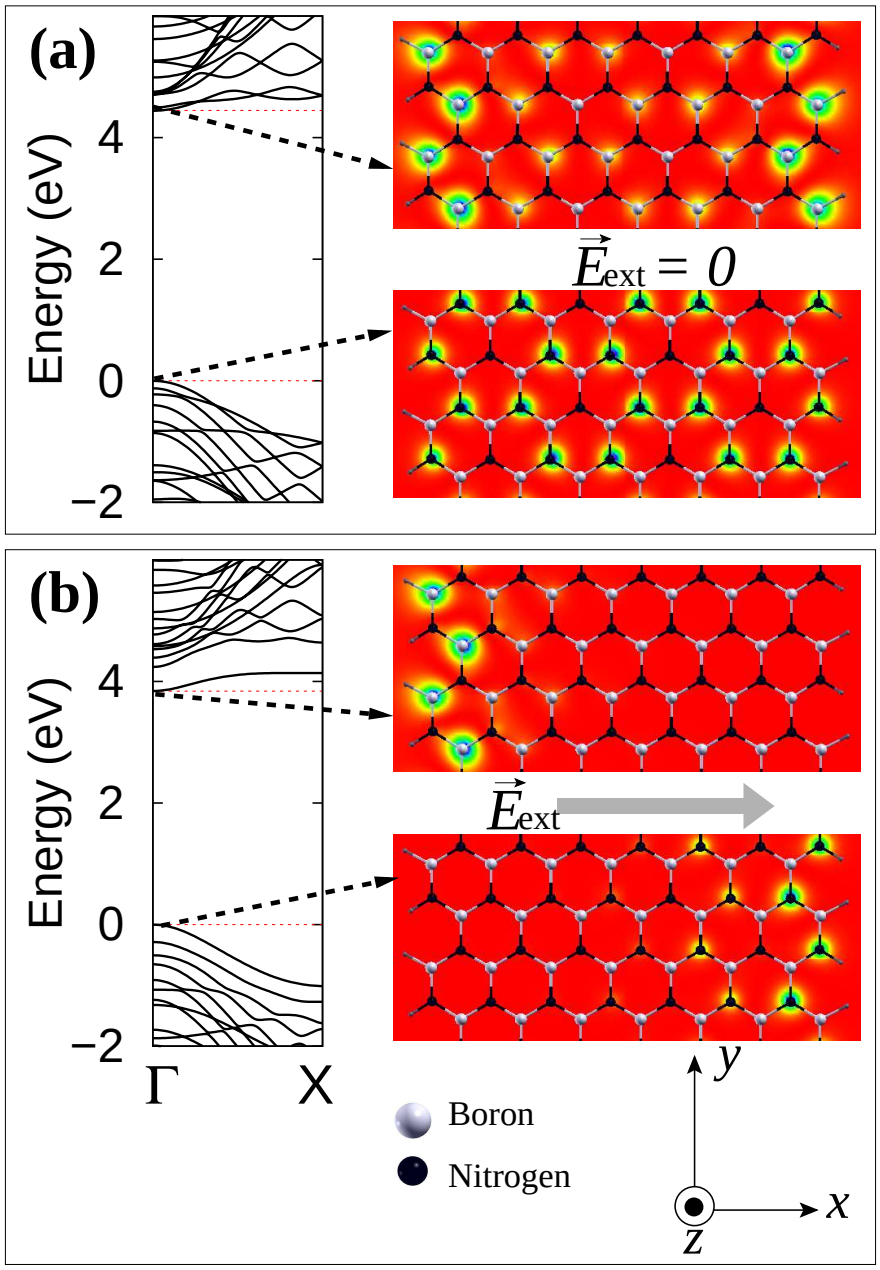

Figure 14.2: LDA energy bandstructure (left) and the squared wavefunctions integrated along z of the highest occupied state (right lower) and the lowest unoccupied state (right upper) of 14-aBNNR under an external electric field $\vec{E}_{\text{ext}}$ of strength (a) zero and (b) 0.1 eV/Å along $+x$ direction. Dashed red lines in the bandstructure indicate the energies of the band edge states. In the wavefunction plots, bright regions are associated with high densities.

of Fig. 14.2(a)]. In contrast, the corresponding state for an armchair GNRs is delocalized throughout the ribbon [293]. The total potential near the edge of the armchair BNNRs is different from that of the bulk. By incorporating this variation into the *on-site potential energies* of a few BN dimer lines near the edges, one could reproduce the main features of the states near the band gap within a tight-binding formulation.

The zigzag BNNRs have the VBM at a point between the X and the Γ points which has wavefunction localized at the nitrogen edge and the CBM at the X point which has wavefunction localized at the boron edge [Fig. 14.3(a)], in agreement with results by Nakamura *et al.* [282]

14.3.2 Stark effect: energy bandgap and carrier effective mass

Figure 14.4(a) shows the band gap variation of the armchair and the zigzag BNNRs with width. The most interesting and somewhat counter-intuitive feature is that as the width increases, band gaps of the armchair and the zigzag BNNRs converge to different values neither of which is that of a BN sheet. This is because the CBM or the VBM are determined by edge-states.

The edge-state band gaps of armchair BNNRs show a family behavior with respect to the number of dimer lines $N_{\rm a}$ [inset of Fig. 14.4(a)], the family with $N_{\rm a} = 3n - 1$ having the smallest gaps where n is an integer. A similar trend is observed in armchair GNRs [294, 293, 183, 295, 296]. The edge-state band gaps of the armchair BNNRs converge to a near constant value roughly when the ribbon is wider than 3 nm [Fig. 14.4(a)]. This characteristic length is related to the decay length of the CBM edge-state. Figure 14.4(b) shows the squared electron wavefunctions of the CBM states of 14-aBNNR and 26-aBNNR integrated in the yz plane. These states are localized on the boron atoms near the two edges. When the width is about 3 nm as in the 26-aBNNR, the wavefunction from the two edges begins to decouple and thus stabling its energy position.

In zigzag BNNRs, the boron edge and the nitrogen edge are negatively and positively charged (electronic plus ionic charge), respectively. Because of this polarization, the potential felt by electrons is higher at the boron edge and lower at the nitrogen edge, contributing a factor which increases the band gap of the narrow zBNNRs since the VBM and the CBM are edge-states localized at the nitrogen edge and the boron edge, respectively [Fig. 14.3(a)]. However, as the ribbon becomes wider, the effective polarization line charge density $\sigma_{\rm eff}$, defined as

$$\sigma_{\rm eff} \equiv \hat{x} \cdot \frac{1}{w_z h_z} \int_{\mathbf{r} \in \text{ unit cell}} d\mathbf{r}\ \rho(\mathbf{r})\ \mathbf{r}$$

where $\rho(\mathbf{r})$ is the total charge density including the core charge, and h_z the spatial period along the y direction [see Fig. 14.1(b)], decreases as $\sim 1/w_z$ [Fig. 14.4(c)] due to an increased screening, resulting in the decrease and convergence of the band gap as w_z increases.

Figure 14.2(b) shows how the bandstructure and wavefunctions of a 14-aBNNR change under a 0.1 eV/Å transverse electric field. Owing to the Stark effect, the wavefunctions of the highest occupied and the lowest unoccupied states now localize at the opposite edges

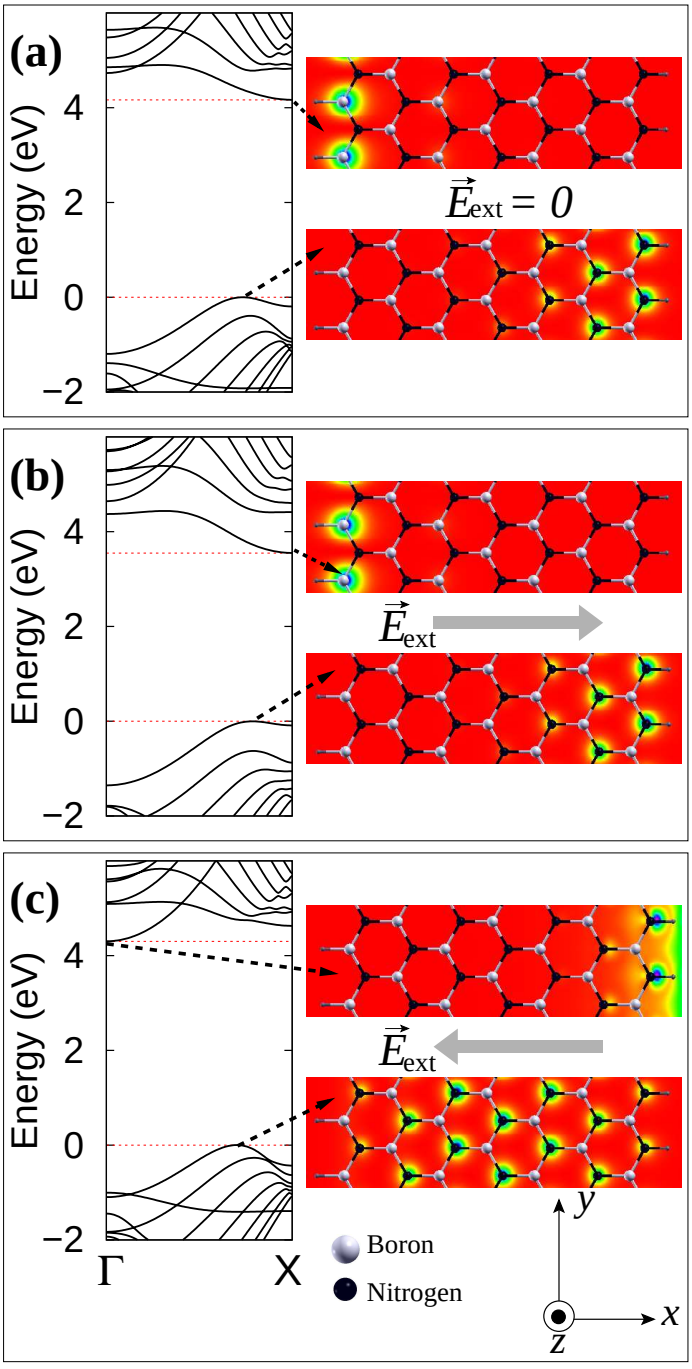

Figure 14.3: LDA energy bandstructure (left) and the squared wavefunctions integrated along z of the highest occupied state (right lower) and the lowest unoccupied state (right upper) of 7-zBNNR under an external electric field $\vec{E}_{\text{ext}}$ of strength (a) zero, (b) 0.1 eV/Å and (c) -0.1 eV/Å along the x direction. Dashed red lines in the bandstructure indicate the energies of the band edge states. In the wavefunction plots, bright regions are associated with high densities.

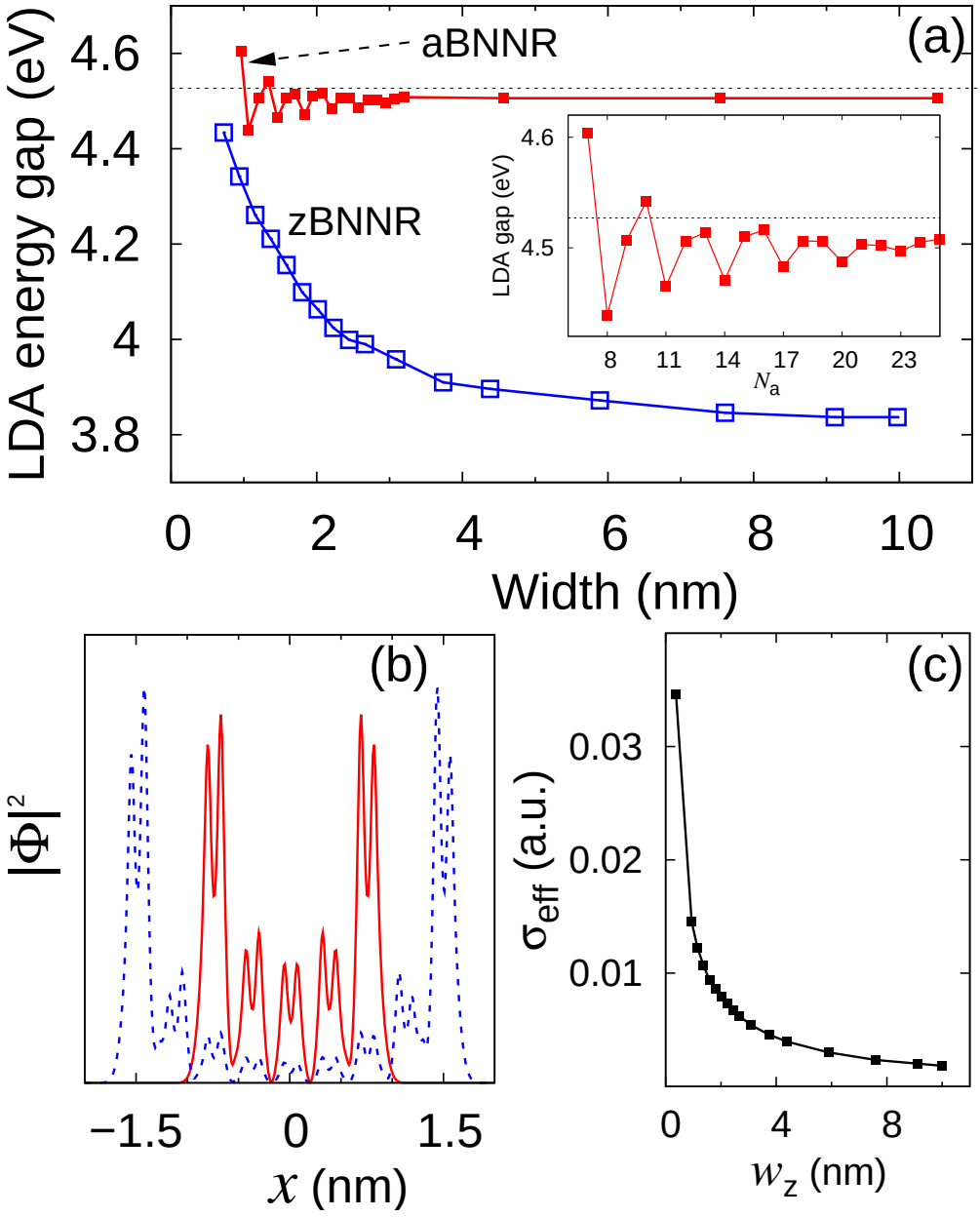

Figure 14.4: (a) Band gaps of armchair (filled squares) and zigzag (empty squares) BNNRs versus their widths. Inset: band gaps of armchair BNNRs versus N_a (see Fig. 14.1). Solid lines are a guide to the eyes. Dashed lines indicate the bulk band gap of a BN sheet with no edges. (b) Probability distributions $|\Phi(\mathbf{r})|^2$ integrated in the yz plane (see Fig. 14.1) versus the distance along the x direction from the ribbon center for the lowest unoccupied state in 14-aBNNR (solid line) and 26-aBNNR (dashed line). (c) The effective polarized line charge density σ_{eff} of zigzag BNNRs versus w_z. The solid line is a guide to the eyes.

where the external electrostatic potential felt by an electron is higher and lower, respectively [right panel of Fig. 14.2(b)]. Thus, the band gaps of armchair BNNRs decrease when a transverse electric field is applied [left panel of Fig. 14.2(b)]. A similar behavior has been predicted [288] and observed [289] in BNNTs.

Figures 14.3(b) and 14.3(c) show how the bandstructure and the edge-state wavefunctions of a 7-zBNNR change under a 0.1 eV/Å transverse electric field. When an electric field is applied toward $+x$ direction, the VBM and CBM edge-state wavefunctions do not change qualitatively [right panel of Fig. 14.3(b)]. Thus, for a similar reason as in the armchair BNNRs, the band gap decreases [left panel of Fig. 14.3(b)]. When the electric field is applied along $-x$ direction, the potential felt by an electron localized at the right edge (the nitrogen edge) is decreased whereas that at the left edge (the boron edge) is increased. Therefore, the energy gap between these two states increases as shown in Fig. 14.3(c). (Actually, the energy of the original lowest empty state has been pushed upward by so much that the state is no longer the CBM state.) At the same time, the VBM states tend to delocalize [right lower panel of Fig. 14.3(c)].

Figures 14.5(a) and 14.5(b) show the band gap variation of BNNRs with field strength. In armchair BNNRs, the band gap decreases when the field strength increases regardless of its direction [Fig. 14.5(a)]. A similar behavior has been observed in SW-BNNTs [288]. For example, for the 10 nm wide 84-aBNNR the LDA band gap is reduced from 4.5 eV to less than 1.0 eV under a 0.1 eV/Å field. In zigzag BNNRs, at *small* field strength, the band gap decreases when the field is along $+x$ direction but increases when the field is reversed [Fig. 14.5(b)]. In other words, zigzag BNNRs show asymmetric Stark effect. However, as the field becomes stronger, the band gap decreases regardless of the direction. Moreover, the band gap variations, when plotted against the difference in the external electrostatic potential between the two edges, fall on a universal curve for ribbons with different widths [insets of Figs. 14.5(a) and 14.5(b)]. This is because the gap determining states localize on different edges as the field becomes strong; thus, the change in their energy difference is directly related to the potential difference between the edges.

Figures 14.5(c) and 14.5(d) show the effective mass of the hole carrier at the VBM for a range of external field strength. In armchair BNNRs, the hole mass of the VBM is independent of the field strength. In contrast, the corresponding effective mass in zigzag BNNRs changes with the external field, and even more interestingly, in an asymmetric way. In particular, when the field is along $-x$ direction, the effective mass decreases substantially. Within ± 0.02 eV/Å variation of the field, the effective mass can be varied by 50 % from 0.6 m_0 to 0.9 m_0 where m_0 is the free electron mass. In the case of electron carriers in zigzag BNNRs, a nearly-free-electron state [276, 288, 292] becomes the CBM if a field stronger than a critical value, depending on the width, is applied [see Fig. 14.3(c)], and the characteristics of charge carriers change significantly. These novel phenomena demonstrate the possibility of tuning carrier mobilities of doped BNNRs by applying a transverse electric field.

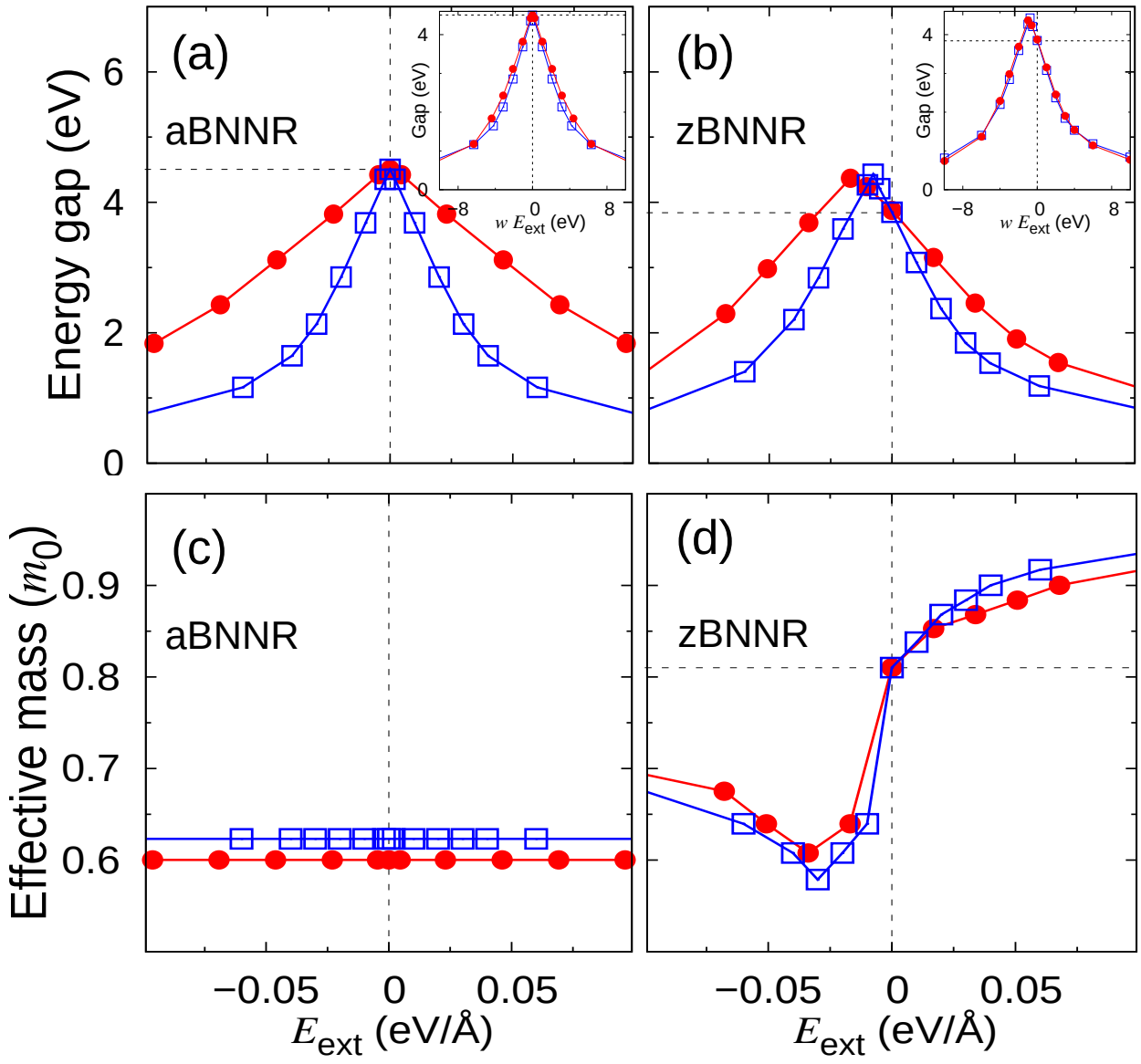

Figure 14.5: (a) and (c): LDA energy gaps and effective hole masses (in units of the free electron mass m_0) of the highest occupied band in 36-aBNNR (filled circles) and 84-aBNNR (empty squares) under a transverse electric field versus the field strength. The inset in (a) shows energy gaps as a function of the external potential difference between the two edges. (b) and (d): Similar quantities as in (a) and (c) for 27-zBNNR (filled circles) and 46-zBNNR (empty squares), respectively.

14.4 Conclusion

In summary, we have studied the electronic properties of BNNRs as a function of width with or without an external transverse electric fields. The band gap of the armchair BNNR and that of the zigzag BNNR are determined by edge-states and thus converge to values different from that of the bulk BN sheet. The electronic and the transport properties of BNNRs are shown to be tunable by an external transverse electric field. Especially, zigzag BNNRs are shown to exhibit asymmetric response to the electric field.

Chapter 15

Excitons and many-electron effects in the optical response of single-walled boron nitride nanotubes

15.1 Introduction

Boron nitride nanotubes (BNNTs) are isoelectronic to carbon nanotubes (CNTs); however, their electronic properties are quite different. Whereas carbon nanotubes are metals or semiconductors with different size bandgaps depending on diameter and chirality [297], BN nanotubes are wide gap insulators [285, 286]. Although BNNTs have been synthesized since 1995 [287], only recently optical measurement on single-walled (SW) BNNTs has been performed [298, 299, 300]. Theoretical calculations [172, 301], as well as experiments [302, 303, 304], have shown that excitonic effects dramatically alter the behavior of the optical response of single-walled CNTs. For the BNNTs, these effects are expected to be even more important due to the wide band gap nature of BNNTs.

Experimentally it is found that BN nanotubes favor zigzag structure in current synthesis processes [305]. Thus, we focus our study on the zigzag tubes. Our calculations on the (8,0) single-walled BNNT show that, indeed, many-electron effects lead to the formation of strongly bound excitons of multi-band character with extraordinarily large binding energies, which dramatically change its optical absorption spectrum.

15.2 Theory and computation

To compute the optical response, we use the method of Rohlfing and Louie [28] in which electron-hole excitations and optical spectra are calculated from first principles in three steps. First, we treat the electronic ground state with *ab initio* pseudopotential density-functional theory in the local density approximation (LDA) [13]. Second, we obtain the quasiparticle energies $E_{n\mathbf{k}}$ within the GW approximation for the electron self-energy Σ [20],

with wavefunctions and screening obtained from the LDA calculation, by solving the Dyson equation:

$$\left[-\frac{\nabla^2}{2} + V_{ion} + V_{Hartree} + \Sigma(E_{n\mathbf{k}})\right] \psi_{n\mathbf{k}} = E_{n\mathbf{k}} \psi_{n\mathbf{k}} \ .$$

Finally, we calculate the coupled electron-hole excitation energies and optical spectrum by solving the Bethe-Salpeter (BS) equation of the two-particle Green's function [28, 306]:

$$(E_{c\mathbf{k}} - E_{v\mathbf{k}})\, A^S_{vc\mathbf{k}} + \sum_{\mathbf{k}'v'c'} \langle vc\mathbf{k}|K^{eh}|v'c'\mathbf{k}'\rangle A^S_{v'c'\mathbf{k}'} = \Omega^S A^S_{vc\mathbf{k}} \ ,$$

where $A^S_{vc\mathbf{k}}$ is the exciton amplitude, K^{eh} is the electron-hole interaction kernel, and $|c\mathbf{k}\rangle$ and $|v\mathbf{k}\rangle$ are the quasielectron and quasihole states, respectively.

The LDA calculations were carried out using a plane-wave basis [41] with an energy cutoff of 100 Ry. *Ab initio* Troullier-Martins pseudopotentials [15] in the Kleinman-Bylander form [17] were used. For convergent results to better than 0.05 eV, up to 32 $\mathbf{k}$ points in the one-dimensional Brillouin zone were used for the *GW* calculations and for solving the BS equation. All calculations were carried out in a supercell geometry with a wall-to-wall intertube separation of 9.5 Å to mimic isolated tubes, together with a truncated Coulomb interaction to eliminate unphysical interactions between periodic images on the different tubes. The Coulomb interaction was truncated with a cutoff of 8 Å in the radial direction and also a cutoff of 70 Å in the tube axis direction. As shown in Ref. [307], it is important to truncate the Coulomb interaction because, if not, the unphysical intertube interactions would increase the effective screening in the system and hence reduce both the self-energy correction and the exciton binding energy. Because of depolarization effects in nanotubes [308], strong optical response is only observed for light polarized along the tube axis ($\hat{z}$). We consider only this polarization.

15.3 Results and discussion

15.3.1 Quasiparticle energy bandstructure

Figure 15.1(a) shows the quasiparticle energy corrections to the LDA energy eigenvalues. These corrections are quite large, in comparison to those for bulk hexagonal BN (h-BN) and SWCNTs. The quasiparticle corrections open the LDA gap of bulk h-BN by ≈1.58 eV near zone center or the Γ-point [276], while the gap opening in the (8,0) SWBNNT near the Γ-point is ≈3.25 eV. This is a consequence of enhanced Coulomb interaction in reduced dimension [301]. Also, due to its larger gap, the quasiparticle corrections to the gap in the (8,0) SWBNNT are larger than those for a similar SWCNT (which are ≈ 1.15 eV near the Γ-point [301]). The quasiparticle corrections also have a complex band- and energy-dependence, so for accurate results they cannot be obtained by a simple scissor shift operation. The corrections depend on the character of the wavefunction. For example, states of the fourth lowest conduction band in the LDA bandstructure are nearly-free-electron (NFE) states localized inside the tube. These tubule states form a separate branch in the quasiparticle correction diagram with significantly smaller corrections. Figure 15.1(b)

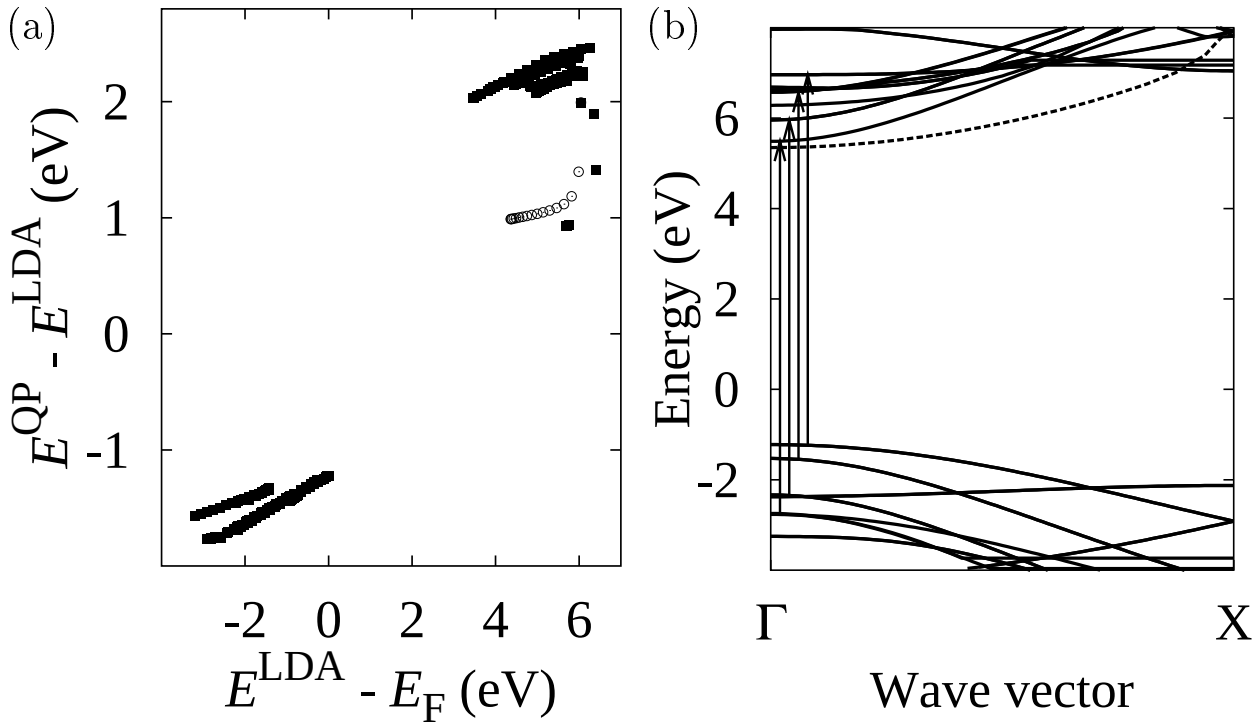

Figure 15.1: Difference between the GW quasiparticle energy and the LDA Kohn-Sham eigenvalue (a) and quasiparticle band-structure (b) for the (8,0) SWBNNT. Empty circles in (a) and the dashed line in (b) show the nearly-free-electron tubule states.

depicts the quasiparticle bandstructure of the (8,0) SWBNNT. The arrows indicate the optically allowed interband transitions between four pairs of bands which give rise to the lowest-energy peak structures in the non-interacting optical spectrum in Fig. 15.2.

15.3.2 Optical response

Figure 15.2 depicts the optical absorption spectrum calculated with and without electron-hole interaction effects. The plotted quantity is the imaginary part of the calculated dielectric susceptibility, $\chi = (\epsilon - 1)/4\pi$, multiplied by the cross-sectional area of the supercell perpendicular to the tube axis. This quantity α, as defined above, gives the polarizability per single tube in units of nm^2; so the susceptibility of an experimental sample containing a density of n infinitely long tubes per unit area may be obtained directly as $\chi = n\alpha$ if inter-tube interaction is neglected. The absorption profile changes dramatically when the electron-hole interaction is taken into account. We use the label I, I', and II to denote distinct series of bright excitons. Subscripts 1, 2, 3 and 4 refer to the ground, first-excited, second-excited and third-excited states of a particular bright exciton series, respectively. K refers to the lowest energy exciton, which is dark. The first absorption peak at 5.72 eV corresponds to a bound exciton (I_1) with a binding energy of 2.3 eV. The area under this peak is 0.87 nm^{2}eV. Excitons I_1 and I_1' are different states, made up of transitions from the same set of four pairs of valence and conduction subbands of the (8,0) BNNT, all of which have similar quasiparticle transition energies from 8.1 eV to 8.3 eV (See arrows in Fig. 15.1(b)). These transitions are coupled strongly to each other by the electron-hole interaction to form the lowest optically active states (the singly-degenerate I_1 and doubly-degenerate I_1'). This behavior is very different from the (8,0) SWCNT in which the exciton states are composed mainly of transitions between a single pair of quasiparticle bands.

15.3.3 Wavefunctions: comparison with carbon nanotubes

The mixing of transitions of different subbands alters the electron-hole wavefunction, localizing further the electron amplitude with respect to the hole position in real space and making it deviate from a one-dimensional behavior with spatial variations in directions perpendicular to the tube axis. Figure 15.3(a) shows the isosurface plots of the electron distribution $|\Phi(\mathbf{r}_e, \mathbf{r}_h)|^2$ with the hole position $\mathbf{r}_h$ fixed (the black star in the figure) for the first bound exciton (I_1). Figure 15.3(b) quantifies the electron-hole correlation for this state by plotting $|\Phi|^2$ along the tube axis after integrating out the electron coordinates in the perpendicular plane (the hole position is set at zero). The position of the peaks in Fig. 15.3(b) corresponds to the position of plane of boron atoms, i.e., the photoexcited electron is localized on the boron atoms near the hole. Thus, as expected, the photo-excitation process corresponds to a transfer of electron from nitrogen atoms to nearby boron atoms; but the resulting electron and hole amplitudes are strongly correlated with an extent of only a few inter-atomic distances. Figure 15.3(c) showes the excited electron probability

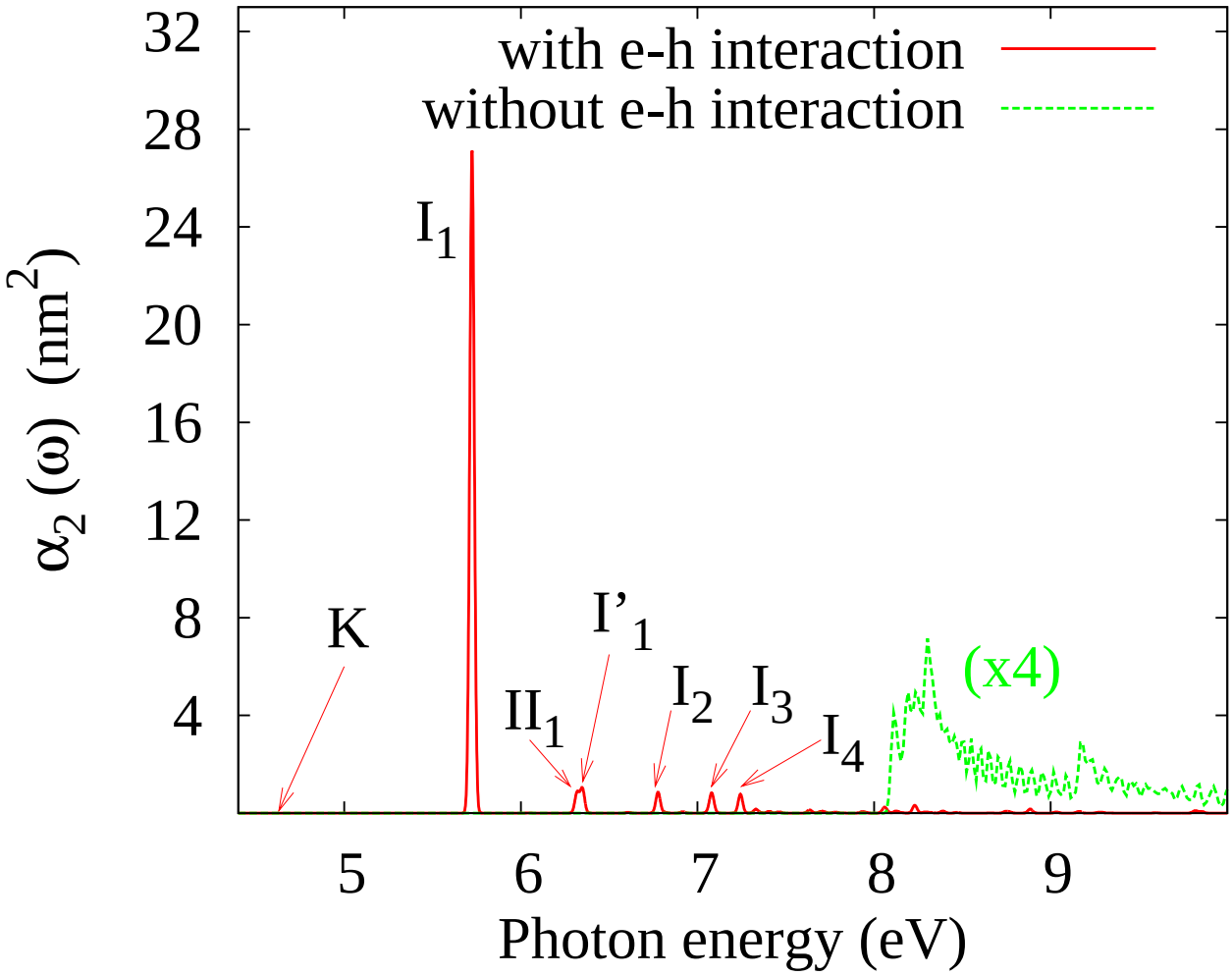

Figure 15.2: Absorption spectra of the (8,0) SWBNNTs. The imaginary part of the polarizability per tube $\alpha_2(\omega)$ is given in unit of nm^2 (see text). The spectra are broadened with a Gaussian of 0.0125 eV.

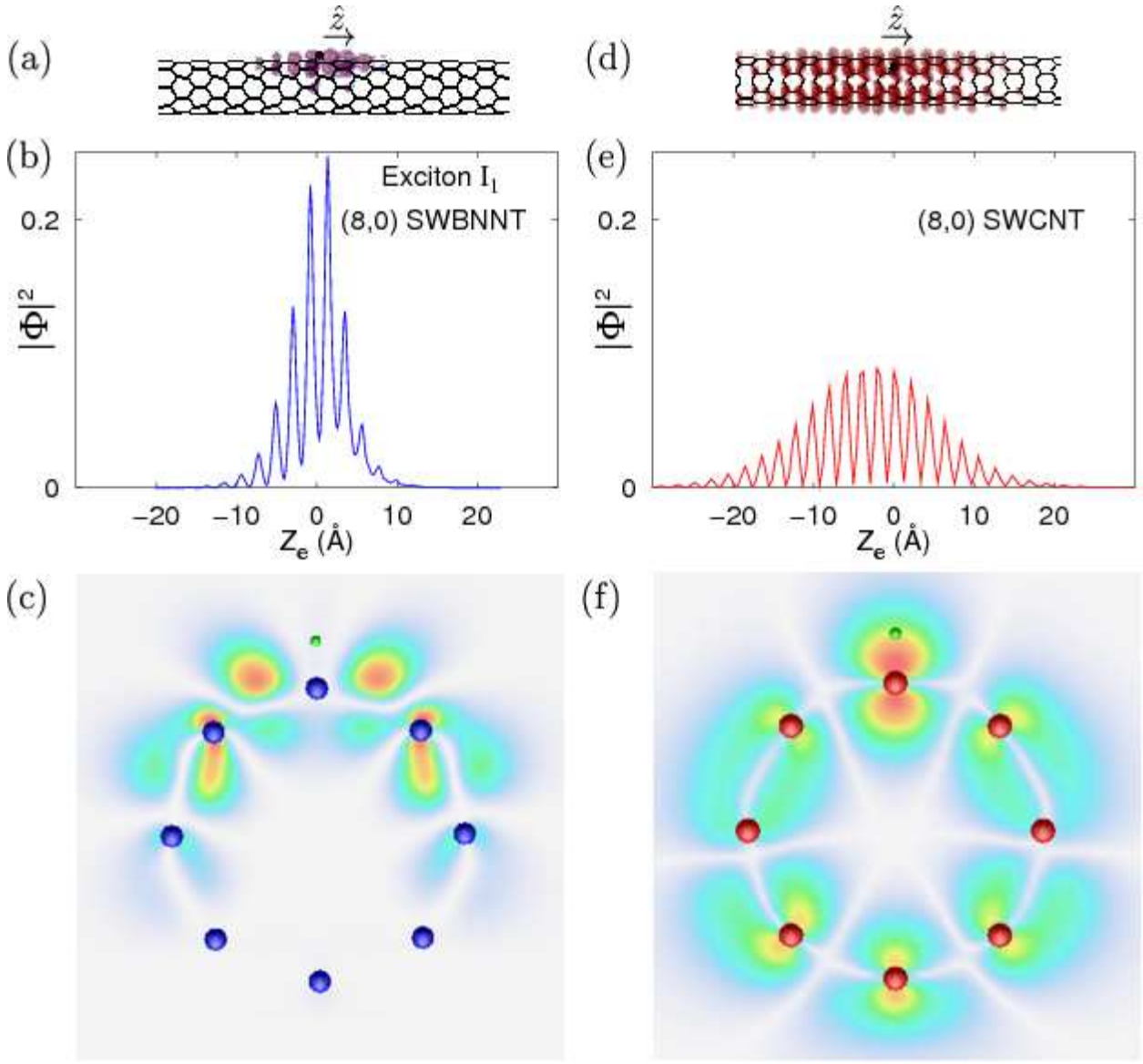

Figure 15.3: (a)-(c): Wavefunction of the lowest energy bright exciton of the (8,0) SWBNNT. (a) Isosurface plot of electron probability distribution $|\Phi(\mathbf{r}_e, \mathbf{r}_h)|^2$ with the hole fixed at the position indicated by black star. (b) $|\Phi(\mathbf{r}_e, \mathbf{r}_h)|^2$ averaged over tube cross section. Hole position is set at zero. (c) $|\Phi(\mathbf{r}_e, \mathbf{r}_h)|^2$ evaluated on a cross-sectional plane of the tube. (d)-(f): Wavefunction of the lowest energy bright exciton of the (8,0) SWCNT. Plotted quantities are similar to those in (a)-(c).

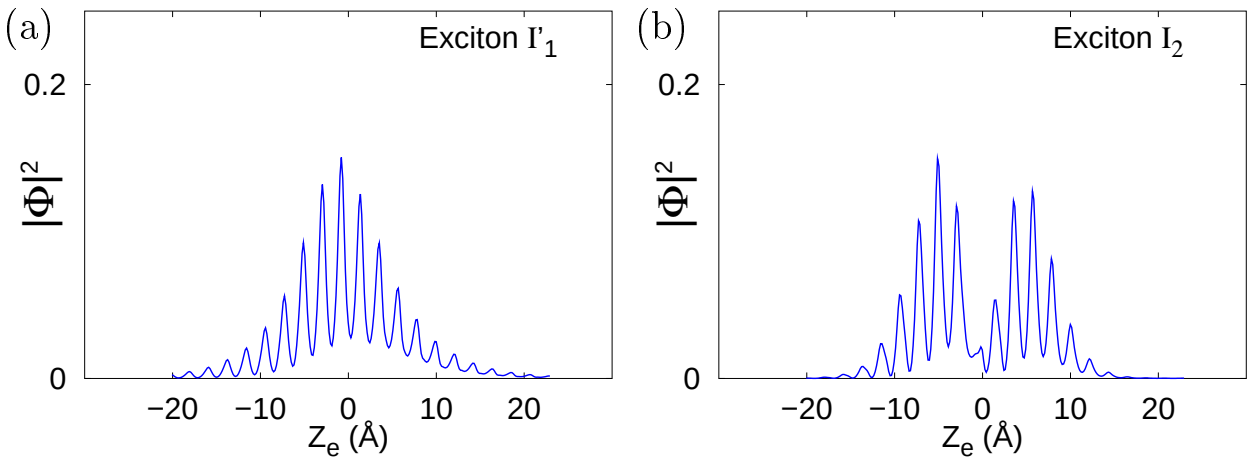

Figure 15.4: Wavefunctions of excitons of the (8,0) SWBNNT. Plotted quantities are similar to those in Fig. 15.3(b).

distribution in a plane perpendicular to the tube axis and containing the hole as well as other nitrogen atoms.

As a comparison to carbon nanotubes, Fig. 15.3(d)-(f) shows similar quantities as in Fig. 15.3(a)-(c) but for the first bright bound exciton in the (8,0) SWCNT [301]. In the figure, the hole is fixed slightly above a carbon atom. The exciton in the (8,0) SWBNNT is significantly more tightly bound than that in the (8,0) SWCNT and cannot really be viewed as a one-dimensional object. The root-mean-square size of the exciton along the tube axis is 3.67 Å for the (8,0) SWBNNT and 8.59 Å for the (8,0) SWCNT, and their binding energies are 2.3 eV and 1.0 eV, respectively. This difference in behavior is due to the wide bandgap and weaker screening in SWBNNT. Also, we note that while the binding energy of the excitons in the bulk h-BN is only 0.7 eV [309, 310], the binding energy in the (8,0) SWBNNT is more than three times larger.

Figures 15.4(a) and 15.4(b) show similar quantities as in Fig. 15.3(b) for the excitons I_1' and I_2. For exciton I_1', the electron is less tightly bound to the hole than in exciton I_1. The state I_2, which is an excited state of exciton I_1, is also more diffuse than I_1 and the electron amplitude is not at a maximum near the hole which is the case for I_1(Fig. 15.3(b)). We also note that, for the (8,0) SWBNNT, there are numerous dark excitons distributed rather uniformly in energy below and among the bright excitons shown in Fig. 15.2. The energy of the lowest doubly-degenerate bound dark exciton (K) is at 4.63 eV. This dark exciton is made up of transitions from the highest valence band to the lowest conduction band (the NFE tubule state) in the quasiparticle bandstructure, and has a binding energy of 1.94 eV with respect to these interband transition energies.

The various lowest-energy exciton states (for both bright and dark excitons) derived from the various different sets of interband transitions, on the average, have a large binding energy of about 1.9 eV. However, the binding energy of the first bright exciton is 2.3 eV. We ascribe

this extra binding energy of about 0.4 eV to the fact that four different sets of interband transitions are strongly coupled in forming the first bright exciton (I_1). This strong coupling mixes states from the different transitions, splits the excitation energy levels, and increases the binding energy of the final lowest-energy exciton.

15.3.4 Comparison with experiment

Arenal et al. [299] and Aloni et al. [300] have recently done EELS measurements of the optical gaps of SW and multiwalled BNNTs. The optical gaps measured in both experiments are 5.8 ± 0.2 eV, independent of the geometry of nanotubes, which is in very good agreement with our calculation (5.72 eV).

Lauret et al. [298] measured directly the optical properties of SWBNNTs and observed three absorption peaks at 4.45, 5.5 and 6.15 eV, respectively. The calculated first peak position for the (8,0) tube is rather close to the observed 5.5 eV peak. Also, the difference between the second and the third observed absorption peak position in the experiment is 0.65 eV, very close to the difference between the first and the second absorption peaks in our calculation which is 0.62 eV, while the difference between the first and the second observed peak position is 1.05 eV. We thus suspect that the observed second peak at 5.5 eV in Ref. [298] is likely due to an exciton, corresponding in nature to our first absorption peak. Moreover, theory predicts that, for the (8,0) BNNT, there are many dark excitons whose excitation energies are 4.63 eV and higher. The excitation energy difference between the first dark exciton (K) and the first bright exciton (I_1) in our calculation is 1.1 eV. This suggests that the 4.45 eV peak in the experiment may be due to some dark excitons with low excitation energies activated by external perturbations. Another possibility is that this extra low-energy feature may arise from impurities. Small differences between calculated excitation energies and measured values are unavoidable due to environmental effects. The theory is for a perfectly isolated tube, whereas experimentally the tubes are surrounded by a dielectric medium which can modify the excitation energies. For SWCNTs, the effect of the surrounding dielectric medium on the optical spectrum is expected to be small (even though it can be important for the exciton binding energy) due to an almost cancellation between the quasiparticle self-energy correction and the binding energy of excitons [301]. For SWBNNTs, screening by external medium may be more important because intrinsic screening of the BNNT is much weaker. In particular, for the isolated (8,0) SWBNNT, we find that the energy difference between the quasiparticle self-energy correction and the binding energy of the exciton is large (about 0.9 eV). In the presence of a dielectric medium, we expect this to decrease, which would likely result in a red-shift in the excitation energies.

Although the average diameter of the tubes measured in the experiments [298, 299, 300] ($\approx$ 1.4 nm) is greater than the diameter of the relaxed (8,0) SWBNNT in our work (0.65 nm), we expect the comparison to be reasonable because the binding energy of SWBNNTs is found to be an insensitive function of its diameter. For example, the exciton binding energy (2.1 eV) of an isolated BN sheet [169], which is equivalent to an infinitely large diameter SWBNNT, is only smaller than that of our (8,0) SWBNNT by 0.2 eV. Since the

exciton binding energy is expected to increase with decreasing diameter, the exciton binding energies for the SWBNNTs in the experiments would be smaller than our calculated value by at most about 0.1-0.2 eV.

Among previous theories of the optical properties of BNNTs, Guo and Lin [311] carried out LDA calculations without considering many-electron effects. Their optical absorption spectra are qualitatively different from the present final results. From their results for the (6,0) and (9,0) tubes, we can deduce an LDA-RPA peak position for the (8,0) tube to be near 4.9 eV, as we find in our LDA-RPA level calculation. The first peak position in Fig. 15.2 with electron-hole interaction included is blue shifted by about 0.9 eV from that of the LDA-RPA calculation.

15.4 Conclusion

In summary, we have done calculation on the (8,0) SWBNNT to study the effects of many-electron interactions on its optical response. The GW corrections to the quasiparticle excitation energies of the SWBNNTs are significantly larger than those for SWCNTs or bulk h-BN. Also, the quasiparticle energy corrections are found to be complicated so that interpolation by a simple scissor shift operation is not a good scheme for accurate calculation. Theory predicts that, unlike the non-interacting case, the absorption spectrum of the (8,0) SWBNNT is dominated by a huge peak at 5.72 eV, due to an exciton with a large binding energy of 2.3 eV. This exciton state is made up of optically-allowed transitions between four different pairs of subbands. Moreover, an intricate set of dark excitons is found to exist. Self-energy and electron-hole interaction effects therefore are even more important in the optical response of the SWBNNTs than in the SWCNTs.

Chapter 16

Effects of stacking on the optical response of hexagonal boron nitride

16.1 Introduction

Hexagonal boron nitride (hBN) [312] has a large bandgap applicable for some optical applications, e. g. , ultraviolet lasers [277]. Also, hBN is a precursor in the synthesis of boron nitride (BN) nanotubes [285, 286, 287, 169, 170] which could play an important role in nano-optics or opto-electronics applications, or of BN nanoribbons [282, 283, 313, 314]. Recently, single or a few layer hBN has been fabricated [315, 316, 317, 318]. Therefore, a basic understanding of the electronic and optical properties of hBN is quite important. However, despite a large amount of experimental studies [319, 320, 321, 322, 323, 324, 325, 326, 327, 328] there is not yet a consensus in the bandgap of hBN; measured bandgaps range from 3.6–7.1 eV [323].

In the commonly believed structure of hBN [Fig. 16.1(a)], boron (nitrogen) atoms in one BN layer lie directly between nitrogen (boron) atoms in the two adjacent layers [312]. Recent density-functional calculations [329, 330, 331] have found that there are three energetically stable structural configurations (global or local minima) containing two BN layers per unit cell [Figs. 16.1(a), 16.1(c), and 16.1(e)], suggesting a way of explaining some of the discrepancies in the measured bandgap.

Electron-hole (e-h) interactions have also been shown to be extremely important in the optical response of hBN in the structure given in Fig. 16.1(a) due to its quasi two-dimensional nature [332, 333]. In this chapter, we present first-principles calculations on the optical response and the excitonic properties of hBN in the three energetically stable structures [329] using the GW – Bethe-Salpeter equation (BSE) approach [20, 28]. We find that the optical response and exciton binding energy of hBN depend significantly on the stacking scheme. We show that the optical measurement could be better explained if these structural variations are taken into account.

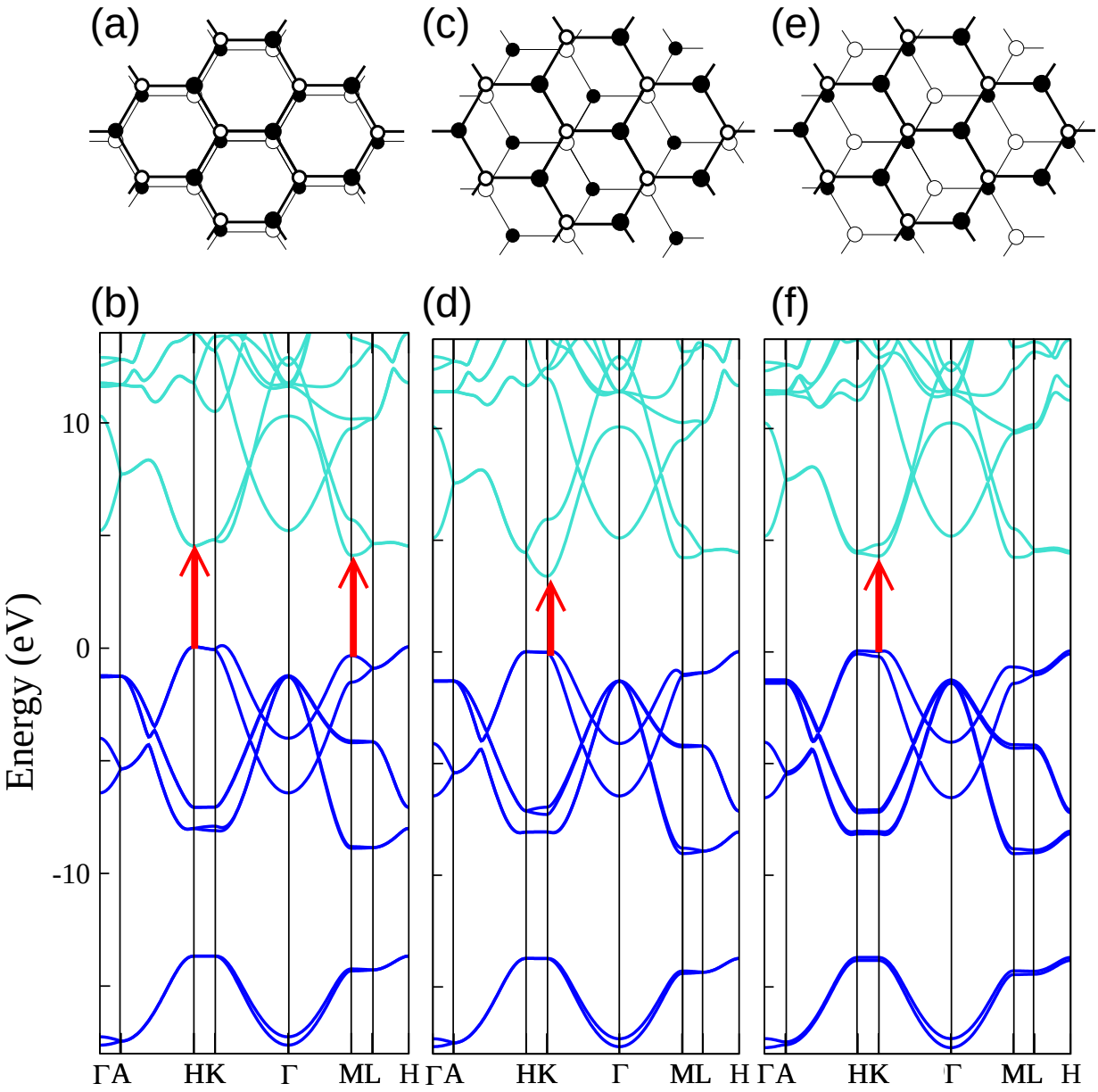

Figure 16.1: (a) and (b): Ball-and-stick model [(a)] and LDA electronic bandstructure [(b)] of hBN with structure A. In (a), empty circles and filled circles represent boron and nitrogen atoms, respectively. In (b), arrows represent the dominant subband transitions responsible for the lowest-energy bound exciton. (c) and (d), and (e) and (f): Same quantities as in (a) and (b) for structures B and C, respectively.

16.2 Theory and computation

We obtain the Kohn-Sham energy eigenvalues and wavefunctions within the local density approximation (LDA) using a plane-wave basis set with a kinetic energy cutoff of 100 Ry. The core-valence interaction is treated by means of norm-conserving pseudopotentials [15]. For convergent results to be better than 0.05 eV, $24 \times 24 \times 8$ **k** points in a randomly shifted grid are used in all the calculations. Dielectric matrices are calculated with a kinetic energy cutoff of 20 Ry. We have used the generalized plasmon-pole model to take into account dynamical effects [20]. We have included 100 conduction bands in the GW calculation for the quasiparticle energies and 6 valence and 6 conduction bands in solving the BSE for the optical spectrum.

We define structure A to be the commonly believed one of hBN [Fig. 16.1(a)]. Structures B and C are obtained from A by shifting or rotating every alternate layer, respectively (Fig. 16.1). The calculated LDA bandstructures in Fig. 16.1 are in good agreement with previous work [329].

16.3 Results and discussion

The two lowest-energy conduction band states near K have wavefunctions that are localized at the boron atoms [276], and the energy separation between them are decided by interlayer boron-boron interactions; hence, hBN in the form of structure B, where the boron atoms in adjacent layers are in contact [Fig. 16.1(a)], shows the largest energy separation between those two bands near K. This interlayer interaction makes a qualitative difference in the optical response of hBN among different structures [see the arrows in Figs. 16.1(b), 16.1(d), and 16.1(f)]. In structure A, the first bound exciton, which is optically active, is composed mainly of interband transitions near the H and M points, whereas in structures B and C, those are composed mainly of transitions near the K point (Fig. 16.1).

Table 16.1 shows that, although the value of the bandgap itself is increased by the GW quasiparticle corrections, its location in k-space is not changed from the LDA results. Calculated quasiparticle bandgap (5.84 eV) and the binding energy of the first bound exciton (0.69 eV) in structure A is in good agreement with Arnaud et al. [332] (5.95 eV and 0.72 eV, respectively). Notably, the optical excitation energy of the first bound exciton in structure B (4.79 eV) is 0.8 eV lower than that in structure A, and the binding energy of the lowest-energy exciton in structure B (0.35 eV) is half of that in structure A. The results for structure C are also different from those of structures A and B (Table 16.1). Therefore, the quasiparticle and optical properties of hBN vary drastically with the way BN layers are stacked.

Now we move on to the optical absorption profile of hBN. We limit our discussion to the absorbance of light linearly polarized in the BN plane, which is stronger than that for the perpendicularly polarized light below 10 eV [332]. The imaginary part of the macroscopic dielectric function $\varepsilon_2(\omega)$ differs significantly among the three different structures, and e-h interactions change this quantity qualitatively (Fig. 16.2). The absorption profile for

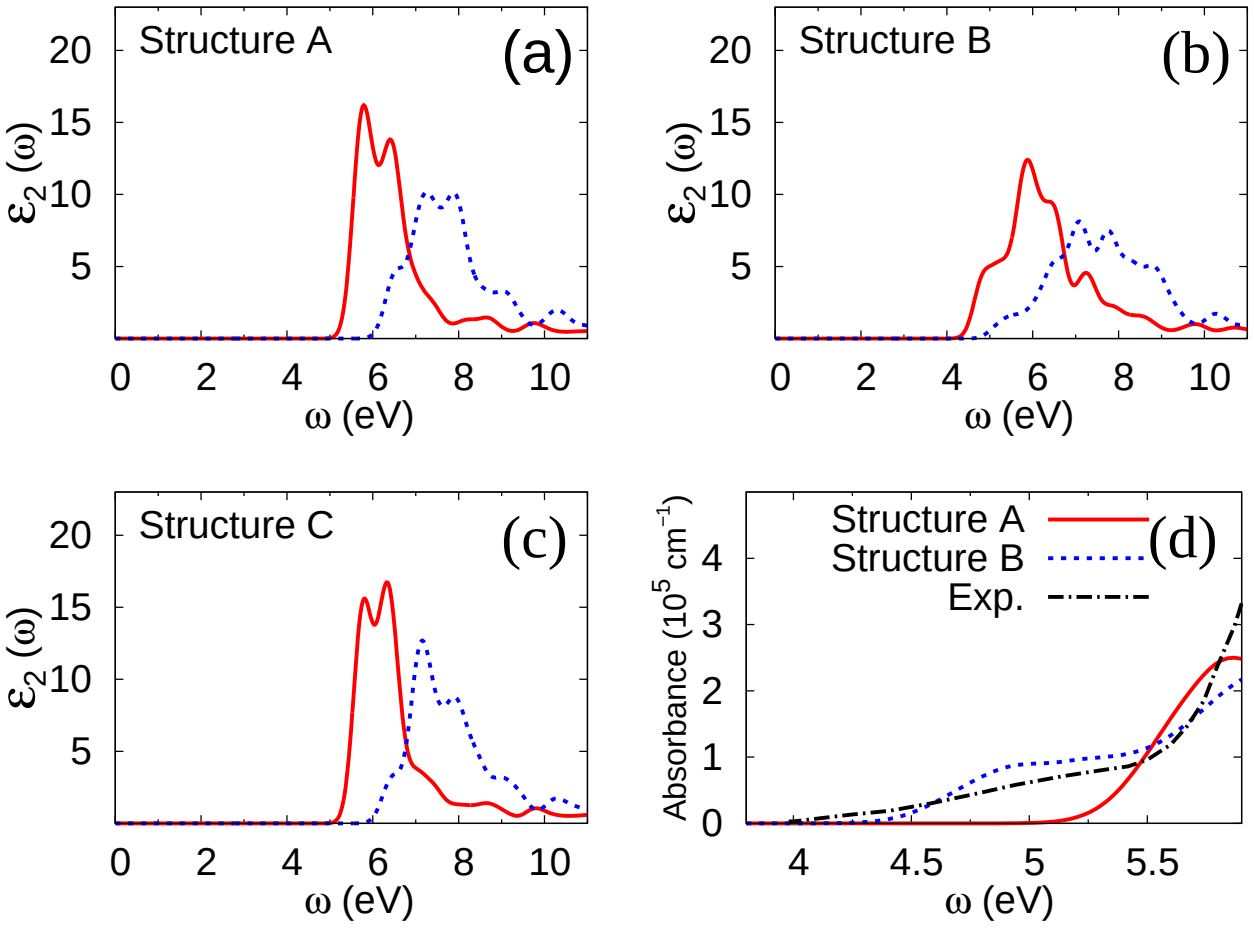

Figure 16.2: (a), (b), and (c): Imaginary part of the dielectric function $\varepsilon_2(\omega)$ of hBN in structures A, B, and C, respectively, for in-plane linearly polarized light. Solid line and dashed line in each figure show results for with and without e-h interactions, respectively. (d): Absorbance per unit length. Solid and dashed lines are the calculated quantities for hBN in structures A and B, respectively, and dash-dotted line is the experimental data [10]. Results for structure C (not shown) are similar to those for structure A. We have used an energy broadening of 0.15 eV.

Table 16.1: Calculated quasiparticle and optical bandgaps of hBN. Direct gap is the minimum energy difference between the lowest conduction band and the highest valence band at a particular wavevector specified in parenthesis. K″ is a point in reciprocal space that lies between K and Γ and the distance from Γ is 9.7 times as large as that from K. $E_{\rm b}$ is the binding energy of the lowest-energy exciton.

Structure	Method	Fundamental gap (eV)	Direct gap (eV)
A	LDA	4.04 (K″ →M)	4.45 (M)
	GW	5.84 (K″ →M)	6.31 (M)
	BSE		5.63 ($E_{\rm b} = 0.69$)
B	LDA	3.38 (H→K)	3.41 (K)
	GW	5.11 (H→K)	5.14 (K)
	BSE		4.79 ($E_{\rm b} = 0.35$)
C	LDA	4.19 (H→M)	4.28 (K)
	GW	6.03 (H→M)	6.15 (K)
	BSE		5.65 ($E_{\rm b} = 0.51$)

structure A [Fig. 16.2 (a)] is in good agreement with Arnaud et.al. [332]. For structure B, $\varepsilon_2(\omega)$ (including excitonic effects) has a shoulder around $4.8 - 5.4$ eV [Fig. 16.2(b)]. This shoulder has its origin in the large dispersion of the lowest-energy conduction bands in structure B, as we discussed (Fig. 16.1). Figure 16.2 (d) shows that the absorption coefficient η, where the intensity of light after proceeding a distance z is given by $I(z) = I(0)\, e^{-\eta z}$, measured from experiments [10] also shows a similar shoulder structure. Thus, the experimental data can be explained better if structures other than A are taken into account.

Figure 16.3 shows the probability for the lowest-energy exciton state of finding an electron at position $\mathbf{r}_e$ when the hole is fixed at the origin, which is 0.6 Å above one of the nitrogen atoms, $|\Phi(\mathbf{r}_e, \mathbf{r}_h = 0)|^2$: both the size and shape vary significantly with the structure. The size is, as expected, smaller in structure with a larger binding energy, confirming that *e-h* interactions in hBN are affected by the way the BN layers are stacked.

16.4 Conclusion

In summary, we have investigated the effects of BN layer stacking on the quasiparticle bandstructure and the optical properties of hBN. We studied hBN in three different metastable structures that are very close in their total energies. It is revealed that the stacking scheme is quite important in determining the optical response of hBN. The binding energy of

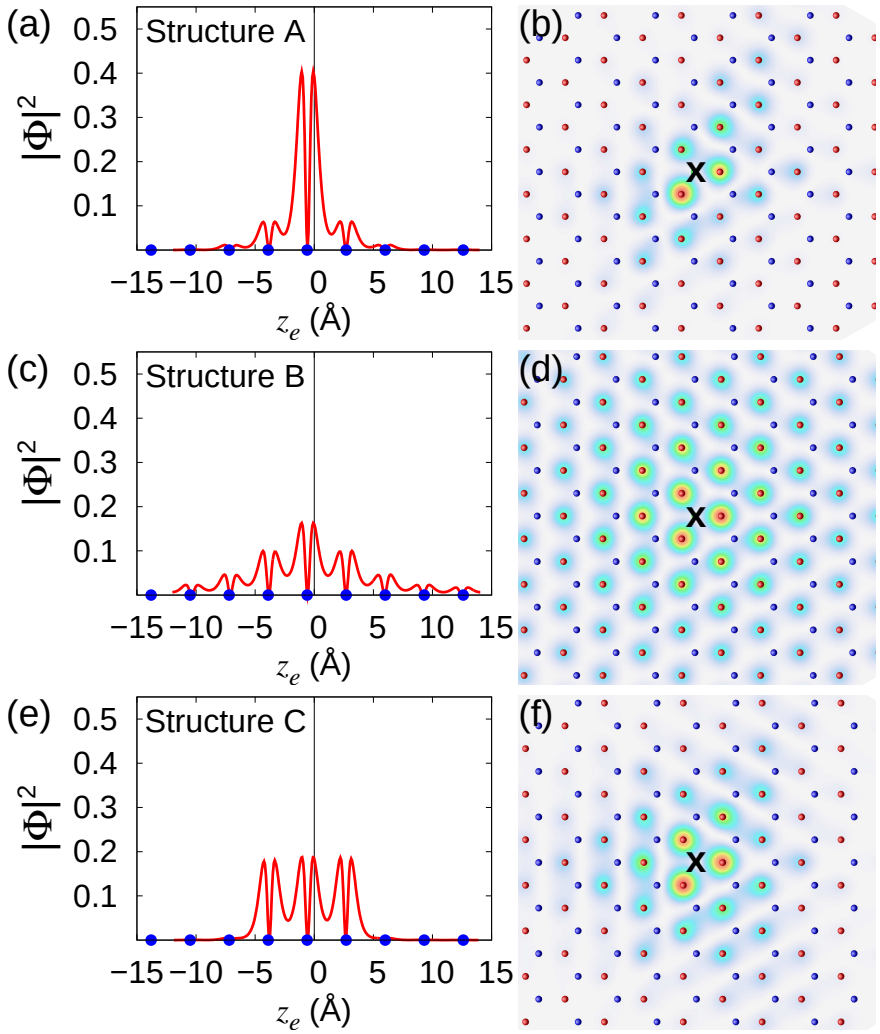

Figure 16.3: (a) The electron (at $\mathbf{r}_e$) probability distribution $|\Phi(\mathbf{r}_e, \mathbf{r}_h = 0)|^2$, with the hole fixed at the origin ($\mathbf{r}_h = 0$) which is 0.6 Å above one of the nitrogen atoms, averaged over the coordinates parallel to the BN layers for the lowest-energy bright exciton in structure A. Here, z_e is the out-of-plane component of the electron coordinate. The positions of BN layers are indicated by blue disks. (b) Cross-sectional plot ($z_e = 0$) of $|\Phi(\mathbf{r}_e, \mathbf{r}_h = 0)|^2$ for the same exciton as in (a). The hole is indicated by an an '**x**' mark. (c) and (d), and (e) and (f): Same quantities as in (a) and (b) for structures B and C, respectively.

the lowest-energy exciton varies from 0.35 eV to 0.69 eV. The interpretation of experimental optical spectrum with the calculated absorption spectra is found to become considerably improved by including all three structures.

Chapter 17

Hydrogen passivation reverses the direction of electric dipole moments in III-V and II-VI compound nanostructures

17.1 Introduction

The electric dipole moment, which is one of the most basic concepts in electrostatics and electrodynamics [116], in general dominantly determines the electric field from a charge-neutral system at long distance and plays an important role in the chemistry or physics of systems confined in one or more dimensions [116]. When neutral atoms gather to form a compound, the electric dipole moment is determined by charge redistribution, following the tendency of each atom or group of atoms to draw electrons.

This tendency to draw electrons, the electronegativity, was first proposed by Pauling [334]. After Pauling's proposal, a number of different ways to define electronegativity have been introduced [335, 336, 337, 338]. They differ in their assignment of values for each element, but the overall trend agrees among one another. In general, in the Periodic Table of elements, electronegativity increases on passing from left to right along a row because the effective nuclear charge seen by the valence electrons increases, and decreases on descending along a column because the size of the atom increases, reducing the interaction between the ionic core and the valence electron [339].

Along the line of this general trend, when two atoms on the same row belonging to groups III and V (groups II and VI), respectively, form a binary molecule, the electric dipole moment is generally accepted as being pointed along the direction from the atom in group V (group VI) to the atom in group III (group II) [Fig. 17.1(b)].

On the other hand, often the edge or surface of a molecular or nanostructured system passivated by groups or atoms that are not the main constituent of the compound, rather

than existing with unstable dangling bonds. The passivation process thus makes the original system stable against further chemical modifications at the surface. The kind of passivation depends on the chemical reagents and procedures used in the fabrication step. Some of the most common forms of passivations are hydrogen passivation, oxidation, and nitration [340].

In this chapter, we show that when a III-V or II-VI binary molecule or nanostructure is passivated with hydrogen forming an sp^2 or sp^3 environment, the direction of the electric dipole moment is reversed. This phenomenon is explained in terms of the electronegativity. Our findings have a general implication on the chemistry and electrostatics of nanostructured III-V or II-VI compound semiconductors in the forms of molecules, nanoribbons, nanoslabs, edges, or surfaces, and point to an additional important role played by chemical passivations.

17.2 Theory and computation

In our study, first-principles density functional theory (DFT) calculations were performed using a B3LYP exchange-correlation functional [341] and the lanl2dz basis set employing the effective core potential [342, 343, 344] using the Gaussian03 package [345]. All the structures were optimized by reducing the force on each atom to be less than 0.0006 Ry/a_0 where a_0 is the Bohr radius.

For calculations on molecules composed of elements in the rows 2 to 4 of the Periodic Table, we have repeated the calculations by using the all-electron cc-pVTZ basis set [346].

Also, for BN compound molecules or nanostructures, we have performed *ab initio* pseudopotential DFT calculations within the local density approximation in a supercell configuration using the SIESTA computer code [291]. We used a double-zeta plus polarization basis set and a charge density cutoff of 400 Ry. To eliminate spurious interactions between periodic images, we used the supercell size (along the non-periodic directions) of up to 20 nm.

All the above calculations were in good agreement among one another: the difference in the atomic position and that in the dipole moment were less than 0.02 a_0 and 0.1 $|e|a_0$, respectively.

17.3 Results and discussion

To find the effects of hydrogen passivation, we performed calculations on the binary III-V and II-VI molecules whose elements are on the same row in the Periodic Table. Figure 17.1(a) shows the electric dipole moment [$\mathbf{p} = \int d\mathbf{r}\rho(\mathbf{r})\mathbf{r}$ where $\rho(\mathbf{r})$ is the charge density at position $\mathbf{r}$] of a BN molecule and its hydrogenated forms H_nBNH_n where n=1, 2, and 3. When the molecule is not passivated by hydrogen atoms, the electric dipole moment is, as expected from the stronger electronegativity of N than B, pointed from N to B. However, the direction of the dipole is reversed upon hydrogen passivation and the magnitude of the electric dipole moment increases further as the number of hydrogen atoms n passivating each atom varies from 1 to 3. The magnitude of the reversed dipole moment for the case $n = 3$ is about twice as large as that of the original dipole moment before hydrogen passivation.

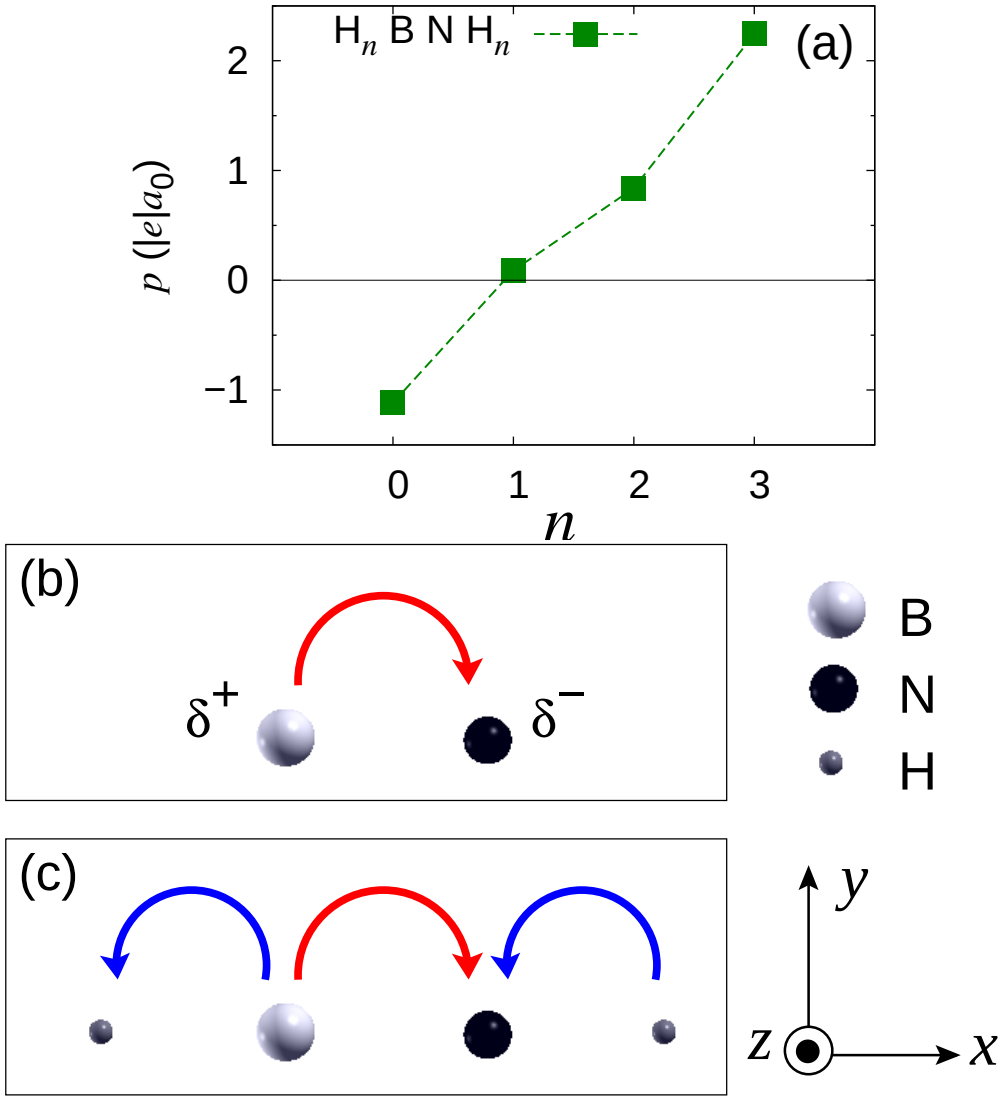

Figure 17.1: (a) Calculated electric dipole moment of a H_nBNH_n molecule (which is along the x direction) versus the number of H atoms n attached to B and N atoms. B and N atoms are aligned as shown in (b). Here, e is the charge of an electron and a_0 is the bohr radius (=0.529 Å). The dashed lines are a guide to the eye. (b) Schematic showing the relative position of B and N atoms in the BN molecule and the *electron* transfer from B to N (the arrow). (c) Schematic showing the relative position of atoms in the HBNH molecule and the *electron* transfers from B to H, B to N, and H to N (the arrows).

Figures 17.1(b) and 17.1(c) schematically show the origin of this electric dipole reversal phenomenon. The electronegativities of H, B, and N atoms according to the Pauling scale [334] are 2.20, 2.04, and 3.04, respectively. In a BN molecule, because the electronegativity of the N atom is higher than that of the B atom, the N atom attracts electrons from the B atom [Fig. 17.1(b)], resulting in a dipole moment pointing along the direction from the N atom to the B atom. When the B and N atoms are passivated by hydrogen atoms, the H atom on the left hand side attracts electrons from the B atom and the N atom attracts electrons from the H atom on the right hand side [Fig. 17.1(c)]. These additional polarizations add a dipole moment pointing in the opposite direction to the original one. In fact, along this line of explanation based on the electronegativity concept, the passivation always results in an additional reverse dipole moment independent of the electronegativity of the passivating atoms, i. e. , the passivating atom does not have to have an electronegativity value in between those of the two originally bonded atoms (see Fig. 17.3). This reverse dipole moment increases with the number of hydrogen atoms used in the passivation, even to a degree that it eventually reverses the direction of the total dipole moment [Fig. 17.1(a)]. In the following, we support our claim through first-principles calculations.

Figures 17.2(a) and 17.2(b) show the difference in the valence charge density between that of a superposition atomic results $[\rho_{\rm a}(\mathbf{r})]$ and that of the calculated results of the molecular system $[\rho(\mathbf{r})]$ integrated along the z direction, i. e. , $\Delta\sigma(x,y) \equiv \int dz\,[\rho(\mathbf{r}) - \rho_{\rm a}(\mathbf{r})]$. The function $\Delta\sigma(x,y)$ in H_2BNH_2 is qualitatively different from that in the non-passivated molecule because the hydrogen atoms contribute in the redistribution of the charge density. Especially, it is noteworthy that the H atom near the B atom is electron-richer than the one near the N atom in agreement with the simple picture schematically shown in Figs. 17.1(b) and 17.1(c). Figure 17.2(c) clearly shows this point. When the BN molecule is passivated by the H atoms, electrons are polarized in the way depicted in Fig. 17.1(c).

Figure 17.3 shows that reversal in the direction of an electric dipole moment upon hydrogen passivation is in fact quite general. We have calculated the electric dipole moment of other III-V and II-VI molecular compounds, whose binary elements are on the same row of the Periodic Table. In all the cases considered, the electric dipole moment reverses its direction upon hydrogen passivation. The magnitude of the reversed electric dipole moment due to hydrogen passivation monotonically decreases on descending along a column in the Periodic Table, in contrast to a non-trivial trend observed in the magnitude of the electric dipole moment of molecules without hydrogen passivation. Also, the II-VI compounds have larger electric dipole moment than the III-V ones in the same row for molecules both with and without hydrogen passivation.

Next, we show that the hydrogen-passivation-induced dipole moment reversing behavior in III-V and II-VI compounds are not restricted to molecules but also predicted in nanosystems periodic in one or two dimensions. Figure 17.4 shows that the direction of the electric dipole moment of BN nanoribbons with zigzag type of edge on both sides is reversed upon hydrogen passivation. In our previous calculations on the hydrogen-passivated BN nanoribbons with zigzag type of edges [314], we reported that the reason why the dipole moment is pointing in the $+x$ direction [Fig. 17.4(b)] is because the B atoms are more negatively charged

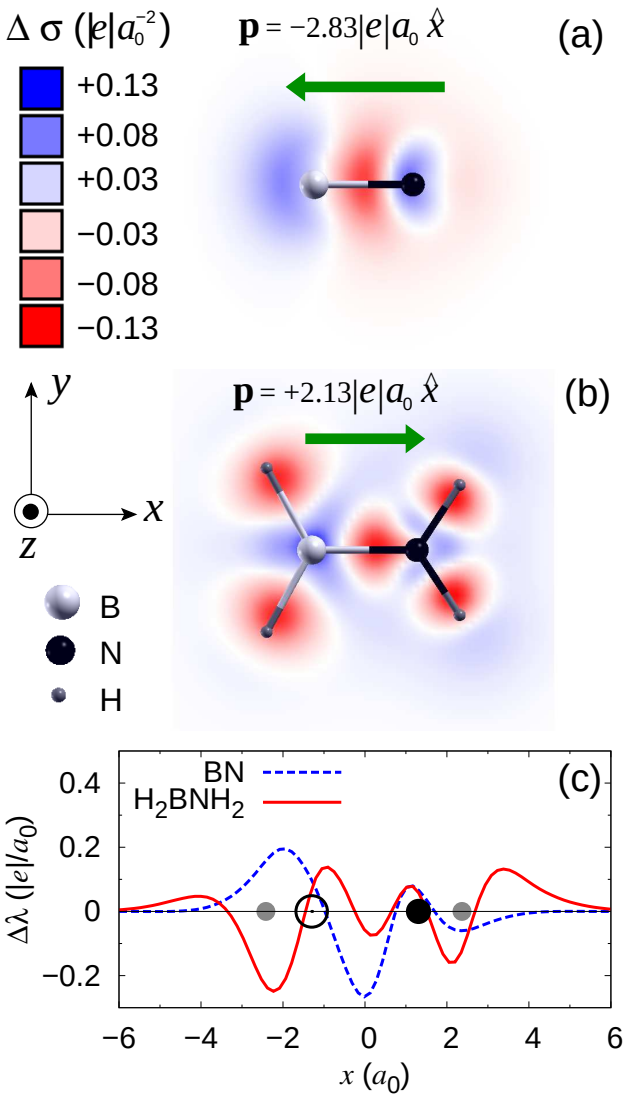

Figure 17.2: (a) and (b): Optimized structure and difference between the calculated valence charge density and atomic valence charge density integrated along the z direction $\Delta\sigma(x,y) \equiv \int dz\,[\rho(\mathbf{r}) - \rho_{\rm a}(\mathbf{r})]$ for (a) a BN molecule and (b) a H_2BNH_2 molecule. We use the convention that the electron charge density is negative, i. e. , $-|e|$ is the charge of an electron and electrons are taken away from the blue regime and put into the red regime when forming a compound molecule. The direction and magnitude of the electric dipole moment is represented by an arrow in each panel. (c) The charge density difference integrated in the yz plane $\Delta\lambda(x) \equiv \int dy\,dz\,[\rho(\mathbf{r}) - \rho_{\rm a}(\mathbf{r})]$. The positions along x of atoms for H_2BNH_2 are represented by the corresponding spheres.

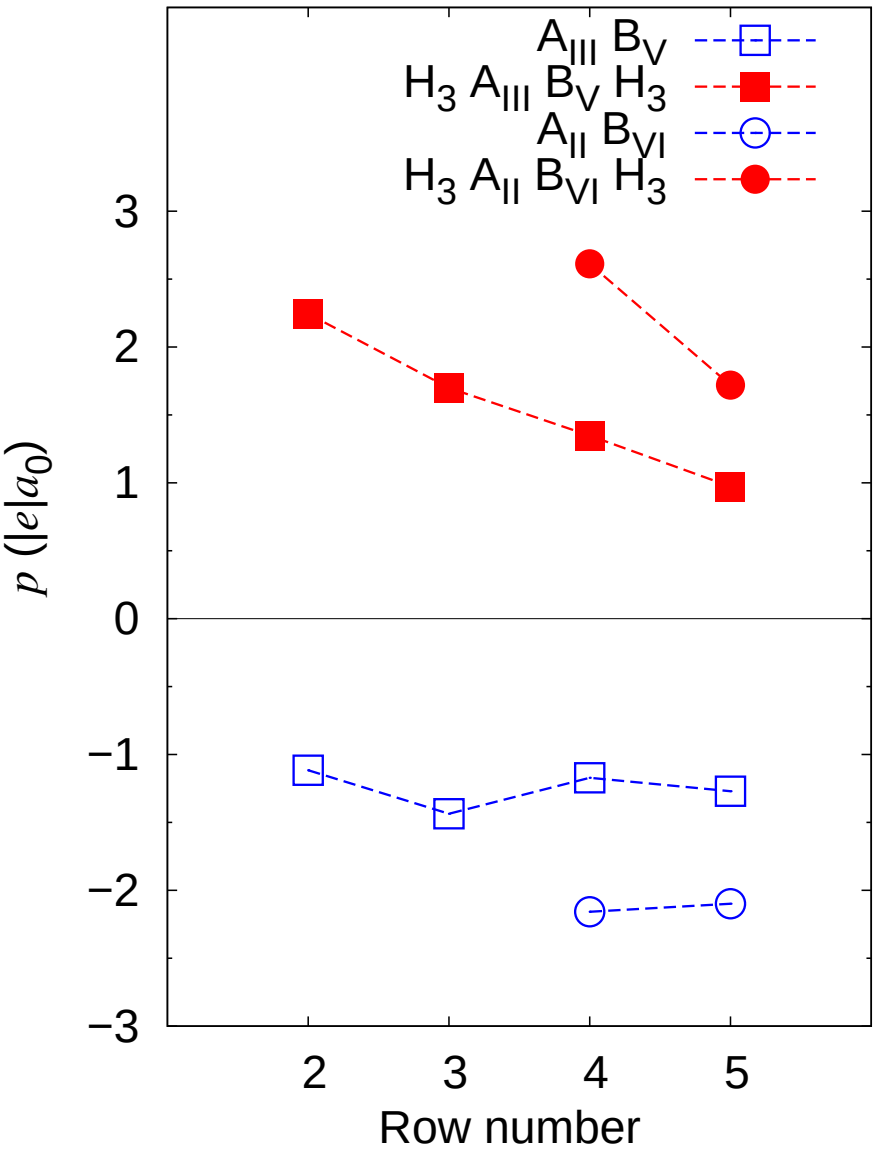

Figure 17.3: Calculated electric dipole moment of $A_{III}B_V$ (squares) and $A_{II}B_{VI}$ (circles) type molecules, where A_{II}, A_{III}, B_V, and B_{VI} belong to groups II, III, V, and VI, respectively, versus the row number to which these elements belong. (When the row number is 2, 3, 4, and 5, A_{III} is B, Al, Ga, and In, respectively, and B_V is N, P, As, and Sb, respectively. Likewise, when the row number is 4 and 5, A_{II} is Zn and Cd, respectively, and B_{VI} is Se and Te, respectively.) Empty symbols and filled ones are quantities for molecules without and with hydrogen passivation (three H atoms per each of the above atom), respectively. The dashed lines are a guide to the eye.

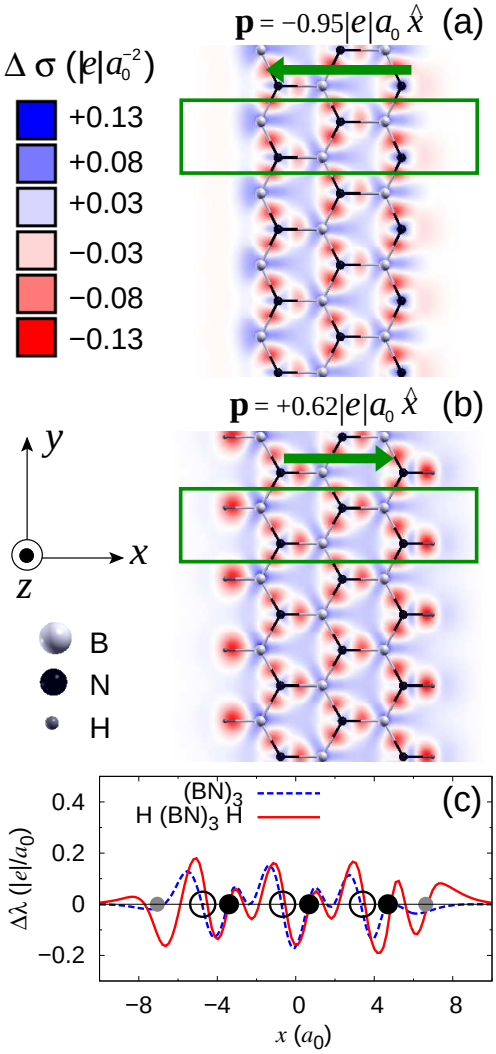

Figure 17.4: (a) and (b): Optimized structure and difference between the calculated valence charge density and atomic valence charge density integrated along the z direction $\Delta\sigma(x,y) \equiv \int dz\,[\rho(\mathbf{r}) - \rho_{\rm a}(\mathbf{r})]$ for zigzag BN ribbons (periodic in the y direction) having 3 BN pairs per unit cell (a) without and (b) with hydrogen passivation. The rectangle shows the unit cell in each panel. Electrons are taken away from the blue regime and put into the red regime. The direction and magnitude of the electric dipole moment per unit cell is represented by an arrow in each panel. (c) The charge density difference integrated in the yz plane $\Delta\lambda(x) \equiv \int_{\rm unitcell} dy \int dz\,[\rho(\mathbf{r}) - \rho_{\rm a}(\mathbf{r})]$. The positions along x of atoms for $H(BN)_3H$ are represented by the corresponding spheres.

than the N atoms. However, this interpretation was not correct and we have shown here that hydrogen passivation plays the key role. The results have a direct implication on the electronic properties of binary compound nanowires or nanoribbons [347, 348, 349, 350, 351].

A similar calculation on a slab of BN with zinc blende structure truncated at the B and N faces, whose surface normal is parallel to $-x$ and $+x$ directions, respectively, has been performed. The particular structure considered here is periodic in the y and z directions, and has a unit cell with 3 BN pairs. The electric dipole moment per unit cell along the x-direction p_x changes from $-0.063\ |e|\, a_0$ to $+1.27\ |e|\, a_0$ upon hydrogen passivation, i. e. , reverses the direction. These results on confined and periodic systems are especially important considering that fabrication techniques for nanostructures with different passivations are rapidly developing nowadays.

Finally, we believe that the dipole moment direction reversal due to hydrogen passivation would be a general phenomenon in other binary systems composed of atoms with different electronegativity than the III-V or II-VI compounds composed of elements in the same row according to our simple argument (Fig. 17.1).

17.4 Conclusion

In conclusion, we have studied the novel phenomenon of hydrogen-passivation-induced electric dipole moment reversal in the III-V or II-VI compounds in various forms such as molecules or nanostructures. Our findings provide an insight in understanding the electrostatic and chemical properties of these materials, and encourage studies on the effects of different types of passivations. Indeed, the introduced simple argument for the dipole moment reversal phenomenon based on the concept of electronegativity suggests that similar behaviors are expected for other kinds of passivations in general.

Bibliography

[1] The e-ph interaction of a conventional metal was modeled by assuming constant density of states, an Einstein spectrum, and a constant e-ph matrix element [S. Engelsberg and J. R. Schrieffer, Phys. Rev. **131**, 993 (1963)]. These quantities were determined in such a way to match the height of the graphene self-energy near the Fermi level.

[2] A. Bostwick, T. Ohta, T. Seyller, K. Horn, and E. Rotenberg, Nature Phys. **3**, 36 (2007).

[3] We used the scaling relations given in Refs. [85, 86, 38] to account for the difference between the experimental doping level ($E_{\mathrm{D}} = -0.87$ eV) and the one considered here ($E_{\mathrm{D}} = -1.0$ eV).

[4] A. Bostwick, T. Ohta, T. Seyller, K. Horn, and E. Rotenberg, Nature Phys. **3**, 36 (2007).

[5] C.-H. Park, F. Giustino, J. L. McChesney, A. Bostwick, T. Ohta, E. Rotenberg, M. L. Cohen, and S. G. Louie, Phys. Rev. B **77**, 113410 (2008).

[6] J. Yan, Y. Zhang, P. Kim, and A. Pinczuk, Phys. Rev. Lett. **98**, 166802 (2007).

[7] J. Yan, E. A. Henriksen, P. Kim, and A. Pinczuk, Phys. Rev. Lett. **101**, 136804 (2008).

[8] Y. Zhang, T.-T. Tang, C. Girit, Z. Hao, M. C. Martin, A. Zettl, M. F. Crommie, Y. R. Shen, and F. Wang, Nature **459**, 820 (2009).

[9] R. W. Winkler, J. P. Kotthaus, and K. Ploog, Phys. Rev. Lett. **62**, 1177 (1989).

[10] A. Zunger, A. Katzir, and A. Halperin, Phys. Rev. B **13**, 5560 (1976).

[11] R. Martin, *Electronic Structure: Basic Theory and Practical Methods* (Cambridge University Press, Cambridge, 2004).

[12] P. Hohenberg and W. Kohn, Phys. Rev. **136**, B864 (1964).

[13] W. Kohn and L. J. Sham, Phys. Rev. **140**, A1133 (1965).

[14] D. M. Ceperley and B. J. Alder, Phys. Rev. Lett. **45**, 566 (1980).

[15] N. Troullier and J. L. Martins, Phys. Rev. B **43**, 1993 (1991).

[16] D. R. Hamann, M. Schlüter, and C. Chiang, Phys. Rev. Lett. **43**, 1494 (1979).

[17] L. Kleinman and D. M. Bylander, Phys. Rev. Lett. **48**, 1425 (1982).

[18] L. Hedin, Phys. Rev. **139**, A796 (1965).

[19] L. Hedin and S. Lundqvist, *Solid State Physics* (Academic Press, New York and London, 1969), Vol. 23, p. 1.

[20] M. S. Hybertsen and S. G. Louie, Phys. Rev. B **34**, 5390 (1986).

[21] S. L. Adler, Phys. Rev. **126**, 413 (1962).

[22] N. Wiser, Phys. Rev. **129**, 62 (1963).

[23] W. Hanke and L. J. Sham, Phys. Rev. B **21**, 4656 (1980).

[24] M. del Castillo Mussot and L. J. Sham, Phys. Rev. B **31**, 2092 (1985).

[25] M. Rohlfing and S. G. Louie, Phys. Rev. Lett. **81**, 2312 (1998).

[26] S. Albrecht, L. Reining, R. D. Sole, and G. Onida, Phys. Rev. Lett. **80**, 4510 (1998).

[27] L. X. Benedict, E. L. Shirley, and R. B. Bohn, Phys. Rev. Lett. **80**, 4514 (1998).

[28] M. Rohlfing and S. G. Louie, Phys. Rev. B **62**, 4927 (2000).

[29] S. Baroni, S. de Gironcoli, A. Dal Corso, and P. Giannozzi, Rev. Mod. Phys. **73**, 515 (2001).

[30] R. P. Feynman, Phys. Rev. **56**, 340 (1939).

[31] F. Giustino, M. L. Cohen, and S. G. Louie, Phys. Rev. B **76**, 165108 (2007).

[32] N. Marzari and D. Vanderbilt, Phys. Rev. B **56**, 12847 (1997).

[33] I. Souza, N. Marzari, and D. Vanderbilt, Phys. Rev. B **65**, 035109 (2001).

[34] K. S. Novoselov, D. Jiang, F. Schedin, T. Booth, V. V. Khotkevich, S. V. Morozov, and A. K. Geim, Proc. Nat. Acad. Sci. U.S.A. **102**, 10451 (2005).

[35] K. S. Novoselov, A. K. Geim, S. V. Morozov, D. Jiang, M. I. Katsnelson, I. V. Grigorieva, S. V. Dubonos, and F. A. A., Nature **438**, 197 (2005).

[36] Y. Zhang, J. W. Tan, H. L. Stormer, and P. Kim, Nature **438**, 201 (2005).

[37] A. Damascelli, Z. Hussain, and Z.-X. Shen, Rev. Mod. Phys. **75**, 473 (2003).

[38] E. H. Hwang, B. Y.-K. Hu, and S. Das Sarma, Phys. Rev. B **76**, 115434 (2007).

[39] G. Grimvall, in *The Electron-Phonon Interaction in Metals*, edited by E. Wohlfarth (North-Holland, New York, 1981).

[40] J. P. Perdew and A. Zunger, Phys. Rev. B **23**, 5048 (1981).

[41] J. Ihm, A. Zunger, and M. L. Cohen, J. Phys. C **12**, 4409 (1979).

[42] M. Fuchs and M. Scheffler, Comput. Phys. Commun. **119**, 67 (1999).

[43] S. Baroni, S. de Gironcoli, A. Dal Corso, and P. Giannozzi, Rev. Mod. Phys. **73**, 515 (2001).

[44] O. Dubay and G. Kresse, Phys. Rev. B **67**, 035401 (2003).

[45] F. Giustino, J. R. Yates, I. Souza, M. L. Cohen, and S. G. Louie, Phys. Rev. Lett. **98**, 047005 (2007).

[46] We used nine maximally localized electronic Wannier functions [N. Marzari and D. Vanderbilt, Phys. Rev. B **56**, 12847 (1997); I. Souza, N. Marzari, and D. Vanderbilt, Phys. Rev. B **65**, 035109 (2001)] spanning an energy window of 30 eV.

[47] Our calculated phonon dispersions are in excellent agreement with previous first-principles results of Ref. [44].

[48] We used an energy cutoff of 6 eV. The resulting self-energy was found to be largely insensitive to this choice.

[49] M. Calandra and F. Mauri, Phys. Rev. B **76**, 205411 (2007).

[50] E. W. Plummer, J. Shi, S. J. Tang, E. Rotenberg, and S. D. Kevan, Prog. Surf. Sci. **74**, 251 (2003).

[51] S. Souma, Y. Machida, T. Sato, T. Takahashi, H. Matsui, S.-C. Wang, H. Ding, A. Kaminski, J. C. Campuzano, S. Sasaki, and K. Kadowaki, Nature **423**, 65 (2003).

[52] S. Y. Zhou, G.-H. Gweon, J. Graf, A. V. Fedorov, C. D. Spataru, R. D. Diehl, Y. Kopelevich, D.-H. Lee, S. G. Louie, , and A. Lanzara, Nature Phys. **2**, 595 (2006).

[53] T. Ohta, A. Bostwick, J. L. McChesney, T. Seyller, K. Horn, and E. Rotenberg, Phys. Rev. Lett. **98**, 206802 (2007).

[54] A. Bostwick, T. Ohta, J. L. McChesney, K. V. Emtsev, T. Seyller, K. Horn, and E. Rotenberg, New J. Phys. **9**, 385 (2007).

[55] J. McChesney, A. Bostwick, T. Ohta, K. V. Emtsev, T. Seyller, K. Horn, and E. Rotenberg, arXiv:0705.3264v1.

[56] T. Ohta, F. E. Gabaly, A. Bostwick, J. McChesney, K. V. Emtsev, A. K. Schmid, T. Seyller, K. Horn, and E. Rotenberg, New J. Phys. **10**, 023034 (2008).

[57] M. Mucha-Kruczyński, O. Tsyplyatyev, A. Grishin, E. McCann, V. I. Fal'ko, A. Bostwick, and E. Rotenberg, Phys. Rev. B **77**, 195403 (2008).

[58] S. Zhou, D. Siegel, A. Fedorov, and A. Lanzara, Nature Mater. **6**, 770 (2007).

[59] S. Zhou, D. Siegel, A. Fedorov, and A. Lanzara, Physica E **40**, 2642 (2008).

[60] C.-H. Park, F. Giustino, M. L. Cohen, and S. G. Louie, Phys. Rev. Lett. **99**, 086804 (2007).

[61] M. Calandra and F. Mauri, Phys. Rev. B **76**, 161406 (2007).

[62] M. Calandra and F. Mauri, Phys. Rev. B **76**, 205411 (2007).

[63] W.-K. Tse and S. D. Sarma, Phys. Rev. Lett. **99**, 236802 (2007).

[64] S. Engelsberg and J. R. Schrieffer, Phys. Rev. **131**, 993 (1963).

[65] M. Hengsberger, D. Purdie, P. Segovia, M. Garnier, and Y. Baer, Phys. Rev. Lett. **83**, 592 (1999).

[66] M. Hengsberger, R. Frésard, D. Purdie, P. Segovia, and Y. Baer, Phys. Rev. B **60**, 10796 (1999).

[67] E. Rotenberg, J. Schaefer, and S. D. Kevan, Phys. Rev. Lett. **84**, 2925 (2000).

[68] A. Kaminski and H. M. Fretwell, New J. Phys. **7**, 98 (2005).

[69] A. A. Kordyuk, S. V. Borisenko, A. Koitzsch, J. Fink, M. Knupfer, and H. Berger, Phys. Rev. B **71**, 214513 (2005).

[70] K. S. Novoselov, A. K. Geim, S. V. Morozov, D. Jiang, Y. Zhang, S. V. Dubonos, I. V. Grigorieva, and A. A. Firsov, Science **306**, 666 (2004).

[71] C. Berger, Z. M. Song, X. B. Li, X. S. Wu, N. Brown, C. Naud, T. B. Li, J. Hass, A. N. Marchenkov, E. H. Conrad, P. N. First, and W. A. de Heer, Science **312**, 1191 (2006).

[72] A. K. Geim and K. S. Novoselov, Nature Mater. **6**, 183 (2007).

[73] S. Nakajima and M. Watabe, Prog. Theor. Phys. **29**, 341 (1963).

[74] This specific value of $\Delta E = 0.3$ eV was chosen under a reasonable assumption that $v_{\mathbf{k}}(E_{\rm F} - \Delta E)$ appearing in Eq. (3.3) is obtained as the average slope between $E = E_{\rm F} - \omega_{\rm ph}$ and $E = E_{\rm F} - 2\omega_{\rm ph}$. We have checked that as the energy range ΔE varies within the interval 0.2$\sim$0.4 eV, the apprent strength $\lambda^{\rm app}$ changes less than 10 % along both KM and KΓ directions.

[75] A. A. Kordyuk, S. V. Borisenko, T. K. Kim, K. A. Nenkov, M. Knupfer, J. Fink, M. S. Golden, H. Berger, and R. Follath, Phys. Rev. Lett. **89**, 077003 (2002).

[76] A. D. Gromko, Y.-D. Chuang, A. V. Fedorov, Y. Aiura, Y. Yamaguchi, K. Oka, Y. Ando, and D. S. Dessau, arXiv:condmat/0205385v1.

[77] P. R. Wallace, Phys. Rev. **71**, 622 (1947).

[78] T. Ando and T. Nakanishi, J. Phys. Soc. Jpn. **67**, 1704 (1998).

[79] P. L. McEuen, M. Bockrath, D. H. Cobden, Y.-G. Yoon, and S. G. Louie, Phys. Rev. Lett. **83**, 5098 (1999).

[80] M. I. Katsnelson, K. S. Novoselov, and A. K. Geim, Nature Phys. **2**, 620 (2006).

[81] C.-H. Park, L. Yang, Y.-W. Son, M. L. Cohen, and S. G. Louie, Nature Phys. **4**, 213 (2008).

[82] C.-H. Park, Y.-W. Son, L. Yang, M. L. Cohen, and S. G. Louie, Nano Lett. **8**, 2920 (2008).

[83] C.-H. Park, L. Yang, Y.-W. Son, M. L. Cohen, and S. G. Louie, Phys. Rev. Lett. **101**, 126804 (2008).

[84] W.-K. Tse and S. D. Sarma, Phys. Rev. Lett. **99**, 236802 (2007).

[85] M. Polini, R. Asgari, G. Borghi, Y. Barlas, T. Pereg-Barnea, and A. H. MacDonald, Phys. Rev. B **77**, 081411 (2008).

[86] E. H. Hwang and S. D. Sarma, Phys. Rev. B **77**, 081412 (2008).

[87] E. Rotenberg, A. Bostwick, T. Ohta, J. L. McChesney, T. Seyller, and K. Horn, Nature Mater. **7**, 258 (2008).

[88] S. Y. Zhou, D. A. Siegel, A. V. Fedorov, F. E. Gabaly, A. K. Schmid, A. H. C. Neto, D.-H. Lee, and A. Lanzara, Nature Mater. **7**, 259 (2008).

[89] S. Y. Zhou, D. A. Siegel, A. V. Fedorov, and A. Lanzara, Phys. Rev. Lett. **101**, 086402 (2008).

[90] A. Mattausch and O. Pankratov, Phys. Rev. Lett. **99**, 076802 (2007).

[91] F. Varchon, R. Feng, J. Hass, X. Li, B. N. Nguyen, C. Naud, P. Mallet, J.-Y. Veuillen, C. Berger, E. H. Conrad, and L. Magaud, Phys. Rev. Lett. **99**, 126805 (2007).

[92] S. Kim, J. Ihm, H. J. Choi, and Y.-W. Son, Phys. Rev. Lett. **100**, 176802 (2008).

[93] C. D. Spataru, M. A. Cazalilla, A. Rubio, L. X. Benedict, P. M. Echenique, and S. G. Louie, Phys. Rev. Lett. **87**, 246405 (2001).

[94] First-principles calculations of the electron velocity renormalization in graphene arising from *e*-*e* interaction have recently been performed [P. E. Trevisanutto *et al.*, Phys. Rev. Lett. **101**, 226405 (2008); C. Attaccalite, A. Grüeneis, T. Pichler, and A. Rubio, arXiv:0808.0786v1].

[95] C.-H. Park, F. Giustino, M. L. Cohen, and S. G. Louie, Nano Lett. **8**, 4229 (2008).

[96] *Conceptual Foundations of Materials: A Standard Model for Ground- and Excited-State Properties*, edited by S. G. Louie and M. L. Cohen (Elsevier, Amsterdam, 2006).

[97] S. Ismail-Beigi, Phys. Rev. B **73**, 233103 (2006).

[98] L. X. Benedict, C. D. Spataru, and S. G. Louie, Phys. Rev. B **66**, 085116 (2002).

[99] S. Logothetidis and J. Petalas, J. App. Phys. **80**, 1768 (1996).

[100] According to our first-principles calculations (unpublished) on the dielectric function $\varepsilon_{\rm SiC}(q,\omega)$ of 3C-SiC, showing dielectric responses very similar to 6H-SiC (Ref. [99]) used in the experiments, $\varepsilon_{\rm SiC}(q,\omega)$ can be well represented by the optical dielectric constant in an energy window $|\omega| < \Delta\omega = 2.5$ eV considered here, and the corresponding wavevector window $|q| < \hbar\Delta\omega/v_{\rm F} = 0.4$ Å^{-1}, with less than 10 % errors, except when the electron wavevector is close to the van Hove singularity.

[101] K. Bolotin, K. Sikes, Z. Jiang, M. Klima, G. Fudenberg, J. Hone, P. Kim, and H. Stormer, Solid State Commun. **146**, 351 (2008).

[102] X. Du, I. Skachko, A. Barker, and E. Y. Andrei, Nature Nanotech. **3**, 491 (2008).

[103] B. Wunsch, T. Stauber, F. Sols, and F. Guinea, New J. Phys. **8**, 318 (2006).

[104] E. H. Hwang and S. Das Sarma, Phys. Rev. B **75**, 205418 (2007).

[105] A. Grüneis, C. Attaccalite, T. Pichler, V. Zabolotnyy, H. Shiozawa, S. L. Molodtsov, D. Inosov, A. Koitzsch, M. Knupfer, J. Schiessling, R. Follath, R. Weber, P. Rudolf, L. Wirtz, and A. Rubio, Phys. Rev. Lett. **100**, 037601 (2008).

[106] For example, see Refs. [352] and [353] which present calculated electron linewidths for sodium arising from the *e*-*e* and the *e*-ph interactions, respectively.

[107] P. E. Trevisanutto, C. Giorgetti, L. Reining, M. Ladisa, and V. Olevano, Phys. Rev. Lett. **101**, 226405 (2008).

[108] C. Attaccalite, A. Grüeneis, T. Pichler, and A. Rubio, preprint available at http://arxiv.org/abs/0808.0786.

[109] X. Wu, M. Sprinkle, X. Li, F. Ming, C. Berger, and W. A. de Heer, Phys. Rev. Lett. **101**, 026801 (2008).

[110] C.-H. Park, F. Giustino, C. D. Spataru, M. L. Cohen, and S. G. Louie, Phys. Rev. Lett. **102**, 076803 (2009).

[111] J. González, F. Guinea, and M. A. H. Vozmediano, Phys. Rev. B **59**, R2474 (1999).

[112] J.-H. Chen, C. Jang, S. Xiao, M. Ishigami, and M. S. Fuhrer, Nature Nanotech. **3**, 206 (2008).

[113] S. Fratini and F. Guinea, Phys. Rev. B **77**, 195415 (2008).

[114] M. L. Cohen, M. Schlüter, J. R. Chelikowsky, and S. G. Louie, Phys. Rev. B **12**, 5575 (1975).

[115] M. Lazzeri, C. Attaccalite, L. Wirtz, and F. Mauri, Phys. Rev. B **78**, 081406(R) (2008).

[116] J. D. Jackson, *Classical Electrondynamics*, 3rd ed. (Wiley, New York, 1998).

[117] S. Das Sarma, E. H. Hwang, and W.-K. Tse, Phys. Rev. B **75**, 121406 (2007).

[118] P. B. Allen and M. L. Cohen, Phys. Rev. Lett. **29**, 1593 (1972).

[119] The relaxed nearest neighbor carbon-carbon distances [b in Fig. 6.1(a)] for pristine graphene, bilayer graphene, and graphite are 1.40 Å, 1.40 Å, and 1.42 Å, respectively. The interlayer distances [d in Fig. 6.1(a)] for bilayer graphene and for graphite are 3.21 Å and 3.26 Å, respectively. The relaxed lattice parameters for monolayer graphene and for graphite are in good agreement with previous calculations [354] as well as with experiments [355, 356].

[120] E. McCann and V. I. Fal'ko, Phys. Rev. Lett. **96**, 086805 (2006).

[121] K. Sugawara, T. Sato, S. Souma, T. Takahashi, and H. Suematsu, Phys. Rev. Lett. **98**, 036801 (2007).

[122] C. S. Leem, B. J. Kim, C. Kim, S. R. Park, T. Ohta, A. Bostwick, E. Rotenberg, H. D. Kim, M. K. Kim, H. J. Choi, and C. Kim, Phys. Rev. Lett. **100**, 016802 (2008).

[123] C. D. Spataru, M. A. Cazalilla, A. Rubio, L. X. Benedict, P. M. Echenique, and S. G. Louie, Phys. Rev. Lett. **87**, 246405 (2001).

[124] A. Grüneis, C. Attaccalite, A. Rubio, D. V. Vyalikh, S. L. Molodtsov, J. Fink, R. Follath, W. Eberhardt, B. Büchner, and T. Pichler, Phys. Rev. B **80**, 075431 (2009).

[125] J. L. McChesney, A. Bostwick, T. Ohta, K. Emtsev, T. Seyller, K. Horna, and E. Rotenberg, arXiv:0809.4046v1.

[126] T. Ando, J. Phys. Soc. Jpn. **75**, 124701 (2006).

[127] M. Lazzeri and F. Mauri, Phys. Rev. Lett. **97**, 266407 (2006).

[128] J.-A. Yan, W. Y. Ruan, and M. Y. Chou, Phys. Rev. B **77**, 125401 (2008).

[129] T. Ando, J. Phys. Soc. Jpn. **74**, 777 (2005).

[130] T. Ando, J. Phys. Soc. Jpn. **76**, 104711 (2007).

[131] S. Pisana, M. Lazzeri, C. Casiraghi, K. S. Novoselov, A. K. Geim, A. C. Ferrari, and F. Mauri, Nature Mat. **6**, 198 (2007).

[132] A. Das, S. Pisana, B. Chakraborty, S. Piscanec, S. K. Saha, U. V. Waghmare, K. S. Novoselov, H. R. Krishnamurthy, A. K. Geim, A. C. Ferrari, and A. K. Sood, Nature Nanotech. **3**, 210 (2008).

[133] A. Das, B. Chakraborty, S. Piscanec, S. Pisana, A. K. Sood, and A. C. Ferrari, Phys. Rev. B **79**, 155417 (2009).

[134] S. Piscanec, M. Lazzeri, F. Mauri, A. C. Ferari, and J. Robertson, Phys. Rev. Lett. **93**, 185503 (2004).

[135] A. Shukla, M. Calandra, M. d'Astuto, M. Lazzeri, F. Mauri, C. Bellin, M. Krisch, J. Karpinski, S. M. Kazakov, J. Jun, D. Daghero, and K. Parlinski, Phys. Rev. Lett. **90**, 095506 (2003).

[136] S. Datta, *Electronic Transport in Mesoscopic Systems* (Cambridge University Press, Cambridge, 1997).

[137] J. B. Oostinga, H. B. Heersche, X. L. Liu, A. F. Morpurgo, and L. M. K. Vandersypen, Nature Mater. **7**, 151 (2008).

[138] A. H. Castro Neto, F. Guinea, N. M. R. Peres, K. S. Novoselov, and A. K. Geim, Rev. Mod. Phys. **81**, 109 (2009).

[139] W.-K. Tse, E. H. Hwang, and S. Das Sarma, Appl. Phys. Lett. **93**, 023128 (2008).

[140] J. M. Dawlaty, S. Shivaraman, M. Chandrashekhar, F. Rana, and M. G. Spencer, Appl. Phys. Lett. **92**, 042116 (2008).

[141] G. Moos, C. Gahl, R. Fasel, M. Wolf, and T. Hertel, Phys. Rev. Lett. **87**, 267402 (2001).

[142] S. Fratini and F. Guinea, Phys. Rev. B **77**, 195415 (2008).

[143] J. Nilsson, A. H. Castro Neto, F. Guinea, and N. M. R. Peres, Phys. Rev. B **76**, 165416 (2007).

[144] E. McCann, Phys. Rev. B **74**, 161403 (2006).

[145] H. Min, B. Sahu, S. K. Banerjee, and A. H. MacDonald, Phys. Rev. B **75**, 155115 (2007).

[146] J. Nilsson and A. H. Castro Neto, Phys. Rev. Lett. **98**, 126801 (2007).

[147] E. V. Castro, N. M. R. Peres, and J. M. B. Lopes dos Santos, phys. stat. sol. (b) **244**, 2311 (2007).

[148] E. V. Castro, K. S. Novoselov, S. V. Morozov, N. M. R. Peres, J. M. B. Lopes dos Santos, J. Nilsson, F. Guinea, A. K. Geim, and A. H. Castro Neto, arXiv:0807.3348v1.

[149] M. Aoki and H. Amawashi, Solid State Commun. **142**, 123 (2007).

[150] P. Gava, M. Lazzeri, A. Marco Saitta, and F. Mauri, arXiv:0902.4615v1.

[151] L. A. Falkovsky, arXiv:0908.3371v1.

[152] T. Ohta, A. Bostwick, T. Seyller, K. Horn, and E. Rotenberg, Science **313**, 951 (2006).

[153] Z. Q. Li, E. A. Henriksen, Z. Jiang, Z. Hao, M. C. Martin, P. Kim, H. L. Stormer, and D. N. Basov, Phys. Rev. Lett. **102**, 037403 (2009).

[154] A. B. Kuzmenko, E. van Heumen, D. van der Marel, P. Lerch, P. Blake, K. S. Novoselov, and A. K. Geim, Phys. Rev. B **79**, 115441 (2009).

[155] A. B. Kuzmenko, I. Crassee, D. van der Marel, P. Blake, and K. S. Novoselov, Phys. Rev. B **80**, 165406 (2009).

[156] A. B. Kuzmenko, L. Benfatto, E. Cappelluti, I. Crassee, D. van der Marel, P. Blake, K. S. Novoselov, and A. K. Geim, Phys. Rev. Lett. **103**, 116804 (2009).

[157] K. F. Mak, C. H. Lui, J. Shan, and T. F. Heinz, Phys. Rev. Lett. **102**, 256405 (2009).

[158] E. V. Castro, K. S. Novoselov, S. V. Morozov, N. M. R. Peres, J. M. B. L. dos Santos, J. Nilsson, F. Guinea, A. K. Geim, and A. H. Castro Neto, Phys. Rev. Lett. **99**, 216802 (2007).

[159] D. S. L. Abergel and V. I. Fal'ko, Phys. Rev. B **75**, 155430 (2007).

[160] L. M. Zhang, Z. Q. Li, D. N. Basov, M. M. Fogler, Z. Hao, and M. C. Martin, Phys. Rev. B **78**, 235408 (2008).

[161] L. Yang, J. Deslippe, C.-H. Park, M. L. Cohen, and S. G. Louie, Phys. Rev. Lett. **103**, 186802 (2009).

[162] W.-K. Tse and A. H. MacDonald, arXiv:0908.0524v1.

[163] L. Benfatto, S. G. Sharapov, and J. P. Carbotte, Phys. Rev. B **77**, 125422 (2008).

[164] E. J. Nicol and J. P. Carbotte, Phys. Rev. B **77**, 155409 (2008).

[165] C. L. Lu, C. P. Chang, Y. C. Huang, R. B. Chen, and M. L. Lin, Phys. Rev. B **73**, 144427 (2006).

[166] F. Guinea, A. H. Castro Neto, and N. M. R. Peres, Phys. Rev. B **73**, 245426 (2006).

[167] C. D. Spataru, S. Ismail-Beigi, L. X. Benedict, and S. G. Louie, Phys. Rev. Lett. **92**, 077402 (2004).

[168] X. Zhao, C. M. Wei, L. Yang, and M. Y. Chou, Phys. Rev. Lett. **92**, 236805 (2004).

[169] L. Wirtz, A. Marini, and A. Rubio, Phys. Rev. Lett. **96**, 126104 (2006).

[170] C.-H. Park, C. D. Spataru, and S. G. Louie, Phys. Rev. Lett. **96**, 126105 (2006).

[171] T.-T. Tang, Y. Zhang, C.-H. Park, B. Geng, C. Girit, Z. Hao, M. C. Martin, A. Zettl, M. F. Crommie, S. G. Louie, Y. R. Shen, and F. Wang, arXiv:0907.0419v1.

[172] T. Ando, J. Phys. Soc. Jpn. **66**, 1066 (1997).

[173] T. Ando, J. Phys. Soc. Jpn. **73**, 3351 (2004).

[174] T. Ando, J. Phys. Soc. Jpn. **74**, 777 (2005).

[175] T. Ando, J. Phys. Soc. Jpn. **76**, 104711 (2007).

[176] T. Ando and M. Koshino, J. Phys. Soc. Jpn. **78**, 034709 (2009).

[177] J. Jiang, R. Saito, G. G. Samsonidze, A. Jorio, S. G. Chou, G. Dresselhaus, and M. S. Dresselhaus, Phys. Rev. B **75**, 035407 (2007).

[178] L. Chaos-Cador and E. Ley-Koo, Int. J. Quantum Chem. **103**, 369 (2005).

[179] F. Wang, D. J. Cho, B. Kessler, J. Deslippe, P. J. Schuck, S. G. Louie, A. Zettl, T. F. Heinz, and Y. R. Shen, Phys. Rev. Lett. **99**, 227401 (2007).

[180] C.-H. Park, F. Wang, and S. G. Louie, *unpublished*.

[181] G. Liu, J. Jairo Velasco, W. Bao, and C. N. Lau, Appl. Phys. Lett. **92**, 203103 (2008).

[182] C. Berger, Z. Song, X. Li, X. Wu, N. Brown, P. N. First, and W. A. de Heer, Science **312**, 1191 (2006).

[183] Y.-W. Son, M. L. Cohen, and S. G. Louie, Phys. Rev. Lett. **97**, 216803 (2006).

[184] Y.-W. Son, M. L. Cohen, and S. G. Louie, Nature **444**, 347 (2006).

[185] M. Y. Han, B. Özyilmaz, Y. Zhang, and P. Kim, Phys. Rev. Lett. **98**, 206805 (2007).

[186] Z. Chen, Y.-M. Lin, M. J. Rooks, and P. Avouris, Physica E **40**, 228 (2007).

[187] L. Esaki and R. Tsu, IBM J. Res. Develop. **14**, 61 (1970).

[188] R. Tsu, *Superlattice to Nanoelectronics* (Elsevier, Oxford, UK, 2005).

[189] M. G. Cottam and D. R. Tilley, *Introduction to Surface and Superlattice Excitations* (Cambridge Univ. Press, Cambridge, UK, 1989).

[190] D. M. Eigler and E. K. Schweizer, Nature **344**, 524 (1990).

[191] M. F. Crommie, C. P. Lutz, and D. M. Eigler, Science **262**, 218 (1993).

[192] H. Hiura, Appl. Surf. Sci. **222**, 374 (2004).

[193] J. C. Meyer, C. O. Girit, M. F. Crommie, and A. Zettl, Appl. Phys. Lett. **92**, 123110 (2008).

[194] J. R. Williams, L. DiCarlo, and C. M. Marcus, Science **317**, 638 (2007).

[195] B. Huard, J. A. Sulpizio, N. Stander, K. Todd, B. Yang, and D. Goldhaber-Gordon, Phys. Rev. Lett. **98**, 236803 (2007).

[196] B. Özyilmaz, P. Jarillo-Herrero, D. Efetov, D. A. Abanin, L. S. Levitov, and P. Kim, Phys. Rev. Lett. **99**, 166804 (2007).

[197] S. Marchini, S. Günther, and J. Wintterlin, Phys. Rev. B **76**, 075429 (2007).

[198] A. L. Vazquez de Parga, F. Calleja, B. Borca, M. C. G. P. Jr, J. J. Hinarejo, F. Guinea, and R. Miranda, Phys. Rev. Lett. **100**, 056807 (2008).

[199] Y. Pan, N. Jiang, J. Sun, D. Shi, S. Du, F. Liu, and H.-J. Gao, arXiv:0709.2858v1.

[200] T. Ando, T. Nakanishi, and R. Saito, J. Phys. Soc. Jpn. **67**, 2857 (1998).

[201] D. P. DiVincenzo and E. J. Mele, Phys. Rev. B **29**, 1685 (1984).

[202] C. Bai and X. Zhang, Phys. Rev. B **76**, 075430 (2007).

[203] W. F. Edwards, Am. J. Phys. **31**, 482 (1963).

[204] F. Guinea, M. I. Katsnelson, and M. A. H. Vozmediano, Phys. Rev. B **77**, 075422 (2008).

[205] T. G. Pedersen, C. Flindt, J. Pedersen, N. A. Mortensen, A.-P. Jauho, and K. Pedersen, Phys. Rev. Lett. **100**, 136804 (2008).

[206] D. Yu, E. M. Lupton, M. Liu, W. Liu, and F. Liu, Nano Research **1**, 56 (2008).

[207] A. L. Vazquez de Parga, F. Calleja, B. Borca, M. C. G. P. Jr, J. J. Hinarejo, F. Guinea, and R. Miranda, Phys. Rev. Lett. **100**, 056807 (2008).

[208] We assume that appropriate constants are subtracted from $V(x)$ and $\alpha(x)$ so that the averages of $V(x)$ and $\alpha(x)$ are both zero.

[209] A similar transform has been performed on the Hamiltonian of a carbon nanotube under a sinusoidal potential [232, 233]. In carbon nanotubes, a finite scattering probability along the periodic direction is given by a boundary condition along the circumferential direction, curvature or magnetic field [232, 233], whereas in graphene, the wavevector component k_y naturally serves the role of scattering along the periodic direction.

[210] If $V(x)$ is even, $\alpha(x)$ is odd [Eq. (10.6) and Ref. [208]]. If we take the complex conjugate of Eq. (10.6) and change x to $-x$, it is evident that $f_l[V]$'s are real.

[211] The matrix M' in Eq. (10.13) belongs to a generalized 2D Weyl Hamiltonian which has previously been employed to describe charge carriers in mechanically deformed graphene or possibly in an organic compound $\alpha-(\mathrm{BEDT}-\mathrm{TFT})_2\mathrm{I}_3$ under pressure (Ref. [357]).

[212] If we remove the assumption that the periodic potential is an even function, Eqs. (10.11) and (10.13) read $M=\hbar v_0\begin{pmatrix} p_x & -if_m p_y \\ if_m^* p_y & -p_x \end{pmatrix}+\hbar v_0\, mG_0/2\cdot I$ and $M'=\hbar v_0\begin{pmatrix} -p_y\,\mathrm{Im}f_m & p_x-i\,p_y\,\mathrm{Re}f_m \\ p_x+i\,p_y\,\mathrm{Re}f_m & p_y\,\mathrm{Im}f_m \end{pmatrix}+\hbar v_0\, m\,G_0/2\cdot I$, respectively. The energy eigenvalue of M' is given by Eq. (10.15). The eigenstate of M' corresponding to Eq. (10.14) is given by $\varphi_{s,\mathbf{p}}=\frac{1}{\sqrt{1+\lambda_{s,\mathbf{p}}^2}}\begin{pmatrix} 1 \\ s\,\lambda_{s,\mathbf{p}}\,e^{i\phi_{\mathbf{p}}} \end{pmatrix}''$, where $\phi_{\mathbf{p}}$ is the polar angle of the vector $s(p_x\hat{x}+p_y\,\mathrm{Re}f_m\,\hat{y})$, and $\lambda_{s,\mathbf{p}}=\left[\sqrt{p_x^2+|f_m|^2p_y^2}+s\,p_y\,\mathrm{Im}f_m\right]/\sqrt{p_x^2+p_y^2\,(\mathrm{Re}f_m)^2}$. In general, $\lambda_{s,\mathbf{p}}$ is not 1, and moreover, varies with the direction of $\mathbf{p}$.

[213] H. van Houten, B. J. van Wees, J. E. Mooij, C. W. J. Beenakker, J. G. Williamson, and C. T. Foxon, Europhys. Lett. **5**, 721 (1988).

[214] J. Spector, H. L. Stormer, K. W. Baldwin, L. N. Pfeiffer, and K. W. West, Appl. Phys. Lett. **56**, 1290 (1990).

[215] U. Sivan, M. Haiblum, C. P. Umbach, and H. Shtrikman, Phys. Rev. B **41**, R7937 (1990).

[216] L. W. Molenkamp, A. A. M. Staring, C. W. J. Beenakker, R. Eppenga, C. E. Timmering, J. G. Williamson, C. J. P. M. Harmans, and C. T. Foxon, Phys. Rev. B **41**, R1274 (1990).

[217] A. Yacoby, M. Heiblum, V. Umansky, H. Shtrikman, and D. Mahalu, Phys. Rev. Lett. **73**, 3149 (1994).

[218] E. Buks, R. Shuster, M. Heiblum, D. Mahalu, and V. Umansky, Nature **391**, 871 (1998).

[219] Y. Ji, Y. Chung, D. Sprinzak, M. Heiblum, D. Mahalu, and H. Shtrikman, Nature **422**, 415 (2003).

[220] D.-I. Chang, G. L. Khym, K. Kang, Y. Chung, H.-J. Lee, M. Seo, M. Heiblum, D. Mahalu, and V. Umansky, Nature Phys. **4**, 205 (2008).

[221] C. W. J. Beenakker, C. Emary, M. Kindermann, and J. L. van Velsen, Phys. Rev. Lett. **91**, 147901 (2004).

[222] A. Palevski, M. Heiblum, C. P. Umbach, C. M. Knoedler, A. Broers, and R. H. Koch, Phys. Rev. Lett. **62**, 1776 (1989).

[223] H. Kosaka, T. Kawashima, A. Tomita, M. Notomi, T. Tamamura, T. Sato, and S. Kawakami, Appl. Phys. Lett. **74**, 1212 (1999).

[224] L. Wu, M. Mazilu, and T. F. Krauss, J. Lightwave Technol. **21**, 561 (2003).

[225] *The Quantum Hall Effect*, edited by R. E. Prange and S. M. Girvin (Springer, New York, 1987).

[226] P. T. Rakich, M. S. Dahlem, S. Tandon, M. Ibanescu, M. Soljacic, G. S. Petrich, J. D. Joannopoulos, L. A. Kolodziejski, and E. P. Ippen, Nature Mat. **5**, 93 (2006).

[227] J. D. Joannopoulos, S. G. Johnson, J. N. Winn, and R. D. Meade, *Photonic Crystals: Molding the Flow of Light* (Princeton University Press, Princeton, New Jersey, USA, 2008).

[228] F. Shedin, A. K. Geim, S. V. Morozov, E. W. Hill, P. Blake, M. I. Katsnelson, and K. S. Novoselov, Nature Mater. **6**, 652 (2007).

[229] K. I. Bolotin, K. J. Sikes, Z. Jiang, M. Klima, G. Fudenberg, J. Hone, P. Kim, and H. L. Stormer, Solid State Commun. **146**, 351 (2008).

[230] V. V. Chelanov, V. Fal'ko, and B. L. Altshuler, Science **315**, 1252 (2007).

[231] J. B. Pendry and D. R. Smith, Sci. Am. **295**, 60 (2006).

[232] Talyanskii, V. I., Novikov, D. S., Simons, B. D., and L. S. Levitov, Phys. Rev. Lett. **87**, 276802 (2001).

[233] D. S. Novikov, Phys. Rev. B **72**, 235428 (2005).

[234] X. Wu, M. Sprinkle, X. Li, F. Ming, C. Berger, and W. A. de Heer, Phys. Rev. Lett. **101**, 026801 (2008).

[235] N. Stander, B. Huard, and D. Goldhaber-Gordon, Phys. Rev. Lett. **102**, 026807 (2009).

[236] A. F. Young and P. Kim, Nature Phys. **5**, 222 (2009).

[237] M. Barbier, F. M. Peeters, P. Vasilopoulos, and J. J. Milton Pereira, Phys. Rev. B **77**, 115446 (2008).

[238] M. R. Masir, P. Vasilopoulos, A. Matulis, and F. M. Peeters, Phys. Rev. B **77**, 235443 (2008).

[239] M. R. Masir, P. Vasilopoulos, and F. M. Peeters, Phys. Rev. B **79**, 035409 (2009).

[240] L. Dell'Anna and A. D. Martino, Phys. Rev. B **79**, 045420 (2009).

[241] S. Ghosh and M. Sharma, J. Phys. Cond. Matt. **21**, 292204 (2009).

[242] T. O. Wehling, A. V. Balatsky, M. I. Katsnelson, and A. I. Lichtenstein, Europhys. Lett. **84**, 17003 (2008).

[243] A. Isacsson, L. M. Jonsson, J. M. Kinaret, and M. Jonson, Phys. Rev. B **77**, 035423 (2008).

[244] P. W. Sutter, J.-I. Flege, and E. A. Sutter, Nature Mater. **7**, 406 (2008).

[245] D. Martoccia, P. R. Willmott, T. Brugger, M. Björck, S. Günther, C. M. Schlepütz, A. Cervellino, S. A. Pauli, B. D. Patterson, S. Marchini, J. Wintterlin, W. Moritz, and T. Greber, Phys. Rev. Lett. **101**, 126102 (2008).

[246] J. Coraux, A. T. N'Diaye, C. Busse, and T. Michely, Nano Lett. **8**, 565 (2008).

[247] A. T. N'Diaye1, J. Coraux, T. N. Plasa, C. Busse, and T. Michely, New J. Phys. **10**, 043033 (2008).

[248] I. Pletikosić, M. Kralj, P. Pervan, R. Brako, J. Coraux, A. T. N'Diaye, C. Busse, and T. Michely, Phys. Rev. Lett. **102**, 056808 (2009).

[249] V. P. Gusynin and S. G. Sharapov, Phys. Rev. Lett. **95**, 146801 (2005).

[250] K. S. Novoselov, E. McCann, S. V. Morozov, V. I. Fal'ko, M. I. Katsnelson, U. Zeitler, D. Jiang, F. Schedin, and A. K. Geim, Nature Phys. **2**, 177 (2006).

[251] The zigzag form of the vector potential we used results in the perpendicular magnetic field of a uniform strength pointing along the $+z$ direction for half the artificial periodicity and along the $-z$ direction for the other half.

[252] Note that these additional massless fermions with $k_x = 0$ are different from those generated at the supercell Brillouin zone boundaries discussed in Ref. [83].

[253] The group velocity along the k_y direction is given by $v_y = v_0 \int_{-L/2}^{L/2} e^{i\alpha(x)}\, dx$ where $\alpha(x)$ for a Kronig-Penney type of superlattice is given by $\alpha(x) = U_0/\hbar v_0 \cdot (|x| - L/4)$ (see Ref. [83]). When Eq. (12.1) is satisfied, $v_y = 0$.

[254] The use of the Dirac equation for this problem is still valid because the new Dirac points are very close to the original Dirac point ($k_x = k_y = 0$), inside the regime where the graphene band is linear. For example, in Fig. 12.1(c), the new massless Dirac points appear at $k_y = 1.1 \cdot 2\pi/L = 0.034$ Å if $L = 20$ nm.

[255] When a vector potential $\mathbf{A}(x) = B\, x\, \hat{y}$ is used, the shift in the center of a Landau state along the x direction is proportional to k_y; hence, in a 1D superlattice periodic along x, the external periodic potential felt by a Landau state varies with k_y, resulting in a finite Landau band width ΔE (Ref. [9]). However, if the level spacing between LLs is much larger than ΔE, the signature of these LLs can be measured from experiments, as in graphene (Refs. [358] and [359]). In our case, we have checked that for the zero-energy LLs plotted in Fig. 5.3, as long as $l_B > L$, ΔE is smaller than 0.2 % of ε_B. Thus, in the conditions considered here, Landau bands can be considered as discrete levels, i. e. , LLs.

[256] In experimentally fabricated TGSs, due to imperfections in periodicity and symmetry of the external potential as well as defects, impurities and finite temperature effects, the energy level where the DOS vanishes will be blurred. However, since the signature of superlattice electronic structure in conventional semiconducting or metallic superlattices are still observed notwithstanding imperfections therein, we expect that this drastic change in the electronic DOS in TGSs will also be observable in experiments.

[257] For a Kronig-Penney superlattice with $L = 20$ nm and $l_B = 2L$ (corresponding to $B = 0.4$ T), the magnetic energy ε_B is 17 meV. In this case, temperature has to be lowered to observe the LL quantization.

[258] L. Brey and H. A. Fertig, Phys. Rev. Lett. **103**, 046809 (2009).

[259] J. W. McClure, Phys. Rev. **104**, 666 (1956).

[260] K. S. Novoselov, Z. Jiang, Y. Zhang, S. V. Morozov, H. L. Stormer, U. Zeitler, J. C. Maan, G. S. Boebinger, P. Kim, and A. K. Geim, Science **315**, 1379 (2007).

[261] G. Grynberg, B. Lounis, P. Verkerk, J.-Y. Courtois, and C. Salomon, Phys. Rev. Lett. **70**, 2249 (1993).

[262] S.-L. Zhu, B. Wang, and L.-M. Duan, Phys. Rev. Lett. **98**, 260402 (2007).

[263] C. Wu, D. Bergman, L. Balents, and S. D. Sarma, Phys. Rev. Lett. **99**, 070401 (2007).

[264] C. Wu and S. D. Sarma, Phys. Rev. B **77**, 235107 (2008).

[265] L. H. Haddad and L. D. Carr, arXiv:0803.3039v1.

[266] L. B. Shao, S.-L. Zhu, L. Sheng, D. Y. Xing, and Z. D. Wang, Phys. Rev. Lett. **101**, 246810 (2008).

[267] *The Physics of the Two-Dimensional Electron Gas*, edited by J. T. Devreese and F. M. Peeters (Plenum, New York, 1987).

[268] E. Ribeiro, E. Müller, T. Heinzel, H. Auderset, K. Ensslin, G. Medeiros-Ribeiro, and P. M. Petroff, Phys. Rev. B **58**, 1506 (1998).

[269] E. Ribeiro, R. D. Jäggi, T. Heinzel, K. Ensslin, G. Medeiros-Ribeiro, and P. M. Petroff, Phys. Rev. Lett. **82**, 996 (1999).

[270] E. Ribeiro, R. Jäggi, T. Heinzel, K. Ensslin, T. G. Medeiros-Ribeiro, and P. M. Petroff, Microelectron. Eng. **61**, 674 (1999).

[271] P. Y. Yu and M. Cardona, *Fundamentals of Semiconductors: Physics and Materials Properties* (Springer, New York, 2001).

[272] The Fourier component W, defined to be the value of the external periodic potential [Fig. 13.1(a)] in Fourier space at the smallest reciprocal lattice vector, is given by $W = \frac{d}{2L} J_1\left(\frac{2\pi d}{\sqrt{3}L}\right) U_0$ where $J_1(x)$ is the first-order Bessel function. For a given U_0, the maximum value of W is $W = 0.172\, U_0$ at $d = 0.663\, L$. In our numerical calculations, we take advantage of this. For comparison, if $d = 0.5\, L$, $W = 0.145\, U_0$.

[273] C. Albrecht, J. H. Smet, D. Weiss, K. von Klitzing, R. Hennig, M. Langenbuch, M. Suhrke, U. Rössler, V. Umansky, and H. Schweizer, Phys. Rev. Lett. **83**, 2234 (1999).

[274] Similar procedures can be applied to find the energy and the wavefunction of massless Dirac fermions with wavevectors near $\mathbf{K}'$ [Fig. 13.1(b)].

[275] Putting Eqs. (13.13) and (13.14) into Eq. (13.12), we obtain, within a phase factor, the eigenvector in the original planewave coefficient basis [Eq. (13.1)]

$$\mathbf{c}(s,\mathbf{k}) = \begin{cases} \sqrt{\frac{2}{3}} \begin{pmatrix} \cos\left(\frac{\theta_{\mathbf{k}}}{2}\right) \\ \cos\left(\frac{\theta_{\mathbf{k}}}{2}+\frac{2\pi}{3}\right) \\ \cos\left(\frac{\theta_{\mathbf{k}}}{2}+\frac{4\pi}{3}\right) \end{pmatrix} & (s=1) \\ \\ \sqrt{\frac{2}{3}} \begin{pmatrix} \sin\left(\frac{\theta_{\mathbf{k}}}{2}\right) \\ \sin\left(\frac{\theta_{\mathbf{k}}}{2}+\frac{2\pi}{3}\right) \\ \sin\left(\frac{\theta_{\mathbf{k}}}{2}+\frac{4\pi}{3}\right) \end{pmatrix} & (s=-1) \end{cases}$$

.

[276] X. Blase, A. Rubio, S. G. Louie, and M. L. Cohen, Phys. Rev. B **51**, 6868 (1995).

[277] K. Watanabe, T. Taniguchi, and H. Kanda, Nat. Mater. **3**, 404 (2004).

[278] K. Nakada, M. Fujita, G. Dresselhaus, and M. S. Dresselhaus, Phys. Rev. B **54**, 17954 (1996).

[279] Z. Chen, Y.-M. Lin, M. J. Rooks, and P. Avouris, Physica E **40**, 228 (2007).

[280] X. Li, X. Wang, L. Zhang, S. Lee, and H. Dai, Science **319**, 1229 (2008).

[281] R. B. Chen, C. P. Chang, F. L. Shyu, and M. F. Lin, Solid State Commun. **123**, 365 (2002).

[282] J. Nakamura, T. Nitta, and A. Natori, Phys. Rev. B **72**, 205429 (2005).

[283] A. Du, S. C. Smith, and G. Lu, Chem. Phys. Lett. **447**, 181 (2007).

[284] Y.-W. Son, J. Ihm, M. L. Cohen, S. G. Louie, and H. J. Choi, Phys. Rev. Lett. **95**, 216602 (2005).

[285] A. Rubio, J. L. Corkill, and M. L. Cohen, Phys. Rev. B **49**, 5081 (1994).

[286] X. Blase, A. Rubio, S. G. Louie, and M. L. Cohen, Europhys. Lett. **28**, 335 (1994).

[287] N. Chopra, J. Luyken, K. Cherry, V. H. Crespi, M. L. Cohen, S. G. Louie, and A. Zettl, Science **269**, 966 (1995).

[288] K. H. Khoo, M. S. C. Mazzoni, and S. G. Louie, Phys. Rev. B **69**, 201401 (2004).

[289] M. Ishigami, J. D. Sau, S. Aloni, M. L. Cohen, and A. Zettl, Phys. Rev. Lett. **94**, 056804 (2005).

[290] Here, we mean by bulk gap the electronic energy band gap of an infinite boron nitride sheet without edges simulated by imposing a periodic boundary condition.

[291] D. Portal, O. Artacho, P. Ordejon, E. Artacho, and J. Soler, Int. J. Quantum Chem. **65**, 453 (1997).

[292] C.-H. Park, C. D. Spataru, and S. G. Louie, Phys. Rev. Lett. **96**, 126105 (2006).

[293] L. Brey and H. A. Fertig, Phys. Rev. B **73**, 235411 (2006).

[294] M. Fujita, K. Wakabayashi, K. Nakada, and K. Kusakabe, J. Phys. Soc. Jpn. **65**, 1920 (1996).

[295] V. Barone, O. Hod, and G. E. Scuseria, Nano Lett. **6**, 2748 (2006).

[296] C. T. White, J. Li, D. Gunlycke, and J. W. Mintmire, Nano Lett. **7**, 825 (2007).

[297] R. Saito, G. Dresselhaus, and M. Dresselhaus, *Physical Properties of Carbon Nanotubes* (Imperial College Press, London, 1998).

[298] J. S. Lauret, R. Arenal, F. Ducastelle, A. Loiseau, M. Cau, B. Attal-Tretout, E. Rosencher, and L. Goux-Capes, Phys. Rev. Lett. **94**, 037405 (2005).

[299] R. Arenal, O. Stéphan, M. Kociak, D. Taverna, A. Loiseau, and C. Colliex, Phys. Rev. Lett. **95**, 127601 (2005).

[300] S. Aloni and A. Zettl, private communication.

[301] C. D. Spataru, S. Ismail-Beigi, L. X. Benedict, and S. G. Louie, Phys. Rev. Lett. **92**, 077402 (2004).

[302] F. Wang, G. Dukovic, L. E. Brus, and T. F. Heinz, Science **308**, 838 (2005).

[303] Y.-Z. Ma, L. Valkunas, S. L. Dexheimer, S. M. Bachilo, and G. R. Fleming, Phys. Rev. Lett. **94**, 157402 (2005).

[304] Y.-Z. Ma, L. Valkunas, S. M. Bachilo, and G. R. Fleming, J. Phys. Chem. B **109**, 15671 (2005).

[305] R. S. Lee, J. Gavillet, M. L. d. l. Chapelle, A. Loiseau, J.-L. Cochon, D. Pigache, J. Thibault, and F. Willaime, Phys. Rev. B **64**, 121405 (2001).

[306] G. Strinati, Phys. Rev. B **29**, 5718 (1984).

[307] C. D. Spataru, S. Ismail-Beigi, L. X. Benedict, and S. Louie, App. Phys. A **78**, 1129 (2004).

[308] H. Ajiki and T. Ando, Physica B **201**, 349 (1994).

[309] B. Arnaud, S. Lebègue, P. Rabiller, and M. Alouani, Phys. Rev. Lett. **96**, 026402 (2006).

[310] L. Wirtz, A. Marini, M. Gruning, and A. Rubio, condmat/0508421.

[311] G. Y. Guo and J. C. Lin, Phys. Rev. B **71**, 165402 (2005).

[312] R. S. Pease, Nature **165**, 722 (1950).

[313] Z. Zhang and W. Guo, Phys. Rev. B **77**, 075403 (2008).

[314] C.-H. Park and S. G. Louie, Nano Lett. **8**, 2200 (2008).

[315] D. Pacilé, J. C. Meyer, Ç. Ö. Girit, and A. Zettl, Appl. Phys. Lett. **92**, 133107 (2008).

[316] W.-Q. Han, L. Wu, Y. Zhu, K. Watanabe, and T. Taniguchi, Appl. Phys. Lett. **93**, 223103 (2008).

[317] C. Jin, F. Lin, K. Suenaga, and S. Iijima, Phys. Rev. Lett. **102**, 195505 (2009).

[318] N. Alem, R. Erni, C. Kisielowski, M. D. Rossell, W. Gannett, and A. Zettl, Phys. Rev. B **80**, 155425 (2009).

[319] P. Gevko, L. Bulusheva, A. Okotrub, V. Koroteev, I. Yushina, L. Bresson, and A. Loiseau, Phys. Stat. Sol. (b) **245**, 2107 (2008).

[320] C.A. Taylor II, S. W. Brown, V. Subramaniam, S. Kidner, S. C. Rand, and R. Clarke, J. Phys. Chem. Solids **65**, 1251 (1994).

[321] K. Watanabe, T. Taniguchi, T. Kuroda, and H. Kanda, Appl. Phys. Lett. **89**, 141902 (2006).

[322] M. G. Silly, P. Jaffrennou, J. Barjon, J.-S. Lauret, F. Ducastelle, A. Loiseau, E. Obraztsova, B. Attal-Tretout, and E. Rosencher, Phys. Rev. B **75**, 085205 (2007).

[323] V. L. Solozhenko, A. G. Lazarenko, J. P. Petitet, and A. Kanaev, J. Phys. Chem. Solids **62**, 1331 (2001).

[324] C. Tarrio and S. E. Schnatterly, Phys. Rev. B **40**, 7852 (1989).

[325] R. D. Carson and S. E. Schnatterly, Phys. Rev. Lett. **59**, 319 (1987).

[326] J. J. Jia, T. A. Callcott, E. L. Shirley, J. A. Carlisle, L. J. Terminello, A. Asfaw, D. L. Ederer, F. J. Himpsel, and R. C. C. Perera, Phys. Rev. Lett. **76**, 4054 (1996).

[327] J. A. Carlisle, E. L. Shirley, L. J. Terminello, J. J. Jia, T. A. Callcott, D. L. Ederer, R. C. C. Perera, and F. J. Himpsel, Phys. Rev. B **59**, 7433 (1999).

[328] D. M. Hoffman, G. L. Doll, and P. C. Eklund, Phys. Rev. B **30**, 6051 (1984).

[329] L. Liu, Y. P. Feng, and Z. X. Shen, Phys. Rev. B **68**, 104102 (2003).

[330] Y. Qi and J. Louis G. Hector, Appl. Phys. Lett. **90**, 081922 (2007).

[331] N. Ooi, A. Rairkar, L. Lindsley, and J. B. Adams, J. Phys.: Cond. Matt. **18**, 97 (2006).

[332] B. Arnaud, S. Lebegue, P. Rabiller, and M. Alouani, Phys. Rev. Lett. **96**, 026402 (2006).

[333] L. Wirtz, A. Marini, M. Grüning, C. Attaccalite, G. Kresse, and A. Rubio, Phys. Rev. Lett. **100**, 189701 (2008).

[334] L. Pauling, J. Am. Chem. Soc. **54**, 3570 (1932).

[335] R. S. Mulliken, J. Chem. Phys. **2**, 782 (1934).

[336] A. L. Allred and E. G. Rochow, J. Inorg. Nucl. Chem. **5**, 264 (1958).

[337] R. T. Sanderson, J. Am. Chem. Soc. **105**, 2259 (1983).

[338] L. C. Allen, J. Am. Chem. Soc. **111**, 9003 (1989).

[339] J. W. Hill, R. H. Petrucci, T. W. McCreary, and S. S. Perry, *General Chemistry*, fourth ed. (Prentice Hall, New Jersey, 2004).

[340] G. Bruno, P. Capezzuto, and M. Losurdo, Vacuum **57**, 189 (2000).

[341] A. D. Becke, J. Chem. Phys. **98**, 5648 (1993).

[342] P. J. Hay and W. R. Wadt, J. Chem. Phys. **82**, 270 (1985).

[343] W. R. Wadt and P. J. Hay, J. Chem. Phys. **82**, 284 (1985).

[344] P. J. Hay and W. R. Wadt, J. Chem. Phys. **82**, 299 (1985).

[345] M. J. Frisch, G. W. Trucks, H. B. Schlegel, G. E. Scuseria, M. A. Robb, J. R. Cheeseman, J. A. Montgomery Jr., T. Vreven, K. N. Kudin, J. C. Burant, J. M. Millam, S. S. Iyengar, J. Tomasi, V. Barone, B. Mennucci, M. Cossi, G. Scalmani, N. Rega, G. A. Petersson, H. Nakatsuji, M. Hada, M. Ehara, K. Toyota, R. Fukuda, J. Hasegawa, M. Ishida, T. Nakajima, Y. Honda, O. Kitao, H. Nakai, M. Klene, X. Li, J. E. Knox, H. P. Hratchian, J. B. Cross, V. Bakken, C. Adamo, J. Jaramillo, R. Gomperts, R. E. Stratmann, O. Yazyev, A. J. Austin, R. Cammi, C. Pomelli, J. W. Ochterski, P. Y. Ayala, K. Morokuma, G. A. Voth, P. Salvador, J. J. Dannenberg, V. G. Zakrzewski, S. Dapprich, A. D. Daniels, M. C. Strain, O. Farkas, D. K. Malick, A. D. Rabuck, K. Raghavachari, J. B. Foresman, J. V. Ortiz, Q. Cui, A. G. Baboul, S. Clifford, J. Cioslowski, B. B.

Stefanov, G. Liu, A. Liashenko, P. Piskorz, I. Komaromi, R. L. Martin, D. J. Fox, T. Keith, M. A. Al-Laham, C. Y. Peng, A. Nanayakkara, M. Challacombe, P. M. W. Gill, B. Johnson, W. Chen, M. W. Wong, C. Gonzalez, and J. A. Pople, gAUSSIAN 03, revision A.1, Gaussian, Inc., Pittsburgh, PA, 2003.

[346] R. A. Kendall, J. Thom H. Dunning, and R. J. Harrison, J. Chem. Phys. **96**, 6796 (1992).

[347] X. Duan, C. Niu, V. Sahi, J. Chen, J. W. Parce, S. Empedocles, and J. L. Goldman, Nature **425**, 274 (2003).

[348] M. Law, D. J. Sirbuly, J. C. Johnson, J. Goldberger, R. J. Saykally, and P. Yang, Science **305**, 1269 (2004).

[349] M. J. Bierman, Y. K. A. Lau, A. V. Kvit, A. L. Schmitt, and S. Jin, Science **320**, 1060 (2008).

[350] M. H. Huang, S. Mao, H. Feick, H. Yan, Y. Wu, H. Kind, E. Weber, R. Russo, and P. Yang, Science **292**, 1897 (2001).

[351] Z. L. Wang and J. Song, Science **312**, 242 (2006).

[352] J. S. Dolado, V. M. Silkin, M. A. Cazalilla, A. Rubio, and P. M. Echenique, Phys. Rev. B **64**, 195128 (2001).

[353] G. Grimvall, Phys. kondens. Materie **6**, 15 (1967).

[354] N. Mounet and N. Marzari, Phys. Rev. B **71**, 205214 (2005).

[355] Y. X. Zhao and I. L. Spain, Phys. Rev. B **40**, 993 (1989).

[356] M. Hanfland, H. Beister, and K. Syassen, Phys. Rev. B **39**, 12598 (1989).

[357] M. O. Goerbig, J.-N. Fuchs, G. Montambaux, and F. Piéchon, Phys. Rev. B **78**, 045415 (2008).

[358] C.-H. Park and S. G. Louie, Nano Lett. **9**, 1793 (2009).

[359] M. Gibertini, A. Singha, V. Pellegrini, M. Polini, G. Vignale, A. Pinczuk, L. N. Pfeiffer, and K. W. West, Phys. Rev. B **79**, 241406 (2009).